Modeling the anaerobic fermentation of CO, H2 and CO2 mixtures at large and micro-scales

Almeida Benalcazar, E.F.

DOI
10.4233/uuid:a152e57f-1c21-4941-b298-55f7b133e2e4

Publication date
2023

Document Version
Final published version

Citation (APA)
Almeida Benalcazar, E. F. (2023). *Modeling the anaerobic fermentation of CO, H2 and CO2 mixtures at large and micro-scales.* [Dissertation (TU Delft), Delft University of Technology, Unicamp, Campinas]. https://doi.org/10.4233/uuid:a152e57f-1c21-4941-b298-55f7b133e2e4

Important note
To cite this publication, please use the final published version (if applicable).
Please check the document version above.

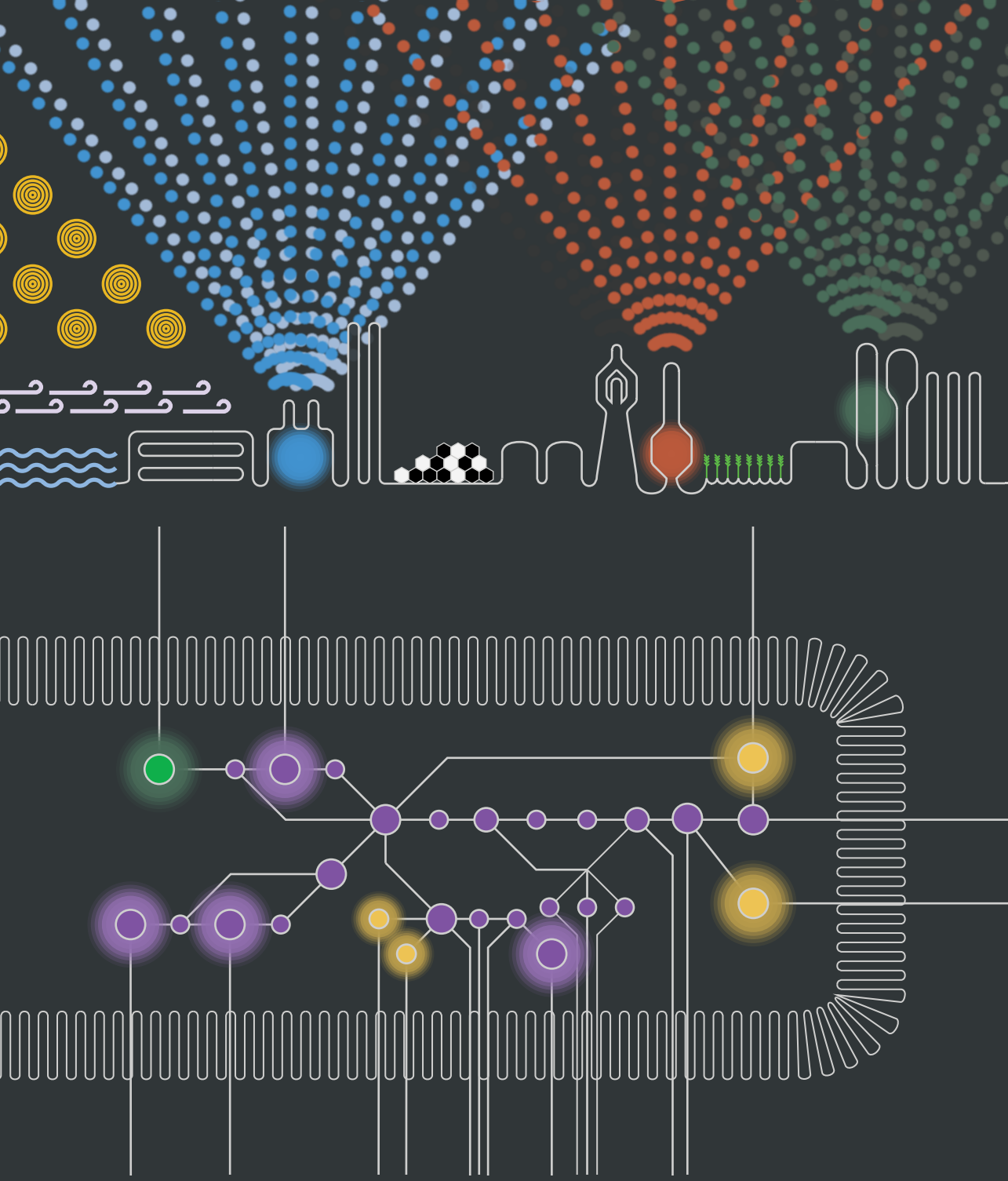

Modeling the anaerobic fermentation of CO, H_2 and CO_2 mixtures at large and micro-scales

Eduardo Almeida Benalcázar

Modeling the anaerobic fermentation of CO, H_2 and CO_2 mixtures at large and micro-scales

Dissertation
for the purpose of obtaining the degree of doctor
at Delft University of Technology,
by the authority of the Rector Magnificus prof. dr. ir. T.H.J.J. van der Hagen
chair of the Board of Doctorates
to be defended publicly on
Monday, December 4th 2023 at 12:30

by

Eduardo ALMEIDA BENALCÁZAR

Master of Science in Life Science & Technology
Delft University of Technology
born in Quito, Ecuador

This dissertation has been approved by the promotors.

Composition of the doctoral committee:

Rector Magnificus	Chairperson
Prof.dr.ir. H.J. Noorman	Delft University of Technology, promotor
Prof.dr. R. Maciel Filho	State University of Campinas, promotor
Dr. J.A. Posada Duque	Delft University of Technology, copromotor

Independent members:

Prof.dr.ir. A.A. Kiss	Delft University of Technology
Prof.dr. A.P. Mariano	State University of Campinas
Assoc.prof.dr. V. Hatzimanikatis	EPF Lausanne
Dr. B. Heijstra	LanzaTech B.V.
Prof.dr.ir. L.A.M. van der Wielen, reserve member	University of Limerick / Delft University of Technology

The studies described in this dissertation were conducted in the context of a joint supervision agreement between the State University of Campinas, Brazil, and the Delft University of Technology, the Netherlands. The project was financed by the BE-Basic Foundation, the Netherlands.

This is a doctoral dissertation from the dual degree program, as agreed between UNICAMP and TU-Delft.

Esta é uma tese de doutorado de co-tutela, conforme acordado entre UNICAMP e TU Delft.

ISBN: 978-94-6384-495-6

Printing by Proefschriftspecialist, the Netherlands

Contents

Samenvatting

Voor het reduceren van klimaatverandering is een transitie vereist, weg van de huidige fossiele koolstofbronnen. Verscheidene technologieën worden ontwikkeld om de uitstoot van fossiele koolstof in de atmosfeer, als een bijproduct van de energieproductie, te beperken. Mengsels van gassen bestaande uit CO, H_2 en CO_2, ook wel synthese gas (syngas) genoemd, hebben de potentie om fossiele koolstofbronnen te vervangen. Elk van deze drie stoffen kan worden geproduceerd vanuit hernieuwbare energie en op basis van koolstof uit hernieuwbare materialen, zoals lignocellulose, biologische gassen of huishoudelijk afval. Dergelijke gasmengsels kunnen worden omgezet in chemicaliën met het reeds ontwikkelde proces van katalytische conversie of door fermentatie van syngas, een technologie die nu volop in ontwikkeling is. Er is nog veel onbekend van het metabolisme van syngas fermenterende micro-organismen en hun gedrag in industriële bioreactoren. De context hiervan wordt beschreven in **Hoofdstuk 1**.

Het werk in dit proefschrift poogt om een conceptueel en rekenkundig kader te ontwikkelen ten einde van *i)* het verkrijgen van nuttige design informatie vanuit syngas fermentatie experimenten op lab schaal, *ii)* het redelijk nauwkeurig voorspellen van parameters, die nu nog onzeker zijn, voor black-box ("zwarte doos") stoichiometrische en kinetische modellen, *iii)* het nauwkeurig kunnen voorspellen van de presentaties van een grote-schaal bioreactor, *iv)* het interpreteren van de grote verscheidenheid aan experimentele resultaten en *v)* het produceren van wiskundige modellen die kunnen helpen in het experimenteel ontwerp en die gericht zijn op het opschalen van het fermentatieproces.

Het meest basale model is een black-box model met een enkele koolstof- en energiebron en een enkel product. Een dergelijk model kan gebruikt worden om conceptuele of runnende industriële processen te simuleren. **Hoofdstuk 2** beschrijft een techno-economische en milieukundige analyse van drie verschillende fermentatieproducten, ethanol, 2,3-butaandiol en hexaanzuur, vanuit biologisch gemaakt synthesegas. Het ontwikkelde productieproces bevat de productie van het biologische synthesegas vanuit vier verschillende grondstoffen die lignocellulose bevatten: suikerrietpulp, maïsafval, eucalyptushout en dennenhout. De grootste bijdragen aan de operationele en kapitale kosten en aan de emissies van broeikasgassen zijn de fermentatie-onderdelen van alle processen. Van alle producten bleek 2,3-butaandiol het meest competitief vergeleken met zijn fossiele tegenhanger, terwijl het productieproces voor ethanol nog verbeterd moet worden.

Een verdere poging werd ondernomen om de betrouwbaarheid van het black-box model te verbeteren, zodat het gebruikt kon worden om een bellenkolomreactor te simuleren voor ethanol productie vanuit gasmengsels met wisselende samenstellingen, van pure CO tot een mengsel van H_2 en CO_2. Dit werk is beschreven in **Hoofdstuk 3.** Het black-

box model werd op twee manieren verbeterd: door het testen van experimentele data over geschatte stoichiometrische en kinetische parameters in het model (biomassa opbrengst, substraatopnamesnelheid, groeisnelheid en substraat half-verzadigingsconstanten, en het valideren van modelvoorspellingen (opgeloste gas concentraties en gas samenstellingen die leiden tot een mogelijk katabolisme van een acetogene bacterie). Het model was niet alleen een voorspellend middel ten behoeve van black-box modellering van syngas fermentatie, maar werd ook een algemeen middel om gerapporteerde experimentele data te interpreteren.

Het verbeterde black-box model werd gekoppeld aan een massaoverdrachtsmodel voor een grote-schaal bellenkolom, gebaseerd op de superficiële gassnelheid en gediscrediteerd op basis van kolomlengte. Hiermee werd de invloed van gasoverdracht getoetst aan de productiviteit, gasbenutting en energieconsumptie.

In **Hoofdstuk 4** wordt dieper ingegaan op het identificeren van combinaties van procesparameters die de technologische prestaties van de bellenkolom bioreactor kunnen verbeteren. Een stochastische simulatie is gedaan om de gevoeligheid van acht variabelen die de fermentatie naar ethanol beïnvloeden te beoordelen. In deze beoordeling werden drie verschillende gasbronnen en hun productieprocessen beschouwd om hun invloed op de economische en milieukundige prestaties van het ethanol-productieproces te bestuderen. De drie bestudeerde gasbronnen zijn, *i)* een CO-rijk afvalgas van de staalproductie, *ii)* syngas gemaakt uit lignocellulose en *iii)* een combinatie van H_2 en CO_2. Het proces vanuit staal afvalgassen was het meest economisch robuuste proces, maar bleek toch de meeste broeikasgassen te produceren gezien de fossiele herkomst van CO.

Om extra kennis te vergaren voor verder onderzoek, werden de productieprocessen geoptimaliseerd met de geïdentificeerde verbeterpunten. Uit deze studie kwam dat de fermentatie van H2/CO2 mengsels, het meeste profiteert van ontwikkelingen in termen van massaoverdracht en microbiële ethanoltoleratie.

Vervolgens werden er drie modellen ontwikkeld om te bestuderen hoe acetogene bacteriën reageren op hun lokale omgeving.

Hoofdstuk 5 beschrijft een verbeterde versie van het black-box model. Dit model simuleert zowel de opname van CO en H_2, alsmede groei en de productie van azijnzuur, ethanol en 2,3-butaandiol. Daarnaast is ook een metabolisch model ontwikkeld gebaseerd op de Wood-Ljungdahl metabole route en energiebehoudsmechanismen in acetogene bacteriën. Beide modellen zijn ontwikkeld met data van stabiele-toestand experimenten en gebruiken als invoer de concentraties van de gasbronnen en hun producten, de pH en de temperatuur. Allebei kunnen ze de drie beste experimentele omstandigheden voorspellen waarin ethanolproductie wordt verhoogd ten koste van azijnzuurproductie, te weten *i)* lage pH, *ii)* hoge azijnzuurconcentraties en *iii)* de

fermentatie van H_2-rijke gassen. Het koppelen van de twee modellen gaf gedetailleerd inzicht in de interne systemen in *Clostridium autoethanogenum*, betreffende *i)* groei, *ii)* azijnzuur export, *iii)* de relatie tussen ATP en Gibbs vrije energieproductie en *iv)* een mogelijke futiele cyclus van waterstofproductie en -consumptie.

Het ontwikkelde metabolisch model diende als basis voor de ontwikkeling van een kinetisch metabolisch model, dat wordt gepresenteerd in **Hoofdstuk 6**. Aangezien het metabolische model metabole routes en reacties samenvoegde, werd gekozen voor een modelstructuur die werkt bij benadering, de linlog-standaard, die veranderingen correleert aan een gefixeerd referentiepunt. De parametrisatie van het model is gedaan op basis van data van een experiment waarin oscillaties worden geproduceerd in een continue fermentatie. Het geparametriseerde model is in staat om het oscillerende gedrag van bacteriën gedurende een experiment te beschrijven met behulp van massabalansen in drie fasen, *i)* het gas, *ii)* de vloeistof buiten de cel en iii) de vloeistof in de cel. Alhoewel het model de nauwkeurigheid mist om informatie te beschrijven betreffende de dynamische metabolische regulaties in de cel, is het te gebruiken *i)* om de dynamiek van metabole poelen te beschrijven op basis van veranderingen in substraat- en productconcentraties buiten de cel, zoals die worden verwacht in grote-schaal bioreactoren, i*i)* het produceren van dynamische condities die ethanolproductie bevorderen. Dit is een eerste stap om te begrijpen hoe de productie van ethanol te controleren is met het design en opereren van een grote-schaal bioreactor. Potentiële verbeterpunten in de modelstructuur werden aangetoond door een analyse van *i)* de fout verbonden aan elke geschatte kinetische parameter en *ii)* de nauwkeurigheid van de voorspellingen van de verschillende opname- en uitscheidingssnelheden.

Summary

The mitigation of global warming requires an urgent shift from the fossil fuel-based productive matrix currently in place. Technological platforms are being developed to reduce the amount of carbon of fossil origin, which is emitted to the atmosphere as a side-product from the production of energy. Gas mixtures containing CO, H_2 and CO_2 are candidates to drive the replacement of such fossil carbon. Each component in the gas mixture called synthesis gas (syngas) can be produced using renewable energy and the carbon from renewable materials, such as lignocellulose, biogas or municipal solid wastes. The production of chemicals from the gas mixtures can be done through the mature thermochemical conversion or through fermentation, a technology still under development. The metabolism of syngas-fermenting microorganisms and their behavior inside large-scale bioreactors are still not well understood. The previous context, detailed in **Chapter 1**, leads to the formulation of this dissertation's research questions and scope.

In overall, the work developed in this dissertation is an effort on building conceptual mathematical frameworks for *i)* extracting design information from syngas fermentation experiments at laboratory scale, *ii)* predict reasonably accurate values of black-box stoichiometric and kinetic parameters that are currently uncertain, *iii)* accurately predict the performance of the large-scale bioreactor, *iv)* interpreting the vast variety of results in reported experiments, and *v)* producing mathematical tools that aid in the planning of experiments aimed at scaling-up the fermentation process.

The most basic of the mentioned framework is a black-box model of bacteria using a single carbon and energy source and a single product. Such model can be used for simulations of conceptual or existing industrial process. **Chapter 2** presents a techno-economic and environmental assessment of three possible products of bio-based syngas fermentation: ethanol, 2,3-butanediol and hexanoic acid. The conceptualized production processes include the site-specific production of the bio-based syngas, from four different lignocellulosic feedstocks: sugarcane bagasse, corn stover, eucalyptus wood and pine wood. The largest contributions to operation and capital costs and for the emissions of greenhouse gases are located at the fermentation unit in all cases. From the products, 2,3-butanediol showed to be competitive with its fossil-based counterpart, while ethanol still needed improvements in the process.

Further efforts were taken to improve the reliability of the black-box model as a predictive tool that allows more detailed simulations of ethanol production in a bubble column bioreactor fed by gas mixtures with different compositions, ranging from pure CO to a mixture of H_2 and CO_2. This work is presented in **Chapter 3**. The improvement of the black-box model was made from two ends, by checking experimental evidence in

literature about the estimated stoichiometric and kinetic constants in the model (biomass yields, maximum substrate uptake and growth rates, and substrate half-saturation constants), and also validating the model's predictions (gas concentrations and compositions that would make the catabolism of acetogenic bacteria feasible). Thus, the model became not only a predictive tool for black-box modeling of syngas fermentation but also a more general framework to interpret reported experimental results.

The improved model of bacteria was then coupled to a mass transfer model of a large-scale bubble column, based on the superficial gas velocity and where the vessel height was discretized, for assessing the influence of gas mass transfer on the bioreactor productivity, gas utilization and power consumption.

The work presented in **Chapter 4** is a further effort to identify combinations of the process parameters that may improve the technical performance of the modelled bubble column bioreactor. A stochastic simulation is performed where eight process variables commanding the bioreactor operation were varied to assess the overall ethanol production process sensitivity to such variables. Three different gas feedstocks, and their production processes were included within the battery limits to understand the effects of the gas feedstock on the overall economic and environmental performance of the ethanol production process; these feedstocks are, *i)* a CO-rich off-gas from steel production, *ii)* lignocellulosic syngas and *iii)* a combination of H_2 and CO_2. The steel off-gas producing the most economically robust process configuration yet the largest greenhouse gas emissions due to the non-fossil nature of the CO-rich gas. To gather additional knowledge on possible focus points for future research, the production processes were optimized considering both the highest performance reported experimentally and potential further improvements. Such assessment found that the fermentation of H_2/CO_2 mixtures may be largely benefited from further developments in mass transfer rates and tolerance to ethanol.

To gain knowledge on how acetogenic bacteria respond to their environment, three more models were developed.

Chapter 5 presents an improved version of the black-box model that allows simulating the simultaneous uptake of CO and H_2, cell growth, and the simultaneous production of acetic acid, ethanol and 2,3-butanediol. In addition, a metabolic model was developed based on the biochemical conformation of the Wood-Ljungdahl pathway and the energy conservation mechanisms in acetogenic bacteria. Both models use the concentrations of the gas feedstocks and the products, as well as pH and temperature as inputs; they were developed using data from experiments at steady state. Both models can reproduce three of the most common experimental conditions under which ethanol production is enhanced over that of acetic acid, the main product of acetogens, *i.e.*, *i)* low pH, *ii)* high

acetic acid concentrations, and *iii)* the fermentation of H_2-rich gases. The coupling between the two models allowed the definition of details about the internal systems in *Clostridium autoethanogenum* important for its fundamental understanding, regarding *i)* growth, *ii)* the export of acetate, *iii)* the relation between ATP and Gibbs free energy production and *iv)* a possible futile H_2 production and consumption cycle.

The designed metabolic network served as the basis for the construction of a kinetic metabolic model, presented in **Chapter 6**. Since the metabolic network lumped conversion pathways and reactions, the chosen kinetic modeling format was approximative, *i.e.*, the linlog format, which correlates changes in reaction rates to changes in substance concentrations with respect to a fixed reference state. The parameterization of the model used data from a reported experiment, where oscillations are produced in a continuous fermentation. The parameterized model can simulate the oscillatory behavior of bacteria during the experiment using mass balances in three phases, *i)* the gas, *ii)* the extracellular liquid and *iii)* the intracellular liquid. Although the model still lacks sufficient accuracy for allowing the extraction of precise information on the dynamic metabolic regulations inside bacteria, it i) is useful for assessing the metabolic pools' responses to dynamic changes in the extracellular concentrations of substrates and products, such as those expected inside large-scale bioreactors, ii) produced first sight to the dynamic conditions that promote ethanol production, a first step towards the understanding on how to control the production of the alcohol from the design and operation of the large-scale bioreactor Lastly, potential improvements in the model structure were targeted through an analysis of *i)* the error linked to each estimated kinetic parameter and the *ii)* accuracy of the predictions of different net uptake and secretion rates.

Chapter 1

General introduction

"I suppose it is tempting, if the only tool you have is a hammer, to treat everything as if it were a nail."

Abraham H. Maslow, *The Psychology of Science: A Reconnaissance*, 1966

1.1. Gas fermentation in the context of climate change mitigation

1.1.1. CO_2 and climate change

As of November 2022, the atmospheric concentration of CO_2 reached 417 ppm and continues to rise at a faster rate each year [1]. Putting this number into context, during the 800,000 years prior to the human industrial revolution, the maximum CO_2 concentration has been estimated at 300 ppm [1,2]. Similar trends have been reported for methane and nitrous oxide, the other two main greenhouse gases (GHG) [3–5]. Such unprecedentedly high concentrations of GHG's are regarded as the main causes of climate change [6]. For the past three decades, scientists have warned about the potential effects of not stopping climate change, *i.e.*, first: rising sea levels, global warming, increased frequency of extreme weather events and shifts in rainfall trends, ultimately: serious disruptions on wildlife diversity, irreversible transformations of ecosystems, breakage of the food supply chains and devastating changes in human society [7].

The responsibility of the offset in the historic patterns of GHG production has been attributed to industrialized anthropogenic activity [8]. The production of heat and electricity, transportation and the manufacturing industries contribute with 49, 21 and 20% of the global GHG emissions, respectively [5] (see Figure 1.1.a). Within the manufacturing industries, the production of metals, chemicals and cement contribute 22, 15 and 13% of the sector's overall emissions, respectively [5] (see Figure 1.1.a). Organized by fuel, the combustion of coal, oil and natural gas generate the 40, 35 and 20% of GHG emissions, respectively [9] (see Figure 1.1.b). Moreover, livestock farming, agriculture, landfills and the activities related to oil, natural gas and coal exploitation generate most of the anthropogenic methane emissions; nitrous oxide emissions are mostly due to agriculture soil management and the combustion of fuels and biomass [8].

The radiative forcing is a measure of the influence that a component of the atmosphere has on the amount of solar energy hitting the outermost layer of the planets' crust [10]. Since the radiative forcing of CO_2 is the highest among the mentioned GHG's (see Figure 1.1.c), researchers and some political and industrial sectors have been pushing for three decades (considering the 1994 Kyoto treaty as the starting point) onto the development and implementation of technologies for capturing this CO_2 and minimizing its generation at the source [11]. The question of how we can accomplish such a transformation in the global socio-economic system generates multidisciplinary academic debate [12,13]. Acknowledging that question as one of the most important questions of our time, this doctoral dissertation does not try to scratch the surface of a possible answer to that

problem; instead, it tries to reduce the uncertainty of a new industrial pathway by which certain patches can be put into place with the objective of starting a transition.

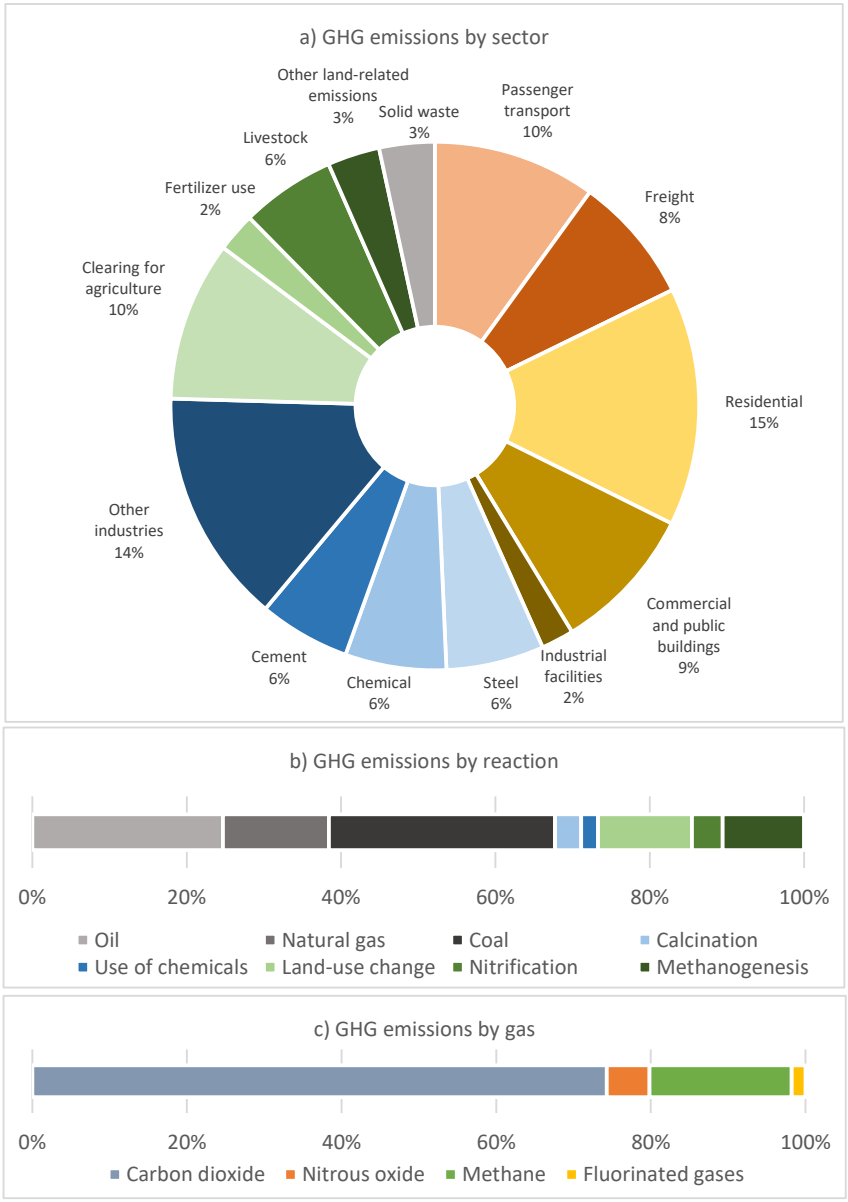

Figure 1.1. Contributions of overall emissions of greenhouse gases, organized a) by sector, b) by chemical reaction producing the gas and c) by specific gas emitted. Data gathered from [14].

1.1.2. The role of carbon capture and storage technolgies

The carbon capture technologies alone aim to separate the gas from the air or from industrial flue-gas streams and store it into plant biomass, liquids or minerals. Since CO_2 is diluted in the air, reforestation and restoration of coastal and marine habitats represent nature-based solutions [15]. A variation from these options involves the design of plants or the fertilization of certain marine environments to improve their natural carbon capture rate and capacities [15]. The artificial capture of CO_2 from industrial flue-gas streams, where it is more concentrated than in air, is achieved mainly using absorption into solvents, and adsorption into solids and membranes [16]. To facilitate the capture process, the concentration of CO_2 in the flue-gas streams can be raised by using improved combustion systems with pure oxygen, for instance. Once artificially captured, CO_2 can be stored for time periods larger than 1000 years into geological formations and deep-sea waters.

The power sector, the largest CO_2 emitting sector, along with other major CO_2 producers in the industrial sector (cement and steel production) slowly started the implementation of carbon capture and storage (CCS) methods when using fossil fuels. However, as CCS in general involves extra fixed and operational costs, its use nowadays is far from being widespread. Nevertheless, the EU, the US and China, the world's three major CO_2 emitters, have programs aiming to reduce 90% of CO_2 emissions by 2050 [16–18].

The implementation of CCS technologies represents a major opportunity for decarbonizing productive sectors where the use of the energy is geographically centralized. On the other hand, for decarbonizing the transportation sector, another major CO_2 emitter, the solution is sought on the production of fuels from alternative feedstocks.

1.1.3. Biomass, a feedstock with low carbon footprint

Apart from being stored, the captured carbon may also be used as a feedstock for the synthesis of commodities, through so-called carbon capture and utilization (CCU). Biomass is a feedstock formed by photosynthesis, the sunlight-powered fixation of CO_2 into glycerol-3-phosphate: one of the most important building blocks for intracellular metabolites and macromolecules in plants [19,20]. Biomass is therefore a renewable feedstock, which within the biorefinery concept can be used for the production of chemicals [21]. If such chemicals were combusted as fuels, *e.g.*, ethanol, the produced CO_2 will create a carbon cycle within the environment.

Its cellulose and lignin-based chemical structure generally gives biomass another name, lignocellulose. Cellulose and lignin are biopolymers formed by saccharide and phenolic

monomers, respectively [22]. Once the polymers are broken and the monomers released, microorganisms can transform them into other substances of commercial interest, such as bulk and fine chemicals. However, the commercial application of lignocellulose is hampered by several challenges related to *i)* the costs of biomass transportation to the production plant, *ii)* the technical challenges, energy use and environmental impacts involved in the polymer breakage, and *iii)* the need for detoxifying the monomers after the pretreatment process [21,23,24].

Moreover, most of currently mature value chains involving fermentations are not based on the use of biomass, but on starch and sucrose from food crops (first-generation feedstocks) *i.e.*, mainly sugarcane and corn. Such is the case for ethanol, the most globally widespread biofuel. In 2017, 121000 million liters of ethanol were produced mostly from 1G feedstocks [25,26]; that throughput represents 6% of what was consumed of fossil gasoline in the same year [27] (corrected by their respective lower heating values - LHV, see Table 1.1).

Table 1.1. Lower heating values of fuels relevant for climate change policy in the context of ethanol production

Fuel	LHV, MJ/kg
Gaseous	
Hydrogen	120.0
Methane	50.0
Natural gas	47.1
Syngas	5.1
Carbon monoxide	10.2
Liquid	
Gasoline	43.4
Diesel	42.6
Ethanol	26.7
Biodiesel (methyl esters)	37.5
Solid	
Charcoal	28.4
Wood (dry)	15.4
Sugarcane bagasse (dry)	15.0

Note: All data was gathered from [28] with the exception of syngas and sugarcane bagasse, which were obtained from [29] and [30], respectively.

The use of dedicated crops for extensive production of biofuels and bulk chemicals is also challenged by the impacts potentially generated during the agricultural stage [21].

Among these impacts lay the environmental runoffs of fertilizers like urea and phosphate, use of water and pesticides, nutrient depletion in soils [31] and the production of nitrous oxides. The possible competition for arable land between food and energy crops is often regarded as one of the main limitations of 1G and 2G feedstocks, however the amount of arable land in the world is much larger than what would be needed to produce commodities. For instance, assuming 5000 L of ethanol are produced from a hectare of beet or sugarcane [32], approximately 0.3 % of the total arable land in the planet (14.0×10^6 km^2 [32]) would be needed to produce enough ethanol to replace gasoline. The yields of second generation-based end products from units of cropped land area are between one third and one half to that of beet or sugarcane [32]. The use of agricultural residues and municipal solid wastes has increasingly gained attention from academia [33] since the environmental impacts and the costs generated during the agricultural stage can be shared with or totally allocated to the food products. Sugarcane bagasse, corn stover, plus rice and wheat straw are the most researched agricultural residues, which traditionally have been combusted for on-site energy production.

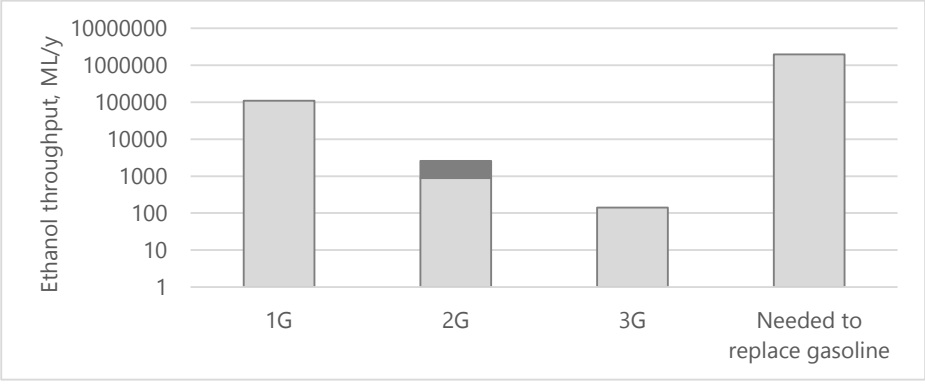

Figure 1.2 Global ethanol throughput. The darker bar over 2G represents the expected production growth until 2024. Data gathered from [25].

The use of 2G feedstocks has also gained attention from industry lately and is currently an essential production route for the European Union's plans of achieving CO_2-neutrality by 2050 [34]. An example is the case of ethanol, of which the throughput from 2G feedstocks has grown to 900 ML/y by 2019 [35] (see Figure 1.2). The throughput is expected to rise to only 1700 ML/y by the year 2024 [25] (see the portion colored with a darker shade of grey above the 2G bar in Figure 1.2) due to the technological and economic challenges outlaid by the pretreatment process [35]. By 2024, the expected 2G ethanol production capacity will represent only 1.3% of the total ethanol production from 1G feedstocks.

1.1.4. Unconventional gaseous sources of carbon and energy

Driven by the technological challenges related to the recovery and use of carbohydrates from the lignocellulosic materials, an alternative conversion process has lately gained attention: gasification. The thermochemical conversion of carbonaceous materials (traditionally coal, petroleum and cokes, more recently biomass and agricultural and municipal solid wastes [36]) into gas mixtures containing CO, H_2 and CO_2 is commonly known as gasification, whereas its gaseous product is known as syngas. Gasification may use oxygen or high-pressure steam as oxidation agents [36]. Syngas can also be produced from methane and other hydrocarbons [37].

Similar to petroleum, gas and coal, syngas is a source of energy and carbon. The production of electricity and heat from syngas is based on its combustion (see Table 1.1), a process that without CCS also releases CO_2 to the atmosphere. As response, due to the need of reducing GHG emissions, prior to the combustion of syngas, modern approaches dictate that most of the CO is converted into CO_2 using the water-gas shift reaction; the CO_2 is then separated from the gas and only the remaining H_2 is combusted. Following the latter processing approach, syngas is also a source of H_2. In fact, coal gasification and the steam reforming of methane and other refinery gases are the source of 78% of the global H_2 production (see Figure 1.3).

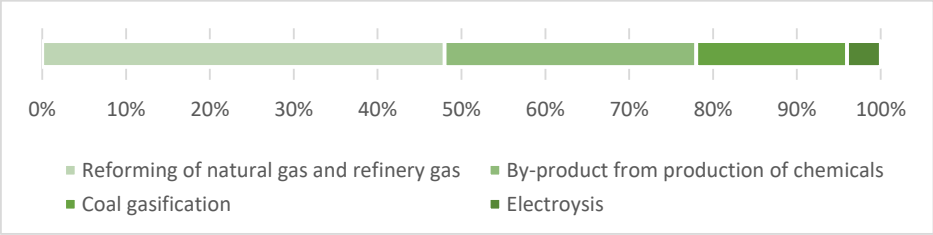

Figure 1.3. Process contribution to global hydrogen production. Data gathered from [38,39].

Out of the 70 Mt/y global H_2 throughput, approximately 96% is obtained from fossil-based feedstocks [38,39]; the remaining fraction is produced through water electrolysis. Besides the production of urea, electrolytic H_2 is used for the production of other chemicals and food processing, among other minor uses [38]. The costs and the environmental impacts linked to this type of H_2 largely depend on the costs and the GHG emissions of the electric energy by which H_2 is produced [40].

Supported by the surge of renewable and low-carbon electric energy (*e.g.*, wind and solar), CO_2 is also an emerging source of carbon for industry. CO_2 captured from the air or industrial off-gases, can be reduced to hydrocarbons, CO, C1 and C2 carboxylic acids and alcohols [41,42]. The electrons for such reductions are provided by electric energy,

directly or indirectly through (electrolytic) H_2, while the conversion is carried out with the aid of chemical catalysts and microorganisms [41,43]. The mentioned conversion routes *i)* are part of CCU, *ii)* bypass the use of biomass, and *iii)* are formed by five main technologies: low-temperature electrolysis, high-temperature electrolysis, microbial electrosynthesis (MES), thermochemical conversions and anaerobic (syn)gas fermentations. The two types of electrolytic conversions plus MES make direct use of electrical current to reduce CO_2. On the other hand, the thermochemical conversions, commonly known as Fischer-Tropsch synthesis, and the anaerobic gas fermentation use the electrons present in the bonds of H_2 and CO. Syngas, CO_2 and CO-containing gas streams, plus H_2 are therefore the main raw materials for CCU.

1.1.5. Gas fermentation as a versatile (yet, currently not well understood) mean for commodities and fine chemicals production

1.1.5.1. Main traits of acetogenic microorganisms

Acetogens are in general microorganisms whose main fermentation product is acetic acid. However, the term 'acetogen' is conventionally used to classify a specific type of ancient anaerobic bacteria and archaea that use the so-called Wood-Ljungdahl pathway (WLP) to fixate the carbon in CO_2 into acetyl-CoA [44]. In a historical overview, acetogenesis, the production of acetic acid from H_2 and CO_2 (see equation 1), was first reported after the study of *Clostridium aceticum*, in 1936 [45]. However, the H_2-powered reduction of CO_2 by unknown microorganisms in sewage was reported four years earlier [46]. The study of acetogenesis by *C. aceticum* stopped after only a few years from its start, during World War II, and the strain was lost [44]. However, acetogenesis was later reported in a thermophilic microorganism, *C. thermoaceticum* [47], whose capacity of synthesizing 3 moles of acetic acid from one mole of glucose (see equations 2 and 3) led to the elucidation of the enzymology of the WLP during the next five decades.

$$4H_2 + 2CO_2 \rightarrow CH_3COOH + 2H_2O \quad (1)$$

Oxidation: $$C_6H_{12}O_6 + 2H_2O \rightarrow 2CH_3COOH + 2CO_2 + 8H^+ + 8e^- \quad (2)$$ [a]

Reduction: $$8H^+ + 8e^- + 2CO_2 \rightarrow CH_3COOH + 2H_2O \quad (3)$$

[a] e^- stands for electrons

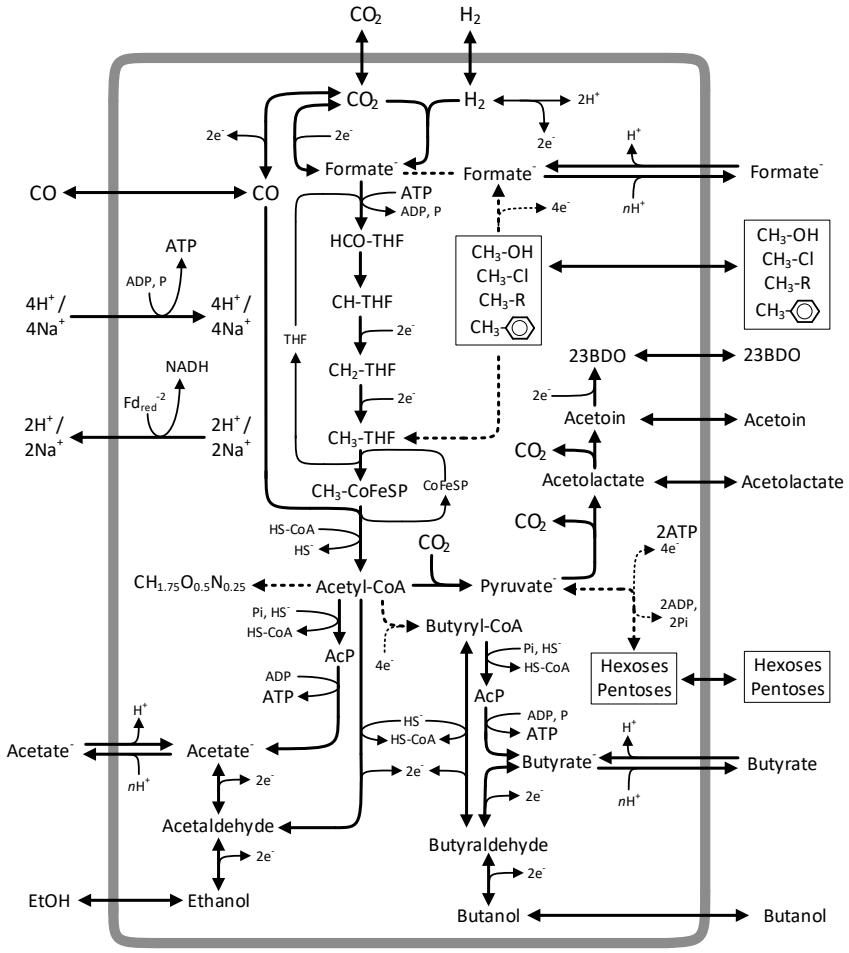

Figure 1.4. Coupling between the Wood-Ljungdahl pathway with the uptake of diverse sources of electrons and carbon and the generation of different metabolites with commercial interest. Figure based on [48–53].

Currently, more than 100 microbial strains have been identified to use the WLP [54], which is defined by Harold Drake as a metabolic pathway that microorganisms use CO_2 as "*i)* a terminal electron-accepting process, *ii)* an energy-conserving process and *iii)* a mechanism for the autotrophic assimilation of carbon" [44]. In their diversity, acetogens are capable of heterotrophically feeding on hexoses and pentoses [47,55], as well as on a variety of C1 compounds like CO, formic acid and methanol [56–58]. The WLP also allows the uptake of methylated compounds such as methyl chloride and other methylated aromatics [49]. Further downstream from the WLP, acetogens may also obtain

energy from primary aliphatic alcohols from C2 to C5 [59,60], diols [60,61] and carboxylic acids [62] (see Figure 1.4.).

Due to such metabolic flexibility, industrial processing units involving acetogens have been idealized within biorefinery concepts [63–66]. However, the first commercialized product of acetogens is ethanol [48,67,68], obtained from gas streams of varied compositions and origins. The first of these production processes uses CO-rich off-gases from steel manufacturing as main source of carbon and electrons for the fermentation. LanzaTech, the company responsible for this development has so far installed six projects which are expected to reach a throughput of 280 ML/y in the coming years. Besides steel off-gases, LanzaTech's projects also involve other types of gases *i.e.*, *i)* syngas derived from the gasification of biomass and *ii)* municipal solid wastes, *iii)* steam reforming of oil-refinery gas and *iv)* mixtures of electrolytic H_2 and captured CO_2 [69]. In this context, the fermentation of gas mixtures containing CO, H_2 and CO_2 interconnects with the utilization of alternative sources of carbon and energy that may further improve the environmental sustainability of transportation fuels [30,70]. Gas fermentation may, therefore, be an important contributor to the Bioenergy with Carbon Capture and Storage (BECCS) concept.

1.1.5.2. The ethanol production puzzle

Despite the success by LanzaTech, reports from academic sources still have not given a clear answer on how ethanol selectivity could be controlled in acetogens feeding on syngas. Most reports acknowledge that acetic acid is the main product of acetogenic microorganisms while ethanol, among other products, is produced only under certain circumstances. According to the structure of the WLP, the synthesis of acetyl-CoA requires the consumption of one molecule of ATP, which is recovered downstream through the production of acetic acid (see Figure 1.4.). Therefore, the substrate-level phosphorylation only secures ATP-neutrality of the WLP. Then, the only source of ATP in acetogens consuming substrates different than carbohydrates is the membrane-based ATP synthase, which is powered by the influx of H^+ or Na^+ ions [62]. Energy conservation is accomplished by the electron transfer from reduced ferredoxin (Fd_{red}^{-2}, $E_0' = -398$ mV [71]) to NADH ($E_0' = -320$ mV [71]), simultaneously enabling the extrusion of H^+ or Na^+ ions to the extracellular space (see Figure 1.4.) and forming a proton motive force.

In scientific literature, there are rather scarce reports of experiments where the selectivity for ethanol surpassed the 80%. One of such reports [72] used a continuous fermentation system of two bioreactors connected in series, the first stage operated at pH 5.5 and the second at pH 4.5. Cells of the popular acetogen *C. ljungdahlii* produced mostly acetic acid (phase known as acetogenesis) in the first bioreactor, where the metabolite accumulates,

and growth of cells is sustained. When cells are introduced into the second bioreactor, equipped with cell recycling, they produced mostly ethanol while growth reportedly stops (phase known as solventogenesis). Another system [73] with a high selectivity for ethanol is a batch fermentation in a 100-L bioreactor. During the first 10 days of this experiment with *C. ragsdalei*, cells mostly produced acetic acid; then, acetic acid production stops, growth slows down, the pH stabilizes at 5 and for the following 36 days, ethanol is the only product generated. In a last reported experiment [74] with a large ethanol selectivity, in contrast with the two former examples, *C. autoethanogenum* was fed with a gas rich in H_2 in a continuous fermentation at pH 5.0. With an ethanol selectivity of only 50%, another experiment where biomass concentrations are controlled with the rate of mass transfer in continuous fermentations, the production of the alcohol was stimulated when the concentration of cells is high (and therefore, the concentration of the electron donors is low) [75]. Thus, among the most common conditions that favor ethanol selectivity are low pH, high concentrations of acetic acid, low concentrations of the electron donors (CO and H_2), plus a dominant H_2 fraction in the gas feed.

Metabolomics, proteomics and transcriptomics-based assessments have suggested that there are no significant differences between the concentrations, activities and the genetic expression of the enzymes in the pathways leading to the production of acetic acid and ethanol, during acetogenesis and solventogenesis [53,75–77]. It has therefore been suggested that ethanol production might be controlled by thermodynamic regulations, while cells are fed with CO-rich gases [53,76]. When bacteria are instead fed with H_2-rich gases, pH might be one of the main variables controlling ethanol production [77].

Due to the scarcity of scale-up protocols for ethanol production from gas fermentation, a systematic approach to scale-up might enlighten the path of development. It is argued that "the perspective of the large-scale" should guide the development and optimization of a biotechnological industrial process [78]. According to this scheme, the first step consists of identifying the rate-limiting mechanisms at the large-scale and then develop a down-scaled experimental configuration that reproduces such rate-limiting mechanisms at the laboratory-scale. The problem for applying this scheme on gas fermentation lies in the fact that even if we gained access to the large-scale bioreactor performance data, a model produced with such data would not be accessible for the public domain. Thus, the bioreactor and the microorganisms in it need to be simulated in a first step using gross assumptions and estimations.

1.2. A process engineering approach to the simulation of microorganisms inside bioreactors

Quantification is an inherent part of the rational design and engineering of industrial processes. The classical approach followed by chemical engineering to the design calculations starts with the construction of mass and energy balances around a defined group of processing units. The idealization of microorganisms inside a bioreactor as a group of processing units connected in parallel allows the implementation of such calculation scheme to the simulation of bioreactors and thus, of bioprocesses. Two types of conversion processes can be achieved in a bioreactor, *i)* fermentation which involves the direct use of living organisms and *ii)* enzymatic reaction, based on extracts derived from microorganisms. The following pages will briefly describe the common techniques employed in the mathematical modeling of fermentation systems in general, and their application to gas fermentation systems specifically.

1.2.1. Mass balances in fermentation processes

Aiming at the fundamental understanding and the further optimization of bioprocesses, the modeling of the fermentation consists of assessing how the environmental conditions set by the bioreactor influence the mechanisms of growth of cell cultures, the consumption of substrates and the generation of products. With different levels of complexity, stoichiometric and kinetic models are used for the study of the interactions between the microbial metabolism and the surrounding physical and chemical environments. Such interactions depend on the timescale. From the fastest reactions, by which cells adapt to small dynamics changes in their environments (*e.g.*, small variations on substrate concentrations), to slower reactions leading to the production of proteins, enzymes and storage metabolites that provide cells with robustness to more severe conditions in their environment (*e.g.*, adaptation for the consumption of a second substrate after the depletion of the first). Metabolic kinetic models can reproduce the fast interactions while steady state models reproduce the longer-term behavior of microorganisms. Both types of models are described as follows.

1.2.1.1. Steady state models

The earliest task in understanding the behavior of fermentation processes, similar to the (in)organic reactions in the chemical industry, is to learn about the yields of the conversion process, from reactants (or substrates) to products.

In the most basic approach, the group of cells performing a fermentation is regarded as a black-box (BB), where all the intracellular biochemical information is neglected [79].

Generally, BB models are used as predictive tools that use the concentrations of substances and pH (variables measured during experiments) in the fermentation broth as inputs, while the net consumption and secretion rates of the substances containing most of the carbon and electrons are the outputs. The inputs and outputs are correlated through a number of kinetic expressions, defined by the degrees of freedom (DOF) of the system. The number of DOF is equal to the difference between the number of substances intervening in the microbial conversion and the number of conservation constraints [80]. The balances of the most abundant elements in the biological systems (*i.e.*, carbon, hydrogen, oxygen, nitrogen, and the electric charge), are common conservation constraints. Balances of other elements (*e.g.*, sulfur, iron, manganese, chlorine), significant for the electron donor and acceptor configuration of specific microorganisms or microbial consortia, can also be used as conservation constraints [80]. Lastly, equilibrium relations can also be used as constraints.

The first kinetic models of fermentation processes [81–83] were developed for microbial growth and substrate consumption after the invention of the chemostat [81], an experimental tool that allowed taking chemical 'snapshots' of microbial metabolism at pseudo-steady state at a fixed (average) specific growth rate; or in other words, when the concentrations of intra and extracellular substances are 'almost' constant in time. The classical kinetic equations, Monod's [81] and Herbert-Pirt's [82,83], proposed between 1949 and 1965, consider cells as black-boxes and they continue to be used in current days for *e.g.*, bioreactor sizing and design, and also for simple links between detailed stoichiometric models of metabolism with the microbes' environment [79,84–86].

A simple example where the two classical equations are applicable is the aerobic growth on glucose. In such system, there are six species, glucose, oxygen, CO_2, water, cells, and a nitrogen source. Carbon, hydrogen, oxygen, and nitrogen elemental balances can be established between these species and therefore, the number of DOF is 6 – 4 = 2. A Monod equation will describe the consumption of glucose while the Herbert-Pirt relation will describe biomass growth.

In increasing level of detail, stoichiometric models of metabolism (or metabolic models) are used to gain knowledge about the intracellular distribution of, *e.g.*, carbon, electrons, or specific substances, aiming at identifying ways (though control of the fermentation process variables or metabolic engineering) to optimize the functioning of the microorganism towards *i)* a more efficient use of the carbon and electrons in the substrate, *ii)* faster production of a certain product, *iii)* faster growth, or *iv)* improved tolerance to determined conditions provided by the bioreactor [79].

Metabolic models are constructed from the knowledge about the enzymology of metabolic pathways and the physiology of the studied microbe(s) [80]. The largest and

more complex stoichiometric models describe the production of the cells' building blocks *i.e.*, aminoacids, nucleic acids, lipids, and carbohydrate oligomers; these models are called genome-scale models (GSM) [87]. GSMs are specific for each microorganism and are constructed from predictions based on genetic information, *i.e.*, specific intracellular reactions are attributed to certain parts of the genetic code [87]. Metabolic models, in general, are assembled within large matrices containing the reactions as columns and the metabolites as rows. The number of DOF is also applied to link the influence of the extracellular conditions and the rates at which the intracellular reactions occur.

In any case, the definition of the level of detail and complexity of a model fundamentally depends on its purpose, which should be defined during the earliest stages of the study of a certain microbial conversion process.

1.2.1.2. Kinetic metabolic models

The combination of large kinetic metabolic models with dynamic simulations of bioreactors, for instance by computational fluid dynamics, are currently powerful high-resolution tools for the design and optimization of industrial bioprocesses [88].

Traditional kinetic models of enzymatic reactions follow a mechanistic approach. Mechanistic kinetic equations predict the rate of specific enzymes and hold valid for a wide range of concentrations of the substances involved. In such models the enzyme reaction rates are defined as functions of: *i)* the concentrations of more than one substrate, *ii)* the presence or absence of activators or inhibitors and, *iii)* allosteric regulatory effects caused by metabolites from other metabolic pathways [79]. The mathematical structures of such rate equations are determined by extensive studies of the enzymes in vitro [89], a highly time and resource-consuming task [90].

Moreover, extending the applicability of mechanistic models to use them as systems of equations to simulate the dynamic behavior of an entire metabolic pathway involve the inherent necessity of estimating a large number of kinetic parameters; this task is made based on in vivo dynamic intracellular data gathered from perturbation experiments [89,91]. However, it is questioned whether all the kinetic parameters can be actually determined through such experiments that usually produce rather small variations in intracellular concentrations of metabolites because cells strive for intracellular stability, *i.e.*, homeostasis [90].

Perturbation experiments consist of provoking changes in the intracellular fluxes and the concentrations of metabolites within specific parts of metabolism at steady state using external stimulus [92]. Such stimulus, or perturbations, are designed specifically to produce a dynamic response on the assessed parts of metabolism [92]. For instance,

perturbations can be pulse or step changes of the concentrations of products or substrates, pH, and temperature, among others. To grasp the characteristics of the metabolic dynamic response, many cell samples have to be withdrawn in short time intervals on the scale of deciseconds (1 ds = 0.1 s); this task involves rapid sampling of the fermentation broth and cells [93], followed by standard metabolomics, transcriptomics and proteomics. The unknown kinetic parameters in a predictive model are then estimated by minimizing the mismatch between the experimental data and the model's generated results [94].

It is argued that during perturbation experiments, cells allow only small variations of the intracellular concentrations of metabolites (due to homeostasis) around a reference value [90]. Therefore, the use of mechanistic kinetics may be deemed unnecessary [95]. As an alternative, approximative kinetic models have been developed in literature, which despite being valid for only narrow ranges of the intracellular concentrations of metabolites, are simpler than mechanistic approaches and involve the estimation of a smaller number of parameters [94]. The performance of approximative kinetic models in dynamic simulations of metabolism has been proven appropriate [94] and they allow the identification of targets (*e.g.*, rate-limiting reactions or metabolite pools) for metabolic engineering [96] and to guide the engineering design of industrial bioreactors [88].

1.2.2. Energy balances in fermentation processes

In parallel to the early development of microbial kinetics in the 1950's and 1960's, a different mathematical tool for studying living systems appeared: the non-equilibrium thermodynamics (NET). One of the first works that used this concept on biological systems did not intend to answer a quantitative question, it addressed instead a rather philosophical one, 'what is life?' [97]. That work explores, besides many others, the idea that a living organism is not a system at equilibrium. Equilibrium would mean that the organism is dead. A living organism is an open system which feeds on substrates and electrons while producing products and more identical organisms through reproduction [98]. The application of NET to microbial fermentations has led to the development of mathematical and conceptual frameworks that allow predicting *i)* product yields, *ii)* the stoichiometry of metabolic reactions, *iii)* cell physiology and systems biology and *iv)* the reasonably accurate simulations of intracellular mechanisms, *e.g.*, the export of carboxylates [52,99].

Under the scope of Biothermodynamics, a living cell is an 'energy transducer', where one exergonic reaction (catabolism) powers another endergonic reaction (anabolism) (see Figure 1.5) [100]. This coupling between the two parts of metabolism is however not 100%

efficient, thus part of the energy released through catabolism is transformed into entropy and enthalpy [98,101].

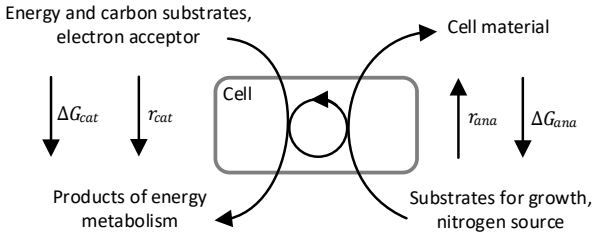

Figure 1.5. Schematic representation of the cell as the energy transducer. The abbreviations 'r_{cat}' and 'r_{ana}' refer to the rates of catabolism and anabolism, respectively. Figure adapted from [100].

Cellular growth is a highly irreversible process, yet it is spontaneous; therefore, it is coupled to the production of entropy. In cells, the production of highly-ordered cellular structures is not linked to the reduction of entropy levels. According to an entropy balance of cells, as open systems [98] (see equation 4), the change in the entropy levels of the open system equals the sum of all the entropy fluxes exchanged with the environment plus the rate of entropy production (S_{prod}). The term Q/T is the enthalpy exchanged with the environment, a parameter measurable using calorimetry [98]. The flow of substances entering and leaving the cells (including newly formed cells; the terms $q_i S_i$ and μS_x are also entropy exchange routes with the environment.

$$\frac{dS}{dt} = \frac{Q}{T} - \sum_i S_i q_i - S_x \mu + S_{prod} \quad (4)$$

The entropy change in the cell (dS/dt) should approach zero to avoid internal disordering in the cells. Therefore, the sum of the three first terms in the right of the equation, should be lower than zero to balance the production of entropy. The term $S_x \mu$ is generally low because of the high order in the newly produced cells. Considering that the q-rates of the substances consumed by the cells are negative by definition, the uptake of generally high-entropy substrates produces large amounts of entropy in the cell; such production is balanced by *i)* the production of high-entropy products, such as gases (*e.g.* CO_2), and/or *ii)* the production of large amounts of heat or enthalpy (a highly positive Q).

More detailed balances could be made at the level of the energy changes in each intracellular reaction. However, there are currently many gaps in the understanding of the multiple interactions between substrates, products, the enzymes and the environment surrounding them (*e.g.* ionic strength, pH) [102,103]. The development of Metabolic Thermodynamics is, in this sense, limited by the accuracy of metabolomics; a calculation

could not proof the feasibility of the glycolysis using ranges of measured intracellular concentrations [104].

1.2.3. Chronology on the development of models for syngas fermentation

During the past decade, from 2011 to 2021, several modeling strategies have been applied to syngas fermentation, from black-box models to the most complex genome-scale models. The first modeling efforts focused on proposing a genome-scale reconstruction for the strain *C. ljungdahlii* [105]. During the next year, in 2014, a kinetic expression that describes CO uptake rate [106] was derived and the first exploration on the economic feasibility of an ethanol production process based on syngas fermentation was published [107]. Since its publication, Mohammadi's kinetic expression [106] has been used in most simulations of acetogens. Chen et al. [84], coupled that expression with the GSM model by Nagarajan et al. [107] and a mass transfer model to simulate a large bubble column bioreactor. In the subsequent years, modifications have been proposed to Mohammadi's expression [108], GSM reconstructions have been derived for five more acetogens [109] and the first report about a kinetic model of metabolism was published [110]. Most of the mentioned reports only consider the mass balances within their scope, yet there are reports about *i)* assessments on the energetics of acetogenic bacteria [111,112], *ii)* thermodynamic feasibility assessments applied to certain intracellular processes [113] and *iii)* the application of thermodynamic constraints to a genome-scale model [114]. Lastly, although numerous simulations of ethanol production have been reported, the production of other substances have also been simulated using models of different levels of complexity [115–117].

1.3. Scope and outline of this dissertation

The amount of experimental information gathered by multiple authors on the anaerobic fermentation of gas mixtures containing CO, H_2 and CO_2 is vast. Experimental works have been reported for different strains of acetogens, growing with different gas feed compositions, fermentation broth compositions, at different values of pH, temperatures, bioreactor configurations and sizes. Some experiments aiming at gaining fundamental understanding about the mechanics of acetogenic metabolism, others aiming at withdrawing stoichiometric and kinetic parameters to be implemented in bioreactor and bioprocess design. It is, therefore, a challenge to build one common framework with wide applicability to acetogenic organisms that can be used for the purpose of *i)* extracting design information from syngas fermentation experiments at laboratory scale, *ii)*

accurately predict the values of black-box stoichiometric and kinetic parameters that are currently uncertain, *iii)* accurately predict the performance of the large-scale bioreactor, *iv)* interpreting the vast variety of results in reported experiments, and *v)* producing mathematical tools that aid in the planning of experiments aimed at scaling-up the fermentation process.

This dissertation was designed embracing those challenges by asking these questions: "for the industrial fermentation of CO, H_2 and CO_2 gas mixtures, *i)* how does the selection of the product, the feedstock, the bioreactor operation conditions and the energy sources impact on the overall process economic and environmental performances, and *ii)* what dependencies are there between the environmental conditions given by a large-scale bioreactor and the growth of cells, their uptake of the gases, and the selectivity between the catabolic products?"

The disentanglement of those questions led to the identification of four sub-questions:

- Is the production of ethanol, 2,3-butanediol and hexanoic acid from lignocellulosic biomass-based syngas fermentation economically feasible and what are the environmental impacts related to their production?
- How reliable are the results obtained from the simulation of bacteria with a black-box model and what can we learn about the operation of the syngas fermentor with such model?
- What are the impacts of the gas feedstock selection, and the bioreactor operation conditions on the economic and environmental performances of a syngas fermentation-based ethanol production process?
- How do the concentrations of substrates and products, pH and temperature in the bioreactor influence on growth, substrate uptake and product secretion by *C. autoethanogenum* developing under steady state and under dynamic conditions?

The answering of the sub-questions subdivided this dissertation into two clearly distinct parts: one that looks at the large industrial-scale and another that dives into metabolic modeling of acetogenic bacteria.

As starting point, the industrial-scale is simulated using a black-box model of bacteria consuming one substrate while producing one product at a time.

As recommended in [118], this work began "with the end in mind"; the end being the desired industrial application of this technology. **Chapter 2** presents a techno-economic and environmental assessment of three possible products of a bio-based syngas fermentation process, ethanol, 2,3-butanediol and hexanoic acid. The syngas production process from four different lignocellulosic feedstocks is also included within the battery

limits of the process. The black-box model was further improved in **Chapter 3**, where the structure of the model and the results delivered by it, regarding only ethanol production, were validated. The validation allowed assessing the applicability of the model as a general framework to interpret the vast variety of reported experimental results from syngas fermentations. The link between the black-box model and a mass transfer model of a large-scale bubble column allowed estimating technical performance indicators of the bioreactor at a defined set of operation parameters. The possibilities for improvement of the technical performance of the conceptual bioreactor are assessed in **Chapter 4**, where a stochastic simulation is performed changing eight process variables commanding the fermentation to assess their sensitivity to the process performance. Three gas feedstocks are included within the process battery limits to assess the influence of the gas feedstock selection on the process performance. To identify focus points for future research, the production processes were optimized with and without current technological constraints of the gas fermentation technology.

This first part of the dissertation is followed by the construction of three more complex models of acetogenic bacteria (one black-box, one metabolic at steady state, and one metabolic kinetic) to extract information about the steady state and dynamic metabolic regulations responsive to the environment surrounding bacteria.

Chapter 5 presents a further improved version of the black-box model and a metabolic model, both that simulate the simultaneous consumption of CO and H_2, cell growth and the production of acetic acid, ethanol and 2,3-butanediol. The inputs for these two models are the concentrations of the gases in the liquid, as well as the concentrations of the products, pH and temperature. The coupling between the black-box and the metabolic models allowed the definition of details about the internal systems in *C. autoethanogenum*, regarding *i)* growth, *ii)* the export of acetate, *iii)* the relation between ATP and Gibbs free energy production and *iv)* a possible futile H_2 production and consumption cycle. The constructed metabolic network served as the basis for the construction of a kinetic metabolic model, presented in **Chapter 6**. Since the metabolic network includes lumped pathways and reactions, the chosen kinetic modeling format is approximative: the linlog format, which correlates changes and rreaction rates to changes in substances concentrations with respect to a fixed reference state for the rates and concentrations. The parameterization of the model used data from a reported experiment, where metabolic oscillations are described in a continuous fermentation. The parameterization of the kinetic model involved the minimization of the mismatch between the experimental concentrations of substances and those calculated by the model. The parameterized model reproduces the experimental oscillations, yet with a considerable error. Therefore, no information about the dynamic regulations in bacteria

could be extracted from the modeling approach. Still, potential improvements in the model structure were targeted.

Chapter 7 summarizes the conclusions derived from this project as well as the proposals for future research aimed to the deployment of syngas fermentation in industry.

Lastly, **Chapter 8** contains all the references from literature that are cited throughout the present dissertation.

Chapter 2

Production of bulk chemicals from lignocellulosic biomass via thermochemical conversion and syngas fermentation: a comparative techno-economic and environmental assessment of different site-specific supply chain configurations

This chapter is based on the article:

Eduardo Almeida Benalcázar, Baudine Gevers Deynoot, Henk Noorman, Patricia Osseweijer and John Posada, 2017, "Production of bulk chemicals from lignocellulosic biomass via thermochemical conversion and syngas fermentation: a comparative techno-economic and environmental assessment of different site-specific supply chain configurations", Biofuels, bioproducts and biorefining, 11(5), 861-886, DOI: 10.1002/bbb.1790

"Yo soy de los del montón
no soy flor de invernadero
soy como el trebol campero
crezco sin hacer barullo
me apreto contra los yuyos
y así lo aguanto al pampero"

Atahualpa Yupanqui, *Copla del payador perseguido*, 1973

2.1. Introduction

The continuous growth of global energy and materials demands, added to the consequent depletion of fossil resources, have given rise to concerns on how to guarantee a continuous supply of products while at the same time limiting the rise of the average global temperature to 2 °C [119]. Thus, sustainable production of bio-fuels and bio-chemicals through novel routes has been encouraged to reduce dependency on non-renewable resources, better cope with volatility of crude oil prices, and mitigate the growing greenhouse gas emissions [119,120]. Feedstocks such as biomass and other short-cycled carbon sources, *e.g.* CO, CO_2 and CH_4, are being investigated as possible replacement of petroleum and its derivatives [121].

Currently, commercial-scale production of bio-based chemicals and fuels is mainly done from sugars, starch and oil-containing crops, although ethical and moral debates have arisen since these feedstocks have traditionally been used for food and feed purposes. In contrast, waste and lignocellulosic biomass have no possible competition with food [21].

Biomass can, in general, be processed by two main technological platforms: biochemical and thermochemical. The former, based on the enzymatic (biochemical) hydrolysis of (ligno)cellulose yields sugars, while the latter, based on the thermochemical conversion of biomass yields mixtures of oils (tars) and gases. Synthesis gas (commonly referred to as syngas) is the product of thermochemical gasification, a process carried out at temperatures ranging between 750 and 1000 °C. Syngas is a gas mixture containing mainly hydrogen, carbon monoxide and carbon dioxide, and small fractions of methane, hydrogen sulfide, ammonia and tars [122]. The composition of syngas depends highly on the type of feedstock, design of the gasifier, type of gasifying agent and processing conditions [123]. Syngas is considered as one of the most prominent chemical platforms for biorefineries [124]. Syngas is currently mainly produced from fossil resources for heat and power generation or it is alternatively converted into fuels and industrial chemicals by catalytic Fischer-Tropsch synthesis [125] and fermentation [48] processes.

Acetogenic bacteria are commonly considered as syngas fermentation workhorses since they are able to utilize CO, H_2 and CO_2 as substrates by withdrawing electrons from H_2 and CO. Their carbon fixation into acetyl-CoA follows a metabolic route known as the Wood-Ljungdahl pathway [48,51]. These bacteria can then produce a variety of substances from syngas, *e.g.*, acetate [126], ethanol [126], butyrate [65], propionate [127], butanol and hexanol [128], 2,3-butanediol, lactate [129] and polymers (*Rhodospirillum bacteria*) [130]. Additionally, fermentation of syngas could drive the production of a wider range of products through further metabolic engineering [131,132] and bio-process integration (*e.g.* towards medium chain fatty acids) [133].

The thermochemical conversion of biomass offers potential advantages over the biochemical route, for instance: *i)* higher carbon yields, *ii)* simpler process configuration, *iii)* more flexibility on feedstock admission and product composition, and *iv)* wider scale-up possibilities [134,135]. Moreover, fermentation also shows possible advantages over the catalytic conversion of syngas since microorganisms can: *i)* work under moderate temperatures and pressures; *ii)* be more tolerant than chemical catalysts to poisoning by sulphur, tars and chlorine; *iii)* accept a wider range of gas compositions; and *iv)* achieve higher conversions and yields [48,125,136,137]. Therefore, a hybrid process, combining thermochemical conversion of biomass and syngas fermentation, could help to reduce capital and operation costs as well as environmental impacts in the production of biofuels and biobased chemicals.

Until 2016, two major companies were working to achieve commercial application of the syngas fermentation technology, INEOS Bio and LanzaTech. However, it was published that the former, which uses lignocellulosic biomass and municipal solid waste as feedstocks for gasification, has produced "very little" ethanol from its 30-million L/y plant due to cyanide toxicity, and is currently selling the plant (Sapp M (www.biofuelsdigest.com)). On the other hand, LanzaTech, which uses mainly CO-rich flue gases from steel industry [48], seems to have successfully developed the fermentation technology, since it has signed an agreement with Primetals and ArcelorMittal for the design of a $96 million producing facility, which was constructed in the latter's steel plant in Ghent, Belgium (http://corporate.arcelormittal.com)) by mid-2017. Initial production started by the end of 2020 and full production has been delayed to the fourth quarter of 2023. This is the first 47-kton-per-year project for the production of ethanol via gas fermentation to be built in Europe (Lane J (www.biofuelsdigest.com)).

Although the syngas fermentation platform has received significant attention in the last years, there is still limited information available regarding integrated assessments of technical, economic and environmental aspects of syngas production from lignocellulosic biomass and its subsequent fermentation into biochemicals and biofuels [138–141]. Therefore, this study presents the design and assessment of entire site-specific supply chains and manufacturing processes (biomass production and delivery, biomass gasification into syngas and cleaning, syngas fermentation into biobased products, and final recovery and purification) for the production of three biobased products, namely: ethanol, 2,3-butanediol and hexanoic acid. For the design of the site-specific supply chains, three locations and four feedstocks are considered as follows: Brazil (with sugarcane bagasse and eucalyptus wood as feedstocks), the United States (with forestry residues and corn stover as feedstocks), and the Netherlands (where these four feedstocks can be imported for further processing into the three biobased products). The

techno-economic and environmental assessments were performed to evaluate and compare the effects of different processing configurations and operating conditions at multiples stages of the supply chains. At last, a sensitivity analysis was performed to both analyze the robustness of the designs and identify possible improvements.

2.2. Methodology

A combination of different methods was applied to develop the conceptual designs of the supply chains and processes, and also to perform the techno-economic and environmental assessments. A detailed explanation is provided in the following sub-sections.

2.2.1. Supply chain and process design

The supply chains considered in this study consist of four processing stages: biomass supply, gasification, syngas fermentation and downstream processing (DSP). Data concerning the type of operations and processing conditions were obtained from scientific literature on experimental work at either laboratory or pilot scale.

The production scale for ethanol production was defined from an average plant producing second generation bioethanol, *i.e.*, 240000 m^3/y (189.4 kton/y) (Hoagland K (biomassmagazine.com)). In the cases of 2,3-butanediol and hexanoic acid, the production scales were set considering that the input of syngas to the fermentation unit was the same as for the ethanol production, in order to establish a common ground for comparison. Therefore, the required biomass supply was calculated accordingly for each case (each type of biomass has different yields to syngas as explained in Sections 2.2.1.1. and 2.2.1.2).

2.2.1.1. Biomass supply

Different biomass supply configurations were designed considering four different feedstocks: forestry residues (FR) and corn stover (CS), produced in the United States (US); and sugarcane bagasse (SB) and eucalyptus wood (EW), produced in Brazil (BR). The Netherlands (NL) has been included only as location for processing, which means that biomass is imported from the other two locations and then processed first into syngas and then into one of the biobased products. The four feedstocks were selected based on availability on the production site, price, and composition.

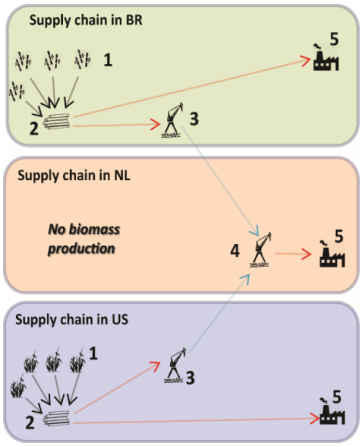

Figure 2.1. Configuration of supply chains according to the geographical location. Arrows represent transport by truck (black), train (red), and ship (blue). Transfer points are: 1. Biomass production site; 2. Central gathering point; 3. Export terminal; 4. Import terminal; and 5. Conversion plant (biomass to syngas and syngas to bio-based fuels and chemicals)

For the design of the biomass supply chains, the approach proposed by [142] was adopted to obtain supply costs, environmental impacts and energy requirements for the delivery of the lignocellulosic biomass [143–145]. Three main process operations were considered to structure the (inter)national biomass supply, they are: *i)* biomass production (seeding, land establishment, land maintenance and collection/harvesting); *ii)* conditioning (chipping, baling, pelletization and drying); and *iii)* transportation (truck, train and ship transport) [142]. The sequence of operations was defined based on generic theoretical chains which contain five transfer points as shown in Figure 2.1: 1) the production site, 2) a central gathering point, 3) a transport terminal for export, 4) a transport terminal for import, and 5) the conversion plant [121,142,146]. In the specific case of international transport, pelletizing of biomass is included to increase its density and make long distance transportation more efficient [142,147]. The location of the central gathering points was defined to reach minimum transport costs between the sites with the highest biomass productivities and the next transfer points (considering road infrastructure and cost-efficiency of the transport type). Determination of the ports was mainly based on infrastructure and scale. Thus, the ports were selected considering that Panamax ships were available to assure large scale biomass transportation [142]. Furthermore, the moisture content of biomass entering the gasification unit is set to be 10 wt.% (reported as the optimum to minimize size and operation costs of the gas-to-liquid plant) [134,148,149].

2.2.1.2. Thermochemical conversion

The gasification process here considered was based on the technology described by NREL [148], which produces syngas suitable for fermentation. Such a process configuration returns low dilution of fermentable gases, produces high carbon conversion into CO while

keeping low CO_2 concentrations and maintains CH_4 as low as possible [150]. The process takes place at atmospheric pressure and uses three fluidized bed reactors, as shown in Figure 2.2: an indirectly heated (allothermal) gasification reactor (R102), a combustion reactor (as heat source) (R106) and a gas conditioning reactor (R104). The gasification and combustion reactors operate with circulating fluidized beds (CFB) while the gas conditioning reactor uses a bubbling fluid bed (BFB). The indirectly heated dual CFB gasifier is considered the most suitable option for biomass conversion into syngas (for fermentation) due to: syngas composition (rich in H_2 and low in CO_2), high carbon conversion, low tar production, flexibility on the type and particle size of fuel accepted and scale-up potential [151]. Furthermore, olivine which is used as bed material (and catalyst), circulates through the three reactors (see Figure 2.2) and is (re)heated in the combustion reactor where char is burned with air.

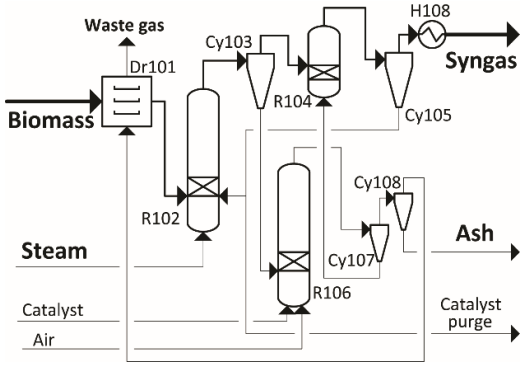

Figure 2.2. Process flow diagram for syngas production from biomass. Dr101: dryer; R102: gasifier; R104: reformer; R106: combustor; Cy: cyclones; H: heat exchangers.

For the gasification process, steam (at 450 °C and 1 bar) is fed to reactor R102. This steam has a double function: it is the fluidizing medium and the oxidizing agent for gasification and tar reforming (as shown in Figure 2.2). The mass flow rate of steam is defined by the steam to biomass ratio which is set at 0.75. [152] The gasification reactions (see Table 2.2) take place when high temperatures are reached (850 °C).

In the tar reforming process, the gas coming from the gasifier is sent to the catalytic tar reformer (R104), where methane and higher hydrocarbons are oxidized into both CO and H_2, while CO into CO_2, and NH_3 converted into both N_2 and H_2 (see Table 2.2) [151,153]. Steam addition to the tar reformer was excluded from the model since the water content in the input gas was already sufficient to drive the reactions and avoid additional costs and gas dilution.

Table 2.1. Biomass data: physicochemical characterization, production requirements and production costs

Characteristics	Forestry residues	Agricultural residues		Energy crops
	Pine wood (PW)	Sugarcane bagasse (SB)	Corn stover (CS)	Eucalyptus wood (EW)
Region of production	US	BR	US	BR
Commodity shape	Chips	Fines	Bales	Logs
Moisture content$_{green\ biomass}$ (wt.%) [a]	45 [121,146]	51 [154]	24 [146,155,156]	45 [146,157]
Ultimate analysis (wt.%)				
Ash	0.6 [158,159]	3.2 [160,161]	6.0 [156,162]	3.4 [159,163]
C	49.7 [158,159]	45.2 [160,161]	47.3 [156,162]	46.0 [159]
H	7.8 [158,159]	5.5 [160,161]	5.1 [156,162]	5.8 [159]
O	41.8 [158,159]	40.7 [160,161]	40.6 [156,162]	44.5 [159]
N	0.1 [158,159]	0.1 [160,161]	0.8 [156,162]	0.3 [159]
S	0.05 [158,159]	0.05 [160,161]	0.22 [156,162]	0.0 [159]
Proximate analysis				
Volatile matter (wt.%)	82.3 [158,159]	83.7 [160,161]	54.6 [156,162]	75.4 [159]
Fixed carbon (wt.%)	17.2 [158,159]	13.2 [160,161]	7.15 [156,162]	21.3 [159]
HHV [b] (GJ/ton$_{dry}$)	20.2 [163]	18.8 [163]	19.0 [163]	18.6 [163]
Avg. particle size (mm)	30	10	10	30
Density (kg/m$_{bulk}^3$)	473 [164]	175 [165]	500 [166,167]	380 [168]
Biomass production				
Average yield (t/(km^2*y))	164 [121]	8500 [169,170]	516 [171]	2810 [172,173]
Cultivation land required (km^2)	3428	214	773	196
Herbicide requirements (kg/(km^2*y))	0.164 [121]	220 [174]	235 [175]	0.84 [175]
Fertilizer requirements (kg/(km^2*y))	16.4 [121]	29000 [170]	31270 [171]	48 [175]
Total diesel consumption(kg/(km^2*y))	0.64 [121]	24.7 [170,176,177]	8.6 [178]	26.8 [121]

[a] Green biomass is defined as wet biomass at its harvesting phase.

[b] HHV: Higher heating value

Table 2.2. List of reactions for: Gasification, tar reforming, syngas fermentation and carboxylic acid chain elongation

Process	Reaction	Reaction number
Gasification	$CH_aO_bN_cS_d^* + eH_2O \rightarrow n_1C + n_2CO + n_3CO_2 + (a/2)H_2 + (c/2)N_2 + dS$	(1)
	$C + H_2O \rightarrow CO + H_2$	(2)
	$C + 2H_2O \rightarrow CO_2 + 2H_2$	(3)
	$C + CO_2 \rightarrow CO$	(4)
	$C + 2H_2 \rightarrow CH_4$	(5)
	$CO_2 + H_2 \rightarrow CO + H_2O$	(6)
	$N + 1.5H_2 \rightarrow NH_3$	(7)

Process	Reaction	Reaction number
	$S + H_2 \rightarrow H_2S$	(8)
Tar Reforming	$CH_4 + H_2O \rightarrow CO + 3H_2$	(9)
	$CH_4 + CO_2 \rightarrow 2CO + 2H_2$	(10)
	$CO + H_2O \rightarrow CO_2 + H_2$	(11)
	$2NH_3 \rightarrow 3H_2 + N_2$	(12)
Ethanol production	$6CO + 3H_2O \rightarrow C_2H_5OH + 4CO_2$	(13)
	$2CO_2 + 6H_2 \rightarrow C_2H_5OH + 3H_2O$	(14)
2,3-butanediol production	$11CO + 5H_2O \rightarrow C_4H_8(OH)_2 + 7CO_2$	(15)
	$4CO_2 + 11H_2 \rightarrow C_4H_8(OH)_2 + +6H_2O$	(16)
Microbial growth	$2CO + 0.5H_2O + 0.25NH_4^+ \rightarrow CH_{1.75}O_{0.50}N_{0.25} + CO_2 + 0.25H^+$	(17)
	$2H_2 + CO_2 + 0.25NH_4^+ \rightarrow CH_{1.75}O_{0.50}N_{0.25} + 1.5H_2O + 0.25H^+$	(18)
Ethanol oxidation	$C_2H_5OH + H_2O \rightarrow CH_3COOH + 2H_2$	(19)
Chain elongation	$C_xH_{2x+1}COOH + C_2H_5OH \rightarrow C_{x+2}H_{2(x+2)+1}COOH + H_2O$	(20)

* Biomass

2.2.1.3. Fermentation

The three fermentation products here analyzed were selected from an initial list of nine components as introduced in Section 2.1 (acetate [126], ethanol [126], butyrate [65], propionate [127], butanol, hexanol [128], 2,3-butanediol [129], lactate [129] and polymers [130]). For this selection, three main criteria were considered: *i)* published experimental achievements considering techniques, yields, titers and productivities; *ii)* energy and mass requirements, and waste generation from possible DSP routes; and *iii)* global market size of products. Thus, 2,3-butanediol, ethanol and hexanoic acid were selected as most attractive syngas fermentation products. The expected uses of ethanol and hexanoic acid are as biofuels either for blending or direct combustion [48,179], however ethanol has also shown to be a prominent chemical building block for further conversion to value-added products [180]. Furthermore, hexanoic acid can also be used for manufacturing of food additives (esters) [181]. 2,3-butanediol is considered as a precursor for multiple chemical products including solvents [129]. Additionally, one co-product was assumed to be produced by each one of the three fermentations here considered: acetic acid, ethanol and butyric acid, for ethanol, 2,3-butanediol and hexanoic acid production, respectively.

The fermentation stoichiometry and kinetics were predicted through thermodynamics [182,183]. The Gibbs free energy dissipated via the catabolic reactions inside the cell (see eq. 13 and 14 as examples for ethanol production) was used to calculate the amount of substrate consumed for microbial growth (see eq. 17 and 18). For ethanol production, the distribution of carbon among main product and the co-product was adjusted according to published experimental results at laboratory scale. For 2,3-butanediol and hexanoic acid production, the amount of co-product generated was set in similar values than ethanol production. The maximum specific substrate consumption rate was estimated

assuming that the amount of Gibbs free energy is collected from the electron donor, at a maximum rate determined by the capacity of the electron transport chain (3 mol electrons per carbon mol of biomass per hour) [183]. With this value, the common microbial energy needs for maintenance and the biomass yield on the carbon source, the maximum growth rate was calculated using Herbert-Pirt equation for anaerobic growth [183]. Additionally, considering that the catabolic reactions must produce at least 15 kJ/mol in order to maintain an active a proton motive force across the membrane, the affinity constants of electron donors were assumed to be close to the concentrations at which the catabolic reaction produces that minimum of Gibbs free energy [183]. All Gibbs free energies of reactions were adjusted to the fermentation conditions of temperature, pH and concentrations of substances involved in the metabolic black-box model. Electron transport capacity and microbial energy needs for maintenance were also adjusted to the operation temperature. For a detailed description on the procedure followed to determine stoichiometric and kinetic parameters of the three fermentations, as well for the fermentors design, please see supplementary information for this chapter.

Ethanol and 2,3-butanediol are produced directly from syngas fermentation [48,129]. The H_2/CO ratio in which the syngas is fed to the fermentation defines the microbial stoichiometry, and thus water and CO_2 can either be consumed or produced (see eq. 13 - 16). For both fermentations, the processing conditions used were 37 °C, 1 bar (top pressure) and pH of 5. The resulting concentrations of gases and biomass were obtained from mass balances and calculated by using the mass transfer capacities (MTC) inside the fermentors. The MTC were calculated for each gaseous substrate and defined from superficial gas velocities and the compound solubilities under actual P-T conditions and the gas phase composition [85].

The syngas fermentors were designed as bubble columns using three main constraints: a maximum liquid volume of 900 m^3, maximum vessel height of 22 m, and gas hold-up of 15 vol.% max [85]. In ethanol production, the amount of syngas required to achieve the maximum hold-up was enough to remove all ethanol produced by evaporation. This amount which resulted in around 400 vol.% stoichiometric excess, also guaranteed sufficient CO and H_2 MTC required by microbes.

Hexanoic acid was assumed to be anaerobically produced from ethanol and acetic acid which are generated in a previous syngas fermentation stage [133]. The synthesis of this carboxylic acid couples an ethanol oxidation reaction with a chain elongation reaction (see eq. 19 and 20). The fermentation conditions were set to be 30 °C, pH 5 and low pressure (0.045 bar) to ensure low H_2 concentration at the bottom of the reactor, hence allowing the ethanol oxidation to be thermodynamically feasible.

The chain elongation reactor was conceptualized to operate at vacuum conditions and was designed as a bubble column; although it does not have any gas input, the broth mixing is achieved through the combined effect of H_2 production and water evaporation. Three key constraints were here used for the fermentor design: liquid volume not larger than 2000 m^3, maximum 15 vol.% gas hold-up at the top of the reactor [85] and a gas-liquid mixture height that would avoid inhibitory H_2 concentrations at the bottom of the vessel.

2.2.1.4. Downstream processing

Different purification routes have been designed for each of the three chosen products, as shown in Figure 2.3.

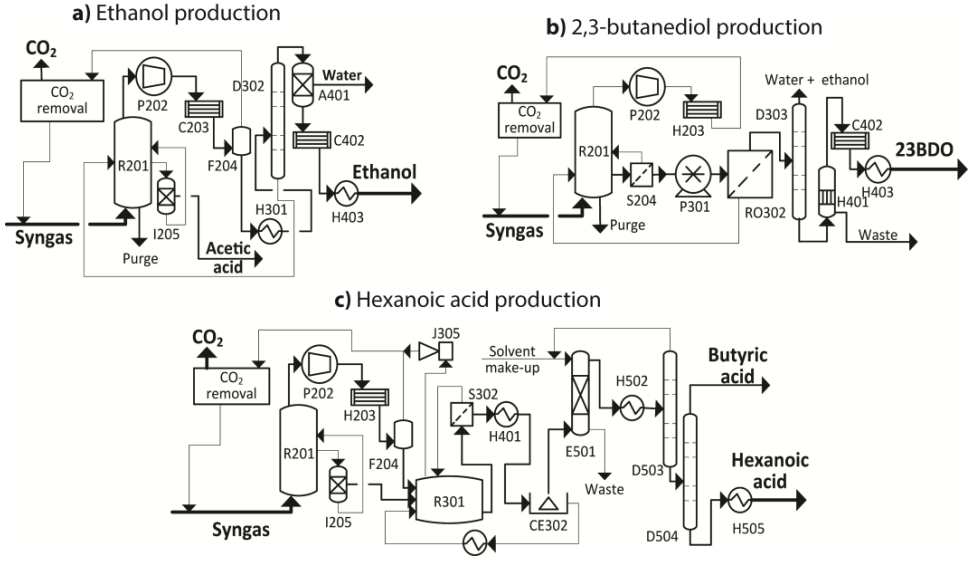

Figure 2.3. Process flow diagrams for syngas fermentation and DSP for producing a) ethanol, b) 2,3-butanediol and c) hexanoic acid.

In the case of ethanol production (see Figure 2.3.a), ethanol is continuously removed from the syngas fermentor (R201) by the gas excess. The resulting stream is compressed (P202) to 3.2 bar and cooled to -7 °C (C203) to condense a mix of water and ethanol. This mix is separated from the gases by flashing (F204), leading to a 61 wt.% ethanol concentration and 96% recovery. The gas stream containing carbon dioxide and non-consumed CO and H_2 is treated in a monoethanolamine (MEA)-based process to remove the CO_2 [184]. The remaining fractions of CO and H_2 are mixed with fresh syngas and then fed back to the fermenter. The pre-concentrated ethanol stream is pre-heated (H301) for an azeotropic distillation (D302); the bottoms stream (containing water, ethanol and acetic acid) is sent

back to the fermentor while the top stream follows a dehydration process by adsorption (A401). Thus, 95% of water is removed by the molecular sieve [185], while the ethanol stream is condensed (C302) and cooled (H303) to storage temperature. The resulting product contains 0.27 wt.% water, while 5.5% of the product is lost through the DSP. The adsorption units (I205) are used to remove acetic acid through ion exchange. [186]

Contrary to the ethanol DSP, 2,3-butanediol (see Figure 2.3.b) is continuously removed from the syngas fermentors (R201) in the liquid phase. Microfiltration (S204) is used first for biomass retention [187] and subsequently water is partially removed by reverse osmosis (RO302) at a flux of 45 kg/(m^2*h) [188]. The product is concentrated up to 390 g/L, while the losses across the membrane account for 3.9% [188]. The permeate is recycled back to the fermentation tank, while the retentate is subjected to distillation (D303) to separate water and ethanol. The resulting bottoms stream is furtherly flash evaporated (H401) to eliminate dissolved solids carried from the fermentation. 2,3-butanediol is finally condensed (C402) and cooled (H403) to storage temperature. The final product purity is 99.8 wt.% (the remaining 0.2% is water) with an overall recovery of 99.9%. Similarly as for the ethanol DSP, this DSP also includes CO_2 removal (by the MEA-based process) [184] from the recycling of off-gas due to its partial consumption during fermentation stage.

The DSP for hexanoic acid (see Figure 2.3.c) starts at the chain elongation reactor (R301) where it is produced from ethanol and acetic acid. The off-gas stream from the chain elongation reactor is partially dehydrated by condensation (C303) and flashing (F304), and then it is directed to an ejector (J305) to generate the vacuum conditions needed for fermentation [189]. The water content (from the steam ejector), temperature and pressure of the off-gas are adjusted before it is recycled back to the syngas fermenters. This recycling helps to improve the CO_2 consumption due to the increase in the H_2 supply. The organic liquid products of the elongation reactor may form a stabilized emulsion with the aqueous phase [190] which is then separated by microfiltration (S302) [187]. The latter process is also used for biomass retention. The oil-water emulsion is ultimately destabilized by thermal treatment (cooling below the acid's freezing point) [191,192], and the two phases are separated by centrifugation (CE402). The inorganic phase is warmed up and recycled back to the chain elongation reactor to provide part of the heating required by the fermentation, while the organic phase (still with a 58 wt.% water content) is mixed with n-decane (E501) to separate the hexanoic acid from water and the polar impurities dragged along from the fermentation. The solvent is then removed and regenerated by distillation (D503) and recycled back to the extractor. Finally, the acids mixture is distilled to produce a hexanoic acid with a purity of 99.9 wt.% and with an overall recovery of 95.9%.

2.2.2. Economic evaluation

The economic analysis of the designed processes was based on the total production costs (considering both capital expenditures (CAPEX) and operational expenditures (OPEX)) and the minimum selling price (MSP) of products. The MSP was understood as the selling price that would bring the net present value (NPV) to zero at a defined number of years (payback time (PBT)), which for the base-cases was set at 5 years. CAPEX was based on multiple factors related to the total equipment purchase costs (EPC) [193], which in turn depends on individual equipment's characteristic size. The EPC of this study were adapted from multiple sources: NREL's reports for all equipment used in the syngas production process [148] and also for adsorbers [185,194]; Seider et al. (2010) [195] for membrane-based operations and compressors; matche.com for fermentors; Husebye et al. (2012) [184] for the CO_2 MEA-based process; SuperPro Designer V9.0 for centrifuges; and Aspen Plus V8.8 for typical processing equipment such as distillation columns, extraction units, heat exchangers, evaporators, condensers and flash separators. When needed, the 6/10 scaling factor rule was used for capacity corrections [193]. In addition, prices for all equipment were updated to 2015 by using the Chemical Engineering Plant Cost Index (CEPCI) (www.chemengonline.com), and the project lifetime was fixed at 15 years.

The aggregation of the OPEX was based on Peters and Timmerhaus (1991) [193], as follows:

Facility-dependent costs (FDC): Depreciation, maintenance, insurance, local taxes and overhead. The FDC's are calculated as a function of the EPC's [193]. Linear depreciation was assumed through the project's lifetime resulting in a salvage value equal to 10% of purchase cost. A yearly maintenance equal to 15% of EPC was also assumed.

Process-related costs (PRC): Raw materials and utilities. Raw materials flows and utilities requirements are derived from the mass and energy balances. Prices of raw materials were obtained from open websites (icis.com and alibaba.com), while the prices of utilities and industrial services were defined according to Vasudevan and Ulrich (2006) [196].

Labor: it was assumed to be 7% of both FDC plus PRC.

Furthermore, the economic performance for each case was adjusted to the different geographical locations here analyzed by using: *i)* location factors for CAPEX [197]; *ii)* specific prices for: fuels (used for defining prices of utilities) [196] and lignocellulosic biomass; and *iii)* local economic indexes: interest rate and taxes on revenue. The used values are shown in Table 2.3.

Table 2.3. Global and local parameters of the economic model for comparison of the different geographical locations of the processing plants.

Global parameters			
Project lifetime (y)	15		
Payback time (y)	5		
Debt time period (y)	10		
Debt-to-equity ratio	1		
Interest type	Compounded		
Inflation rate	0		
Depreciation type	Linear		
Salvage value	10% of EPC		
Equipment maintenance	15% of EPC		
Labor	7% of (FDC + PRC)		
Working capital	1/12 of OPEX		
Start-up costs	22% of OPEX		
Local parameters			
Country	*US*	*NL*	*BR*
Location factor [197]	1.03	1.19	1.01
Fuel price ($/GJ)	5.075 [198]	12.19 [198]	4.220 [b]
Electricity price ($/MWh)	70.14 [198]	118.0 [198]	134.9 [c]
Interest rate (%) [a]	1.80	1.00	14.25
Tax on revenue (%) [a]	39.0	25.0	34.0
Cost of feedstock ($/ton$_{wet}$) (at year)			
Pine wood	15 (2011) [199,200]	-	-
Sugarcane bagasse	-	-	17 (2012) [201,202]
Corn stover	24 (2011) [146,171,203]	-	-
Eucalyptus wood	-	-	31 (2011) [146,157]

[a] (ww.tradingeconomies.com)
[b] (br.investing.com)
[c] (ANEEL.gov.br (http://relatorios.aneel.gov.br))

2.2.3. Life Cycle Assessment

The LCA was performed according to the guidelines ISO 14040 and 14044 [204,205]. The goal was to estimate and compare the environmental impacts of the different supply chains, followed by a comparison with data reported in literature for the same products (or comparable products with equivalent functionalities, depending on data availability) from first (1G) and second (2G) generation feedstocks and from fossil sources. A "cradle-to-gate plus incineration" approach [206] was defined for the system boundaries which include feedstock's supply, syngas production, fermentation and DSP stages. Additionally, to produce a fair comparison between the impacts of the products with fossil counterparts, the system was expanded to include the final combustion (neglecting its distribution) of the products. The environmental impact categories analyzed in this study were the primary energy use (calculated as non-renewable energy use, NREU) and the

global warming potential (GWP) (determined as greenhouse gases emissions, GHG). The functional unit for the inventory analysis and the impacts assessment is the production of 1 kg of end product for 2,3-butanediol and hexanoic acid, while for ethanol, the unit used is 1 MJ calculated at its lower heating value (LHV: 29.7 MJ/kg).

Individual impact characterization factors for materials and energy carriers were taken from the Ecoinvent V2.2 database, literature and internet references (see Table 2.4). The environmental impacts data for sugarcane bagasse and corn stover were adopted from literature by applying economic allocation (used factors are: 0.18 for SB, and 0.21 for CS) since they are considered as waste materials [207,208].

Table 2.4. Individual impact characterization factors for materials and energy carriers for NREU and GWP [a]

Component	Unit	NREU (MJ/unit)	GWP (g_{CO2eq}/unit)	Component	Unit	NREU (MJ/unit)	GWP (g_{CO2eq}/unit)
Diesel	MJ	1.19	11.2	Ammonia	kg	50.86	2929.4
Electricity (US)	MJ	2.13	188.8 [c]	Process water	kg	0.08	6.6
Electricity (BR)	MJ	0.46	80.0 [c]	KOH	kg	32.56	2240.7
Electricity (NL)	MJ	2.06	144.6	HCl	kg	6.60	397.0
Cooling water	kg	0.01	0.3	Decane	kg	77.24	2173.3
Heat [b]	MJ	1.56	100.5	Solid waste removal	kg	0.04	2.5
Fertilizer	kg	62.45	1571.6	Primary WWT	kg	0.12	18.6
Herbicide	kg	221.00	7930.0	Secondary WWT	kg	0.25	83.2
Olivine	kg	0.13	39.2	Microbial biomass combustion	kg	0.001	3.1

[a] Most data, excluding the referenced to footnotes, was obtained from Ecoinvent v2.2 database.

[b] Referred to all types of industrial heat *e.g.*, steam and, excluding cooling water. The same value is used for all locations.

[c] Calculated as a function of the renewable fraction in the national grid mixture [209] (Kahraman Z, Ringenbach C and Benichou L (http://www.tsp-data-portal.org)) and taking the data for NL as reference for linear regression.

2.2.4. Sensitivity analysis

During the development of the conceptual designs of the supply chains and related processes, some assumptions for specific variables were adopted. A sensitivity analysis is performed on the most critical variables to determine their influence on the techno-economic and environmental performances, and also to identify opportunities for further improvements.

Three variables specifically apply to syngas production: *i)* gasification temperature was varied from 650 °C to 1050 °C; *ii)* the tar reformer unit in the gasification process was removed; and *iii)* two possible uses for the heat produced in gasification was evaluated, *i.e.,* generation of electricity or steam. The gasification temperature has been reported to have a strong influence on the syngas composition [152], therefore its influence has been analyzed and subsequently optimized. Three other variables were studied for the fermentation stage: *iv)* gas flow rate across the syngas fermentors (which has influence on the mass transfer capacity, and therefore on the productivity); *v)* output concentration of products in the fermentation tank (which determines the size of the DSP operations); and *vi)* the hexanoic acid production throughput (which is related to its application and market, and therefore its selling price). Finally, three variables directly influencing the economic evaluation have been considered: *vii)* interest rate (which has shown variations during the past ten years in the three considered plant locations); *viii)* fermentor purchase cost; and *ix)* payback time of the investment (which relates to the risks that investors would be willing to take). The fermentor purchase costs were varied from half to the double of the base value used for each single equipment (M$3.7 and M$8.5 for the syngas and chain elongation fermentors, respectively); the interest rate was varied in the ranges 0.20 – 2.45% (for NL), 7.25 – 16.50% (for BR), and 0.25 – 5.25% (for US); while the payback time was analyzed for 3 to 7 years.

2.3. Results and discussion

2.3.1. Process design

The biomass supply chains were designed to produce syngas with a composition that is suitable for fermentation into chemicals [150]. Table 2.5 shows the resulting yields of syngas on biomass and the composition of the resulting syngas for each feedstock. The highest syngas yield is obtained from pine wood because of its high hydrogen content and low presence of ash and nitrogen compared to the other feedstocks. This syngas yield has, in general, a low variability (*i.e.,* +/- 5.3%).

After the syngas fermentation and DSP, the purity obtained is 99.6, 97.9 and 99.9 wt.% for ethanol, 2,3-butanediol and hexanoic acid, respectively; with a product loss, after gasification, of 5.6, 0.1 and 4.1% respectively. The highest overall mass yield of whole supply chain was obtained for 2,3-butanediol from pine wood, which is 13% higher than for ethanol production and 33% higher than for hexanoic acid production when the same feedstock is used. An advantage of using pine wood at the fixed steam to biomass ratio and gasification temperature, is that it produces the most elementary and molecularly compatible syngas for the three final products. In other words, the CO_2 consumption for

products synthesis increases with higher H_2/CO ratios fed to the fermenter as shown in Figure 2.4. This higher consumption of CO_2 concentrated the CO and H_2 in the bioreactors, improving the mass transfer capacity and reducing further the requirements for CO_2 removal before syngas recycling. Nevertheless, since syngas composition is strongly influenced by gasification conditions [152], optimal combinations of temperature and steam to biomass ratio could be determined, in order to produce syngas with a composition optimized to the type of fermentation product wanted, from a defined available feedstock. However, this analysis has not been performed in this study.

Table 2.5. Yields of biomass, syngas and final products. And composition of the resulting syngas at a gasification temperature of 850 °C.

Process feature	PW	SB	CS	EW
Syngas composition (vol.% dry)				
H_2	60.9	57.0	55.4	56.5
CO	28.1	28.6	30.0	29.0
CO_2	9.9	13.1	13.0	13.2
N_2	1.0	1.2	1.5	1.2
CH_4 (ppm)	593.2	379	412	386
NH_3 (ppm)	12.4	12	13	12
H_2S (ppm)	160.6	189	822	0
H_2/CO molar ratio	2.2	2.0	1.8	1.9
LHV (kJ/kg)	5101	5451	5378	5446
Biomass Yield ($kg_{biomass\ dry}/kg_{biomass\ wet}$) [a]	0.59 (NL), 0.60 (US)	0.18 (NL), 0.18 (BR)	0.81 (NL), 0.83 (US)	0.59 (NL), 0.77 (BR)
Syngas Yield ($kg_{syngas}/kg_{biomass\ dry}$)	1.20	1.14	1.18	1.19
Yield to product from biomass				
$kg_{ethanol}/kg_{biomass\ dry}$	0.43	0.38	0.37	0.38
$kg_{2,3\text{-}butanediol}/kg_{biomass\ dry}$	0.49	0.41	0.41	0.42
$kg_{hexanoic\ acid}/kg_{biomass\ dry}$	0.36	0.32	0.31	0.32

[a] Locations in brackets indicate the place where biomass is converted into syngas.

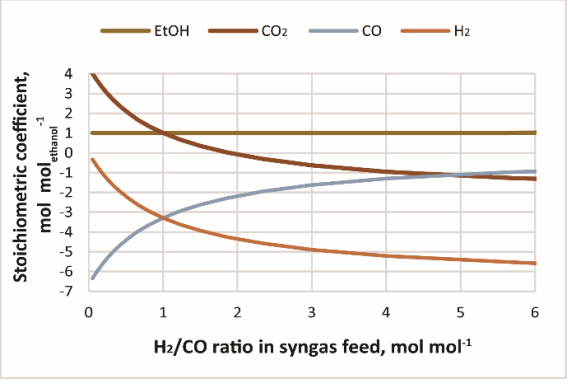

Figure 2.4. Stoichiometric dependence of CO_2 consumption/production with respect to the H_2/CO ratio in the syngas input stream.

2.3.2. Economic evaluation

Results of the economic evaluation are discussed considering two main processing stages: *i)* biomass supply and gasification to syngas, and *ii)* bulk chemicals production via syngas fermentation and subsequent DSP. The direct comparison between the obtained MSP's and the available data for selling prices in the global market was considered as indicator to determine potential economic feasibility of the products. Additionally, the ethanol production costs are used to draw comparisons against data reported in literature for ethanol, produced from lignocellulosic biomass through different platforms: *i)* the thermochemical pathway (*i.e.,* gasification and FTS) and *ii)* the biochemical route (*i.e.* pretreatment, hydrolysis and fermentation).

Table 2.6 shows the costs contribution for syngas production from the four feedstocks with their respective region of origin and according to the location for biomass gasification.

When syngas production takes place in the region of the feedstock's origin, the lowest production costs are obtained for CS in the US. However, when syngas production takes place in NL after biomass import, the lowest syngas production costs among all feedstocks are obtained when PW from the US is used. For the biomass import cases (Figure 2.5.a), the biomass supply costs represent the largest share of the total syngas production costs; *i.e.* around 50% (accounting for biomass production, sizing, drying, densification, truck transport, train transport, and ship transport). The relative contribution of the biomass supply to the total costs is larger when biomass gasification takes place in the same region of the feedstocks production (see local cases in Figure 2.5.b). For instance, when syngas is produced in the US, the biomass supply costs represent 55% for PW and 45% for CS, while in BR this contribution is 38% for SB and 51% for EW. Utilities are the second largest contributor to the syngas production costs (see Figure 2.5.a and Figure 2.5.b); they account for 20-25% of the total costs

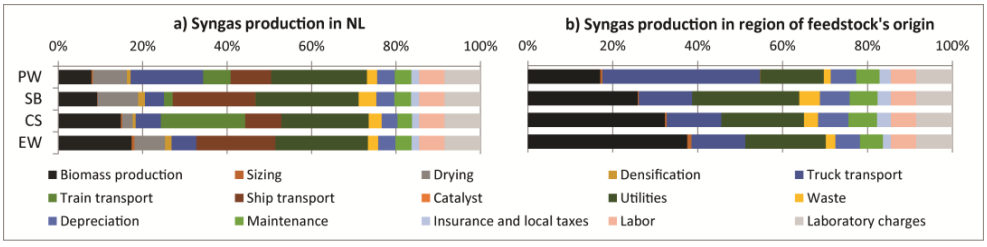

Figure 2.5. Cost contribution (in %) of syngas production for: a) syngas production in NL, and b) syngas production at the same region where feedstock is produced

Table 2.6. Total production costs of syngas: contribution analysis by feedstocks and location

Cost item	PW (US)		SB (BR)		CS (US)		EW (BR)	
	(NL case) [a]	(Local case) [b]	(NL case) [a]	(Local case) [b]	(NL case) [a]	(Local case) [b]	(NL case) [a]	(Local case) [b]
Costs contribution ($/ton$_{syngas}$)								
Biomass production	15.0	24.6	18.3	33.6	32.5	38.5	34.4	56.3
Sizing	0.7	0.8	0.2	0.4	0.7	0.6	1.3	1.5
Drying	15.4	-	19.0	-	5.4	-	14.4	-
Densification	1.6	-	3.2	-	1.7	-	3.1	-
Truck transport	32.8	53.6	8.9	16.4	13.0	15.4	11.6	19.0
Train transport	12.4	-	4.2	-	43.8	-	-	-
Ship transport	18.3	-	38.7	-	18.6	-	37.1	-
Catalyst	0.01	0.01	0.01	0.01	0.01	0.01	0.01	0.01
Utilities (see below)	43.3	21.7	48.5	32.7	45.2	23.1	43.5	28.5
Waste treatment	4.6	2.4	8.3	6.3	6.8	4.0	4.7	3.4
Depreciation	8.0	8.6	8.5	9.2	8.2	8.6	8.1	8.7
Maintenance	7.4	8.0	7.8	8.5	7.6	8.0	7.5	8.1
Insurance & local taxes	3.5	3.8	3.8	4.1	3.6	3.8	3.6	2.7
Labor	11.4	8.7	11.9	7.8	13.1	7.1	11.8	9.0
Laboratory charges	16.3	12.4	16.9	11.1	18.7	10.2	16.9	12.8
Total production costs	190.7	144.5	198.2	130.0	218.7	119.3	198.0	150.0
Contribution of utility costs ($/ton$_{syngas}$)								
Electricity	0	1.9	0	4.2	0	1.4	0	3.6
Steam	26.3	9.4	27.9	13.6	26.9	9.6	26.8	13.0
Cooling water	12.4	7.9	12.2	8.7	11.5	8.2	12.0	8.5
Solid waste treatment	0.3	0.1	4.3	3.2	2.9	2.2	1.6	1.2
CO_2 removal	4.2	2.3	3.8	3.1	3.8	1.7	2.9	2.1
WWT	0.2	0	0.2	0	0.1	0	0.2	0
Total utility costs	43.4	21.6	48.4	32.8	45.2	23.1	43.5	28.4

[a] NL case: syngas production takes place in NL

[b] Local case: syngas production takes place in the region where the feedstock is produced

The second part of the production costs is related to the syngas fermentation into bulk chemicals and their further DSP. For the four feedstocks considered, the syngas production is the largest contribution to the total OPEX followed by the facility dependent costs which are related to the capital expenditures. Results are illustrated in Figure 2.6 and in Figure 2.7; syngas contribution to OPEX is in average 39, 29 and 34%, for ethanol, 2,3-butanediol and hexanoic acid, respectively (see Figure 2.6.b for "raw materials" in combination with Figure 2.6.c for "syngas"), while the facility dependent costs are 30, 32, and 30%, respectively (see Figure 2.6.b). The rest of the OPEX contribution comes mainly from the pH controlling substances, nutrients, and make-up solvents. All the process water required in the chemical production phase originates from the gasification process and is recovered from the syngas cooling; thus, no external process water is required.

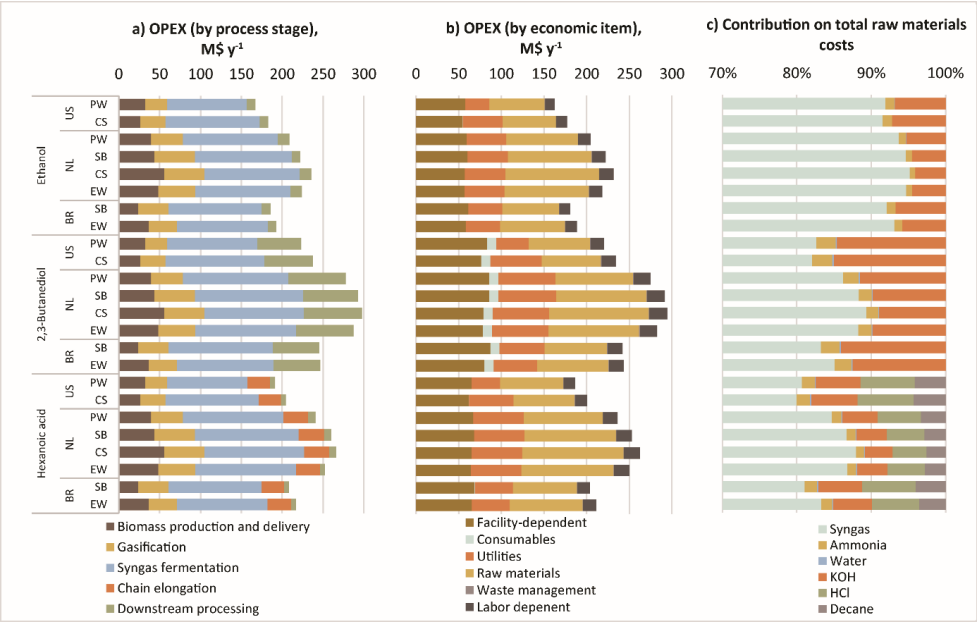

Figure 2.6. Break-down of operational costs for bulk chemicals production in all scenarios via the hybrid process. a) Composition of OPEX by process stage; b) composition of OPEX by major economic item; and c) cost contribution of raw materials.

The total production costs are obtained by adding up the contributions from biomass supply, syngas production, syngas fermentation and DSP. The lowest production costs were obtained for PW with production in the US, while the ethanol turned out to be the least costly chemical to produce, followed by 2,3-butanediol and lastly, by hexanoic acid (see Figure 2.7.a).

In general, the syngas fermentation gives the largest contribution to the production costs for the three products: 50-63%, 41-52% and 44-53%, for ethanol, 2,3-butanediol and hexanoic acid, respectively (see Figure 2.7.a). The main reason for this significant contribution is the large requirements of equipment and energy to overcome the low CO and H_2 mass transfer capacities in the bioreactors, which results in large fermentation volumes and power input for gas compression. In the case of hexanoic acid, the combination of the chain elongation unit (second fermentation step) with the DSP, represent only a minor part of the total production costs, due to the significantly lower fermentation volumes (no mass transfer limitation) and the relatively easier operations proposed for purification. The cost contribution of the DSP for ethanol production is relatively low due to the fact that most of the product concentration is achieved within the fermentation stage, as ethanol is stripped out of the broth by the excess of syngas (see Section 2.2.1.4). Finally, although the recovery efficiency and conversion yield for 2,3-

butanediol production are the highest among the three products compared, its DSP is the most resource intensive due to the limited concentration achieved within the fermentation. The 2,3-butanediol production process has also the highest CAPEX (see Figure 2.7.b), which is mainly the due to the presence of the reverse osmosis unit (see Figure 2.3.b) needed for partial broth dehydration.

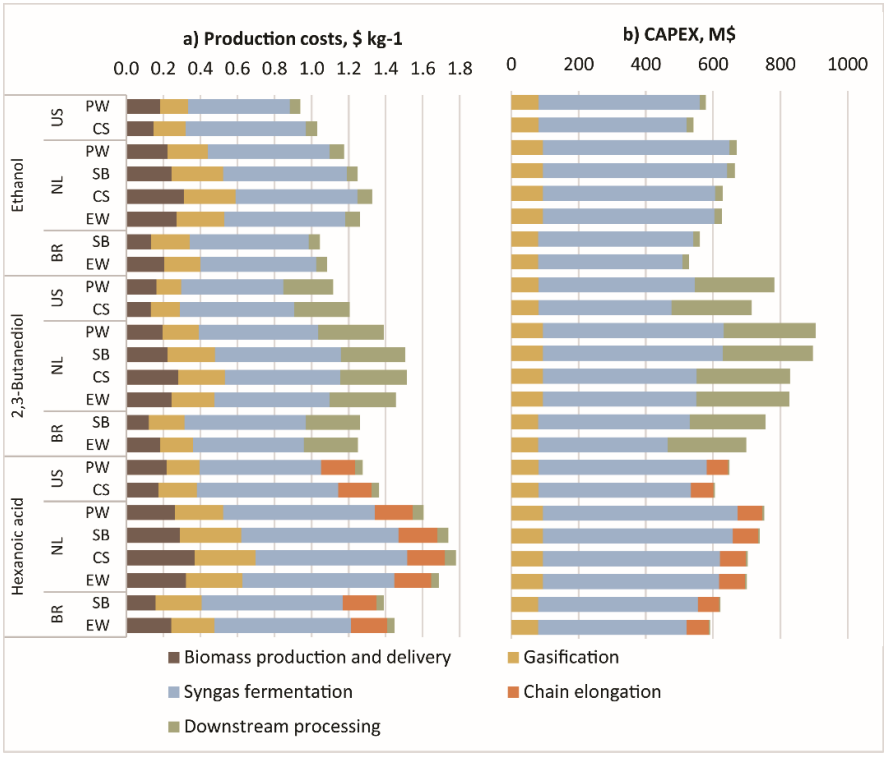

Figure 2.7. Break-down of total production costs and CAPEX by process stage. a) Production costs; and b) CAPEX.

The total production costs of ethanol here obtained are compared to those reported in literature for similar hybrid processes, *i.e.* the sugar platform (with biochemical pretreatment) and Fischer-Tropsch (after biomass gasification) as shown in Figure 2.8. Reported data show a substantial variation depending on considered process configurations and assumptions. In general, most data show that the hybrid conversion route is the least cost-competitive option for ethanol production from lignocellulosic biomass. Thus, process optimizations are still required within this production pathway.

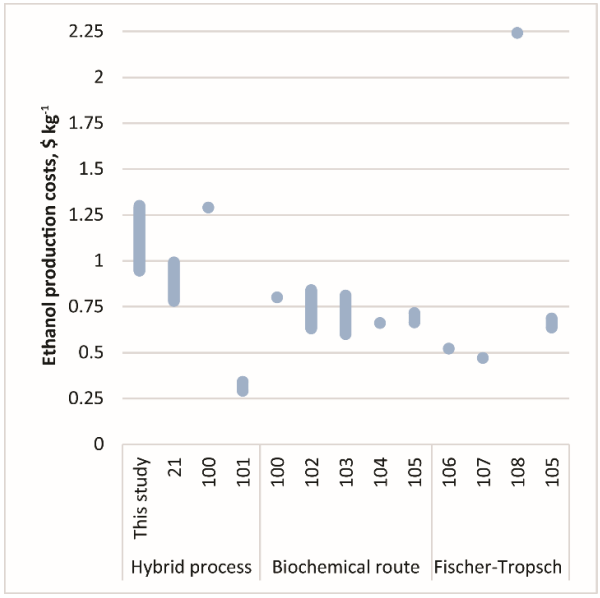

Figure 2.8. Comparison of total production costs for lignocellulosic ethanol by different platforms. Dots show punctual numbers, while lines show ranges. Numbers on the x-axis denote the respective literature reference, as follows: 21: [135], 100: [210], 101: [211], 102: [212], 103: [213], 104: [214], 105: [215], 106: [216], 207: [217] and 108: [218].

The MSP results for each case are shown in Figure 2.9. The lowest values, independently from the final product, are obtained when production takes place in the US from PW. The main reason for his result is the fact that the US has relatively low values for: electricity costs, interest rate on loans, location factor, tax on revenue, fuel prices, and biomass production costs. On the contrary BR is the least attractive case (even considering that it has the lowest production costs of syngas) due to its highest values for electricity price and interest rates on loans.

The obtained MSP for ethanol are higher than the selling prices observed in the international market during the last ten years (Nasdaq Inc. (www.nasdaq.com)) (see Figure 2.9), meaning that the designed production chains cannot compete with commercially available routes for ethanol production. Due to limited access to international market prices for 2,3-butanediol, the MSP obtained for this product are compared to those reported for 1,4-butanediol [219]; the MSP fit within the price range reported for 1,4-butanediol (see Figure 2.9), making this 2,3-butanediol a potentially attractive product of the syngas fermentation platform. The MSP's of hexanoic acid are compared to two types of products (see Figure 2.9): jet fuel and food-grade hexanoic acid. It is stated that hexanoic acid can be used as precursor of biofuels [220] and other products such as polymers, dyes or esters which require high purity of the acid [221]. The MSP's for the

acid are significantly higher than market prices observed for both fossil and bio-based jet fuel, however they are comparable (or lower) than those reported for food-grade hexanoic acid. However, there is a large difference between the global market size of both applications (*i.e.* as fuel or as high-quality feedstock); a discussion on the influence of production scale of hexanoic acid with respect to the MSP is included in Section 2.3.4.6.

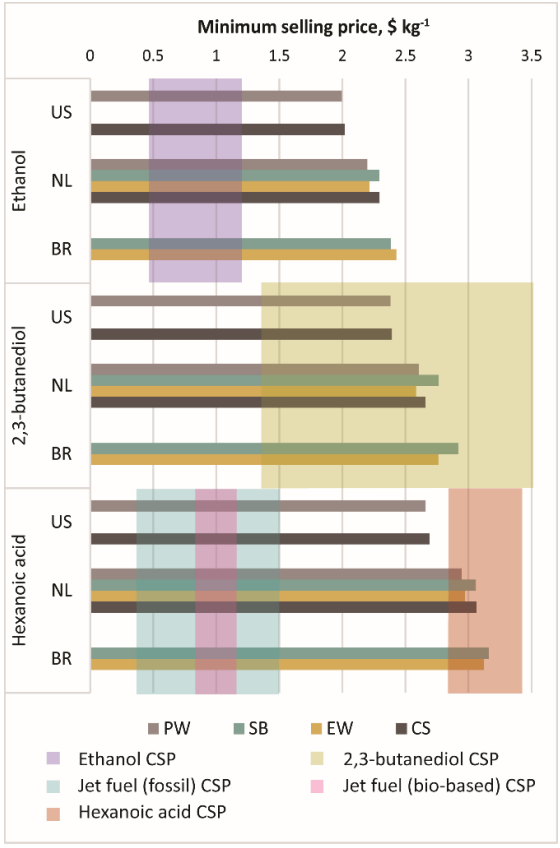

Figure 2.9. MSP for all products considering different locations for biomass production and gasification. Vertical colored rectangles represent the range of commercial selling prices for: ethanol (in violet), 1,4-butanediol (as equivalent to 2,3-butanediol, in golden), fossil jet fuel (in green), bio-based jet fuel [222] (in pink) and bio-based hexanoic acid(in red). CSP means commercial selling prices.

2.3.3. Life cycle assessment

For a better understanding of the composition of the environmental impacts, the contribution from biomass production up to syngas production is discussed in first instance, and then the impacts analysis is done for the entire production chain.

The obtained environmental impacts (GWP and NREU) for syngas production in the three locations (NL, BR and US) from PW, SB, CS and EW are shown in Table 2.7. Eucalyptus usage in BR and NL and pine usage in US lead to the lowest GWP, while sugarcane bagasse in BR leads to the lowest NREU. Corn stover has the highest environmental

impacts for GWP, both in NL and US. The worst NREU results are for PW and EW in NL. With respect to the geographical location, BR leads in general to the lowest impacts, while NL produces the highest impacts due mainly to additional impacts from international transport. Figure 2.10 shows a contribution analysis for GWP and NREU; two key factors contributing to the environmental impacts of syngas production are: steam consumption for gasification and biomass production. The contribution of the latter is larger since it includes biomass conditioning and delivery.

Table 2.7. Environmental impacts (GWP and NREU) of syngas production

Environmental impact category	Units	NL				BR		US	
		PW	SB	CS	EW	SB	EW	PW	CS
GWP	(kg_{CO2eq}/kg_{syngas})	0.26	0.26	0.32	0.21	0.23	0.20	0.21	0.29
	(kg_{CO2eq}/MJ_{syngas}) [a]	0.051	0.047	0.059	0.038	0.042	0.036	0.041	0.053
NREU	(MJ/kg_{syngas})	5.87	3.71	5.20	5.99	3.13	3.74	3.46	4.09
	(MJ/MJ_{syngas}) [a]	1.15	0.68	0.97	1.10	0.57	0.69	0.68	0.76

[a] LHVs are calculated based on the resulting syngas composition from each feedstock as shown in Table 2.5.

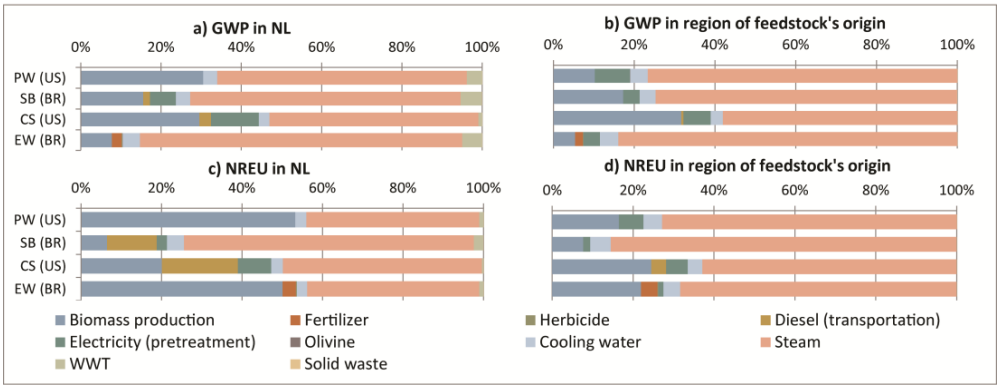

Figure 2.10. Contribution analysis for environmental impacts of syngas production: a) GWP in NL; b) GWP in the region of feedstocks origin; c) NREU in NL; d) NREU in the region of feedstocks origin

The environmental impacts, and their contributions from the process inputs for the entire supply chain and for each product are shown in Figure 2.11. The main contributor is electricity consumption, followed by syngas production and heat requirements. This tendency is consistent in all scenarios, however, the impacts from electricity are lower in BR compared to those in the US and NL.

Figure 2.12 compares the environmental performance of chemicals produced by the hybrid process against alternative production methods by considering other technologies and/or other feedstocks. In the cases of 2,3-butanediol and hexanoic acid, equivalent

products were included as benchmark assuming that the syngas-based products can function as potential replacement of these products. Ethanol produced from lignocellulosic biomass via the hybrid process generally shows higher environmental impacts (both NREU and GWP, 100 and 85% higher) when compared to ethanol derived from first (1G) and second (2G) generation resources (see Figure 2.12.a and Figure 2.12.d). Furthermore, the usage of lignocellulosic materials (*e.g.,* wood in the European Union (EU) and maize straw in the US) can lead to 45% lower impacts than those for 1G raw materials (*e.g.,* wheat and sugarcane). Finally, when compared with gasoline, ethanol through the hybrid process could generate up to 48 and 64% lower environmental impacts than the fossil fuel, in terms of NREU and GWP.

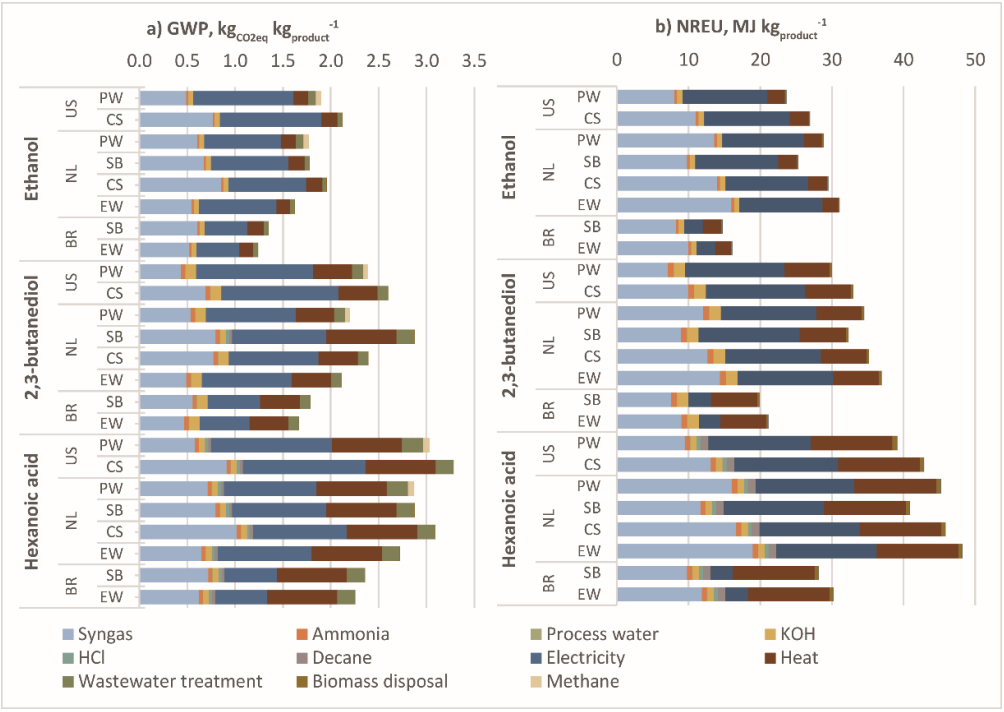

Figure 2.11. Environmental impacts of the supply chain for bulk chemicals production in the US from PW via the hybrid process. a) GWP and b) NREU.

Production of 2,3-butanediol via the hybrid process resulted in a better environmental performance in comparison to 1,4-butanediol and 1,3-propanediol (both from fossil and bio-based feedstocks, see Figure 2.12.b and Figure 2.12.e). The GHG emissions obtained for the hybrid process show a potential reduction as high as 76 and 93% in GWP and NREU from values reported for the two other fossil-based diols. In the case of hexanoic acid, this product exhibits a similar performance as the one reported for fatty acids

derived from vegetable oils, and until 80% lower GWP for adipic acid (a six-carbon-chain dicarboxylic acid in whose production, large amounts of N_2O are released) (see Figure 2.12.c and Figure 2.12.f). Although the obtained results for 2,3-butanediol and hexanoic acid are in general encouraging for further process development, these results should also be prudently considered for future research given the lack of environmental impacts reported in literature for the production of these two products through other pathways.

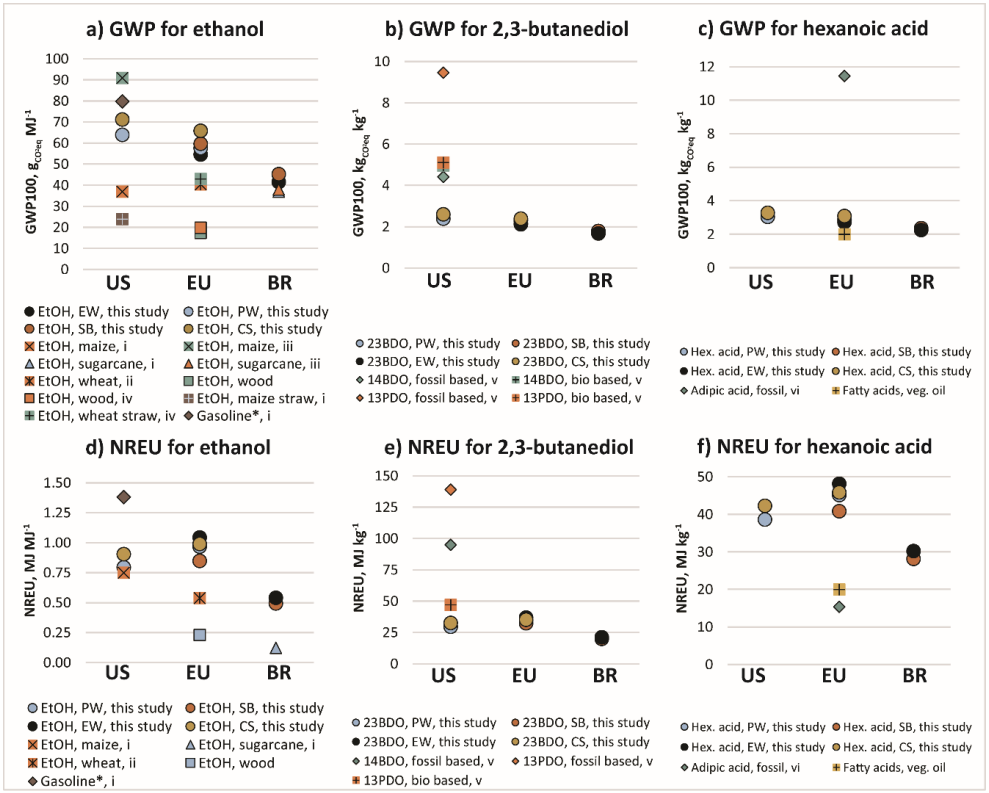

Figure 2.12. Environmental impacts of the hybrid process-based products and comparison with data reported in literature for different routes. GWP of a) ethanol, b) 2,3-butanediol, c) hexanoic acid; and NREU of d) ethanol, e) 2,3-butanediol, f) hexanoic acid. List of references: i: [223]; ii: [224]; iii: [225]; iv: [226]; v: [227]; vi: [228] . 2G feedstocks considered in ethanol production follow the pathway with bio-chemical pre-treatment of cellulose.
* Gasoline is fossil-based, and its impacts include CO_2 emissions from final combustion.

Although the three products of the hybrid process could potentially yield significant reductions on GHG emissions and NREU when compared against fossil-based counterparts, the economic performance of ethanol and hexanoic acid will not be promising if current oil and its products' prices are maintained and more optimized

processes are not designed. However, 2,3-butanediol could become a key product as it has shown a competitive performance with its bio and fossil-based equivalents.

2.3.4. Sensitivity analysis

The analysis shown in the previous sections are considered here as the base cases; these are used as reference points for the sensitivity analysis here discussed.

2.3.4.1. Gasification temperature

The gasification temperature for all feedstocks was varied between 650 and 1050 °C to analyze its impact on the resulting syngas composition. The changes in the syngas composition showed a similar trend in all cases. Results are exemplified using only the data for pine wood gasification (see Figure 2.13). Higher gasification temperatures lead to higher concentrations of H_2 and CO, thus favoring the subsequent syngas fermentation in terms of mass yields and lower CO and H_2 dilution. Furthermore, the optimal gasification temperature is here considered as the one that produces minimum amounts of CH_4 and CO_2 (< 10%), while keeping the H_2/CO ratio around 2. Hence, the optimal gasification temperature for all feedstocks was determined as shown in Table 2.8.

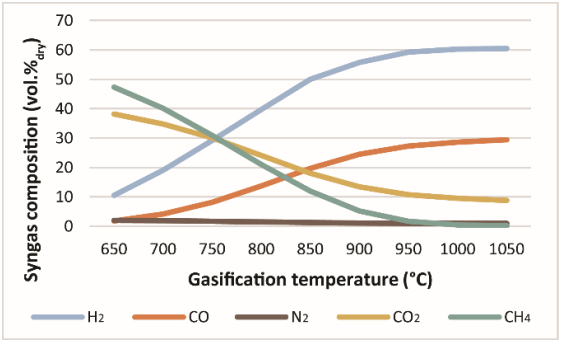

Figure 2.13. Influence of gasification temperature on the raw syngas composition for pine wood

2.3.4.2. Tar reformer

Considering that the tar reformer represents 25% of the purchase equipment cost for the gasification plant and that this unit may be removed when gasification is done at the optimal temperature (see Section 2.3.4.1), its exclusion could help to reduce the overall production costs; however the final viability of this decision will depend on the effects on the syngas composition and its suitability for fermentation. In the case of PW, the syngas production costs are reduced by 20%. Positive effects are also obtained for the environmental performance, GWP and NREU are reduced by 14% and 16% respectively as shown in Table 2.9. Unfortunately, the resulting ammonium concentration with tar

reformer exclusion (770 ppm, see Table 2.10) is much higher than the value reported as tolerable for fermentation, 40 ppm [229].

Although the resulting syngas is not fully free of impurities for fermentation, results suggest that a higher microbial tolerance to contaminants would significantly improve the overall economic and environmental performance of the process.

Table 2.8. Optimal gasification temperature for each feedstock and accompanied syngas compositions in vol.%.

Optimal gasification condition	Feedstock			
	PW	**SB**	**CS**	**EW**
Temperature (C°)	1000	950	850	900
Composition (vol.% dry)				
H_2	60.3	55.6	43.8	52.1
CO	28.6	28.3	22.5	25.8
N_2	1.0	0.0014	0.002	1.3
CO_2	9.5	14.9	22.9	16.6
CH_4	0.47	1.1	9.9	3.9
H_2S	0.017	0.021	0.1	0
NH_3	0.077	0.12	0.86	0.28
H_2/CO ratio	2.1	2.0	2.0	2.0

2.3.4.3. Heat recovery in the syngas production phase

The heat drawn from syngas during its final cooling (unit H108 in Figure 2.2) was considered to be a useful source of energy, thus two potential uses for the heat recovered were analyzed: generation of electricity or steam.

Table 2.9. Effects of exclusion of the tar reformer on the syngas flow, composition, production costs and environmental impacts. Results presented for gasification of PW at 850°C with tar reformer vs. gasification of PW at 1000°C (optimal temperature) excluding tar reforming.

Gasification variable	Gasification at 850 °C with tar reformer	Gasification at 1000 °C and exclusion of the tar reformer
Flow rate (kg/s)	13.95	17.7
Composition (vol.%dry)		
H_2	60.9	60.3
CO	28.1	28.6
CO_2	9.9	9.5
N_2	1.0	1.0
CH_4 (ppm)	593.2	500
NH_3 (ppm)	12.4	770
H_2S (ppm)	160.6	170
H_2:CO ratio	2.1	2.1
LHV (kJ/kg)	5101	6553
Production cost ($/ton$_{syngas}$)	144.50	115.45
Environmental impacts		
GWP (kg_{CO2eq}/kg_{syngas})	0.21	0.18
NREU (MJ/kg_{syngas})	3.46	2.90

When electricity is generated and used within the process, the syngas production costs significantly increase (16–19% for NL, 21–31% for BR, and 35–45% for the US) as shown in Table 2.10. This increase is due to the low thermal efficiency of the steam turbine and additional equipment costs; not enough electricity is generated to compensate for the additional overall costs. On the other hand, the environmental impacts are reduced by 13–26% and 12–20% for GWP and NREU respectively.

When steam is internally produced, a slightly larger reduction on the environmental impacts is achieved (19–31% for GWP and 19–23% for NREU), while the syngas production costs are significantly reduced (22–29%) as shown in Table 2.10. The largest influence of steam generation on the economic and environmental performances occurs when syngas production takes place in NL, this is because steam is the second largest contributor to the production costs after feedstocks.

Table 2.10. Economic and environmental performances for the base cases and the two strategies for heat recovery in the syngas production phase: *i)* electricity production and *ii)* steam generation

Cases	NL				BR		US	
	PW	SB	CS	EW	SB	EW	PW	CS
Base cases								
Production cost ($/ton)	190.73	198.21	218.72	197.96	129.98	150.00	144.50	119.27
GWP (kg_{CO2eq}/kg)	0.26	0.26	0.32	0.21	0.23	0.20	0.21	0.29
NREU (MJ/kg)	5.87	3.71	5.20	5.99	3.13	3.74	3.46	4.09
Electricity production								
Yield (MJ/kg_{syngas})	0.92	0.84	0.85	0.84	0.84	0.84	0.92	0.85
Production cost ($/ton)	221.49	237.20	254.97	233.52	169.80	181.79	194.84	172.65
GWP (kg_{CO2eq}/kg)	0.22	0.20	0.28	0.18	0.17	0.16	0.18	0.25
NREU (MJ/kg)	5.08	3.21	4.60	5.27	2.51	3.10	3.01	3.56
Steam production								
Yield (kg/kg_{syngas})	1.21	1.10	1.11	1.10	1.10	1.10	1.21	1.11
Production cost ($/ton)	134.98	150.92	170.24	149.42	123.76	140.80	144.14	120.96
GWP (kg_{CO2eq} /kg)	0.20	0.18	0.26	0.16	0.17	0.16	0.18	0.24
NREU (MJ/kg)	4.51	2.89	4.17	4.74	2.54	3.13	2.95	3.47

2.3.4.4. Gas flow rate across fermentors and product concentration

The influence of gas flow rate across the syngas fermentors and product concentration are studied only for ethanol and 2,3-butanediol, since: *i)* these two are the only direct products of syngas fermentation, and *ii)* hexanoic acid is assumed to be produced at saturation concentration during chain elongation. At first, syngas fermentations were modelled considering the ethanol and 2,3-butanediol concentrations of 10 and 33 g/L, respectively, with corresponding to the maximal gas flow rates of 5565 and 5413 mol/s (see Figure 2.14.b). Lower gas flow rates proved to reduce the mass transfer capacity as

well as the volumetric production capacity, resulting in a larger number of reactors to maintain the same throughput. However, at the highest gas flow rates (in which gas hold-up in the bioreactors is around 15%), compressors require more energy and larger capacities. Thus, a reduction on the gas flow rate from the highest to the lowest value, would increase of the MSP of ethanol and 2,3-butanediol by 140 and 103% respectively (see Figure 2.14.a). Furthermore, in the case of ethanol, its concentration in the fermentor depends on the gas flow rate due its removal by stripping. Thus, lower gas flow rates results in higher concentrations, and in consequence to higher MSP (see Figure 2.14.b) due to the extra fermentation volume required. In the case of 2,3-butanediol, which is removed along with the broth, a five-fold increase in concentration would lead to a significant size reduction, and therefore on equipment investment, especially of the reverse osmosis unit. This investment decrease would lead to a MPS reduction of 21% as shown in Figure 2.14.b. However, further concentration increments beyond 30 g/L would only have minor economic benefits given the asymptotic trend of the MSP function observed in Figure 2.14.b.

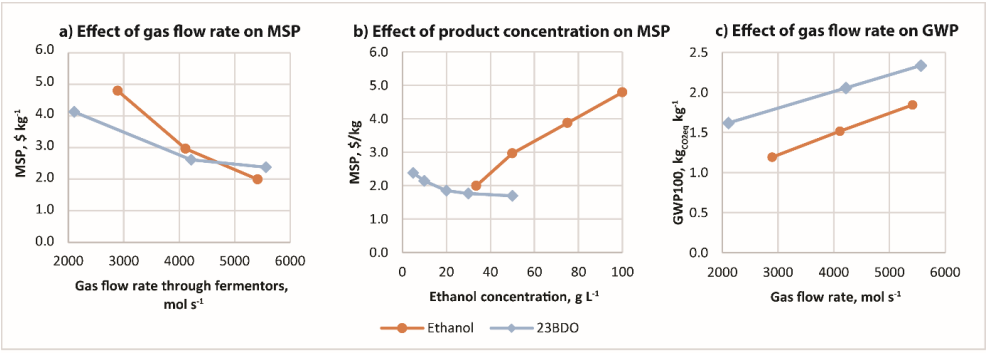

Figure 2.14. Influence of two syngas fermentation parameters on the economic and environmental performance of ethanol and2,3-butanediol production (from PW in the US): a) effect of gas flow rate on MSP; b) effect of ethanol concentration on MSP; and c) effect of gas flow rate on GWP

The GWP performance of both products showed to be proportional to gas flow rate (see Figure 2.14.c) due to direct relation between the gas flow rate and the electricity consumption in the compressors. These relative potential reductions on environmental impacts resulted to be similar for both products. However for ethanol, at even the lowest gas flow rate, the GWP is still 125% higher than that reported for 1G bio-ethanol produced in BR from sugarcane [223]. When the concentration is varied instead, the impacts related to ethanol production follow and inverse relation as the one observed in Figure 2.14.c; but for 2,3-butanediol the change is barely noticed, with a variation of 0.11% on its GWP (results not shown).

2.3.4.5. Interest rate and payback time

Figure 2.15.a shows the effects of the interest rates on the MSP for ethanol production, where the middle points represent the cases discussed in Section 2.3.2. Decrease of the interest rates would only result in minor reductions on the ethanol MSP: 7.4, 3.2 and 13.5% for the US, NL and BR, respectively. Thus, the US is the best geographical option (even at the highest interest rate). BR could become an interesting place for production if the interest rates are on the low side of the last ten years tendency; however, this country has the highest uncertainty of the three locations analyzed which may represent a risk to possible investments.

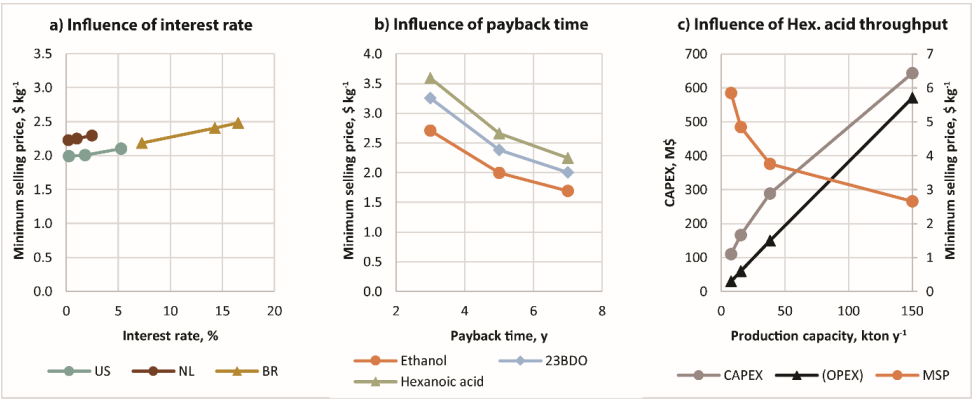

Figure 2.15. Sensitivity analysis. a) Influence of interest rate on MSP for ethanol production (US: 0.25-5.25%, NL: 0.20-2.45%; BR: 7.25-16.50%); b) Influence of PBT on MSP; and c) influence of hexanoic acid production capacity on CAPEX, OPEX and MSP (from 8 to 150 kton/y).

The effects of the PBT on the MSP (see Figure 2.15.b) are significantly larger than those of the interest rates. In average, an MSP decrease of 38% is obtained when the PBT increases from 3 to 7 years. However, the pay-back time preferred by investors is generally between 3 and 5 years [193,197].

2.3.4.6. Hexanoic acid production capacity

CAPEX and OPEX are known to be reduced when the production capacity increases due to the economy of scale. This is also the case for the MSP. However, in this case, two different production scales for hexanoic acid can be considered according to the expected application, already explained in Section 2.3.2. The global market for the former fuel application would be able to absorb large production volumes (*e.g.* 150 kton/y) while the demand for the latter high-quality applications would only be able to handle small scale production before saturating the market (due to lack of published data, the market size for decanoic acid was considered as reference: 70 kton/y)

(www.transparencymarketresearch.com). The MSP of hexanoic acid at large scale production is significantly higher than the commercial price of jet fuel (0.33–1.44 $/kg) in the international market (see Figure 2.15.c). It is also higher than the MSP reported for bio-jet fuel production via hydrothermal liquefaction of PW, EW and from macauba oil [222]. Finally, for small scale production, the obtained MSP is comparable to the commercial price of food-grade hexanoic acid in the international market (2.8–3.4 $/kg) (Alibaba.com) only when the annual production is in the range of 50-75 kton which could already be at near saturation of the market. Hence, hexanoic acid is doubtfully an attractive product of the hybrid process.

2.3.4.7. Fermentor purchase cost

If the purchase cost of each syngas fermenter is lowered to the half of the value assumed, the MSP for ethanol and 2,3-butanediol are lowered by 18 and 13%, respectively (see supplementary information). On the case of hexanoic acid, if the chain elongation fermentor would cost the half, the product's MSP is lowered by 7%. On the other hand, if the purchase costs are doubled, the MSP of ethanol, 2,3-butanediol and hexanoic are raised by 36, 27 and 13%, respectively. From this analysis, two things became evident, *i)* the existing large uncertainty on the economic performance of ethanol and butanediol, and *ii)* the fact that the contribution of the fermentors purchase cost to ethanol specially, is much more determinant than for the two other products.

2.4. Conclusions

Results suggest that the syngas platform, through the hybrid process (biomass gasification followed by syngas fermentation), is a potentially competitive route to produce 2,3-butanediol. This platform showed also to perform slightly poorer, in both economic and environmental terms, than more developed 2G technologies for ethanol production. In the case of 2,3-butanediol, the designed supply chain and process lead to better economic and environmental performances than those of the fossil and bio-based technologies reported for its equivalents 1,4-butanediol and 1,3-propanediol. In fact, production of ethanol, 2,3-butanediol and hexanoic acid though the hybrid process could potentially return lower GHG emissions than their respective fossil-based counterparts. However, uncertainties still exist within the economic performance due to the lack of commercial-scale projects that could serve as reference for cost-related data.

In the hybrid process, the fermentation stage makes use of the low-cost syngas platform, compared to the expensive sugar-based platform, as carbon source. However large CAPEX and OPEX are still associated to the syngas fermentation (mainly due to low CO and H_2 MTC and large power consumption by gas recycling) and DSP (in the case of 2,3-

butanediol, due mainly to the low concentration of products). Yet, further improvements may be possible by increasing the gas-liquid mass transfer capacity inside the syngas fermenters or by process integration and optimization. Thus, heat recovery from the gasification stage showed to be beneficial from an environmental and economic point of view. In general terms, the application of the hybrid process has shown to be an interesting option to produce bulk chemicals that otherwise would require complex DSP to separate and purify the main product from the fermentation broth; that is the case of, for example, 2,3-butanediol.

2.5. List of abbreviations

1G	First generation	LCA	Life cycle assessment
2G	Second generation	MEA	Monoethanolamine
BFB	Bubbling fluidized bed	MSP	Minimum selling price
BR	Brazil	MTC	Mass transfer capacity
CAPEX	Capital expenditures	NL	The Netherlands
CFB	Circulating fluidized bed	NPV	Net present value
CS	Corn stover	NREU	Non-renewable energy use
DSP	Downstream processing	OPEX	Operational expenditures
EPC	Equipment purchase cost	PBT	Payback time
EW	Eucalyptus wood	PRC	Process related costs
FDC	Facility dependent costs	PW	Pine wood
FTS	Fischer-Tropsch synthesis	SB	Sugarcane bagasse
GHG	Greenhouse gas	US	United States of America
GWP	Global warming potential	WWT	Wastewater treatment

Supplementary Information

SI.2.1 Definition of stoichiometry for fermentations

This section shows the sequence of steps followed to estimate the stoichiometry and kinetics of the fermentations.

SI.2.1.1 Catabolic and anabolic reactions

This section will show the steps followed to theoretically define the stoichiometry of the three fermentation processes: ethanol, 2,3-butanediol and hexanoic acid production.

Experimental data published in the scientific literature has been taken as reference to define the stoichiometry of the ethanol production process. Data considered is shown in Table SI.2.1. As appreciated, ethanol is generally produced at temperatures around 37 °C and pH between 4 and 5, reaching concentrations between 18 and 60 g/L (in Table SI.2.1 shows the time needed to achieve the stated concentration under batch fermentations) [48]. Acetic acid is generally the main co-product and is generated in ratios ranging from 1:3 to 1:21 moles of acid to moles of alcohol (see Table SI.2.1), and reaching concentrations between 4 and 6 g/L. Biomass concentrations are typically low, in the range of 0.2-1 g/L; however, when cell recycle strategies are applied, the biomass concentrations can reach 9.3 g/L [72]. Further, in the case of 2,3-butanediol production, published experimental results on syngas fermentation still do not show evidence of final titers higher than 10 g/L; ethanol is generally the main product when 2,3-butanediol is the target [129,230].

Table SI.2.1 Review of published experimental results for ethanol production via syngas fermentation

Titer, g/L	Productivity, g/L/d	Remarks / co-products	Type	References
48.0 at 550 h	Not stated	Ethanol: acetic acid 21:1 mol/mol	Batch	[126]
36.0 at 537 h	60.0	Not stated	Batch	[231]
25.3 at 1400 h	0.9	Ethanol: acetic acid 6.8:1 mol/mol Ethanol: 2-propanol 3.6:1 mol/mol	Batch	[73]
18.0	8.2	Ethanol: acetic acid 3.0:1 mol/mol 2 stages (acidogenesis and solventogenesis)	Continuous	[72]
19.0	7.2	Ethanol: acetic acid 5.5:1 mol/mol	Continuous	[232]

Ethanol, acetic acid and 2,3-butanediol are considered to be produced in association with metabolic energy generation during the syngas fermentation, therefore, the reactions leading to their production from syngas are considered as catabolic reactions [125]. Table SI.2.2 shows these reactions (eq. SI.2.1 – SI.2.6) as well as two anabolic reactions using CO and H_2 as electron donors (eq. SI.2.7 and SI.2.8). Electron balancing was applied to determine the stoichiometry of these reactions [182].

Table SI.2.2 Overall catabolic and anabolic reactions linked to production of ethanol, acetic acid and 2,3-butanediol through syngas fermentation, as well as the ethanol oxidation catabolic reaction and anabolic chain elongation reaction to butyric acid

Ethanol	$CO + {}^{1}/_{2}\,H_2O \rightarrow {}^{1}/_{6}\,C_2H_5OH + {}^{2}/_{3}\,CO_2$ $CO_2 + 3H_2 \rightarrow {}^{1}/_{2}\,C_2H_5OH + {}^{3}/_{2}\,H_2O$	(SI.2.1) (SI.2.2)
Acetic acid	$CO + {}^{1}/_{4}\,H_2O \rightarrow {}^{1}/_{4}\,CH_3COOH + {}^{1}/_{2}\,CO_2$ $CO_2 + 2H_2 \rightarrow {}^{1}/_{2}\,CH_3COOH + H_2O$	(SI.2.3) (SI.2.4)
2,3-butanediol	$CO + {}^{5}/_{11}\,H_2O \rightarrow {}^{1}/_{11}\,C_4H_8(OH)_2 + {}^{7}/_{11}\,CO_2$ $CO_2 + {}^{11}/_{4}\,H_2 \rightarrow {}^{1}/_{4}\,C_4H_8(OH)_2 + {}^{3}/_{2}\,H_2O$	(SI.2.5) (SI.2.6)
Biomass	$2CO + 0.5H_2O + 0.25NH_4^+ \rightarrow CH_{1.75}O_{0.50}N_{0.25} + CO_2 + 0.25H^+$ $2H_2 + CO_2 + NH_4^+ \rightarrow CH_{1.75}O_{0.50}N_{0.25} + 1.5H_2O + 0.25H^+$	(SI.2.7) (SI.2.8)
Ethanol oxidation	$C_2H_5OH + H_2O \rightarrow CH_3COOH + 2H_2$	(SI.2.9)
Chain elongation	$CH_3COOH + C_2H_5OH \rightarrow C_3H_7COOH + H_2O$	(SI.2.10)
	$C_3H_7COOH + C_2H_5OH \rightarrow C_5H_{11}COOH + H_2O$	(SI.2.11)
Anabolic reaction for chain elongation	$CH_3COOH + 0.5C_2H_5OH + 0.25NH_4^+ \rightarrow CH_{1.75}O_{0.50}N_{0.25} + 0.5C_3H_7COOH + H_2O + 0.25H^+$	(SI.2.12)

It is clear, for all the reactions shown in Table SI.2.2, that intake of CO leads to inefficiencies in carbon utilization, since CO_2 is produced along with the main and the co-product. On the other hand, when bacteria feed on CO_2 and H_2, all the carbon in CO_2 is metabolized into the main product or the co-product.

For hexanoic acid production, ethanol and acetic acid are used as intermediate feedstocks; ethanol is used for two purposes: *i)* production of acetic acid through oxidation (eq. SI.2.9), where protons function as the electron acceptors producing hydrogen gas, and *ii)* as building block for the chain elongation reaction of the carboxylic acid. In the former case, as first step of chain elongation, the produced (or separately sourced) acetic acid becomes then the electron acceptor to produce butyric acid (eq. SI.2.10), while ethanol acts as the electron donor. Then for a subsequent step, butyric acid becomes the electron acceptor, while ethanol remains as the electron donor, and hexanoic acid is produced (eq. SI.2.11).

For the anabolic reaction, it is assumed that ethanol is again the electron donor, while one carboxylic acid is the electron acceptor, hence generating a more reduced acid. In this work, it was assumed that acetic acid was the electron acceptor and butyric acid was produced accordingly (see eq. SI.2.12).

SI.2.1.2 Process reactions

In order to link the catabolism and anabolism into a process reaction, the concept of free energy dissipation was used [233]. This concept implies that the amount of Gibbs free energy dissipated during catabolism depends on the number of carbon atoms (NoC) and

the degree of reduction (γ) of the carbon source, according to eq. SI.2.13. This dissipated free energy, added to the Gibbs free energy spent in anabolism, determines the catabolic rate in order to produce enough free energy to synthesize 1 carbon-mol of biomass (λ_{Cat} in eq. SI.2.14). From this last quantity, the maximum biomass yield ($Y_{X/S}^{Met}$) can be determined using eq. SI.2.15. All free energy changes were calculated at metabolic conditions (internal pH and assumed concentrations of metabolites within the microbial cells).

$$\Delta G_{Dis} = 200 + 18(6 - NoC)^{1.8} + \exp[\{(3.8 - \gamma)^2\}^{0.16}(3.6 + 0.4NoC)] \quad \text{(SI.2.13)}$$

$$\lambda_{Cat} = \frac{\Delta G_{An} - \Delta G_{Dis}}{-\Delta G_{Cat}} \quad \text{(SI.2.14)}$$

$$Y_{X/S}^{Met} = -\frac{1}{Y_S^{An} + \lambda_{Cat} \cdot Y_S^{Cat}} \quad \text{(SI.2.15)}$$

The correction of Gibbs free energy for temperature (ΔG^{0T}) is performed using the Helmholtz equation (eq. SI.2.16), while the correction for metabolic concentrations of substances is done with eq. SI.2.17 which includes the intracellular concentrations of products and reactants (C) as well as their stoichiometric coefficients (δ). The correction for CO, H_2 and CO_2 (sub-index j in eq. SI.2.17) was done from their logarithmic mean partial pressures (P*) inside the fermentors, since their values change with the liquid height. Internal pH of 6 was assumed for both syngas fermentations [76], while internal pH of 7 was assumed for the bacteria responsible of chain elongation. The used fermentation conditions, including concentrations of substrates and products, can be found in Table SI.2.3.

Table SI.2.3 Fermentation conditions and extracellular concentrations of substrates and products for all the studied fermentations, when pine wood is used as feedstock

Parameter	Units	Fermentation		
		Ethanol production	2,3-butanediol production	Hexanoic acid production
Temperature	°C	37	37	30
pH	-	5	5	5
Concentration				
CO	mol/m³	0.0002	0.0001	-
H_2	mol/m³	0.206	0.206	0.013
CO_2	mol/m³	3.866	3.843	-
Biomass (X)	mol/m³	120.3	106.0	49.1
Ethanol	mol/m³	729.4	11.57	1.000
2,3-butanediol	mol/m³	-	111.0	-
Acetic acid	mol/m³	63.20		0.045
Butyric acid	mol/m³	-	-	51.66
Hexanoic acid	mol/m³	-	-	92.98
Log mean pressure	atm	1.723	1.720	0.208
Partial pressures				
CO	atm	0.463	0.464	-

Parameter	Units	Fermentation		
		Ethanol production	2,3-butanediol production	Hexanoic acid production
H_2	atm	1.003	1.007	0.004 (at top) 0.017 (log mean) 0.044 (at bottom)
CO_2	atm	0.177	0.173	-

In eq. SI.2.16 and SI.2.17, T is the temperature, in K; Tref is the standard temperature, 298.15 K; R is the ideal gas constant; ΔG^0 is the Gibbs free energy change of the reaction at standard conditions; and, ΔG^{01} is the Gibbs free energy of the reaction corrected to metabolic conditions.

The results of this analysis are shown in Tables SI.2.4 – SI.2.6. In Table SI.2.4, it can be seen that theoretically, CO would be the preferred electron donor as its catabolic reactions yield more free energy than H_2. Under the same argument, acetic acid would be the preferred product in the metabolic pathway that leads to ethanol and acetic acid. Similarly, biomass yields are higher when CO is the electron donor.

$$\frac{\Delta G^{0T}}{T} = \frac{\Delta G^0}{T_{ref}} + \Delta G^0 \left(\frac{1}{T} - \frac{1}{T_{ref}}\right) \quad \text{(SI.2.16)}$$

$$\Delta G^{01} = \Delta G^{0T} + RT \sum \delta_i \, ln(C_i) + RT \sum \delta_j \, ln\left(P_j^*\right) \quad \text{(SI.2.17)}$$

Table SI.2.5 suggests that ethanol is the preferred side product in the production of 2,3-butanediol. CO is a better electron and carbon source (C-source) since it produces more free energy than H_2 and dissipates less free energy than CO_2 when catabolized. A similar case to ethanol production.

Table SI.2.4 Energies involved in metabolism during ethanol production, in kJ/mol of carbon source*

Electron donor	CO			H_2		
Product	Ethanol	Acetic acid	Biomass***	Ethanol	Acetic acid	Biomass***
ΔG^0	-37.4	-33.8	-48.6	-52.3	-27.5	-8.5
ΔH^0	-57.4	-65.1	-87.9	-178.8	-134.6	-92.3
ΔG^{0T}	-36.6	-32.5	-47.0	-47.2	-23.2	-5.1
ΔG^{01}	-37.6	-43.2	-51.9	-42.6	-39.6	-5.1
ΔG_{Dis} of C-source, kJ/C-mol$_X$*	651			986		
λ_{Cat} *, mol$_{C\text{-source}}$/C-mol$_X$	18.7			23.3		
$Y_{X/S}^{Met}$ *, C-mol$_X$/mol$_{C\text{-source}}$	0.060			0.045		

* CO_2 is the carbon source when H_2 is the electron donor. CO on the other hand, is both carbon source and electron donor.

** Parameters shown for main product (ethanol).

*** Energies for biomass production are expressed in kJ/C-mol$_X$.

Table SI.2.5 Energies involved in metabolism during 2,3-butanediol production, in kJ/mol of carbon source

Electron donor	CO			H_2		
Product	**2,3-butanediol**	**Ethanol**	**Biomass****	**2,3-butanediol**	**Ethanol**	**Biomass****
ΔG^0	-35.3	-37.4	-48.6	-41.9	-52.3	-8.5
ΔH^0	-10.4	-57.4	-87.9	-34.6	-178.8	-92.3
ΔG^{0T}	-36.3	-36.6	-47.0	-42.2	-47.2	-5.1
ΔG^{01}	-37.7	-39.9	-52.0	-39.1	-49.4	-5.1
ΔG_{Dis} of C-source, kJ/C-mol$_X$*	651			986		
λ_{Cat} *, mol$_{C\text{-source}}$/C-mol$_X$	18.7			25.4		
$Y_{X/S}^{Met}$ *, C-mol$_X$/mol$_{C\text{-source}}$	0.054			0.039		

* Parameters shown for main product (2,3-butanediol).

** Energies for biomass production are expressed in kJ/C-mol$_X$.

Table SI.2.6 Energies involved in metabolism during hexanoic acid production, in kJ/mol of electron donor (ethanol)

Product	C2***	C4***	C6***	Biomass$^{\text{ϟ}}$
ΔG^0	49.6	-38.6	-38.8	-0.3
ΔH^0	88.3	-46.7	-47.0	19.0
ΔG^{0T}	48.9	-38.3	-38.4	-0.7
ΔG^{01}	-19.9	-3.3	-19.1	44.0
ΔG_{Dis} of C-source, kJ/C-mol$_X$*	706			
λ_{Cat} *, mol$_{C\text{-source}}$/C-mol$_X$	37.2			
$Y_{X/S}^{Met}$ *, C-mol$_X$/mol$_{C\text{-source}}$	0.027			

* Calculated at the log mean H_2 partial pressure (see Table SI.2.3).

** Parameters shown for main product (hexanoic acid).

*** C2: acetic acid; C4: butyric acid; C6: hexanoic acid.

ϟ Energies for biomass production are expressed in kJ/C-mol$_X$.

The distribution of carbon between product and co-product was defined from available experimental data for ethanol production (see Table SI.2.1). The distribution for the two other fermentations was assumed to be selective for the main products (see Table SI.2.7). The biomass yield was defined from the thermodynamic analysis explained previously.

Table SI.2.7 Used distribution of products

Fermentation	Products	Product distribution	
		mol.%	**w.%**
Ethanol production	Ethanol	85	86
	Acetic acid	9	11
	Biomass	6	3
2,3-butanediol production	2,3-butanediol	71	88
	Ethanol	7	4
	Biomass	22	8
Hexanoic acid production	Hexanoic acid	84	93
	Butyric acid	6	5
	Biomass	11	3

For hexanoic acid production, the thermodynamic feasibility of the ethanol oxidation reaction has shown to be sensitive to the fermentation conditions. Figure SI.2.1 presents the dependence of the Gibbs free energy of the said reaction with respect to the partial pressure of hydrogen and the internal pH of bacteria.

In order for the ethanol oxidation reaction to be thermodynamically feasible, and also to be capable of yielding sufficient energy (15 kJ/mol$_{e\text{-donor}}$) [183] to maintain an active proton motive force (avoiding product inhibition by H_2), at intracellular pH of 7, the partial pressure of hydrogen gas should not exceed 0.046 atm at any point in the bioreactor (see Figure SI.2.2). Therefore the fermentation process was assumed to be carried out under hypobaric conditions.

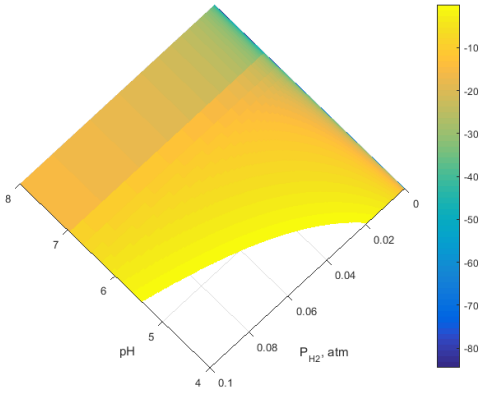

Figure SI.2.1 Gibbs free energy change of the ethanol oxidation reaction to acetic acid at metabolic conditions, in kJ/mol of ethanol: effect of pH and H_2 partial pressure (values above zero are excluded to mark off the range where reaction is thermodynamically feasible)

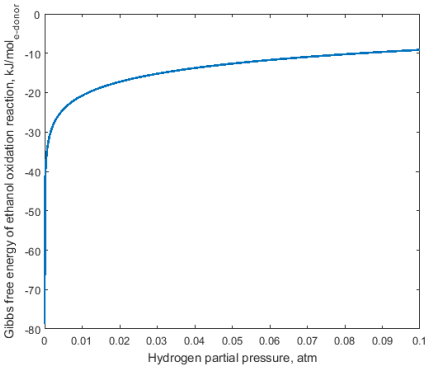

Figure SI.2.2 Gibbs free energy of the ethanol oxidation reaction at metabolic conditions, in kJ/mol of ethanol: effect of H_2 partial pressure at internal pH 7.

For the syngas fermentations, the two metabolic reactions (one for each electron donor, CO and H_2) can be combined into one process reaction, in a proportion assumed to be determined by the CO and H_2 content in the syngas fed to the bioreactor. This assumes that the ratio of H_2/CO inside the reactor remains unchanged. Four different syngas

compositions were considered since four different feedstocks have been studied for the production of syngas, *i.e.,* pine wood, sugarcane bagasse, corn stover and eucalyptus wood; thus, the fermentation process reactions were different for each specific feedstock. As an example, the resulting stoichiometry of the combination of the two metabolic reactions is shown in Table SI.2.8 for pine wood as feedstock.

Table SI.2.8 Stoichiometric coefficients for the combination of the two process reactions, for each of the three fermentations studied, when syngas is produced from pine wood

Substance	Fermentation		
	Ethanol production	**2,3-butanediol production**	**Hexanoic acid production**
CO	-2.066	-3.863	-
H_2	-4.476	-8.386	1.681
CO_2	-0.205	-0.661	-
Ammonium	-0.018	-0.078	-0.032
Ethanol	1.000	0.100	-2.907
2,3-butanediol	-	1.000	-
Acetic acid	0.100	-	-0.291
Butyric acid	-	-	0.067
Hexanoic acid	-	-	1.000
Biomass	0.071	0.313	0.131
Water	1.240	2.918	1.290
Protons	0.118	0.084	0.808

(+) for production, (-) for consumption.

SI.2.2 Kinetics

In order to size the fermentors, a black box kinetic model for microbial growth was derived from thermodynamics [183]. The parameters of the Herbert-Pirt equation (eq. SI.2.18) for substrate consumption are defined by using equations SI.2.15 and SI.2.19. The calculation of the biomass yield ($Y_{X/S}^{Met}$) was explained in section SI.2.1.2. The substrate requirements for microbial maintenance processes (ms) are calculated assuming that microbes, in general, require 4.5 kJ/C-mol$_X$ at 25 °C [183]. The parameters obtained through this approach are shown in Table SI.2.9.

In order to derive a value for the maximum specific substrate uptake rate, ${q_S}^{max}$, it is assumed that microbes have a maximum electron transport capacity across the membrane. [183] The correlation shown in eq. SI.2.20 is used to define an electron transport capacity (ETC) as a function of the temperature, [183] while eq. SI.2.21 relates ETC to both the catabolic energy production and the amount of electrons involved in the reaction (NoElec) [183].

$$q_S = a\mu + m_S; \;\; a = \lambda_{Cat} \tag{SI.2.18}$$

$$m_S = 4.5exp\left[\frac{-69000}{R}\left(\frac{1}{T}+\frac{1}{298.15}\right)\right]\left(\frac{1}{\Delta G_{Cat}^{01}}\right) \tag{SI.2.19}$$

Table SI.2.9 Estimated parameters for the Herbert-Pirt equation*

Fermentation	Electron donor	Parameter	
		a, $mol_{C\text{-}source}/C\text{-}mol_X$	m_S, $mol_{C\text{-}source}/C\text{-}mol_X/h$
Ethanol production	CO	17.94	0.351
	H_2	24.01	0.310
2,3-butanediol production	CO	17.91	0.351
	H_2	26.09	0.338
Hexanoic acid production	Ethanol	37.72	0.357

* Parameters shown applicable for main product generation only

$$ETC = 3exp\left[\frac{-69000}{R}\left(\frac{1}{T}+\frac{1}{298.15}\right)\right] \quad \text{(SI.2.20)}$$

$$q_S{}^{max} = ETC\left(\frac{\Delta G_{Cat}^{01}}{NoElec}\right) \quad \text{(SI.2.21)}$$

The maximum consumption/production rates of all substances involved in the overall process reactions were calculated by linking the obtained maximum uptake rate of the electron donor to the stoichiometry of each process reaction specific to each electron donor; the two kinetic behaviors (one for each electron donor) were coupled in the same manner as the overall stoichiometry was defined for each fermentation process: in a proportion determined by the CO and H_2 content in the syngas fed to the bioreactor. For instance, in ethanol production the sum of the uptake rate of both electron donors, CO and H_2 returns 4.304 $mol_{e\text{-}donor}/C\text{-}mol_X/h$, which is the maximum uptake rate calculated for each electron donor in its specific process reaction. The results when pine wood is used as feedstock, are shown in Table SI.2.10.

Table SI.2.10 Maximum q-rates for all process reactions when syngas is produced from pine wood

Substance	Maximum production/consumption rate *, $mol_i/C\text{-}mol_X/h$		
	Ethanol production	2,3-butanediol production	Hexanoic acid production
CO	-1.391	-1.389	-
H_2	-3.013	-3.015	1.373
CO_2	-0.138	-0.238	-
Ammonium	-0.012	-0.028	-0.026
Ethanol	0.673	0.036	-2.374
2,3-butanediol	-	0.360	-
Acetic acid	0.067	-	-0.237
Butyric acid	-	-	0.054
Hexanoic acid	-	-	0.817
Biomass	0.048	0.112	0.106
Water	0.835	1.049	1.054
Protons	0.079	0.030	0.660

* (+) for production, (-) for consumption.

As already indicated in the main article (section 2.2.1.3), the affinity constants could also be estimated from thermodynamics. Table SI.2.11 shows the obtained partial pressures and the corresponding saturation concentrations in the liquid phase.

Table SI.2.11 Affinity constants for the substrates of the different fermentations

Fermentation	Substrate	Parameter	
		K_S, mg/L	Partial pressure at concentration equal to K_S, atm
Ethanol production	CO	1.63E-3	7.24E-5
	H_2	4.12E-2	2.82E-2
	CO_2	4.31E-3	3.94E-6
2,3-butanediol production	CO	1.59E-3	7.09E-5
	H_2	4.91E-2	3.36E-2
	CO_2	1.65E-2	5.51E-5
Hexanoic acid production	Ethanol	1.41E-4	-

SI.2.3 Fermentor sizing and design

The capacity of fermentors was adjusted to the desired throughput. The definition of the plants capacities is shown in the main chapter content, section 2.2.1. Table SI.2.12 shows the capacities of the proposed fermentation processes.

Table SI.2.12 Production capacity of the fermentation units

Product	Production capacity, kg/s
Ethanol	6.84
2,3-butanediol	7.34
Hexanoic acid	5.37

Two general assumptions can be applied for all the bioreactors that have been designed, these are listed below:

- Operation at steady state, for continuous fermentation.
- The concentrations of substances and products, including biomass are assumed to be homogenously distributed within the bioreactor length. Inversely, the saturation concentrations of dissolved gases do vary as function of hydrostatic pressure, hence they vary depending on the bioreactor height. The gas phase was assumed as perfectly mixed since the fermentors are large and their aspect ratio is below 3 [85].

SI.2.3.1 The ethanol case

The main challenge within the syngas fermentors is the supply of substrate at a rate that supports microbial consumption, while maintaining biomass concentrations high enough

to keep the bioreactor volume as low as possible. Therefore, the starting point for the design of the ethanol-producing syngas fermentors, is to determine a gas flow rate that is high enough to fulfil the stated objective. The proposed configuration (see Figure 2.3.a in the main document), with gas recycle brings several advantages:

- the excess of gas removes all the ethanol produced while pre-concentrating it,
- the gas removes more water than what is produced by the metabolic reaction,
- the gas removes a fraction of the acetic acid produced as well, which lowers the needs for pH control and acetate removal operations,
- evaporation of liquids removes part of the heat produced by the exothermic process reaction,
- biomass separation/retention for downstream processing will be minimal, avoiding possible stress or damage to cells.
- liquid outflow from the bioreactor will only be needed for control of salts concentrations and for removal of the of acetate produced.
- The amount of gas circulation through the bioreactors was assumed to be sufficient to generate a recommended maximum gas hold-up of 15 vol.%, [85] in order to provide high mass transfer capacities while avoiding microbial stress due to turbulence and excessive energy expenses on gas supply. The ethanol concentration in the fermentors was calculated according to the gas flow rate using gas-vapor liquid equilibria data (obtained from Aspen Plus V8.8, using NTRL thermodynamic model). Moreover, from a biomass mass balance inside the fermentors, its concentration was determined by the CO and H_2 mass transfer capacities.

The mass transfer capacities of CO and H_2, were determined by the product of the mass transfer coefficients and the concentration driving force of the gases ($C_{saturation\ in\ the\ liquid} - C_{actual\ in\ the\ liquid}$). The volumetric gas flow rate and the saturation concentrations of the substrates in water were calculated as functions of the hydrostatic pressure and averaged logarithmically over the height of the bioreactor; syngas was always treated as an ideal gas. Further, the mass transfer coefficients (k_La) for CO, CO_2 and H_2 were calculated as function of the superficial gas velocity, also corrected for average pressure, ${v_{Gs}}^C$ [234]; since the model used determines the k_La for oxygen gas-liquid transfer at 20 °C, its value was corrected for CO, CO_2 and H_2 gas diffusivities in water (D_i - obtained using the Wilke-Chang equation (see eq. SI.2.27 and Table SI.2.13)) [235], and for temperature. All this is done by using equations SI.2.22 – SI.2.27. According to the Wilke-Chang equation, the diffusivity of a solute in water is a function of the temperature (T), the molecular weight of water (M), the molar volume of the solute (V_i) and the viscosity of water (η).

$$v_{Gs} = \frac{\dot{V}_{log\,mean}}{A_T} \quad \text{(SI.2.22)}$$

$${v_{Gs}}^C = v_{Gs}\frac{(P_t + P_b)}{2}\frac{ln\left(\frac{P_b}{P_t}\right)}{P_b - P_t} \quad \text{(SI.2.23)}$$

$$k_L a_{O_2,20°C} = 0.3{v_{Gs}}^{C^{0.7}} \quad \text{(SI.2.24)}$$

$$k_L a_{O_2,T} = k_L a_{O_2,20°C} 1.022^{(T-20)} \quad \text{(SI.2.25)}$$

$$k_L a_{i,T} = k_L a_{O_2,T}\frac{D_i}{D_{O_2}} \quad \text{(SI.2.26)}$$

$$D_i = 7.4E - 8\left[\frac{T\left(2.6M^{1/2}\right)}{\eta {V_i}^{0.6}}\right] \quad \text{(SI.2.27)}$$

Table SI.2.13 Diffusivities of gases in water calculated through the Wilke-Chang equation (e.q. SI.2.27)

Substance	Diffusion coefficient at 37 °C, m²/s
O_2	3.21E-09
CO	2.88E-09
H_2	4.55E-09
CO_2	2.70E-09

The total volume of the liquid was then obtained through an ethanol mass balance inside the bioreactor. It was assumed that the ethanol production capacity (see Table SI.2.12) equals the product removal rate within the gas phase (eq. SI.2.28).

$$V_L = \frac{Capacity}{q_{et}X} \quad \text{(SI.2.28)}$$

The gas hold-up (ε_G) was calculated from the superficial gas velocity for the heterogeneous and homogeneous gas flow regimes (eq. SI.2.29 and SI.2.30, respectively) [234] and the volume of the gas-liquid mixture was found.

$$\varepsilon_G = 0.6{v_{Gs}}^{C^{0.7}} \quad \text{(SI.2.29)}$$

$$\varepsilon_G = \frac{{v_{Gs}}^C}{0.25} \quad \text{(SI.2.30)}$$

Then, the final volume and height of the bioreactor was calculated assuming a headspace of 20 vol.%. Iterations were performed until the rate of CO consumption equals the rate of gas-liquid mass transfer capacity.

SI.2.3.2 The 2,3-butanediol case

The fermentation units for 2,3-butanediol production have three commonalities with the ones for ethanol production: *i)* amount of feedstock (syngas) used; *ii)* maximum gas hold-up of 15 vol.% and *iii)* a threshold volume of each bioreactor: 900 m^3.

In this case, the product removal does not follow the same pre-concentration scheme as in the case of ethanol production (see section SI.2.3.1) since 2,3-butanediol is far less volatile than ethanol. Therefore, liquid removal was needed. The algorithm used is the same as for the ethanol case, with the difference that a lower amount of gas will be removed from the broth (less ethanol), and all of it will be recycled after CO_2 removal (see section 2.2.1.4 in main document).

SI.2.3.3 The hexanoic acid case

The design of the chain elongation bioreactor was somehow simpler than the previous ones in terms of mass transfer since in this case, no gases are fed into the fermenter. Given the hypobaric conditions, large amounts of water are evaporated, thus the heat supply became the main limitation for the biomass concentration and thus reactor productivity. Due to this fact, heat was thought to be provided by two means, *i)* internal heating with an immersed coil and *ii)* a warmed-up liquid recycle stream coming from the centrifuge in which hexanoic acid is separated from the aqueous phase. Moreover, since this fermentation is carried out anaerobically, and as already stated no gas is fed to the bioreactor, a maximum allowable volume of each bioreactor was assumed to be 3000 m^3.

SI.2.3.4 Results on bioreactor sizing

Table SI.2.14 shows the operation parameters and main dimensions of all the bioreactors designed.

Table SI.2.14 Dimensions and main operation parameters of the conceptually designed fermentors

Parameter	Units	Main product		
		Ethanol production	2,3-butanediol production	Hexanoic acid production
Total liquid volume*	m^3	8100	8100	4081
Liquid volume in a single bioreactor	m^3	579	579	2040
Total volume of a single bioreactor**	m^3	855	850	3000
Number of bioreactors	-	14	14	2
Tank diameter (T)	m	7.1	7.1	22.1
Tank height (H)	m	21.5	21.5	7.0
Aspect ratio (H/T)	-	3.0	3.0	0.3
Top pressure	atm	1.00	1.00	0.047
Bottom pressure	atm	2.66	2.66	0.63

Parameter	Units	Main product		
		Ethanol production	2,3-butanediol production	Hexanoic acid production
Superficial gas velocity, P. corrected	m/s	0.135	0.137	0.03
Gas hold-up	vol.%	14.8	14.9	10.5
k_La CO	s^{-1}	0.102	0.103	-
k_La H_2	s^{-1}	0.162	0.163	-
k_La CO_2	s^{-1}	0.096	0.097	-
Syngas excess in feed***	vol.%	437	447	-
Off-gas composition				
Ethanol	vol.%	1.6	0.2	-
Water	vol.%	2.8	3.7	89.3
CO	vol.%	26.9	27.2	0.5
H_2	vol.%	58.4	58.9	9.5
CO_2	vol.%	10.3	10.1	0.7

* Broth density was assumed as 1000 kg/m^3.

** Assuming 20 vol.% headspace.

*** Defined as: Excess = (Ffeed – Fstoichiometric) / Fstoichiometric X 100%.

SI.2.3.5 Evaluation of mixing

The mixing time, t_m, was calculated through eq. SI.2.31 [236]; it is a function of the tank diameter, T, and the specific power input by the gas flow, e (eq. SI.2.32). The mixing number, N_{mix}, is assumed as 16 since the H/T ratio in all bioreactors [236], after the iteration procedure, resulted to be 3 for the syngas fermentors, and 0.4 for the chain elongation bioreactor. The liquid circulation velocity, v_{lc}, was calculated using eq. SI.2.33, while the liquid mixing flow, Q_L, was obtained from eq. SI.2.34. Additionally, the amount of gas mixing was analyzed with eq. SI.2.35, in the form of a dispersion coefficient, Deg. To finalize, the non-dimensional Bodenstein (Bo) number was determined (eq. SI.2.36) for each bioreactor in order to check whether the gas phase is ideally mixed. For instance, a well-mixed system has a Bo < 0.1, while a plug flow would return Bo > 20. [237]

$$N_{mix} = \frac{t_m e^{1/3}}{T^{2/3}} = 16 \quad \text{(SI.2.31)} \qquad e = g v_{Gs}{}^{C} \quad \text{(SI.2.32)}$$

$$v_{lc} = 0.9(gT v_{Gs}{}^{C})^{1/3} \quad \text{(SI.2.33)} \qquad Q_L = 0.3T^{5/3} F_G{}^{1/3} g^{1/3} \quad \text{(SI.2.34)}$$

$$D_{eg} = 78(v_{Gs}{}^{C} T)^{1.5} \quad \text{(SI.2.35)} \qquad Bo = \frac{(v_{lc} + 0.25)H}{D_{eg}} \quad \text{(SI.2.36)}$$

Table SI.2.15 shows that the calculated liquid mixing times are consistent with average values reported for large vessels [85], suggesting that there are no serious problems expected with mixing in the liquid phase of each designed bioreactor. As the Bo number is low (within the scale between 0.1 and 20), it is assumed that the gas in the fermentor has some axial dispersion. This is seen for all cases, since the large amounts of gas that circulate through each fermentor guarantee good mixing properties.

Table SI.2.15 Evaluation of mixing properties in the designed fermentors

Parameter	Units	Main product		
		Ethanol production	2,3-butanediol production	Hexanoic acid production
Specific power input	W/kg	1.32	1.34	0.26
Mixing time	s	53.9	53.7	197
Liquid circulation velocity	m/s	1.90	1.91	1.61
Liquid mixing flow	m^3/s	88.8	74.9	255
Gas mixing dispersion coefficient	m^2/s	73.4	75.2	38.8
Bo number	-	0.63	0.62	0.36

SI.2.3.6 Energy requirements

The heating or cooling requirements of the fermenters can be retrieved from the energy balance, which is mainly determined by the heat produced through the process reactions and the heat removed by evaporation of liquids. The enthalpy given by the syngas fed to the syngas fermentors was neglected since the temperature at which it is delivered to the fermentation was set close to the fermentation temperature.

The heat produced by the fermentation was calculated from the standard heat of formation of the substances involved, in combination with their stoichiometric coefficients for each reaction. The heat removed through evaporation of liquids was calculated from their mass flows and latent heat of evaporation of volatile contents. Further, the heat transfer capacity of the fermentation units was calculated multiplying the wall surface area in contact with the gas liquid mixture, the temperature gradient between the cooling fluid and the bulk of broth, and an average heat transfer coefficient recommended for agitated dilute solutions and jacketed vessels with water as the cooling agent. [238] For the chain elongation reactor, a heating agent was required instead of cooling, and also an immersed coil was assumed in order to produce a larger area and heat transfer coefficient [238]. Table SI.2.16 shows the results of the parameters used in the evaluation.

Table SI.2.16 Parameters for evaluation of energy requirements

Parameter	Units	Main product		
		Ethanol production	2,3-butanediol production	Hexanoic acid production
Liquids evaporation rate	mol/s	425.7	359.1	359.2
Water thermal conductivity	W/m/K	0.63	0.63	0.63
Heat capacity of water	J/kg/K	4178	4178	4178
Heat transfer coefficient	$W/m^2/K$	500	500	600
Wall area available for heat transfer	m^2 per reactor	384.3	384.7	1087 (coil)
Temperature gradient for heat transfer	°C	15.0	10.0	20.0

Parameter	Units	Main product		
		Ethanol production	2,3-butanediol production	Hexanoic acid production
Heat produced by reaction	MW	55.70	15.28	0.78
Heat removed in evaporation	MW	17.87	15.26	31.38
Heat supplied by liquid recycle	MW	-	-	4.5
Required heat transfer capacity per bioreactor	MW per reactor	2.71	0.01	15.3
Available heat transfer capacity per bioreactor	MW per reactor	2.88	1.92	15.3

The reaction which generates the most heat is the ethanol production process, in which the heat removed by evaporation withdraws only 32% of the total heat produced. In the case of the 2,3-butanediol production, the evaporation removes nearly all the heat produced. In the case of the chain elongation bioreactor, the heat removal through evaporation is 40 times higher than the heat produced by the process reaction. Finally, Figures SI.2.3.a and SI.2.3.b show the energy requirements for cooling or heating in the three analyzed fermentation processes.

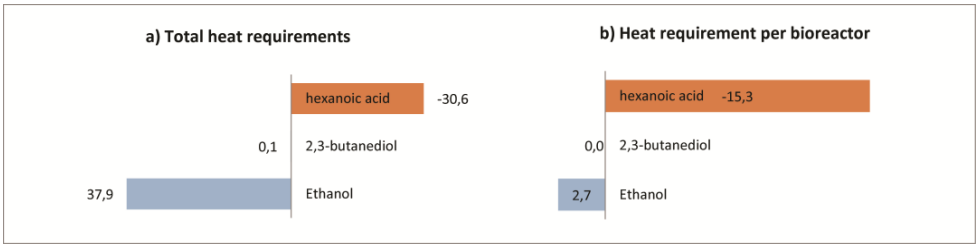

Figure SI.2.3 Heat requirements by the fermentations, in MW.

* Red for heating, blue for cooling requirements

SI.2.4 Sensitivity analysis for fermentor purchase costs

The purchase costs used for the base cases shown in the main document were obtained from matche.com. The value obtained for "fermentor" directly from the website was multiplied by a factor of 2, assumed due to the special requirements driven that the anaerobic conditions, and the handling of hydrogen in high concentrations in the three types of fermentors designed. Therefore, the sensitivity analysis of this variable was thought to be needed in order to identify the uncertainty present in the assumption. Figures SI.2.3 – SI.2.5 show the results which are briefly discussed in the main document, section 2.3.4.7.

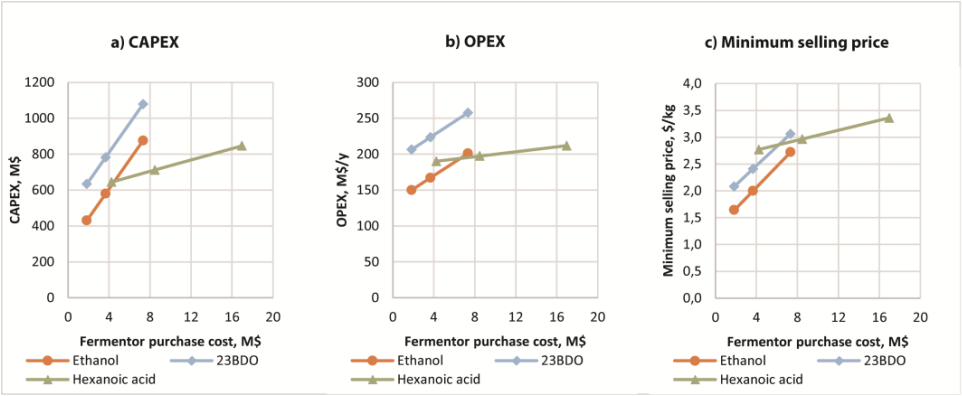

Figure SI.2.4 Influence of fermentor purchase cost on a) CAPEX, b) OPEX and c) products' minimum selling prices.

SI.2.5 List of symbols

Table SI.2.17 List of abbreviations used within the supplementary information

Symbol	Name	Units
NoC	Number of carbon atoms in the carbon source	$mol_{Carbon}/mol_{C\text{-}source}$
γ	Degree of reduction	$mol_{electrons}$/C-mol
ΔG_{Cat}	Gibbs free energy of catabolic reaction	kJ/C-$mol_{C\text{-}source}$
ΔG_{An}	Gibbs free energy of anabolic reaction	kJ/C-$mol_{C\text{-}source}$
ΔG_{Dis}	Gibbs free energy dissipation	kJ/C-$mol_{C\text{-}source}$
ΔG^0	Gibbs free energy at standard conditions	kJ/mol
ΔG^{0T}	Gibbs free energy temperature corrected	kJ/mol
ΔG^{01}	Gibbs free energy at metabolic conditions	kJ/mol
λCat	Stoichiometric coefficient of C-source in metabolic reaction	$mol_{C\text{-}source}$/C-mol_X
$Y_{X/S}^{Met}$	Biomass yield	C-molX molC-source
Y_S^{An}	Stoichiometric coefficient of C-source in anabolic reaction	$mol_{C\text{-}source}$/C-mol_X
Y_S^{Cat}	Stoichiometric coefficient of C-source in catabolic reaction	$mol_{C\text{-}source}$/C-mol_X
C	Concentration in liquid	mol/m^3
δ	Stoichiometric coefficient	-
T	Temperature	K
R	Ideal gas constant	J/mol/K
q	Specific uptake/production rate	mol/C-mol_X/h
μ	Biomass growth rate	h^{-1}
m_S	Maintenance coefficient	$mol_{C\text{-}source}$/C-mol_X/h
ETC	Electron transport capacity	$mol_{electrons}$/C-mol_X/h
q_S^{max}	Maximum specific uptake rate	mol_S/C-mol_X/h
$NoElec$	Number of electrons donated in anabolism	$mol_{electrons}/mol_{C\text{-}source}$/h
H	Tank height	m
T	Tank diameter	m
H/T	Aspect ratio	-
V_L	Volume of liquid	m^3
A_T	Cross-sectional area	m^2
v_{Gs}	Superficial gas velocity	m/s
v_{Gs}^C	Superficial gas velocity, pressure corrected	m/s

Symbol	Name	Units
P_t	Top pressure	atm
P_b	Bottom pressure	atm
$\dot{V}_{log\ mean}$	Logarithmic mean of volumetric flow rate across fermentor	m^3/s
$k_L a$	Mass transfer coefficient	s^{-1}
D	Diffusivity in water	m^2/s
M	Molecular weight	g/mol
V_i	Molal volume of solute i	mL/g/mol
η	Viscosity	cP
ε_G	Gas hold-up	$m_{gas}^3/m_{gas\text{-}liquid\ mixture}^3$
e	Specific power input	W/kg
t_m	Mixing time	s
N_{mix}	Mixing number	-
g	Acceleration of gravity	m/s^2
v_{lc}	Liquid circulation velocity	m/s
F_G	Gas flow rate	m^3/s
Q_L	Liquid mixing flow	m^3/s
D_{eg}	Fermentor dispersion coefficient	m^2/s
Bo	Bodenstein number	-
h	Heat transfer coefficient	$W/m^2/K$

Chapter 3

Modeling ethanol production through syngas fermentation: A biothermodynamics and mass transfer-based hybrid model for microbial growth in a large-scale bubble column bioreactor

This chapter is based on the article published as:

Eduardo Almeida Benalcázar, Henk Noorman, Rubens Maciel Filho and John Posada, 2020, "Modeling ethanol production through syngas fermentation: A biothermodynamics and mass transfer-based hybrid model for microbial growth in a large-scale bubble column bioreactor", Biotechnology for Biofuels, 13:59, DOI: 10.1186/s13068-020-01695-y.

"This is the night, what it does to you.
I had nothing to offer anybody except my own confusion."

Jack Kerouac, *On the road*, 1957

3.1. Introduction

Gas mixtures containing CO_2, H_2 and CO are commonly known as syngas, which is typically produced by two processes *i.e.*, thermochemical conversion (gasification) of carbonaceous materials like coal and oil, and reforming of natural gas [125]. Lignocellulosic biomass, food, municipal and packaging wastes are alternative raw materials that can also be used for gasification [239,240] and could lead to production processes with improved sustainability attributes as compared to fossil-based feedstocks [30,241]. For this reason, syngas from non-fossil sources is considered a key feedstock for the circular economy.

Driven by technical and sustainability limitations of Fisher-Tropsch synthesis [242], experiments performed since the late 1980's explored the potential of certain types of autotrophic acetogenic bacteria to catabolize the three main components of syngas into ethanol [48]. Although with generally low productivities, these microorganisms are also able to produce a variety of other substances of commercial importance *e.g.* 2,3-butanediol, butanol and butyric and lactic acids [129,243], however ethanol is the first commercialized bioproduct [48].

Acetogens convert carbon into acetyl-CoA through the Wood-Ljungdahl metabolic pathway (WLP) [51]. In the reductive direction, the WLP is considered the most efficient non-photosynthetic and the only linear CO_2 fixation pathway to acetyl-CoA [125,244]. Two molecules of CO_2 and/or CO are fixated following two separate branches, the methyl (eastern) and the carbonyl (western) branches. Thorough descriptions on the configuration of the WLP and its link with the particular energy conservation strategies of acetogens can be found elsewhere [50,125,243,245]. The WLP is able to use CO as a source of energy and carbon [246–249], whereas H_2 has to be combined with a carbon source that can be CO_2 [243,250]. It has been proposed that CO fermentation would yield higher amounts of Gibbs free energy and adenosine triphosphate (ATP) than H_2 [111,118], while H_2 fermentation offers advantages on improved mass transfer due to higher solubilities and diffusion rates than those for CO [118]. Yet, the influence of the gas composition on the technical, economic, and environmental performances of the fermentation process still remains quantitatively uncertain, basically due to the inaccuracy of currently available models of the metabolism of acetogenic bacteria.

Several types of mathematical models have been proposed for understanding and predicting the behavior of microorganisms in gas fermentations [84,114,251–255]; other simpler models have been used for estimating process performance [30,107,108,116,241,256]. The most popular of the modeling strategies employed recently by researchers is the genome-scale modeling (GSM), which has been used for assessing

several features of the intracellular processes in *C. ljungdahlii* and *C. autoethanogenum* during syngas fermentations *e.g.*, the influence of the link between energy conservation and carbon metabolism on the selectivity between ethanol and acetic acid [74–76,114], the co-factor specificity of certain enzymes linked to energy conservation [74,75,105], the formation of biofilms [254], the possibility of boosting ATP production by supplying arginine [257], and the feasibility of gene knock-out to reach overproduction of native and non-native products of acetogens [115]. Alternatively, with issues generally regarding on the accuracy of the quantitative predictions, GSM has also been used to assess the behavior of simulated microorganism inside large-scale bioreactors [84,115,254,258]; the main cause for these latter issues may be credited to the interlinking between the intracellular processes and the environmental conditions given by the bioreactor, besides GSM's large dependency on the objective function and the constraints applied to solve the intracellular rates of reaction [114]. The low detail of intracellular kinetics in viewed as another limitation of GSM [87] that becomes relevant given the fact that microorganisms do not reach steady-state inside large-scale bioreactors [88].

Moreover, in most publications reporting models of gas fermentations, scarce effort was invested on comparing the simulation results with experimental data reported by other research groups. Such task is challenging considering the large variety of microbial strains, gas compositions, process conditions used in the reported experiments and the high strain-specificity of more complex models of microbial metabolism. Thus, a general model that focuses on the basic thermodynamic interactions driving the catabolism of CO, CO_2 and H_2 by a hypothetical strain of acetogenic bacteria (such as in [116]) might be able to consolidate the diversity of reported results.

On the same line, the present study focuses on reinforcing the quantitative aspects of a previously published model [30] by validating the stoichiometric and kinetic parameters of microbial reactions with data and observations reported in scientific literature. The model is then applied to the simulation of an industrial ethanol production case and used to assess the influence of dissolved gas concentrations on bioreactor performance, gas flow profiles, supported accumulation of cells and energy requirements of the fermentation plus downstream processing of the alcohol. The model is intended to be sufficiently flexible and accurate that its results could guide further process design and optimization through model-based scaled-down experiments [78]. Finally, the model construction scheme here presented could be adapted to other process configurations, modes of fermentation and after further refining, coupled to GSM's, intracellular kinetics and Euler-Lagrange modeling strategies [259].

3.2. Results and discussion

This section begins with an assessment of the estimations delivered by the thermodynamics-based black-box model of microbial reactions; the analysis focuses on the predictions' quantitative reliability by comparing the estimations with data and observations reported in literature for microorganisms that perform similar metabolic reactions. Then the analysis is extended to the characterization of two bioreactor operation regimes in terms of gas flow profiles, supported biomass accumulations, restrictions suggested by thermodynamic feasibility of catabolic reactions at different heights of the bioreactor and finally, process performance. The analysis is lastly closed with the influence of the kinetic parameters on process performance.

3.2.1. Analysis of black-box model of microbial reactions

3.2.1.1. Gibbs free energy change of catabolic reactions

Figure 3.1 shows the dependence of the Gibbs free energy change in the catabolic reactions ($\Delta G_{cat}^{0\prime}$) (see equations 1 and 2 in Table 3.1) on dissolved gas concentrations; results are presented for independent catabolism of CO and H_2/CO_2 in Figure 3.1.a and Figure 3.1.b, respectively. They show that at dissolved concentrations of the electron donors (C_D) lower than 1 mM, the amount of energy harvested from CO catabolism is larger than that from H_2/CO_2 catabolism. Consequently, H_2 threshold concentrations ($-\Delta G_{cat}^{0\prime}$ = 9.1 – 15 kJ/mol) for catabolic ethanol production fall between $3x10^{-3}$ – $3x10^{-1}$ mM and lower than $4x10^{-4}$ mM for CO, depending on the CO_2 concentration (C_{CO_2}). Increasing C_{CO_2} diminishes the amount of energy harvested from CO catabolism where CO_2 is a product; whereas C_{CO_2} is beneficial for energy production in H_2/CO_2 catabolism where CO_2 is the carbon source (see equations 1 and 2).

Neither CO nor H_2 threshold concentrations have been reported for acetogens during solventogenesis; however, there are reports for acetogens during acetogenesis. In one of these reports, CO uptake (see equation 3) by *Carboxydothermus hydrogenoformans* at 65 °C stopped at a CO partial pressure (p_{CO}) of $3.9x10^1$ Pa when CO_2 was allowed to accumulate in the overhead (reaching $1.3x10^5$ Pa); when CO_2 was instead withdrawn from the overhead (p_{CO_2} of $3.5x10^2$ Pa), CO uptake stopped at p_{CO} of $2.0x10^{-1}$ Pa [260]. At these two points, $\Delta G_{cat}^{0\prime}$ estimated with equation 5 is -21 and -15 kJ/mol$_{CS}$, respectively (see Figure SI.3.1 at the Supplementary Information - SI); intracellular acetate concentration is assumed at 10 mM and the total pressure is $2x10^5$ Pa. Similarly, another report mentions that *Acetobacterium woodii* started growing on H_2 and CO_2 at 30 °C only after p_{H_2} was higher than $2.5x10^2$ Pa while p_{CO_2} was $2.0x10^4$ Pa [261]. Assuming *A. woodii* H_2/CO_2 catabolism followed equation 4, $\Delta G_{cat}^{0\prime}$ is estimated by equation 5 at -17.9 kJ/mol$_{CS}$ (see

Figure SI.3.2 at the SI); the intracellular acetate concentration is assumed at 10 mM and the reported total pressure is $1x10^5$ Pa. This brief analysis shows that equation 5 may be used to predict threshold concentrations for acetate production from gas fermentations with an acceptable level of approximation. Therefore, since energy conservation in acetogenic bacteria is possible during solventogenesis [111], then threshold concentrations might as well be predicted by equation 5 for catabolic ethanol production from CO and H_2.

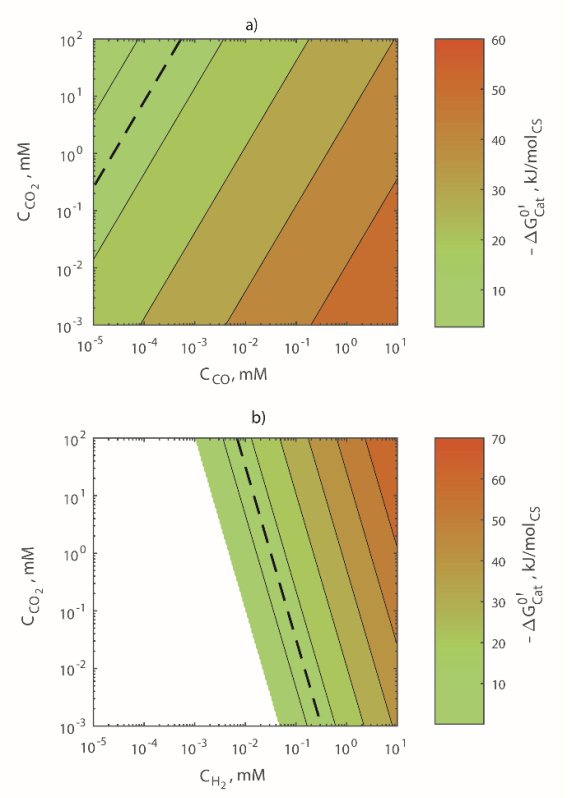

Figure 3.1. Gibbs free energy generation through independent a) CO and b) H_2/CO_2 catabolism for ethanol production. The dashed lines indicate where $\Delta G^{0\prime}_{cat}$ = −15 kJ/mol$_{CS}$. H_2/CO_2 catabolism is cut-off at $\Delta G^{0\prime}_{cat}$ = 0, where the catabolic reaction would be at equilibrium and no energy could be released from it; the white region represents the gas concentrations where the inverse reaction (H_2/CO_2 production from ethanol) would be spontaneous.

$$\Delta G_r^{0\prime} = \left[\frac{\Delta G_r^0}{298.15} + \Delta H_r^0\left(\frac{1}{T} + \frac{1}{298.15}\right)\right]T + \mathcal{R}T\sum_{j=1}^{m} v_j^r \ln C_j \qquad (5)$$

The importance of predicting threshold concentrations relies on the fact that the large-scale bioreactor should be designed to avoid reaching such concentrations.

Table 3.1. Catabolic reactions leading to the production of ethanol and acetate and related standard changes in Gibbs free energy and enthalpy

Reaction [a]	ΔG_r^0		ΔH_r^0		Eq nr.
	kJ/mol$_{CS}$	kJ/mol$_P$ [b]	kJ/mol$_{CS}$	kJ/mol$_P$ [b]	
$-6CO - 3H_2O + C_2H_5OH + 4CO_2$	-37.4	-224.4	-57.4	-344.0	(1)
$-6H_2 - 2CO_2 + C_2H_5OH + 3H_2O$	-52.3	-104.6	-178.8	-357.6	(2)
$-4CO - 2H_2O + C_2H_3O_2^- + H^+ + 2CO_2$	-33.6	-134.3	-65.0	-260.0	(3)
$-4H_2 - 2CO_2 + C_2H_3O_2^- + H^+ + 2H_2O$	-28.1	-56.2	-134.7	-269.5	(4)

[a] The stoichiometry of anabolic reactions and the energy changes are defined to satisfy balances on all elements involved, charge and degree of reduction. Standard Gibbs free energy and enthalpy of formation of the compounds involved in equations 1 – 4 were retrieved from the supplementary material in [182].

[b] Results are expressed per mole of product *i.e.,* the product in equations 1 and 2 is ethanol while acetate is the product in equations 3 and 4

3.2.1.2. Biomass yields

Since biomass yields ($Y_{x/CS}$) depend on $\Delta G_{cat}^{0\prime}$ (see equation 6) they are a direct function of C_D and follow a similar trend as $\Delta G_{cat}^{0\prime}$ when plotted against C_{CO_2} and C_D (see Figure SI.3.3). Biomass yields for CO catabolism are estimated between 0.022 and 0.080 Cmol$_x$/mol$_{CS}$ which are slightly higher than those estimated for H_2/CO_2 (0.015 – 0.067 Cmol$_x$/mol$_{CS}$) mainly due to the larger amounts of Gibbs free energy dissipated by cell growth using CO_2 as CS (see equation 2).

$$\frac{1}{Y_{x/CS}} = \frac{\Delta G_{dis}}{\Delta G_{cat}^{0\prime}} + \frac{\gamma_x}{\gamma_D \nu_D^{an}} \quad (6)$$

Similar to threshold concentrations, biomass yields have not been reported for gas fermentations during solventogenesis. However, there are specific rates of CO and H_2 consumption reported for continuous fermentations at steady-state [72,74,75] that can be used to estimate biomass yields. Since in those reports, CO and H_2 were simultaneously consumed whereas CO_2, acetic acid and ethanol were produced, the biomass yield is estimated by dividing the dilution rate (assuming the rate of cell lysis is negligible) by the reported specific CO uptake rate (q_{CO}). The estimated biomass yields range between 0.044 and 0.090 Cmol$_x$/mol$_{CS}$ (the specific data used for his calculation is shown in Table SI.3.1) which are slightly higher (yet, within the same order of magnitude) than the estimations given by equation 6 for ethanol catabolic production.

3.2.1.3. Assessment of kinetic parameters

3.2.1.3.1. Maximum specific substrate uptake and growth rates

Regarding the predicted kinetic parameters, the thermodynamics-based black-box model returns a maximum substrate uptake rate (q_D^{max}) of -4.4 $mol_D/Cmol_x/h$ (see equation 7) for both catabolic energy sources, CO and H_2. The result is the same for both electron donors since they have the same degree of reduction (2 mol_{e-}/mol_D). In addition, as explained in section 3.4, the maximum consumption and production rates of all compounds involved in the microbial reactions are estimated by linearly relating the predicted stoichiometry with the maximum substrate uptake rates. As consequence, the maximum growth rate (μ^{max}) was estimated at 0.29 and 0.19 h^{-1} for CO and for H_2/CO_2 fermentations respectively. μ^{max} for H_2/CO_2 fermentation is two times lower than CO fermentation because although q_D^{max} is the same on both cases, y_{x/H_2} (per mole of electron donor) for H_2/CO_2 fermentation is also two times lower than the $y_{x/CO}$ (see equations 1 – 4 and Figure SI.3.3).

$$q_D^{max} = 3\exp\left[\frac{-69000}{\mathcal{R}}\left(\frac{1}{T}+\frac{1}{298.15}\right)\right]\left(\frac{1}{\gamma_D}\right) \quad (7)$$

Mohammadi et al., 2014 [106] calculated a q_{CO}^{max} and a μ^{max} of -0.87 $mol_D/Cmol_x/h$ (assuming the same molar mass for cell material as here) and 0.195 h^{-1}, respectively. q_{CO}^{max} was estimated by fitting batch dissolved CO concentrations (calculated using a method similar to [262]) into the kinetic equation for CO uptake (see section 3.4.1.1), while μ^{max} was found by fitting batch growth data from the same experiment. In that study, syngas with a H_2/CO ratio of 1 was used and H_2 consumption was acknowledged; however, q_{CO}^{max} was calculated without accounting for the electrons taken up from H_2 and the carbon from CO_2. If H_2 and CO_2 uptake would have been considered, the maximum electron uptake rate would be twice as large as reported *i.e.*, -1.74 $mol_D/Cmol_x/h$. That value is 2.5 times lower than that predicted by equation 7. In addition, their reported μ^{max} is close to the value estimated with the black-box model. Thus, it could be argued that *C. ljungdahlii* has a 60% reduced electron uptake capacity compared to the maximum estimated for *E. coli* [263]; yet, more steady-state data with different carbon sources is needed to confirm such conclusion. Accounting for this uncertainty, the bioreactor simulation is performed using the value estimated with equation 7 and the influence of a reduced maximum uptake rate on the operation of the gas fermentor is explored as part of the sensitivity analysis (see section 3.2.3).

In addition, since growth rates estimated by genome-scale reconstructions of *C. ljungdahlii* and *C. autoethanogenum* [114,115] used the same μ^{max} value reported by

[106], their estimations are also comparable with those made by the biothermodynamics-based black-box model (see Figure SI.3.4).

3.2.1.3.2. CO and H_2 half saturation constants

A value of 1.7x10^{-2} mM has been calculated for the CO half-saturation constant in (K_{CO}) *C. ljungdahlii* from CO consumption curve fitting [106] whereas K_{H_2} has been estimated to range between 4x10^{-2} and 3x10^{-1} mM from assays using enzymatic extracts from acetogens [264–267]. In nature, wetland peats and marine waters oxidize CO with K_{CO} values ranging from 1x10^{-6} to 4x10^{-5} mM [268,269], while the averaged CO concentration in Earth's troposphere is equivalent to a concentration of 5x10^{-7} mM in pure water [270]. Similarly, K_{H_2} for H_2 consumption by soils and methanogenic sludge has been estimated between 7x10^{-8} and 1x10^{-6} mM [271,272], while the equivalent saturation from H_2 concentration in the troposphere is 4x10^{-7} mM [273].

As consumption of 1 mole of CO results in higher Gibbs free energy gains than 1 mole of H_2, it could be postulated that cells in nature control metabolic activity at low dissolved gas concentrations by stimulating H_2 uptake (with higher affinity, $K_{H_2} < K_{CO}$). This argument is in accordance with the affinities by which microbes consume H_2 and CO in nature. However, most H_2 consumption studies have focused on methanogens. H_2 threshold concentrations for catabolic methane production (see equation 8) can be as low as 5x10^{-6} mM, assuming pre-industrial atmospheric concentrations for CO_2 and CH_4 (230 ppm and 540 ppb, respectively [274]) and using equation 5. Moreover, evidence suggests that acetogens may promote H_2 production (from H^+ ions) to avoid harmful concentrations of reduced energy carriers when feeding on CO [53,74]. Therefore, K_{H_2} might not necessarily be lower than K_{CO}, in agreement with the ranges of H_2 and CO threshold concentrations estimated for ethanol production (see section 3.2.1.1) and reported data for acetogens.

$$-4H_2 - CO_2 + CH_4 + 2H_2O \quad (8)$$

It has been argued that half saturation constants of poorly soluble substances can be overestimated by two orders of magnitude if they are derived from the fitting of consumption curves obtained under mass transfer or other rate limitations [272]. Therefore the K_{H_2} and K_{CO} values of 4x10^{-2} and 5x10^{-3} mM, respectively, were randomly picked aiming to reconcile the information reported in literature (which is prone to overestimation) with the threshold concentrations criteria. Thus, the value for K_{CO} falls midway between the estimated threshold range (see Figure 3.1) and the reported value for *C. ljungdahlii*, while K_{H_2} is located in the middle of the threshold range while simultaneously agreeing with the values determined from enzymatic extracts.

Nevertheless, the effect of the value of substrate half saturation constants on the operation of the gas fermentor is discussed in detail as part of the sensitivity analysis (see section 3.2.3).

3.2.1.4. Main limitation of the black-box model of microbial reactions

Since the black-box model of microbial reactions is based on the electron transfer from one electron donor to one electron acceptor, it is not compatible with the simultaneous uptake of more than one electron donor or the generation of more than one product. Thus, the documented influence of process conditions such as pH [72,230], acetic acid concentration [275], gas compositions [74] and gas dissolved concentrations [75] on the selectivity for either electron donor or for the production of ethanol and acetic acid, could not be reproduced. To perform such analysis, the black-box may be opened and include the mechanisms by which cells adjust the amounts of Gibbs free energy used for ATP production, depending on the specific requirements for growth, maintenance, transport of metabolites across the membrane and motile functions [71,263,276].

3.2.2. Analysis of mass transfer-based model of the large-scale bioreactor

3.2.2.1. Basis of analysis

Although the algorithm that links the black-box model of the microbial reactions with the mass transfer-based model of the large-scale bioreactor uses C_{CO} and C_{H_2} as independent variables, dissolved gas concentrations are not independent during bioreactor operation. Moreover, within this section bioreactor performance is discussed from the perspective of a non-dimensional specific uptake rate of the electron donors (q'_D, see equation 9) in order to partly bypass the uncertainties related to the value of q_D^{max}.

$$q'_D = \frac{q_D}{q_D^{max}} \tag{9}$$

The dependence of ethanol productivity and gas utilization on q'_D reveals the existence of two operational regimes of the bioreactor at steady-state: *i)* one where mass transfer is suboptimal and *ii)* one where mass transfer is sufficient. Sections 2.2.2 and 2.2.3 describe the features of each regime.

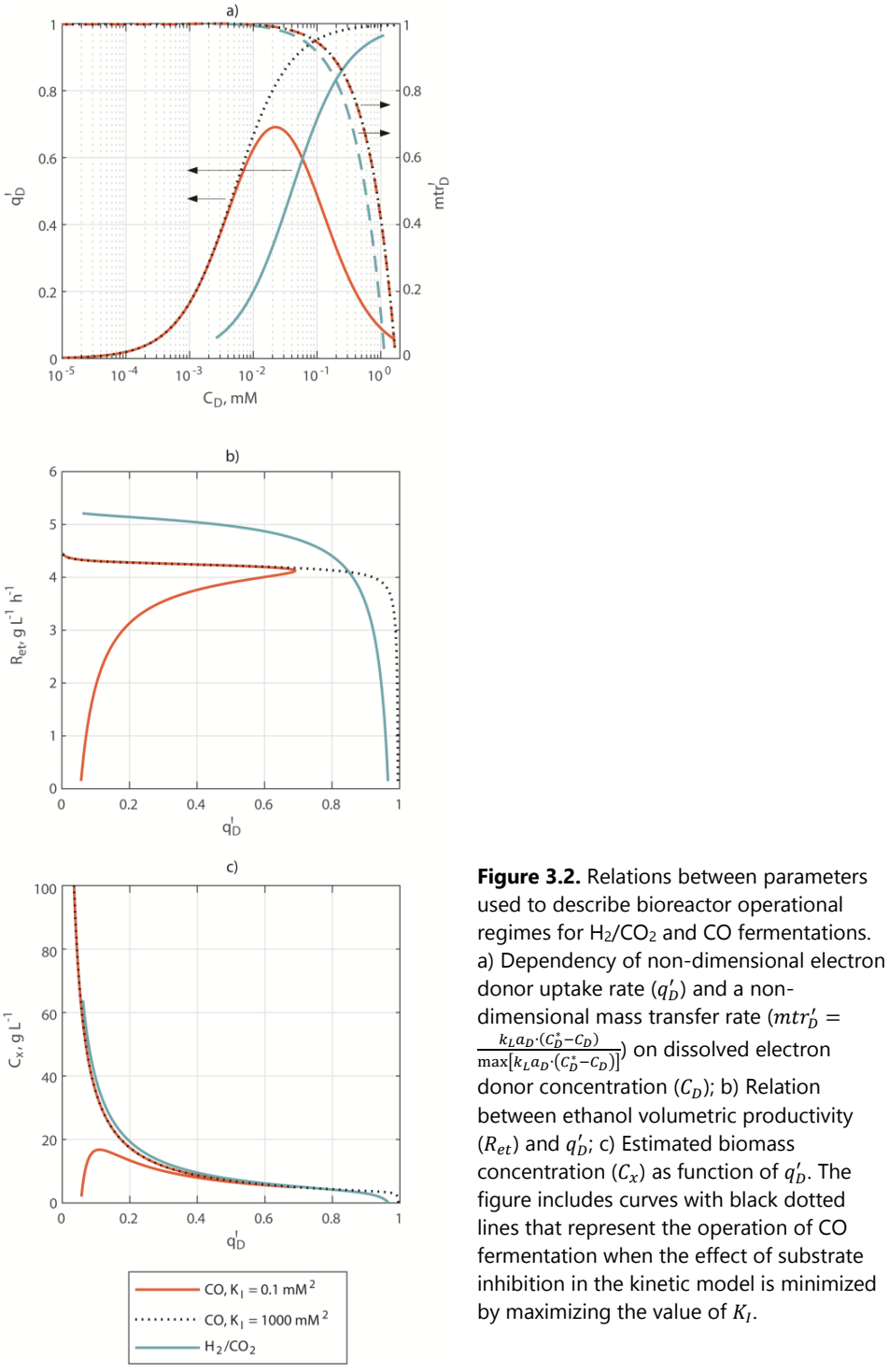

Figure 3.2. Relations between parameters used to describe bioreactor operational regimes for H_2/CO_2 and CO fermentations. a) Dependency of non-dimensional electron donor uptake rate (q'_D) and a non-dimensional mass transfer rate ($mtr'_D = \frac{k_L a_D \cdot (C^*_D - C_D)}{\max[k_L a_D \cdot (C^*_D - C_D)]}$) on dissolved electron donor concentration (C_D); b) Relation between ethanol volumetric productivity (R_{et}) and q'_D; c) Estimated biomass concentration (C_x) as function of q'_D. The figure includes curves with black dotted lines that represent the operation of CO fermentation when the effect of substrate inhibition in the kinetic model is minimized by maximizing the value of K_I.

3.2.2.2. The 'suboptimal' operation regime

The suboptimal regime is characterized by a low performance of the bioreactor and a q'_D approaching to 1 in H_2/CO_2 fermentation; due to the inhibition term used on the CO uptake kinetic equation, q'_D approaches to zero as CO concentration is highest (see Figure 3.2.a) resulting in a dual solution for q'_D as function of C_{CO}. According to the mass balances (see Table SI.3.2 in the SI), bioreactor productivity linearly depends on the mass transfer rate of the electron donors. Mass transfer rate concurrently depends on the mass transfer coefficient ($k_L a$) and the driving force (dissolved gas concentration gradient). $k_L a$ is determined by bioreactor design, the composition of the liquid phase, gas flow rate and gas sparging method [277], while the driving force is ruled by C_D and the solubility of the gas components. As biomass concentrations (C_x) are low within the suboptimal regime (see Figure 3.2.a and c), C_D is close to saturation. An elevated C_D causes two unfavorable effects over bioreactor operation: *i)* in the case of CO fermentation, it might inhibit CO consumption (see section 3.2.1.1) mainly at the lower regions of the liquid column where the partial pressure is highest; and *ii)* it limits the mass transfer driving force, which consequently hampers gas utilization and bioreactor productivity (see Figure 3.2.b). Yet, bioreactor performance improves sharply as C_x increases and q'_D decreases to approximately 0.7, where mass transfer rate achieves 90% of its estimated maximum. This point marks the start of the optimal regime.

3.2.2.3. The 'optimal' operation regime

The optimal regime runs from a q'_D of 0.7 until it approaches zero. Within this range, mass transfer rate, ethanol volumetric productivity and gas utilization are above the 90% of their estimated maximum values (see Figure 3.2.a, b and Figure SI.3.5). Since the value of C_x (see Figure 3.2.c) is calculated by the optimization algorithm to linearize the term $q_{CO} \cdot C_x$ with respect to the mass transfer rate (see Table SI.3.2), large increments on C_x (or equivalently, large reductions on C_D and q'_D) would only return moderate improvements in bioreactor performance (see Figure 3.2.b). Therefore, working within the optimal regime would be desirable for continuous operation of the large-scale gas fermentor.

3.2.2.4. Influence of gas composition on bioreactor performance

This section compares bioreactor performance and the features of its operation between CO and H_2/CO_2 fermentations within the optimal regime. It may be assumed that a process fed by a gas with a composition falling in a determined point between the two composition boundaries (100% CO and 100% 3:1 H_2:CO_2 mixture), will behave proportionately to the contribution of each boundary.

3.2.2.4.1. C_{et}, R_{et} and U_S

One parameter that showed to have a significant influence over bioreactor operation for CO and not for H_2/CO_2 fermentation is the liquid outflow rate ($\dot{V}_{L,o}$), which as well as C_x is adjusted by the optimization algorithm to fulfill mass balances. $\dot{V}_{L,o}$ allows the removal of cells and the ethanol fraction that was not evaporated and transferred to the off-gas. In CO fermentation, $\dot{V}_{L,o}$ is controlled by the biomass production rate for most of the q'_D range; this causes excessive ethanol removal along the liquid, preventing its accumulation within the bioreactor. Consequently, the ethanol concentration does not reach 45 g/L only until q'_{CO} is as low as 0.10 (where C_{CO} is 1x10^{-3} mM and C_x approximates to 20 g/L) where biomass production rate lowers sufficiently; this could become another challenge for the fermentation process development since sustaining such low q'_D values can be difficult [75]. In H_2/CO_2 fermentation the relatively lower biomass production rates indirectly allow ethanol accumulation throughout the whole optimal regime due to the lower biomass yields (per mole of electron donor).

In order to lower the influence of $\dot{V}_{L,o}$ over bioreactor operation, biomass withdrawal may be decoupled from the removal of fermentation broth. Biomass retention within biofilms is known for increasing bioreactor productivity, yet in prolonged periods could lead to clogging [278]. If the biofilms were shaped into granules instead, clogging may be avoided and larger hydraulic loads can be handled by gas-lift bioreactors due to the high settling velocity of the granules [279]. Up to date there is no report on a gas fermentation set-up that uses biomass retention within granules, however a recent publication showed that *C. ljungdahlii* produces biofilms under stress by NaCl [280].

In general, the estimated biomass concentrations fermentation may seem unrealistic since the maximum C_x reported for a continuous syngas fermentation using cell recycle is 10 g/L [72]. Although an explanation for this limitation has not been given in literature for gas fermentation, one hypothesis may be formulated based on the fact that the abiotic phase in a bioreactor undergoes spatial and temporal variations on the intensities of mixing and mass transfer [259]. If at one given moment inside one portion of the bubble column, the local value of C_{CO} or C_{H_2} was on the order of 0.01 mM, a 6% decrease in the local mass transfer coefficient (caused by the turbulent flow of the liquid phase) is enough to cause a cells in a concentration of 10 g/L to lower that local C_D by 10-fold in approximately 0.03 seconds. Such variations may cause cells to temporarily (yet frequently) circulate through zones where the C_D approaches to their thresholds, causing starvation. The detrimental effects of starvation on product generation and cells viability have been linked to the depletion of certain metabolic pools in fungi [88]. Considering the fact that depletion of the acetyl-CoA pool prevented *C. autoethanogenum* from achieving C_x higher than 1.4 g/L in [75], it could be argued that the achievement of high

values of C_x in gas fermentations is not limited by the averaged rates of mass transfer, but instead to the slight spatial and temporal variations on those rates of mass transfer.

Table 3.2 shows a summary of relevant parameters estimated within the optimal regime of CO and H_2/CO_2 fermentations; the values in the table describe the bioreactor operation at the liquid column height where the mean log pressure is found. The operation points shown were selected from the q'_D to satisfy the following conditions: *i)* mass transfer is above the 90% of its maximum, *ii)* CO does not inhibit its consumption at the bottom of the vessel (see Figure 3.3.a), *iii)* the rate at which microbial biomass is being produced allows C_{et} to reach 45 g/L in the liquid, *iv)* H_2 does not reach threshold concentrations at the top of the liquid column (see Figure 3.3.b), and *v)* the concentration of biomass is not higher than 10 g/L.

In such points of operation, H_2/CO_2 fermentation returns a 19% higher ethanol productivity (5.1 g/L/h) than fermentation of CO (4.3 g/L/h); this difference is attributed to a higher mass transfer rate in H_2/CO_2 fermentation mainly because the higher H_2 diffusivity in water (see section 3.4.1.1) makes k_L in $k_L a$ 58% higher for H_2 compared to CO (see Table 3.2). Considering that ethanol productivities have reportedly reached 8 g/L/h through fermentation of CO-rich syngas [281], and that commercial sugar-based fermentations commonly fall between 1.5 and 2.0 g/L/h [282], it can be argued the estimations made in this study do not fall out of context and even more important, they could be subjected to further improvement.

Moreover, the higher mass transfer rates in H_2 have a similar effect on gas utilization (U_s, see section 3.4.1.1) in relation to CO fermentation. However, U_s does only reach 23% in absolute terms, which makes the gas recycling step (see section 3.4.3) a necessity to guarantee full use of the fresh gas fed to the process. Therefore, an upstream operation for gas composition control is essential to avoid the accumulation of gases within the gas recycle.

Table 3.2. Summary of relevant parameters of bioreactor operation and process performance for H_2/CO_2 and CO fermentations

Variable	Symbol	Unit	CO fermentation	H_2/CO_2 fermentation
Performance indicators				
Ethanol volumetric productivity	R_{et}	g/L/h	4.25	5.1
Gas utilization	U_S	%	17.1	22.9
Gas outflow composition				
Hydrogen	y_{H_2}	mol/mol	0.00	0.71
Carbon dioxide	y_{CO_2}	mol/mol	0.11	0.24
Carbon monoxide	y_{CO}	mol/mol	0.84	0.00

Variable	Symbol	Unit	CO fermentation	H_2/CO_2 fermentation
Ethanol	y_{et}	mol/mol	0.01	0.01
Water	y_w	mol/mol	0.04	0.04
Concentrations in the fermentation broth [h,i]				
Hydrogen	C_{H_2} ($C^*_{H_2}$)	mol/m³	0.00 (0.00)	0.025 {0.033; 0.018} (1.15 {1.63; 0.78})
Carbon dioxide	C_{CO_2} ($C^*_{CO_2}$)	mol/m³	0.32 {0.00; 4.22}	12.46 {17.11; 8.94} (13.09 {18.51; 8.86})
Carbon monoxide	C_{CO} (C^*_{CO})	mol/m³	$2.7x10^{-3}$ {$3.6x10^{-3}$; $2.0x10^{-3}$} (1.62 {2.45; 1.01})	0.000 (0.000)
Ethanol	C_{et}	mol/L (g/L)	0.96 (44.3)	0.98 (45.0)
Biomass	C_x	$Cmol_x/m^3$ (g_x/L)	395 (10.0)	399 (10.1)
Parameters estimated with thermodynamics [h]				
Catabolic energy production	$\Delta G^{0\prime}_{cat}$	kJ/mol_{CS}	-29.2 {-48.2; -24.0}	-19.9 {-23.0 -16.45}
Biomass yield	$Y_{x/CS}$	$Cmol_x/mol_{CS}$	0.041	0.020
Biomass specific consumption/production rates (logarithmic mean)				
Hydrogen	q_{H_2}	mol/$Cmol_x$/h	0.00	-1.67
Carbon dioxide	q_{CO_2}	mol/$Cmol_x$/h	1.00	-0.56
Carbon monoxide	q_{CO}	mol/$Cmol_x$/h	-1.52	0.00
Ethanol	q_{et}	mol/$Cmol_x$/h	0.23	0.28
Water	q_w	mol/$Cmol_x$/h	-0.73	0.84
Cells	μ	h^{-1}	0.06	0.01
Non-dimensional electron donor uptake rate	q'_D	-	0.35	0.38
Streams entering and leaving the bioreactor				
Gas flow rate at the top	$F_{G,t}$ ($\dot{V}_{G,t}$)	mol/s (m^3/s)	462 (7.8)	418 (7.1)
Gas flow rate at the bottom	$F_{G,b}$ ($\dot{V}_{G,b}$)	mol/s (m^3/s)	479 (4.0)	528 (4.4)
Liquid outflow rate	$\dot{V}_{L,o}$	m^3/h	30.0	39.3
Fresh syngas	F_S	mol/s	80.0	118
Parameters regarding gas and liquid flows and mixing (logarithmic mean)				
Gas flow rate	F_G ($\dot{V}_G$)	mol/s (m^3/s)	471 (5.6)	471 (5.6)
Superficial gas velocity (pressure-corrected)	v^c_{SG}	m/s	0.14	0.14
Liquid flow rate	$\dot{V}_L$	m^3/s	26.9	26.9
Mixing time	t_m	s	60.4 [j] 54.3 [k]	61.2 [j] 54.3 [k]

Variable	Symbol	Unit	CO fermentation	H_2/CO_2 fermentation
Mass transfer coefficients (logarithmic mean)				
Hydrogen	$k_L a_{H_2}$	s^{-1}	0.000	0.164
Carbon dioxide	$k_L a_{CO_2}$	s^{-1}	0.000	0.098
Carbon monoxide	$k_L a_{CO}$	s^{-1}	0.104	0.000

[h] The average value is shown first, followed by the values at the top and the bottom of the liquid column between curly brackets.

[i] The values between round brackets represent the saturation concentrations of CO, H_2 and CO_2.

[j] Simulated using the 9 vertically stacked compartments model.

[k] Calculated with equation 20.

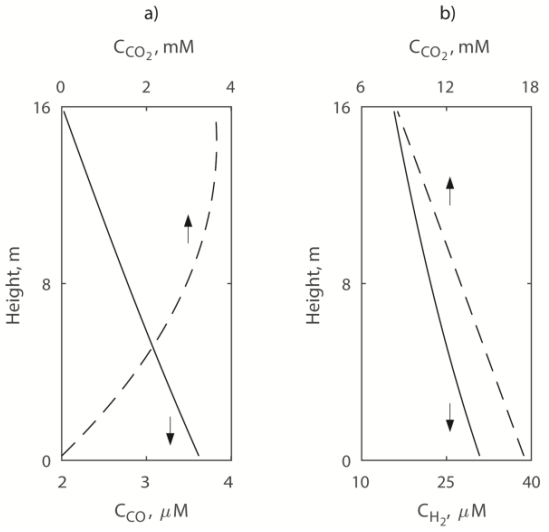

Figure 3.3. Gas concentration profiles along the liquid column for a) CO fermentation and b) H_2/CO_2 fermentation

Lastly, the CO, H_2 and CO_2 mass transfer coefficients used in the present work range between 0.05 – 0.21, 0.08 – 0.33 and 0.05 – 0.20 s^{-1}, respectively. Unfortunately, mass transfer coefficients for the transfer of CO, H_2 and CO_2 are available only for laboratory-scale bioreactors [283–285] where the heterogeneous bubbling regime may not be achieved [277] and therefore, the predicted values cannot be compared with reported experiments. However, the estimated ranges agree well with the experimental data (corrected with the gas diffusivities in water, see section 3.4.1.3) reported for oxygen transfer within large bubble columns by [286].

3.2.2.4.2. Energy requirements

When CO is fed to the reactor, roughly 60% of its carbon goes to CO_2. This causes the molar gas flow rate across the reactor to slightly decrease (see Table 3.2). Contrarily, when

the 3:1 H_2:CO_2 mixture is fed to the fermentor, the two gases are consumed and none is produced; thus the molar gas flow diminishes by 20%. This difference in gas flow profiles impacts significantly on the two largest contributors to total energy requirements *i.e.*, compression of the gas streams (in agreement with [84]) and product distillation (see Table 3.4).

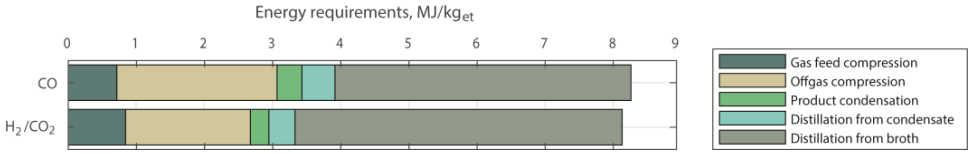

Figure 3.4. Breakdown of energy requirements of the proposed process configuration

In H_2/CO_2 fermentation less power is needed to compress the recycling off-gas compared to CO fermentation. Furthermore, as the productivity in H_2/CO_2 fermentation is higher and the off-gas' ethanol evaporation capacity lower (due to lower off-gas flow rate), the liquid outflow in the chosen point of operation (see Table 3.4) is larger than in CO fermentation. As consequence, the distillation of the diluted broth consumes more energy in the H_2/CO_2 fermentation. All in all, the total absolute energy requirements are higher for the H_2/CO_2 fermentation; however due to the higher ethanol productivity, the energy needed per unit of ethanol produced is lower than in CO fermentation (see Figure 3.5).

3.2.3. Sensitivity analysis

The sensitivity analysis assesses the impact of the value that half saturation constants and maximum substrate uptake rate would apply on bioreactor performance. If K_{CO} and K_{H_2} decreased by 10-fold, the appearance of the optimal regime of operation would occur at higher q'_D (see Figure 3.5), which in an industrial setting could improve bioreactor operation robustness to withstand fluctuations on C_x and k_La. In the opposite case, if K_{CO} and K_{H_2} were 10 times higher than what was fixed in section 3.2.1.3.2, the preservation of a stable optimal regime could require delicate control of low q'_D. This last case could severely affect H_2/CO_2 fermentation as C_{H_2} needs to be kept at relatively higher values (see Table 3.2) to avoid reaching a threshold concentration at the top of the fermentor. Therefore, K_{H_2} as well as K_{CO} need to be in the order of 1x10^{-2} mM or lower.

When the maximum uptake rate is decreased by 60% from the value estimated with equation 7, a negligible effect is seen on bioreactor productivity and gas utilization within the optimal regime of bioreactor operation.

Further, as the relation between the rates of mass transfer and consumption of the electron donors is highly linear (see mass balances in Table SI.3.2), a 100% improvement on the mass transfer coefficients (with respect to the values shown in Table 3.2) would result in an 86% improvement on bioreactor productivity. That means that ethanol productivity for CO and H_2/CO_2 fermentations could be as high as 7.9 and 9.4 g/L/h, respectively. Similarly, due to the improvement on gas transfer to the liquid, gas utilization would rise to 31 and 38% for CO and H_2/CO_2 fermentations, respectively. If contrarily, mass transfer coefficients were 50% smaller than predicted for gas transfer to pure water (see section 3.4.1.3) both ethanol productivity and gas consumption would roughly be cut by half.

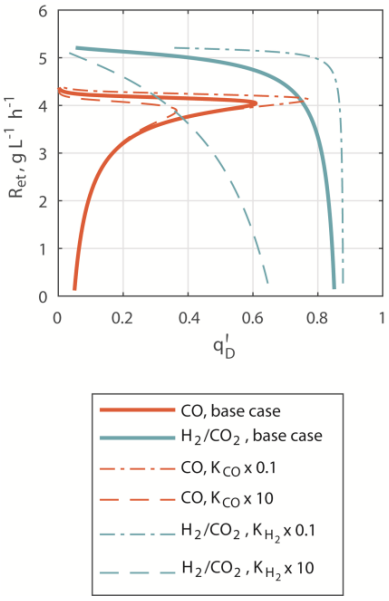

Figure 3.5. Influence of half saturation constants on ethanol productivity in the large-scale gas fermentor

The effect of an increased microbial tolerance to ethanol such that C_{et} may be maintained at 80 g/L, is only reflected on the energy requirements which in the case of H_2/CO_2 fermentation would decrease by 30% to 5.8 MJ/kg_{et}. A similar decrease in energy requirements would be seen for the fermentation of CO as long as the concentration of biomass climbed to 25 g/L at a q'_D of 0.13, where μ is low enough to allow ethanol concentration to rise from 45 g/L.

Moreover, if the aspect ratio was increased to 10 while maintaining the volume at 700 m^3 (vessel height and diameter will be 44.7 and 4.5 m, respectively), the gas utilization will climb to 35 and 44% for CO and H_2/CO_2 fermentations, respectively, mainly due to the increased gas retention times. As consequence of the increased gas utilization, the

ethanol productivity may slightly rise to 5.3 and 6.7 g/L/h for the same two cases as previously. Finally, since the hydrostatic pressure at the bottom of the bioreactor will increase with the height of the liquid column, the total power requirements will consequently rise by an average of 11% for the two gas compositions because increase need for gas compression. Furthermore, since the relation between the gas hold-up and the productivity is also highly linear, a 100% increase in the hold-up to 0.30 m_G^3/m_{G+L}^3 will be reflected as an equivalent increase on ethanol productivity to 8.6 and 9.4 g/L/h for CO and H_2/CO_2 fermentations, respectively. However, due to the reduced gas retention time, the gas utilization will fall to 11 and 14% for the two fermentation cases. Therefore, a balance may have to be established between the height of the bioreactor and the gas hold-up to guarantee that productivity rises without significantly affecting the gas consumption or the energetic demands of the overall process.

Finally, if the gases provided to the fermentation were not pure, as it is likely in an industrial setting, the gas recycling will not be possible. Such process configuration may cause the energy requirements to rise by 15% to 9.6 and 9.5 MJ/kg_{et} for CO and H_2/CO_2 fermentations, respectively. The reason behind this result is the fact that the energy savings on the off-gas compression are not sufficiently high to counter the extra expenses derived from the compression of higher amounts of gas at the bioreactor inlet. Industrial sources of CO, H_2 and CO_2, such as syngas and steel manufacturing off-gases, which contain impurities that if recycled may accumulate inside the bioreactor, may have to deal with the extra energy expenses of not using gas recycle. On the other hand, the fermentation of mixtures between H_2 produced for example, through the electrolysis of water, and CO_2 recovered from a generic combustion process may be benefited by the energetic advantage of using gas recycling.

3.3. Conclusions

An alternative model for simulating gas fermentation within a large-scale bubble column bioreactor was developed. The model coupled a thermodynamics-based black-box model of main microbial reactions with a mass transfer-based model of the bioreactor. A significant amount of effort was put on validating the black-box model predictions with trends and data found in literature for acetogens or microorganisms using similar catabolic processes:

- The estimated threshold concentrations for CO, H_2 and CO_2 agreed with reported data for acetogens during early and late growth stages at different temperatures.
- Predicted biomass specific uptake rates for CO and H_2 consumption surpassed reported values by 250% suggesting that there might exist a potential for strain improvement.

- Estimation of substrate half saturation constants form threshold concentrations proved to yield results comparable with data reported for CO and H_2 consumption by acetogenic and methanogenic microorganisms.

The large-scale gas fermentor simulation showed that ethanol productivities may reach between 4.3 and 5.1 g/L/h and CO and H_2 utilization per step may not surpass 23%. If instead, mass transfer coefficients were 100% higher than the estimated by the model developed for oxygen transfer to pure water, then productivities may achieve 7.9 and 9.4 g/L/h while gas utilization may climb to 38%. Such performance indicators are obtained if H_2 does not achieve threshold concentrations at the top of the liquid column, CO consumption is not inhibited at the bottom of the bioreactor, ethanol concentration reaches 45 g/L and if biomass withdrawal from the bioreactor was decoupled from the fermentation broth removal.

It is recommended that multi-objective optimizations are done to further validate the bioreactor performance results by comparing them with reported data and process configurations that have been proposed and patented. The model could also be used to acquire a broader view on how process performance, especially gas utilization, could be further improved. In addition, the black-box model may be extended to include intracellular processes relevant for energy conservation and guide further understanding on the factors influencing the selectivity between ethanol and acetic acid in acetogens.

3.4. Methodology

This section describes the structure of the hybrid model, the estimation of relevant parameters and how process performance is assessed.

3.4.1. The hybrid model

A deterministic model for simulating ethanol production in a large-scale gas fermentor is proposed. The model consists of two main parts: *i)* a thermodynamics-based black-box model of the microbial reactions and *ii)* a model of the fermentor hydrodynamics. Two gas compositions are evaluated separately to represent the two boundaries of possible compositions that acetogenic bacteria are able to catabolize, *i.e.* pure CO and a 3:1 mixture of H_2 and CO_2, which respectively may be obtained industrially from the off-gas of steel manufacturing [281] and by mixing the CO_2 recovered from a generic combustion process with H_2 produced from, for instance, the electrolysis of water [287].

The simulation of the large gas fermentor is here done by assuming that a generic acetogenic bacterial strain has been adapted, modified or that the conditions in the

bioreactor are such that the net rate of acetic acid production is zero, although it is commonly reported that the main product of acetogens is acetic acid while ethanol is generally a co-product. The assumption is sustained on the fact that ethanol production form CO and H_2 as electron donors is thermodynamically feasible on its own, disregarding the current understanding of the physiology of acetogens and the limitations of gene editing techniques applied to these bacteria.

3.4.1.1. Thermodynamics-based black-box model of microbial reactions

The microbial metabolism is considered to be formed by catabolism and anabolism. Ethanol is a product of CO or H_2/CO_2 catabolism, while cells are the product of anabolism starting from the same energy and carbon sources; CO and H_2 are the energy sources or electron donors (D), while CO and CO_2 are the carbon sources (CS). Table 3.1 shows the stoichiometry of catabolism (equations 1 – 4) whereas equations 10 and 11 show the stoichiometries of anabolism. If thermodynamically feasible ($\Delta G^{0\prime} < 0$), the amount of Gibbs free energy released by catabolism is mainly used to support cell growth. Biomass yields ($Y_{x/CS}$ in equation 6) are then calculated from the ratio between Gibbs free energy dissipation during growth (ΔG_{dis} in equation 12, where c is the number of carbon atoms in the CS and γ is its degree of reduction – electrons available for redox exchange) and free energy change in catabolism ($\Delta G_r^{0\prime}$ in equation 5) plus the ratio between the degrees of reduction of biomass material and of D [183]. In equation 6, the term ($\Delta G_{dis}/\Delta G_{cat}^{0\prime}$) represents the amount of CS needed to produce the necessary amount of free energy to produce 1 Cmol of biomass (x); the term (γ_x/γ_D) represents the amount of CS required for stoichiometrically building 1 Cmolx. Finally, the term ν_D^{an} (stoichiometric coefficient of D in anabolism) in equation 6, is used since D is not the CS in H_2 catabolism. Moreover, the stoichiometric coefficient of any j-th component in the metabolic reactions ($mol_j/Cmol_x$) is determined by adding the contributions of the catabolic and anabolic reactions (see equation 13).

$$-2\mathrm{CO} - \frac{1}{4}{\mathrm{NH_4}}^{+} - \frac{1}{2}\mathrm{H_2O} + \mathrm{CH_{1.75}O_{0.5}N_{0.25}} + \mathrm{CO_2} + \frac{1}{4}\mathrm{H}^{+} \tag{10}$$

$$-2\mathrm{H_2} - \mathrm{CO_2} - \frac{1}{4}{\mathrm{NH_4}}^{+} + \mathrm{CH_{1.75}O_{0.5}N_{0.25}} + \frac{3}{2}\mathrm{H_2O} + \frac{1}{4}\mathrm{H}^{+} \tag{11}$$

$$\Delta G_{dis} = 200 + 18(6-c)^{1.8} + \exp\left\{\left[\left(3.8 - \frac{\gamma_{CS}}{c}\right)^2\right]^{0.16}(3.6 + 0.4c)\right\} \tag{12}$$

$$\nu_j^{met} = \nu_j^{cat}\left(\frac{\Delta G_{dis}}{\Delta G_{cat}^{0\prime}}\right) + \nu_j^{an}\left(\frac{\gamma_x}{\gamma_D \nu_D^{an}}\right) \tag{13}$$

Since the Gibbs free energy change ($\Delta G_r^{0\prime}$ in equation 5) is calculated at physiological conditions, its magnitude and the parameters derived from it (*e.g.,* biomass yield and

stoichiometry of metabolic reactions) will depend on temperature and the activity of the m products and substrates at the intracellular space. It has been argued that "the choice of the species used for calculation of $\Delta G_r^{0\prime}$ of a reaction r should be based on the species for which the activity is closest to the reference activity (*i.e.* 1 mol/L for aqueous species, 1 atm for gases)" [182]. Therefore, the value of C_j in equation 7 corresponds to the aqueous concentrations for: ethanol, NH_4^+ and H^+ ions, while for the gases: CO, H_2 and CO_2, their partial pressures are used.

Water intervenes as product and reactant in the catabolic reactions (see equations 1 – 4). However, the concentration of electron donors, ethanol, CO_2 and H^+ ions are generally very low and catabolic reactions take place within a "dilute aqueous system" [183]. Therefore, the concentration of water is not considered in the calculation of $\Delta G_r^{0\prime}$ with equation 5 [183,263].

As CO, H_2 and CO_2 are uncharged gases, they can freely diffuse across the cell membrane and thus their concentrations are assumed to be the same inside and outside the cells. The same is assumed for ethanol whose concentration (C_{et}) is used as a fixed value at 45 g/L, which approximates to the highest concentration achieved in a syngas fermentation [288].

The concentration of the dissolved gases is assumed to vary within a large range since, as it will be explained in section 3.4.1.4, they are the link between the model of microbial reactions and the mass transfer model and largely influence the bioreactor performance. Table 3.3 summarizes the values of intracellular concentrations of the reactants and products of catabolic reactions (equations 1 – 4).

The effect of ionic strength is neglected from the calculation of Gibbs free energy changes since an ionic strength as high as 0.1 M would result in variations of maximum 0.6 kJ/mol for the reactions shown in Table 3.1 [102]. Therefore, the activity coefficients of all substrates involved in the considered microbial reactions are rounded to 1.

The reaction rates of microbial metabolism are calculated by linearly linking their stoichiometry to the hyperbolic substrate uptake kinetics of the electron donors (*i.e.,* CO and H_2 – see equations 14 and 15). Such kinetic relations were reported to be applicable to CO consumption by *C. ljungdahlii* [106] and H_2 consumption by *C. ragsdalei* P11 [264]. In equations 14 and 15, K_{CO} and K_{H_2} are the half saturation constants while K_I is the inhibition constant for CO (0.1 mol^2/m^6 [106]); section 3.4.1.2 describes the procedure followed to assess and set the values for the half saturation constants. The maximum substrate uptake rate (q_D^{max}) is calculated for CO and H_2 from the theoretical maximum rate of electron consumption by cells, as shown in equation 7 [263]. q_D^{max} is a function of the temperature and the degree of reduction of the electron donor. Equation 7 was

formulated based on a "maximum rate of electron transport in the catabolic energy production" of 3 $mol_{e-}/Cmol_x/h$ at 20 °C and which was found to fit uptake data from *E. coli* growing on different substrates [263].

Table 3.3. Intracellular concentrations of substance involved in catabolic reactions

Substance	Concentration, mol/L
Fixed values	
H^+ ions	$1.0x10^{-7}$ [71]
NH_4^+ ions	$1.0x10^{-1}$ [102] [c]
Ethanol	$9.8x10^{-1}$
Ranges of values [b]	
CO	$1x10^{-8} – 1x10^{-3}$
H_2	$1x10^{-8} – 1x10^{-3}$
CO_2	$1x10^{-6} – 1x10^{-1}$

[a] Defined from a 0.1 M ionic strength.

[b] Ranges of dissolved gas concentrations were defined based on the corresponding range of partial pressures between $1x10^{-5}$ to 1 atm.

$$q_{CO} = q_{CO}^{max} \frac{C_{CO}}{K_{CO} + C_{CO} + \frac{{C_{CO}}^2}{K_I}} \tag{14}$$

$$q_{H_2} = q_{H_2}^{max} \frac{C_{H_2}}{K_{H_2} + C_{H_2}} \tag{15}$$

3.4.1.2. Model validation

The thermodynamics-based black-box model of microbial reactions is validated by comparing its results against general tendencies observed in reported experiments and data. The estimations of the Gibbs free energy change of catabolic reactions is compared to published experimental data in terms of threshold concentrations of the gases *i.e.*, the concentrations at which the catabolic reaction returns a minimum amount of energy necessary to power the proton motive force (- 15 kJ/mol_{H+} [183], although it could be as low as - 9.1 kJ/mol_{H+} in acetogens [112]).

In addition, it has been suggested that the value of the substrate half saturation constants are likely close to the threshold concentrations of that substance; further in poorly soluble substances, the same constants can also be expected to approximate to their solubility in the aqueous phase [183]. Thus, the values of the K_{CO} and K_{H_2} found in literature are first judged against those two criteria and when necessary, modified to a value in accordance with the restrictions.

Lastly, the estimated values for maximum substrate uptake rates and biomass yields are also compared with published data for acetogens or microorganisms that use similar catabolic routes.

3.4.1.3. Mass transfer-based model of the industrial bioreactor

The height and volume of the industrial bubble column bioreactor are both fixed at 20 m and 700 m^3, respectively. The stated height is common in industry [289] while the volume is relatively large yet regarded as cost efficient [290]. Considering that the reactor will have a 20% overhead space and a gas hold-up fixed at 15% [85], the fermentation broth (liquid phase) will occupy 476 m^3. More details of the model parameters for the bubble column are shown in Table 3.4. In addition, since the aspect ratio and the gas hold-up are parameters which can adopt different values in industry, the effect of different values that those shown in Table 3.4, is assessed within the sensitivity analysis.

The mass transfer model is defined considering the coexistence of two phases inside the bioreactor: *i)* a liquid phase which initially is assumed to have a homogeneous composition, and *ii)* a gaseous phase which behaves as a plug flow. Although bacterial cells would constitute a third phase within the bioreactor, they are considered to occupy a negligible volume and to be homogeneously distributed within the liquid phase; thus biomass would not influence mass transfer. As a first approach, the fermentation broth is assumed to be a coalescing liquid despite the fact that ethanol inhibits water coalescence depending on the alcohol concentration [291]. For simplicity, the liquid dynamically behaves as pure water under a heterogeneous bubbling regime inside the bubble column [277]; bubbles are thus assumed as coarse with a 6 mm average diameter [277]; with these assumptions, the volumetric mass transfer coefficients ($k_L a_S$) and the gas hold-up (ε_G) are estimated from the pressure-corrected superficial gas velocity (v_{Gs}^c) using equations 16 and 17 [85,277]; such equations have been derived by fitting experimental data obtained in bubble columns with a diameter and height between 0.08 – 11.6 m and 0.3 – 21 m, respectively [277]. v_{Gs}^c is estimated from the logarithmic mean of the volumetric gas flow rates across the bioreactor calculated at normal conditions of temperature and pressure (see Table SI.3.3 for the specific equations used for the calculation). The gas flow rates and the estimated v_{Gs}^c are ultimately constrained to return a ε_G fixed at 0.15. Although the gas hold-up is not a proper design closing criterion, it was chosen to limit further maximization of mass transfer coefficients and subsequent minimization of gas use (see section 3.4.4.1).

Table 3.4. Model parameters for bubble column bioreactor design and operation during gas fermentation

Parameter	Unit	Value
Operation conditions		
Temperature	K	310.15
Top pressure	Pa	1.52×10^5
Gas hold-up	m_G^3/m_{G+L}^3	0.15
pH	-	5.0
Maximum ethanol concentration [e]	mol/m^3	1304
Bioreactor dimensions		
Volume	m^3	700
Height	m	20
Aspect ratio	-	3.0
Diameter	m	6.7
Overhead space	%	20
Height of gas-liquid mixture	m	16
Relevant gas properties for the mass transfer model (at 37 °C)		
Diffusivities [f]		
O_2	m^2/s	3.21×10^{-9}
CO		2.88×10^{-9}
H_2		4.55×10^{-9}
CO_2		2.70×10^{-9}
Henry's coefficient [g]		
CO	$mol_S/m^3/Pa$	0.79×10^{-5}
H_2		0.72×10^{-5}
CO_2		24.6×10^{-5}

[e] Liquid-vapor equilibria data for the ethanol/water system were estimated using the non-random two liquid model for calculating activity coefficients (see Table SI.3.3)

[f] Estimated according to the method presented by Wilke and Chang, 1955 [235].

[g] Estimated according to the method presented by Sander, 2015 [292].

$$k_L a_S = \left(0.32 {v_{Gs}^c}^{0.7}\right)\left[1.022^{(T-293.15)}\right]\left(\frac{\mathcal{D}_S}{\mathcal{D}_{O_2}}\right) \quad (16)$$

$$\varepsilon_G = 0.6 {v_{Gs}^c}^{0.7} \quad (17)$$

Mass balances are established around the gas fermentor for all species involved in the metabolic reactions leading to ethanol and bacterial biomass production (see Table SI.3.2). Furthermore in the energy balances, the power requirement for compression of the gas feed and the off-gas for gas recycle is estimated assuming adiabatic operation of compressors with a mechanical efficiency of 0.7 [116]. The heat required for gas cooling is obtained using average heat capacities within the applied temperature ranges, assuming that condensation will occur only when the final cooling temperature has been reached; a refrigeration coefficient of performance of 3.7 is assumed [293]. Table SI.3.4 shows the specific equations used for estimating energy requirements.

3.4.1.4. Interlink between both models

The thermodynamics-based model of microbial reactions as well as the mass transfer-based model of the bioreactor converge in the concentration of the dissolved gases and ethanol in the liquid phase. The dissolved concentration of the electron donor (C_D where D is either, CO or H_2) is fixed before solving the mass balances to avoid unnecessary issues with convergence into a solution. Thus, a range of steady-state operation points of the gas fermentor are estimated for a range of values of C_D. Although the system has no degrees of freedom (see the list of decision variables below and equations SI.3.1 to SI.3.8), it does have multiple solutions; therefore, an optimization is used to obtain a solution that maximizes the ethanol volumetric productivity (R_{et} in equation 17) while minimizing power consumption.

$$R_{et} = q_{et} C_x \tag{17}$$

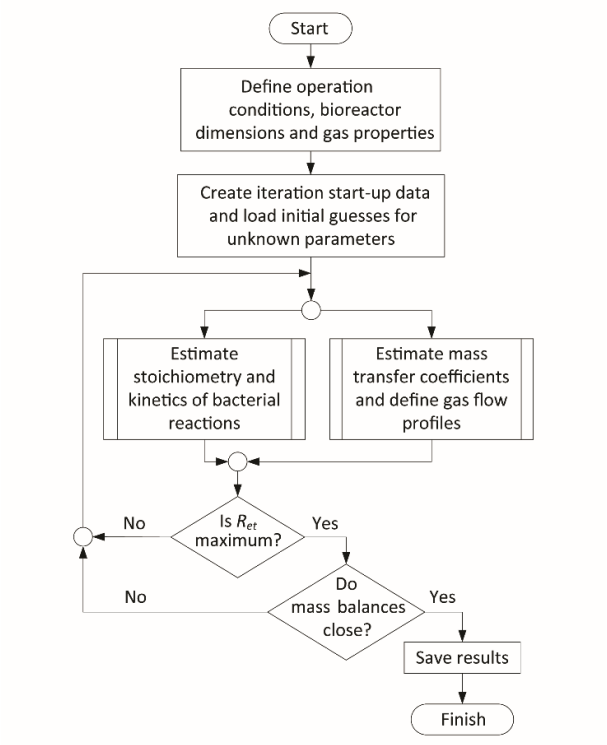

Figure 3.6. General structure of the calculation process for optimizing productivity. The figure is based on [294].

The optimization uses the fraction of ethanol that exits the bioreactor along the liquid phase as objective function; whereas, the biomass concentration, the molar gas inflow and outflow rates, the CO, H_2 and CO_2 contents in the off-gas, the concentration of ethanol and CO_2 (only in the case of H_2/CO_2 fermentation) in the liquid phase and the

liquid outflow rate from the bioreactor are the decision variables. The optimization is executed by a sequential quadratic programming ('sqp') algorithm implemented in the 'fmincon' function in MatLab R2017b. The system of mass balance equations outlaid for the bioreactor model and thermodynamic feasibility of the catabolic reactions are used as constraints within the optimization. The calculation process is schematized in Figure 3.6.

3.4.2. Gas concentration profiles

It is important to assure that at a determined operation point, the microbial uptake of electron donors does not meet gas concentrations that lead to either unfeasible catabolic reactions at the top of the liquid column or inhibition at the bottom (in the case of CO). Thus the dissolved CO, CO_2 and H_2 concentration profiles along the height of the liquid column are estimated by linearly discretizing the y-axis into 9 ideally mixed compartments stacked vertically. The initial assumption of the liquid phase having a homogenous composition is corrected by this calculation.

The approach is similar to that used in [236], where the height of the liquid column (H_{mix}) has three mixing cells stacked vertically (see equation 18 [236]); then each cell is subdivided into three compartments stacked horizontally which recreate the effect of dispersion on the radial direction assuming the liquid flow will follow a helicoidal stream line.

$$n_c = 0.8\frac{H_{mix}}{\tau} \tag{18}$$

Mass balance equations are constructed in each compartment assuming the liquid phase will be exchanged between the adjacent segments at a flow rate determined by equation 19 [277]; biomass concentration is assumed homogeneously distributed within the whole liquid volume. The gas phase is assumed to behave as a plug flow. Mass transfer properties in each segment are found using the same methodology as explained in section 3.4.1.3 since it is assumed that each compartment would behave as a shallow bubble column.

$$\dot{V}_L = 0.3\tau^{\frac{5}{3}}\left(g\dot{V}_G\right)^{\frac{1}{3}} \tag{19}$$

The compartmentalization scheme is validated by calculating the mixing time using two approaches *i.e., i)* using equation 20 [236] and, *ii)* simulating a mixing time- determination experiment, in which a tracer is injected at the top compartment; the mixing time is defined as the time it takes for the tracer concentration at the top compartment to reach 95% of the final concentration.

$$t_m = \frac{N_{mix}\tau^{\frac{2}{3}}}{(g v_{Gs}^{c})^{\frac{1}{3}}} \quad (20)$$

3.4.3. Process configuration

Fresh gas is first mixed with a stream of recycled off-gas and is then fed to the large-scale bioreactor. The fermentable gas is consumed during fermentation and ethanol is produced. At the exit, the off-gas is compressed to 3.1x10^5 Pa (a pressure equal to the bioreactor bottom pressure – see Table 3.4) and cooled to -6 °C in order to condense nearly 100% of the water-ethanol mixture. This condensate stream along with the fermentation broth is sent to distillation. Figure 3.7 shows the conceptualized process configuration.

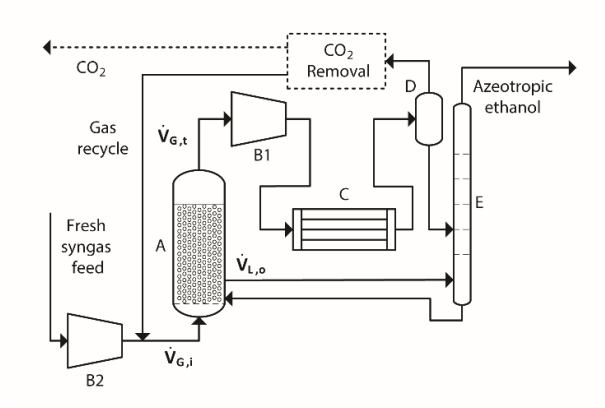

Figure 3.7. Conceptual process configuration; A: bubble column bioreactor, B1 and B2: gas compression, C: cooling and condensation, D: flash separation, E: azeotropic distillation. For the case in which the H_2/CO_2 mixture is fed into the bioreactor, the CO_2 removal unit is not needed.

When pure CO is fed to the fermentation, the dry off-gas undergoes CO_2 removal prior to recycling; this operation is not needed if H_2/CO_2 was used as feedstock. Since gas recycling has not been included in process designs reported in literature [70], the possible effects of not including it are discussed within the sensitivity analysis.

3.4.4. Process assessment

3.4.4.1. Technical performance

In addition to R_{et}, the process technical performance is evaluated from the perspective of the gas utilization 'per step' (U_S) inside the bioreactor (equation 21) and the energy requirements of the fermentation plus the ethanol separation processes. U_S is calculated as the ratio between the amounts of D depleted across the reactor and the D fed (fresh plus recycled). Energy requirements account for: *i)* power for compression of the gas feed

and the off-gas, *ii)* power for condensation of evaporated ethanol and water and, *iii)* heat for the ethanol azeotropic distillation from both: the fermentation broth outflow and the stream recovered from the off-gas (data taken from [295]). The power requirements for cooling of bioreactor contents and compressed gases are not accounted for since the utility that would be used is cooling water at ambient temperature and thus its energetic burden is negligible.

$$U_S = \frac{y_{D,i}F_{G,i} - y_{D,o}F_{G,o}}{y_{D,i}F_{G,i}}100\% \quad (21)$$

3.4.4.2. Sensitivity analysis

Process performance is evaluated at different values of the constants governing the electron donor uptake kinetics (equations 14 and 15) *i.e.,* half saturation constants (K_D) and the maximum specific uptake rates (q_D^{max}). This analysis is made due to *i)* uncertainty generated by the scarce information available in literature about these parameters, *ii)* uncertainties associated with the methodologies used to fix these parameters (see section 3.4.1.2) and *iii)* their paramount importance for the model reliability in quantitative terms.

Additionally, bioreactor performance is also assessed using different values of the mass transfer coefficients, the concentration of ethanol, the height of the liquid column and the gas hold-up. Specifically, 100% higher and 50% lower values of the mass transfer coefficients for CO, H_2 and CO_2 (as predicted by equation 16) are used. The range of possible $k_L a$ values was selected considering that: *i)* the possible presence of surfactants that may hamper mass transfer by 70% at concentrations as low as 10 ppm [296], *ii)* the uncertain effect of ethanol concentration on mass transfer since it has been reported that ethanol at a wide range of concentrations may rise the gas hold-up by four times [291] while at 50 g/L, the mass transfer coefficient would increase by 50% [297] and *iii)* the proven ability of *C. ljungdahlii* and *C. carboxydivorans* [65,89–91] to form biofilms which, if shaped into granules may enhance mass transfer by 30% due to intraparticle liquid circulation forced by pressure gradients caused by the circulation of bacteria inside the bioreactor [300].

Similarly, the maintenance of ethanol concentrations at 80 g/L are assessed considering that long term adaptation experiments of *C. thermocellum* led to a 100% increase in its tolerance to both, ethanol and n-butanol [301], promoted in part by a change in the structural composition of its membrane.

Finally, disregarding possible conflicts with legislation and safety measures, the effect of an increased aspect ratio of the bubble column, from 3 to 10, is also assessed. Moreover, considering that 15 and 30% are regarded as standard values for large bubble column

bioreactors to maintain high productivites [85], the effects of using a gas hold-up value of 30% on the process and the bioreactor performance are also assessed in the sensitivity analysis.

3.5. List of symbols

Latin letters		**Greek letters**	
ATP	Adenosine triphosphate	γ	Degree of reduction, mol_{e^-}/mol
C	Concentration in fermentation broth, mol/m^3	ΔG^0	Standard Gibbs free energy change, kJ/mol
		ΔG_{dis}	Gibbs free energy dissipation in anabolism, kJ/mol
CS	Carbon source, *i.e.,* CO or CO_2		
D	Electron donor of catabolism *i.e.,* CO, H_2	$\Delta G^{0'}$	Gibbs free energy change at physiological conditions, kJ/mol
$\mathcal{D}$	Diffusivity in pure water, m^2/s		
F	Molar flow rate, mol /s	ΔH^0	Standard enthalpy change, kJ/mol
g	Gravity's acceleration, 9.8 m/s	ε	Hold-up
H_{mix}	Height of gas-liquid column in bioreactor, m	μ	Biomass growth rate, h^{-1}
		τ	Diameter of bioreactor vessel, m
$k_L a$	Gas-liquid mass transfer coefficient, s^{-1}	ν	Stoichiometric coefficient; positive for products, negative for reactants.
K	Half saturation constant, mol/m^3		
K_I	CO inhibition constant, mol/m^3	**Subscripts and superscripts**	
N_{mix}	Mixing number, 16 [236]	an	Anabolism
n_c	Number of mixing cells in the bioreactor	b	Calculated at bottom of fermentor
p	Pressure, Pa	cat	Catabolism
q	Biomass specific production/consumption rate, $mol/Cmol_x/h$	$cons$	Theoretically consumed
		et	Ethanol
R	Volumetric productivity, $g_{ethanol}/L/h$	e^-	Electron
$\mathcal{R}$	Ideal gas constant, 8.134 m^3*Pa/mol/K	G	Gas
SI	Supplementary Information	i	At gas inlet
T	Process temperature, K	L	Liquid fermentation broth
t_m	Mixing time, s	max	Maximum
U_S	Gas utilization, %	met	Metabolism
v_{sG}^c	Pressure corrected superficial gas velocity, m/s	o	At bioreactor outlet
		r	Reaction
$\dot{V}$	Volumetric flow rate, m^3/s	S	Gas components *i.e.*, CO, H_2, CO_2
WLP	Wood-Ljungdahl pathway	t	Calculated at top of fermentor
y	Molar fraction in gas phase	w	Water
$Y_{x/CS}$	Biomass yield per mole of carbon source, $Cmol_x/mol_{CS}$	x	Dry microbial biomass
		0	Calculated at standard conditions, 101 kPa and 0 °C

3.6. Acknowledgements

The authors thank Sef Heijnen and Wouter van Winden for their respective critical assessments on the construction of the black-box model of microbial reactions and the validation of the 9-compartment model for estimating concentration profiles.

Supplementary Information

SI.3.1 List of equations used to estimate liquid-vapor equilibrium data for the ethanol-water mixture using the non-random two liquid model

The activity coefficients (eq SI.3.1 - SI.3.2) for ethanol (1) and water (2) are calculated from the composition (molar fractions) of the liquid phase. The composition of the vapor phase is finally estimated using Antoine's equation (see eq SI.3.7) and a modified Raoult's law (see eq SI.3.9). Figure SI.3.1 shows vapor liquid equilibrium data generated by the non-random two liquid (NRTL) model.

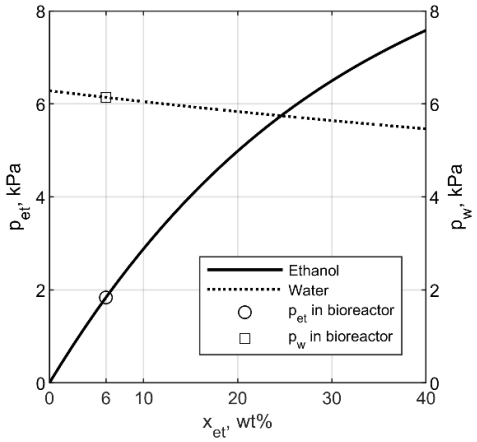

Figure SI.3.1. Equilibrium partial pressures for ethanol and water as functions of ethanol concentration in water. Ethanol partial pressures are shown at the left y-axis while water is shown at the right y-axis. The plot was generated using the NRTL model at 37 °C.

Table SI.3.1 List of equations used to estimate liquid-vapor equilibrium data for the ethanol-water mixture by the NRTL model

	Equation	Additional information
SI.3.1	$\ln \gamma_1^a = {x_2}^2 \left[\tau_{21}\left(\frac{G_{21}}{x_1 + x_2 G_{21}}\right)^2 + \frac{\tau_{12} G_{12}}{(x_2 + x_1 G_{12})^2}\right]$	Substance 1 is ethanol, substance 2 is water. γ_1^a is the activity coefficient of substance 1.
SI.3.2	$\ln \gamma_2^a = {x_1}^2 \left[\tau_{12}\left(\frac{G_{12}}{x_2 + x_1 \cdot G_{12}}\right)^2 + \frac{\tau_{21} \cdot G_{21}}{(x_1 + x_2 \cdot G_{21})^2}\right]$	
SI.3.3	$\ln G_{12} = -\alpha_{12}\tau_{12}$	$\alpha_{21} = \alpha_{21} = 0.3$
SI.3.4	$\ln G_{21} = -\alpha_{21}\tau_{21}$	
SI.3.5	$\tau_{12} = \frac{u_{12} - u_{22}}{RT}$	$u_{12} - u_{22} = 368.2$ J/mol [302]
SI.3.6	$\tau_{21} = \frac{u_{21} - u_{11}}{RT}$	$u_{21} - u_{11} = 4083.6$ J/mol [302]

Equation		Additional information
SI.3.7	$\log(p_1) = A_1 - \frac{B_1}{C_1 + T}$	Component / A / B / C 1 (ethanol) / 7.24215 / 1596.044 / -46.655 2 (water) / 7.11572 / 1684.123 / -43.568 * Pressure is obtained in kPa, T is in K. data gathered from [303]
SI.3.8	$p_{mix} = p_1 + p_2$	
SI.3.9	$y_1 = p_{mix} x_1 \gamma_1^a$	

SI.3.2 List of equations used to calculate the gas flow rate flowing across the bioreactor from the pressure-corrected superficial gas velocity

Table SI.3.2 List of equations used to calculate the gas flow rate flowing across the bioreactor from the pressure-corrected superficial gas velocity

Equation		Additional information
SI.3.10	$v_{sG}^C = v_{sG}^0 p^0 \left[\frac{\log\left(\frac{p_b}{p_t}\right)}{p_b - p_t}\right]$	superficial gas velocity is determined at normal conditions of temperature and pressure
SI.3.11	$v_{sG}^0 = \frac{\dot{V}_{ml}^0}{A_T}$	A_T is the cross-sectional area of the bioreactor vessel.
SI.3.12	$\dot{V}_{ml}^0 = \frac{\dot{V}_{ml} p_{ml} 273.15}{101325T}$	p_{ml} is the log mean pressure inside the bioreactor. It is also assumed that the gas will behave as an ideal gas
SI.3.13	$\dot{V}_{ml} = \frac{F_{ml} R 1000 T}{p_{ml}}$	

SI.3.3 Mass Balances and constraints used to guide convergence of the optimization algorithm

Table SI.3.3 List of mass balance equations and constraints used for convergence of the optimization algorithm

Equalities (the optimization algorithm ensures these constraints are equal to zero)	
SI.3.14	Electron donor balance in the liquid phase $0 = k_L a_D (C_D^* - C_D) 3600 - q_D C_x - \dot{V}_{L,o} C_D$
SI.3.15	Electron donor balance in the gas phase $0 = F_{G,i} y_{D,i} - F_{G,o} y_{D,o} - k_L a_D (C_D^* - C_D) V_L 3600$
SI.3.16	Overall CO_2 balance (used in CO fermentation) $0 = q_{CO_2} C_x V_L - F_{G,o} y_{CO_2,o} - \dot{V}_{L,o} C_{CO_2,ml}$
SI.3.17	CO_2 balance in the liquid phase (used in H_2 fermentation) $0 = k_L a_{CO_2} (C_{CO_2}^* - C_{CO_2}) V_L 3600 - q_{CO_2} C_x V_L - \dot{V}_{L,o} C_{CO_2}$
SI.3.18	CO_2 balance in the gas phase (used in H_2 fermentation) $0 = F_{G,i} y_{CO_2,i} - F_{G,o} y_{CO_2,o} - k_L a_{CO_2} (C_{CO_2}^* - C_{CO_2}) V_L 3600$

SI.3.19	Overall ethanol balance $0 = q_{et} C_x V_L 3600 - F_{G,o} y_{et,o} - \dot{V}_{L,o} C_{et}$	
SI.3.20	Molar fraction summation in off-gas $0 = 1 - y_{D,o} - y_{CO_2,o} - y_{et,o} - y_{w,o}$	
SI.3.21	Definition of the mean log molar gas flow rate $0 = F_{G,ml} - \frac{\left\lvert F_{G,o} - \frac{F_{G,i}}{1 - \frac{p_{mix}}{p_b}} \right\rvert}{\left\lvert \ln\left(\frac{F_{G,o}}{\frac{F_{G,i}}{1 - \frac{p_{mix}}{p_b}}} \right) \right\rvert}$	The correction $\frac{F_{G,i}}{1-\frac{p_{mix}}{p_b}}$ was applied to the gas flow rate at the fermentor inlet to account for the amount of evaporated water/ethanol mixture at the bottom of the fermentor
Inequalities (the optimization algorithm ensures these constraints are always negative)		
SI.3.22	Thermodynamic feasibility constraint $0 > \Delta G_{cat}^{0\prime}$	
SI.3.23	Positive liquid outflow rate constraint $0 > -\dot{V}_{L,o}$	
SI.3.24	Overall water mass balance constraint (used in H_2 fermentation) $0 > q_w C_x V_L 3600 - F_{G,o} y_{w,o} - \frac{V_{L,o}(1 - C_{et} MW_{et})}{MW_w}$	

SI.3.4 Equations used for calculation of energy requirements

Table SI.3.4 List of equations used for calculation of energy requirements

Power for gas compression	
SI.3.25	$P_{C,i} = \left(\frac{\Upsilon_i}{\Upsilon_i - 1}\right) p_{atm} \dot{V}_{G,stoich} \left[\left(\frac{p_b}{p_{atm}} \right)^{\left(\frac{\Upsilon_i - 1}{\Upsilon_i}\right)} - 1 \right] \frac{1}{0.7}$
SI.3.26	$\Upsilon_i = \frac{c_{P\,G,i}}{c_{V\,G,i}}$
SI.3.27	$\dot{V}_{G,stoich} = \frac{\left(\frac{q_D C_x V_L}{y_{D,i} 3600}\right) RT}{p_{atm}}$
SI.3.28	$P_{C,o} = \left(\frac{\Upsilon_o}{\Upsilon_o - 1}\right) p_t \dot{V}_{G,o} \left[\left(\frac{p_b}{p_t} \right)^{\left(\frac{\Upsilon_o - 1}{\Upsilon_o}\right)} - 1 \right] \frac{1}{0.7}$
SI.3.29	$\Upsilon_o = \frac{c_{P\,G,o}}{c_{V\,G,o}}$
Power for reactor cooling	
SI.3.30	$P_{cool} = \Delta H_{met}^T [k_L a_D (C_D^* - C_D) \cdot V_L] + \left(\frac{p_{mix} F_{G,o}}{p_t}\right) \left[\lambda_w^T \left(\frac{y_{w,o}}{y_{w,o} + y_{et,o}} \right) + \lambda_{et}^T \cdot \left(\frac{y_{et,o}}{y_{w,o} + y_{et,o}} \right) \right]$
SI.3.31	$\Delta H_{met}^T = \Delta H_{met}^0 + \int_{298.15}^{T} c_{P\,m}\, dT$
SI.3.32	$c_{P\,m} = \sum_{j=1}^{n} \nu_j^{met} \cdot c_{P\,j}$

Power for condensation of evaporated water/ethanol mixture	
SI.3.33	$P_{cond} = \left[\lambda_w^{-6℃}\left(\frac{y_{w,o}}{y_{w,o}+y_{et,o}}\right) + \lambda_{et}^{-6℃}\left(\frac{y_{et,o}}{y_{w,o}+y_{et,o}}\right)\right] F_{G,o}\left(\frac{p_{mix}}{p_t}\right)\left(\frac{1}{3.7}\right)$
Power for distillation of ethanol in off-gas condensate	
SI.3.34	$P_{dis,G} = 22.194(100x_{et}^{G})^{-0.794} f_{et}^{G}$
SI.3.35	$f_{et}^{G} = \frac{y_{et,o} F_{G,o} 3600}{q_{et} C_x V_L}$
SI.3.36	$x_{et}^{G} = \frac{\left(\frac{y_{et,o}}{y_{w,o}+y_{et,o}}\right) MW_{et}}{\left[\left(\frac{y_{et,o}}{y_{w,o}+y_{et,o}}\right) MW_{et} + \left(\frac{y_{w,o}}{y_{w,o}+y_{et,o}}\right) MW_w\right]}$
Power for distillation of ethanol in fermentation broth	
SI.3.37	$P_{dis,L} = 22.194(100x_{et}^{L})^{-0.794} f_{et}^{L}$
SI.3.38	$f_{et}^{L} = \frac{C_{et} F_{L,o} 3600}{q_{et} C_x V_L}$
SI.3.39	$x_{et}^{L} = \frac{C_{et} MW_{et}}{1000000}$

SI.3.5 Predicted biomass yields and data used for their validation

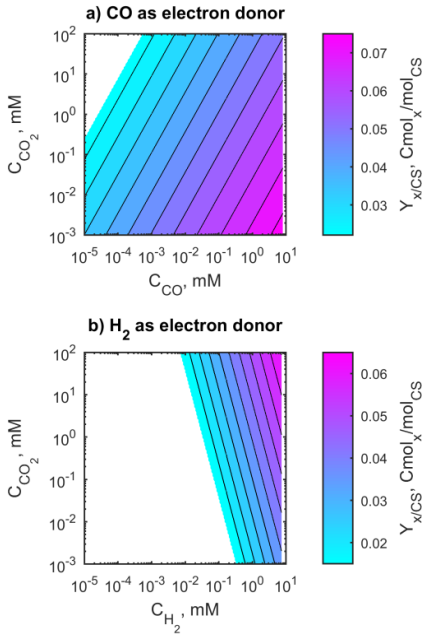

Figure SI.3.2. Biomass yields when acetogens produce ethanol for the fermentation of a) CO and b) H_2/CO_2

Table SI.3.5 Reported experimental data used for the validation of biomass yields

Experiment nr.	Reported q rates, mol/Cmol$_x$/h						Estimated parameters	
	μ	q_{CO}	q_{H_2}	q_{CO_2}	q_{et}	q_{HAc}	$\frac{q_{et}}{q_{et}+q_{HAc}}$	$Y_{x/CS}$
Data from Valgepea et al., 2017 [75]								
1	0.042	0.49	0.33	0.14	0.03	0.17	0.15	0.086
2	0.042	0.46	0.31	0.14	0.03	0.15	0.16	0.090
3	0.042	0.62	0.32	0.22	0.06	0.13	0.32	0.067
4	0.042	0.80	0.31	0.33	0.09	0.11	0.47	0.052
5	0.042	0.75	0.29	0.31	0.10	0.10	0.49	0.056
Data from Valgepea et al., 2018 [74]								
1	0.042	0.78	0.00	0.53	0.10	0.16	0.38	0.053
2	0.042	0.52	0.76	0.11	0.29	0.10	0.75	0.080
Data from Richter et al., 2013 [72]								
1	0.039	0.88	0.55	0.11	0.022	0.299	0.07	0.044

SI.3.6 Gas utilization inside the large syngas fermentor

Figure SI.3.3 represents the influence of the non-dimensional CO and H_2 uptake rates on gas utilization inside the large-scale syngas fermentor.

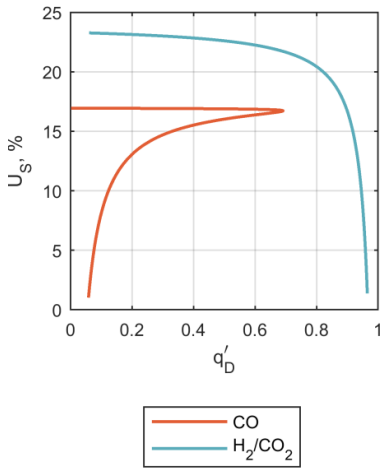

Figure SI.3.3. Relation between gas utilization inside the large-scale syngas fermentor and the non-dimensional uptake rate of the electron donor CO and H_2

SI.3.7 List of symbols

Table SI.3.6 Nomenclature table

Abbreviations		Greek	
C	Concentration in fermentation broth, mol/m^3	Υ	Heat capacity ratio
C^*	Saturation concentration, mol/m^3	λ	Latent heat, kJ/mol
c_P	Heat capacity at constant pressure, kJ/mol/K	Subscripts	
c_V	Heat capacity at constant volume, kJ/mol/K	atm	Atmospheric
f	Fraction of overall production, mol/mol$_{et+HAC}$	b	Fermentor bottom
F	Molar flow rate, mol/s	cat	Catabolism
$\Delta G^{0'}$	Gibbs free energy change at physiological conditions, kJ/mol	$cond$	Condensation
		$cool$	Cooling of fermentor contents
ΔH^0	Standard enthalpy change, kJ/mol	C	Compression
ΔH^T	Enthalpy change at process temperature, kJ/mol	dis	Distillation
		D	Electron donor of catabolism i.e. CO, H_2
$k_L a$	Gas-liquid mass transfer coefficient, s^{-1}	et	Ethanol
MW	Molar mass, g/mol	G	Gas
P	Specific power consumption, kJ/kg$_{ethanol}$	i	At syngas inlet
p	Absolute pressure, Pa	L	Fermentation broth
p_{mix}	Vapor pressure of water-ethanol mixture, Pa	m	Temperature averaged
q	Biomass specific production/consumption rate, mol/Cmol$_x$/h	met	Metabolism
		mix	Water-ethanol mixture at equilibrium with fermentation broth
R	Ideal gas constant, 8.134 m^3*Pa/(mol*K)		
T	Fermentation temperature, K	ml	Logarithmic mean
V	Volume, m^3	o	At syngas outlet
$\dot{V}$	Volumetric flow rate, m^3/s	$stoich$	Stoichiometrically needed
x	Mass fraction in ethanol-water mixture	t	Fermentor top
y	Molar fraction in gas phase	w	water
		x	Dry microbial biomass
		Superscripts	
		L	At the liquid phase
		G	At the gas phase

Chapter 4

Decarbonizing ethanol production via gas fermentation: impact of the $CO/H_2/CO_2$ mix source on greenhouse gas emissions and production costs

This chapter is based on the article published as:

Eduardo Almeida Benalcázar, Henk Noorman, Rubens Maciel Filho and John Posada, 2022, "Decarbonizing ethanol production via gas fermentation: impact of the $CO/H_2/CO_2$ mix source on greenhouse gas emissions and production costs", Computers and Chemical Engineering, 159, p.10767, DOI: 10.1016/j.compchemeng.2022.107670.

"Without some artistic touch, sir, you'll never come up with a new idea. We've got to be poets if we want to keep the world turning"

Karel Čapek, *War with the newts*, 1936.

4.1. Introduction

Global policy efforts aiming to reduce the anthropogenic emissions of greenhouse gases (GHG) and to guarantee the security of energy supply converge into the need for progressive replacement of fossil-based fuels by low-carbon and renewable fuels [8,304], such as ethanol. The use of sugarcane juice and corn as feedstocks for large-scale production of ethanol is currently a mature and widespread technology that achieves significant reductions on GHG emissions compared to fossil-based gasoline and diesel [8]. However, there are concerns about the (direct and indirect) land use change and potential conflicts with animal and human food supply derived from these feedstocks [305,306]. In response, the use of gaseous feedstocks has gained attention from academia and industry in recent years [252,307,308].

Syngas is a gas mixture of CO, CO_2 and H_2 that can be produced from the thermochemical conversion of lignocellulosic biomass, municipal solid wastes or other industrial organic wastes [307], and also via reforming of methane [309]. Syngas can be used for the production of bulk chemicals and fuels through fermentation [30,310]. Such process exploits the ability of acetogenic bacteria to retrieve the energy contained in CO and H_2 while fixing the carbon from CO and CO_2. The main native products of these types of microorganisms are formic, acetic and lactic acids, ethanol and 2,3-butanediol [111,244,307,311]. In addition, since acetogens are able to catabolize the components of syngas in a wide range of compositions [246,312], industry and academia have contemplated other sources of fermentable CO, H_2 and CO_2 *e.g.*, industrial off-gases from steel manufacturing [313] and gas mixtures containing H_2 derived from the electrolysis of water [314] and CO_2 derived from the combustion of carbonaceous materials.

The diversity of laboratory and pilot-plant set-ups for ethanol production through gas fermentations is wide as they include different microbial strains (*e.g.*, mesophilic and thermophilic bacteria) [232], batch and continuous operations [73,74], fermentation in single and multiple stages [72,315], thermophilic [316,317] and high pressure operation [311], plus the use of an assortment of internals (monoliths, membranes, external recycles, among others) as part of the bioreactors [285,298,299,318–322]. This variety altogether converges into the search of overcoming the low solvent productivity, which is commonly credited to the poor solubility of CO and H_2 in the fermentation broth. From an analysis of the published literature on gas fermentation it is clear that, although the limitation of low productivity has been addressed during the past two decades, it is uncertain what other variables controlling the fermentation may benefit the development and scale-up of the process.

It has been advocated that the design of experiments at laboratory scale aimed at the development of industrial-scale fermentation processes must be guided by "the perspective of the large-scale" [78]. For this purpose, the only publicly available report based on corporate data is an environmental sustainability assessment for the production of ethanol from the fermentation of steel manufacturing off-gases [70], which concluded that the global warming potential (GWP) of such process equals 31 g_{CO2eq}/MJ of ethanol. To put this number into perspective, one can consider that ethanol's net standard enthalpy of combustion is 26.8 MJ/kg [28] and that at full combustion 1 kg of the alcohol will release 1913 g of CO_2, thus the production of the biofuel should not generate more than 71.3 g_{CO2eq}/MJ of ethanol. In the same study [70], unrevealed data from the bioreactor performance is also used to estimate the GWP of ethanol produced from biomass-derived syngas in the range of 2 and 12 g_{CO2eq}/MJ. Moreover, research efforts have been made to understand the linkage between the syngas fermentation conditions (in combination with the up and downstream processes) and the techno-economic and environmental performances of different process configurations. Such studies use Aspen Plus to simulate the bioreactor, with simplified models and their simulations offer little detail about the operation of the bioreactor, a unit with still large development challenges ahead. Another study, was devoted to gaining insights on variables that may optimize the economic and environmental performance of the bioreactor and the downstream processing of ethanol [323]; however, that study left the production of the syngas feedstock out of the battery limits, disregarding the large potential for heat integration offered by the hot gas stream.

As a starting point, we developed a black-box model of bacteria to simulate ethanol production in a 700 m^3 bubble column bioreactor fed by CO, H_2 and CO_2 mixtures [324]. Then a stochastic bioreactor simulation using the same model suggested that ethanol volumetric productivity and gas utilization have a 50% probability of reaching values between 2.5 – 6.8 g/L/h and 30 – 66%, respectively [325]. However, it is unclear whether such indicators will render, the overall ethanol production process, economically and environmentally attractive, and to what extent the potential for commercial success would depend on the selection of a gas stream source with a specific composition. Thus, this study seeks to identify key parameters and their combinations that may drive the fermentation process to simultaneously achieve minimal ethanol production costs and GHG emissions. The assessment is applied to three process configurations which primarily differ in the gas source and its production process to provide gas mixtures of different compositions. Finally, the assessment also seeks to: *i)* determine the potential of such process configurations to constitute viable options to replace fossil-based fuels and other bio-based ethanol production routes (*e.g.* 1G and 2G ethanol) at a competitive cost in

the medium term, and *ii)* provide direction for future research efforts on design and integration of the fermentation stage with the up and downstream operations.

4.2. Methodology

This section details the sequence of steps followed to assess the robustness and to simultaneously minimize the economic performance and environmental impacts of ethanol production from three different gas mixtures containing CO, H_2 and CO_2. Both, the sensitivity analyses and the optimizations are performed by varying eight process variables that command the operation of the fermentation process, namely: *i)* process temperature (T), *ii)* top reactor pressure (p_t), *iii)* gas feed dilution (f_{Dil}), *iv)* maximum ethanol concentration (C_{et}^{max}), *v)* liquid column height (h_L), *vi)* mass transfer coefficient factor ($f_{k_L a}$), *vii)* acetic acid production factor (f_{Ac^-}) and *viii)* the pressure-corrected superficial gas velocity (v_{sG}^{c}). These eight variables are referred to as input variables (IV's), while the indicators used to quantify the overall economic performance and environmental impacts of the ethanol production process are called output variables (OV's). The following sections describe how the IV's are processed in order to obtain the OV's.

4.2.1. Process configurations

Three process configurations are analyzed in this study; they differ primarily on the gas source, meaning different compositions and production processes. The selection of the gas source is based on three major aspects: *i)* the gas compositions should range between pure CO and a mixture of H_2/CO_2, *ii)* there must be reports showing academic and industrial interest in the specific gas mixture, and *iii)* the environmental impacts at the gas production stage should be diverse among the choices. Thus, the considered gas feedstocks are:

- CO-rich basic oxygen furnace (from here referred to as BOF) off-gas from the steel manufacturing process [70].
- A 3:1 mixture of H_2 and CO_2 (from here referred to as HAC), where H_2 is derived from water electrolysis, and CO_2 scrubbed from a generic industrial combustion flue-gas [309,314]. The 3:1 mixture comes from the stoichiometric relation between the two gases for producing ethanol at the fermentation.
- Bio-based syngas (from here referred to as BBS) with a H_2/CO ratio of 2 and produced by gasification of lignocellulosic biomass [30].

All process configurations have a fixed ethanol throughput of 220 kton/y, a scale that may be regarded as conservative, considering that the National Renewable Energy Laboratory bases its popular conceptual second-generation ethanol designs on a 2000

ton/d (660 kton/y assuming a year of 330 operative days) capacity in the United States [194].

As shown in Table 4.1, the BOF off-gas (or converter gas) is generated at a temperature of 1100 °C and at ambient pressure [326,327]; the BOF off-gas is then conditioned to remove main impurities, cooled and compressed before entering to the fermentation [70]. In the H_2/CO_2 mixture, H_2 is produced at 70 °C and a pressure of 10 bar [328,329], while CO_2 is obtained pure and compressed after scrubbing it from a flue-gas stream using monoethanolamine [184]; no conditioning is required for this gas mixture prior entering to the fermentation. Finally, the BBS is produced at 900 °C and ambient pressure; the gas is then conditioned and cooled before entering the fermentation [30].

Table 4.1. Compositions, temperature and pressure at which the three gas feedstocks are available

Gas source	Composition [a], (%)			Temperature, (°C)	Absolute pressure, (atm.)
	CO	CO_2	H_2		
BOF	55 - 100	0 – 45	0	1100	1
HAC	0	25 – 58.7	41.3 – 75	70	10
BBS	18.3 – 33.3	16.7 – 54.2	27.5 – 50	900	1

[a] The ranges of compositions have been approximated from literature reports for BOF off-gas [330] and BBS [30,331]. CO_2 content in BBS is higher from what is commonly reported in literature as here, extra CO_2 was used for simulating the effect of the dilution of syngas with any inert component.

The fermentation process consists of a 700 m^3 bubble column fermentor (a common volume in industry [289]) fed by the gas mixture (see Figure 4.1). The ethanol produced inside the fermentor exits through two routes: *i)* along the liquid fermentation broth outflow, and *ii)* pre-concentrated along the off-gas (from where it is subsequently condensed and recovered by flash separation). The alcohol is separated from the two streams by atmospheric distillation and purified with a molecular sieve. The acetic acid and the cells produced in the fermentation are directed to wastewater treatment where they are converted into biogas which is subsequently combusted for heat integration (see section 4.2.2.3).

In the cases of BOF off-gas and BBS fermentations, the unconsumed gas is treated as a waste and combusted before being released into the atmosphere, as proposed by [70]. For HAC instead, the unconsumed gas is recycled to the fermentation to avoid waste of the expensive gases. Gas recycling would not be feasible for the BOF off-gas and the BBS fermentations because the gas feedstocks have impurities (mainly CH_4 and N_2 [332]) that may accumulate if the bioreactor off-gas was recycled.

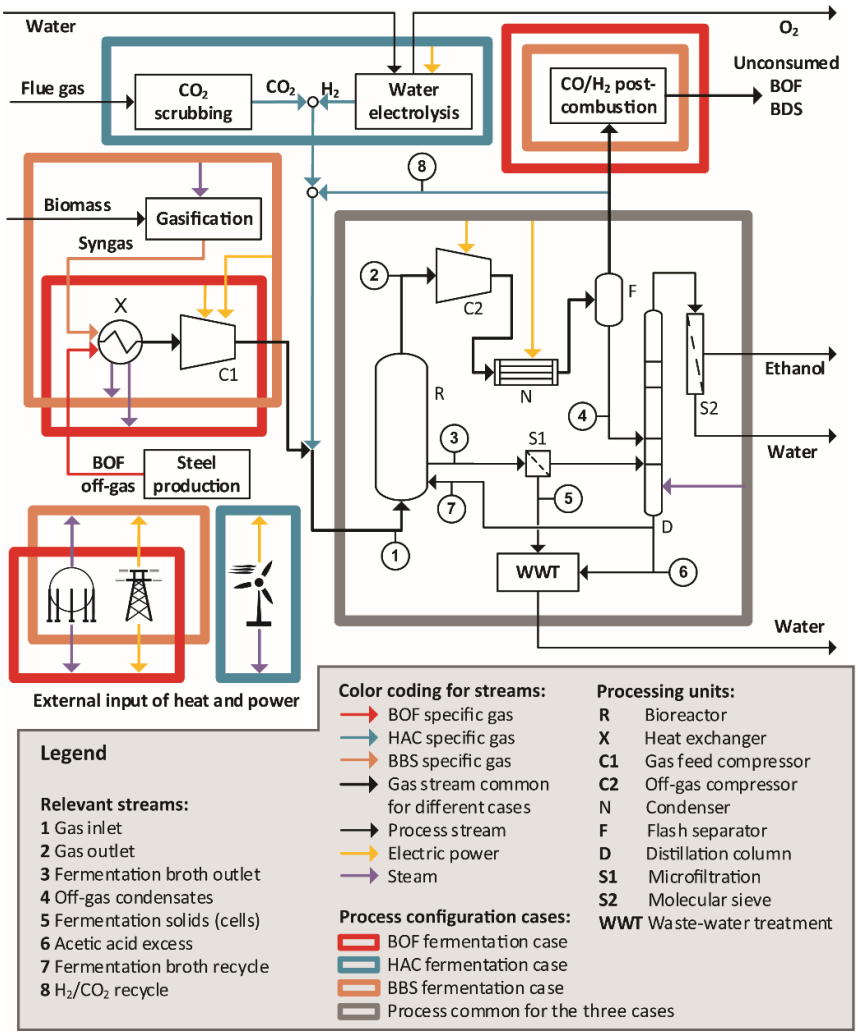

Figure 4.1. Configurations of the ethanol production processes depending on gas production. The units concealed inside the colored battery limits are the units included in the economic and environmental assessments.

4.2.2. Strategy for process simulation

Mass and energy balances at the fermentation stage allow integration with ethanol downstream processing and the upstream gas production processes. The fermentation stage comprises the unit operations directly linked to the fermentation *i.e.*, the bioreactor (R in Figure 4.1), the inlet and outlet gas compressors (C1 and C2 in Figure 4.1) plus the condenser and the flash separation drum (N and F in Figure 4.1, respectively). Since more than 50% of the ethanol production costs and environmental impacts may be derived

from the operations constituting the fermentation stage [30], the model for the fermentation is the most detailed of all unit operations in the three process configurations; the simulations of the bioreactors are described below.

4.2.2.1. Simulation of the bioreactor for the BOF and the HAC fermentations

The bioreactor model used in this study has been presented, thoroughly described and partially validated elsewhere [324]; therefore only the model's basic structure is detailed in this section. The consumption of CO and H_2 are simulated independently since the applied black-box model of microbial reactions is not able to consider the uptake of more than one electron donor at a time. The method for simulating the fermentation of syngas which contains both electron donors, CO and H_2, is introduced in section 4.2.2.2.

The fermentation model interlinks a thermodynamics-based black-box model of main microbial reactions and a mass transfer-based model of a large-scale bubble column bioreactor. In the black-box model, a simplified reaction is constructed to describe the microbial metabolism from the combination of catabolic (see equations 1 – 4 in Table 4.2) and anabolic reactions (see equations 5 and 6). Ethanol and acetic acid are assumed the two only possible products of catabolism which harnesses the chemical energy contained in the electron donors. Other products, such as formic acid or 2,3-butanediol [74,311] are not considered in this study because the drivers favoring their selectivity by bacteria are not clearly understood and also because the effect of a reduction on the ethanol yield is already simulated by the co-production of acetic acid. The black-box model is built such that the kinetic and stoichiometric parameters are dependent on the process temperature and the intracellular concentrations of CO, H_2, CO_2, ethanol, acetic acid and H^+ ions. Since CO, H_2, CO_2 and ethanol diffuse freely across the bacterial membrane, their intracellular concentrations are assumed equal to the extracellular ones. The intracellular concentration of H^+ ions is assumed constant at $1x10^{-7}$ M (neutral pH) whereas the intracellular concentration of acetate ions is electrochemically dependent on the extracellular pH and the concentration of acetate [52]. Since it is unknown whether the acetate ions will be at equilibrium at both sides of the bacterial membrane, the intracellular concentration of acetate is assumed to be 100 mM [77] while the extracellular pH and the total concentrations of acetate plus acetic acid are assumed constant at 4.5 and 142.5 mM [72].

The equations used by the black-box model to estimate the thermodynamic feasibility of catabolism (when the Gibbs free energy change, $\Delta G_{cat,D}^{T\prime} < -9$ kJ/mol [112]), as well as the stoichiometric and kinetic parameters of the microbial reactions are shown in Table SI.4.1 in the Supplementary Information (SI) given at the end of this chapter.

Table 4.2. Catabolic and anabolic reactions considered by the black-box model of microbial reactions

Phase of metabolism	Reaction	Equation nr.
Catabolism	$6CO + 3H_2O \rightarrow C_2H_5OH + 4CO_2$	(1)
	$6H_2 + 2CO_2 \rightarrow C_2H_5OH + 3H_2O$	(2)
	$4CO + 2H_2O \rightarrow CH_3COO^- + H^+ + 2CO_2$	(3)
	$4H_2 + 2CO_2 \rightarrow CH_3COO^- + H^+ + 2H_2O$	(4)
Anabolism	$2CO + \frac{1}{4}NH_4^+ + \frac{1}{2}H_2O \rightarrow CH_{1.75}O_{0.5}N_{0.25} + CO_2 + \frac{1}{4}H^+$	(5)
	$2H_2 + CO_2 + \frac{1}{4}NH_4^+ \rightarrow CH_{1.75}O_{0.5}N_{0.25} + \frac{3}{2}H_2O + \frac{1}{4}H^+$	(6)

Furthermore, it is assumed that the bioreactor operates in continuous mode at steady-state. In the bioreactor, gas-to-liquid mass transfer is driven by the energy input provided by gas sparging and the dissolved gas concentration gradients [85,234]. Thus, mass transfer coefficients ($k_L a_S$) are estimated as function of the v_{sG}^c. The saturation concentrations of the gas components (C_S^*) are estimated using Henry's equation; the temperature-dependent Henry's coefficients are gathered from [292]. The specific equations used by the mass transfer model are shown in Table SI.4.2 at the SI.

Since both, the black-box model of microbial reactions and the mass transfer model, depend on the dissolved concentration of the gas components (C_S), the operation of the bioreactor is evaluated at 200 different values of the mean-log dissolved concentration of the electron donor (C_D)[b] *i.e.*, CO for BOF, and H_2 for HAC fermentations, respectively. The values of C_D are set to range between the saturation concentration and their thermodynamic thresholds (where $\Delta G_{cat,D}^{T\prime}$ = -9 kJ/mol). The system of equations formed by the mass balances is fully specified and has multiple solutions. Therefore, an ethanol productivity optimization function is used to determine operation points of the bioreactor at each value of C_D. For further details on this optimization, the reader is referred to [324]. The reader is also advised that this optimization is not yet the multi-objective process optimization, which will be explained in section 4.2.5.

From the whole range of 200 possible bioreactor operation points, one is selected to characterize the bioreactor operation at a defined combination of input variables (IV's). Such point must fulfill five conditions to assume that the fermentation process operates at an optimal state that is comparable to a bioreactor operating with a different set of IV's: *i)* mass transfer rate exceeds the 90% of its maximum (evaluated at the CO and H_2 thresholds); *ii)* electron donors do not fall below threshold concentrations at the top of

[b] Solving the system of mass and energy balances is more stable when the loop uses the solutions of an adjacent point as initial guesses. The 200 points gives a leveled balance between resolution and processing speed.

the liquid column; *iii)* CO concentration does not exceed 0.06 mM at the bottom of the column, so CO uptake inhibition [106,333] could be evaded; *iv)* the biomass production rate is low enough such that the liquid outflow rate ($\dot{V}_{L,o}$) from the bioreactor does not prevent ethanol from achieving C_{et}^{max}; and *v)* the biomass concentration in the bioreactor does not surpass 10 g/L [72]. When several points fulfill these conditions, the one with the highest ethanol volumetric productivity is selected.

Figure 4.2 shows a schematic representation of the connections between the model IV's (light pink blocks in Figure 4.2) and OV's (light orange in Figure 4.2). The IV's T, p_t, h_L and v_{sG}^c are directly set into the model. In turn, the f_{Dil} is conceived as a consequence of the gas-supply process configurations and is included in the algorithm by adding an excess of CO_2 into the gas feed. Stoichiometrically, any CO_2 present in BOF off-gas or in BBS (with a H_2/CO ratio of 2) is considered an excess and therefore 'dilution' (considering the ratios of CO, H_2 and CO_2 needed for the catabolic production of ethanol from CO - equation 1 and from H_2 and CO – equation 7). Moreover, the IV C_{et}^{max} is introduced in the ethanol productivity optimization as an upper boundary to constrain the ethanol concentration solutions [324]. Lastly, the ratio between the biomass-specific acetate production rate and the total rate of product generation (IV f_{Ac^-}), which determines how much acetate is produced along ethanol, is introduced in the model as a factor defined by equation 8.

$$6H_2 + 2CO \rightarrow C_2H_5OH + 3H_2O \quad (7)$$

$$f_{Ac^-} = \frac{q_{Ac^-}}{q_{Ac^-} + q_{et}} \quad (8)$$

The C_D profiles along the height of the liquid column, inside the bioreactor, are estimated by discretizing the height of the column into a number of equal parts that are determined following the methodology recommended in [324]. Mass balances are solved for each portion of the column assuming that concentration of cells and ethanol are homogeneous and that the gas phase behaves as a plug-flow.

4.2.2.2. Simulation of the bioreactor for BBS fermentation

Since the black-box model of microbial reactions is only able to simulate the consumption of one electron donor at a time, the fermentation of bio-based syngas, which contains two electron donors, CO and H_2, is simulated indirectly. Each k-th mass and energy stream (MES) going in and out the BBS fermentation stage is estimated by adding the contributions of the independent fermentations that use pure CO and the 3:1 H_2/CO_2 mixture, at their respective operation points. Such fractional contributions (contained

within parentheses in equation 9) are determined by the H_2/CO ratio (HC) in the BBS fermentor.

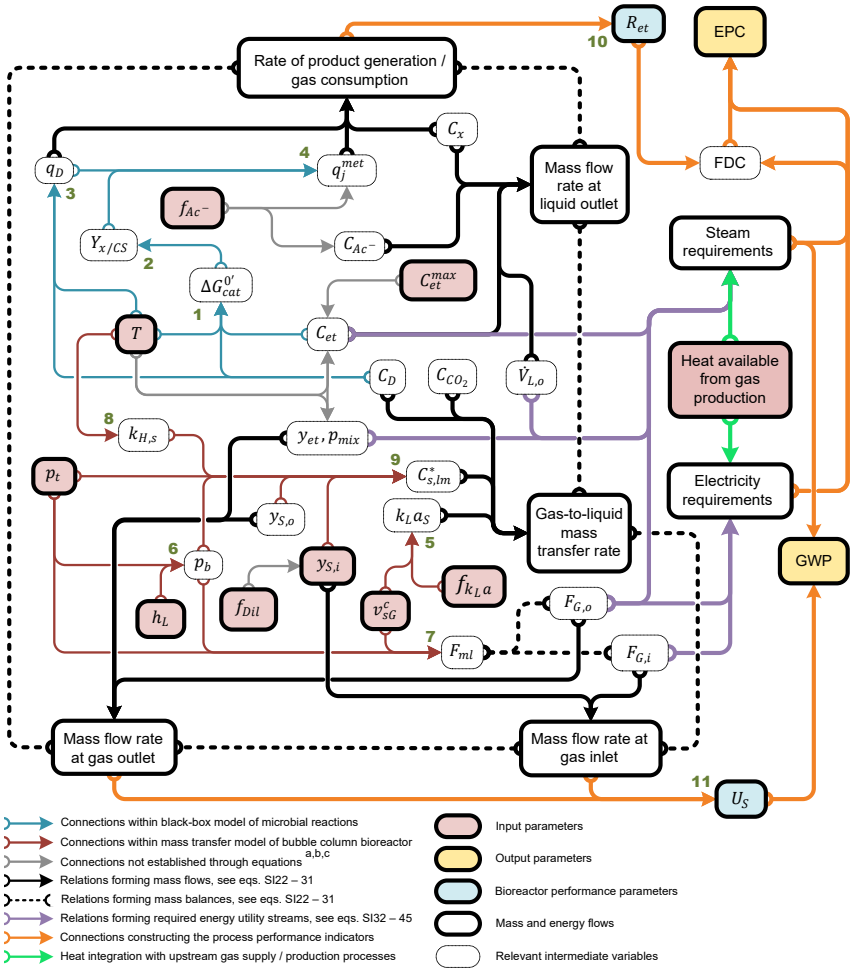

Figure 4.2. Map of connections between the model's input and output variables. Numbers 1 to 11 represent the system of equation used as follow: 1: eq. SI.4.1; 2: eq. SI.4.2, SI.4.3; 3: eq. SI.4.4, SI.4.5; 4: eq. SI.4.6, SI.4.7; 5: eq. SI.4.8, SI.4.9; 6: eq. SI.4.14; 7: eq. SI.4.11 – 15; 8: eq. SI.4.16; 9: eq. SI.4.17 – 19; 10: eq. 20; 11: eq. 21. See the list of symbols at section 4.5.

[a] IV's with indirect entrance to the model: f_{Ac^-} defines how much of the carbon directed towards ethanol and acetic acid, corresponds specifically to acetic acid, $f_{k_L a}$ multiplies the $k_L a$ estimated for pure water, f_{Dil} controls gas feed dilution with excess CO_2, C_{et}^{max} is introduced as an upper bound to constrain the ethanol concentration solutions within the bioreactor simulation (see [324]). The input parameter $y_{S,i}$ stands for the composition of the gas feed, it represents the different gas feedstocks used in the analysis, the BOF off-gas, the bio-based syngas and the H_2/CO_2 mixture.

[b] NRTL-based vapor-liquid equilibria for the ethanol-water system (data gathered from [334]).

$$MES_{k,BDS} = MES_{k,CO}\left(\frac{1}{1+HC}\right) + MES_{k,H_2/CO_2}\left(\frac{HC}{1+HC}\right) \quad (9)$$

A thorough description of the streams considered for the mass and energy balances is included in Table SI.4.2 and SI.4.3.

4.2.2.3. Sources of energy and heat integration

The energy requirements of the fermentation stage plus the ethanol downstream processing consider: *i)* the electric energy required by the inlet and outlet gas compressors, *ii)* the electric energy needed by the cryogenic condensation (at -6 °C) of ethanol and water stripped from the bioreactor by the off-gas, and *iii)* the steam needed by the distillation. The energy needed by the unit operations that use cooling water as utility (*i.e.* the bioreactor, and the off-gas cooling prior to the condensation) is not included in the energy accounting because it is negligible [30].

The BOF off-gas and the BBS streams are available at high temperatures (see Table 4.1) and they are cooled before entering the fermentation (unit X in Figure 4.1). Thus the sensible heat from the cooling operation is recovered to produce steam (see violet arrows leaving unit X in Figure 4.1) with an energetic efficiency of 85% [70]. The produced steam is used at the ethanol distillation in the BOF case and in biomass gasification in the BBS case; for the scenarios in the stochastic simulation in which the steam produced by heat integration does not cover the needs of the distillation and the gasification, additional steam is produced as a utility; on the other hand, an excess of steam produced by the heat integration will not bring any benefits because although the extra steam could be used for the production of electricity, the purchase costs of the turbine are too large. For the BOF and BBS cases, electric energy is supplied from the local grid, whereas the steam that is not heat-integrated is produced from LPG combustion (see units at the bottom-left in Figure 4.1).

All the power required by the HAC process is wind-based (see units at the bottom-left in Figure 4.1). In this process configuration, there is no power required for inlet gas compression since CO_2 and H_2 are both supplied at higher pressure than that at the bottom of the bioreactor [328,329,335]. The energy required for the production of H_2 through water electrolysis is 141.3 MJ/kg_{H2} [329].

4.2.3. Models and indicators for economic performance and environmental impacts

The overall process economic performance is evaluated using the ethanol production costs (EPC), while the environmental impacts are quantified through the GWP category. In addition, the CO_2 abatement costs (CAC) are used because it amalgamates the information of the GWP and the EPC and thus, *i)* it provides a common ground for comparison between the different gas composition cases and *ii)* it allows identifying the conditions where lowering either, the GWP or the EPC, is most relevant for decarbonizing ethanol production. Throughout the presentation and discussion of the results, the process performance of the gas fermentation configurations are compared to fossil-based and second generation ethanol whose economic and environmental performance data is collected from [24,223,336–338].

The economic and environmental performance indicators are calculated considering that the industrial facilities are located in Europe.

4.2.3.1. Calculation of the global warming potential

The calculation of the GWP follows a life cycle perspective with a cradle-to-grave approach, considering combustion as the end-of-life of ethanol. The GWP is the sum of the CO_2 equivalents emitted through: *i)* the overall gas production stages, *ii)* the generation of steam and electric energy (gathered from the local grid for BOD and BBS cases and derived from wind for the HAC case), *iii)* the flaring of the bioreactor off-gas, *iv)* the disposal of bacterial biomass and acetate through wastewater treatment (allocation by weight is used), and *v)* the final combustion of ethanol. The components CO and CO_2 contained in the gas feedstocks of the BOF and the HAC cases are assumed to be avoided emissions that would otherwise be released to the atmosphere; therefore, for accounting purposes, the carbon in these streams is regarded as credits. The carbon contained in the syngas of the BBS case is instead biogenic. The credits as well as the biogenic carbon are subtracted from final GWP accounting.

Moreover, there are specific considerations for each gas feedstock regarding the emissions derived from their production stages:

- In the steel production process, the heat of combustion of the BOF off-gas is used at a first stage, the making of the sinter; according to the data presented by [339], the flaring of the BOF off-gas contributes with the 0.11% of this stage's energy requirements, where most of the energy comes from coal and electricity (71 and 12%, respectively). Because of that fractional contribution of BOF off-gas, the emissions related to the production of the BOF off-gas, may be left as part of

steel's GWP, as proposed by [70]; all the results presented in this study use this assumption. Another possibility for counting the GHG emissions related to the diversion of the BOF off-gas from the steel production without modifying the GWP of steel, is assigning the GWP of the extra electricity or coal needed for covering the energy gap left by the BOF off-gas (see a schematic representation of the process-level assignment of GHG emissions to the BOF off-gas Figures SI.4.1.a and SI.4.1.b). The analysis of that possibility is included in the results (section 4.3.1) assuming a GWP of 356 g_{CO2eq}/KWh for coal [340]; the GWP of electric energy is shown below.

- In the HAC case, the emissions related to the production of H_2 and the capture of CO_2 are considered. The production of H_2 considers the contributions of the electrolysis of water and the compression of H_2 (213 g_{CO2eq}/kg_{H2} [40]). The scrubbing of CO_2 includes the contributions of the chemicals used in the process plus the heat and wind-based power (25 g_{CO2eq}/kg_{CO2} [341]).
- In the BBS case, the value 57.5 g_{CO2eq}/kg_{syngas} [30] considers biomass production and local transportation, drying and syngas production. The same value also considers that part of the steam needed by the gasification is produced by heat integration with syngas cooling.

Due to low contributions, the assessments neglects the nutrients and bases (for pH control) in the fermentation, water consumption (since a large reuse stream is used, see line 7 in Figure 4.1), the construction of the electrolyzer and, the distribution of the fuel to the final consumers [30,70,342].

The production of steam and electric energy for the BOF and BBS cases generate 189 and 101 kg_{CO2eq}/GJ [30], respectively. On the HAC case, the electric energy produced by wind turbines generates 2.8 kg_{CO2eq}/GJ [343].

4.2.3.2. Calculation of the ethanol production costs

The EPC include the contributions of both, variable and fixed costs. The EPC are thus the sum of the expenses related to: *i)* the production of the gas feedstock on the HAC and BBS cases, *ii)* the generation of steam and electric energy, and, *iii)* the facility dependent costs. The costs of the utilities and the gas feedstocks are presented in Table 4.3. The production costs of the BOF off-gas are determined using the costs of the equivalent amount of electric energy needed by the production of the sinter in the steel production process; this is the cost of the BOF-gas used for the estimation of all the results presented in this study. However, similar to the assignment of the GWP to the BOF off-gas, the production costs of the gas feedstock depend on what is assumed to be the replacement of the BOF off-gas at the steel production process. Therefore, a discussion is presented

in the results (section 4.3.1) about the consequences of assigning the costs of the equivalent amount (in energetic terms) of coal to the costs of BOF off-gas. The cost of coal is taken as the five-year average of 54 €/ton presented in euracoal.eu.

Table 4.3. Cost data about utilities, raw materials and purchase cost data for processing units based on techno-economic assessments reported in literature

Costs of utilities and raw materials				
Utility / raw material	**Cost, (€)**	**Functional unit**	**Used in case**	**Literature reference**
Steam production	22.30	GJ	BOF, BBS	[30]
Purchase of electric energy from local grid	13.72	GJ	BOF, BBS	[24]
Acquisition of biomass plus the production of syngas	120.35	ton of syngas	BBS	[30]
Wind-based electric energy [a]	4.92	GJ	HAC	[344]
CO_2 scrubbing [b]	37	ton of CO_2	HAC	[184]
Purchase costs of processing units				
Processing unit	**Cost, (€)**	**Year**	**Reference capacity**	**Literature reference**
Ethanol dehydration plant	2.75×10^6	2000	24564 $kg_{ethanol}$/h	[345]
Heat recovery boiler	1.57×10^7	2001	891 kg_{gas}/s	[346]
Alkaline water hydrolysis-based hydrogen production plant	4.40×10^6	2017	90 kg_{H2}/h	[347]
Amine based CO_2 capture plant	1.25×10^8	2012	70.2 kg_{CO2}/s	[184]
Biomass gasification plant [c]	7.22×10^7	2017	51892 kg_{syngas}/h	[30]

[a] For the HAC case, the specific cost related to the production of H_2 is reported as 'gas production costs' because, although the cost item is part of the electric energy costs, the differentiation allows comparing the cost of the gas feedstock with the BOF and BBS cases.

[b] It is assumed that the concentration of CO_2 in the flue gas is 20%v/v.

[c] Purchase costs include the tar reforming unit as part of gas cleaning.

Note: Find the detailed purchase costs estimated for all process equipment and plants for the three gas supply options on Table SI.4.6.

Due to low contributions, the cost accounting neglects the costs related to the nutrients, alkalis and water consumption in the fermentation [30].

The facility dependent costs (FDC) are assumed to represent the 10% of the CAPEX, which is in turn calculated by multiplying the total purchase costs of main industrial equipment by 6.8. The two latter simplifications are assumed based on the results reported in [30]. The purchase costs of the off-gas condensers, flash separation drums and the distillation columns are gathered from Aspen Plus v8.8; the cost of the bioreactor is taken from [30]; the costs of the gas compressors (C1 and C2 in Figure 4.1) are obtained from [195]. The purchase costs of the ethanol dehydration unit, the H_2 and syngas production facilities, as well as the heat recovery boiler that produces steam from the cooling of the gas feedstocks are adapted from reported techno-economic assessments (see Table 4.3). All the purchase costs are corrected for capacity and year by using a scaling factor of six-

tenths [193] and adjusted by inflation to 2019 with the chemical engineering plant cost index [348] (see Table SI.4.7), respectively; and lastly, those costs that are found in USD in literature, are converted to a 2019 EUR by multiplying by a factor of 0.885.

4.2.3.3. CO_2 abatement costs

The CAC are considered as the costs of reducing GHG emissions through the production and use of gas fermentation-based ethanol compared to fossil-based gasoline (see equation 10). The GWP of gasoline is assumed as 83.8 g_{CO2eq}/MJ (which considers oil extraction and refinement into gasoline plus its combustion) [349]. The units of CAC are €/ton_{CO2eq}.

$$CAC = \left(\frac{EPC}{GWP_{gasoline} - GWP_{ethanol}}\right)1000 \quad (10)$$

4.2.4. Sensitivity analysis

Due to the non-linear relation between the model's IV's and OV's, a non-parametric method is used for assessing the sensitivity of the EPC, the GWP and CAC to the model IV's. The sensitivity is assessed by the Monte Carlo filtering method [350,351], which consists of, first, a stochastic (Monte Carlo) process simulation using 5000 randomly generated combinations of the eight model IV's for each of the three gas composition cases (the final number of simulations is 15000). The total number of simulations for each case is subsequently divided into two subsets according to a base criterion: belonging to the 10% best performing simulations according to each OV. This subset is called the behavioral subset, while the rest of the simulations form the non-behavioral subset. One behavioral subset is obtained for each OV by choosing the 500 simulations that independently produced the lowest GWP, or EPC, or CAC.

The sensitivity (S) of one OV to each IV is identified by the difference between the distribution of each IV in the behavioral subset ($\bar{B}$) and the distribution of the same IV in the non-behavioral subset (B). The OV's sensitivity to the specific IV is proportional to the difference in those distributions [350,351]. The difference in the distributions is visualized in plots of the empirical cumulative distribution functions (ECDF's) and quantified using the Smirnov's statistical two-sample test [351] (see equation 11), which is based on the estimation of the maximum difference ($d^{B-\bar{B}}$) between the ECDF's of the B and $\bar{B}$ subsets. For comparison between the sensitivities of different IV's, $d^{B-\bar{B}}$ is normalized by dividing it by the difference between the high and the low limits within which, each specific IV was varied (see Table 4.4).

$$d_{IV_i,OV_j}^{B-\bar{B}} = \max(\ |\mathrm{ECDF}(B) - \mathrm{ECDF}(\bar{B})|\ ) \quad (11)$$

The upper and lower limits used for the eight IV's are shown in Table 4.4. The limits are based on information reported in literature; such information is also shown in Table 4.4.

Table 4.4. Variation limits of the IV's

IV	Low limit	High limit	Comments about the selection of the limits
T [°C]	25	67	Range based on the diversity of optimal growth temperatures reported for acetogens [54].
p_t [atm]	0.5	3.5	No comment
f_{Dil} (%vol.) [a]	0	45	The upper limit is based on the data reported for the BOF off-gas and syngas compositions [330,332].
C_{et}^{max} [g/L]	30	120	The upper limit is based on reported data for ethanol production with Saccharomyces cerevisiae [352] (disregarding limitations of currently known bacterial strains).
h_L [m]	8	64	The upper limit is selected considering reported dimensions of air-lift bioreactors [353] (disregarding possible limitations in legislation, construction costs and safety).
f_{k_La} [-]	0.5	2.0	The limits are selected considering that surfactants could reduce the k_La estimated for gas transfer to pure water by 50% [296], and in contrast, the presence of ethanol [291] added to possible effects of granulated biofilms formation [300] might double the value of k_La from the value estimated for gas transfer to pure water.
f_{Ac^-} [-]	0.00	0.15	The limits are selected considering that the highest reported selectivities for ethanol lay between 85 and 95% [72,73].
v_{SG}^c [m/s]	0.04	0.30	The lower and upper limits are chosen considering the on-set of the heterogeneous bubbling regime [234] and the maximum value for the gas hold-up in bubble columns [85], respectively.

[a] The dilution of the feed was not applied to the HAC case because it is assumed that the gas feed composition could be finely adjusted from the pure H_2 and CO_2 streams.

4.2.5. Process optimizations

The process optimizations simultaneously minimize two objective functions, the GWP and the EPC; the decision variables are the model's IV's. The GWP and the EPC are often conflicting indicators, therefore, the optimization ends in the construction of Pareto frontiers. To identify potential environmental and economic gains of future developments on strain modifications for higher selectivity and tolerance to ethanol, as well as a more delicate control of the gas feedstock dilution, the multi-objective optimizations are organized into two steps. The first step consists of finding an 'ideal' set of IV's for each process configuration; in this step, the optimization is constrained by the IV's lower and upper limits, as shown in Table 4.4. The second step on the other hand, considers that f_{Dil} will not be lower than 15% (a common dilution of syngas and BOF off-gas [330,332]),

f_{Ac^-} is fixed at 0.05 (a selectivity claimed by LanzaTech on their reactors [354]), C_{et}^{max} will not be higher than 50 g/L (the maximum ever reported for a gas fermentation [126]) and mass transfer coefficients will not surpass those estimated for transfer into pure water by more than 50% (f_{k_La} < 1.5, possibly attained with a 50 g/L ethanol solution [297]). The second step finds more 'realistic' solutions. Lastly, since it has been recently suggested that ethanol inhibits the consumption of the electron donors [108], an inhibition term is added to the kinetic equation for electron donor uptake (see equation 12) to perform the optimizations under the 'realistic' conditions. The inhibition constant ($K_{I,et}$) equals 500 mM (value estimated with a thermodynamic-metabolic model currently under construction).

$$q_D = q_D^{max}\left(\frac{C_D}{K_D + C_D}\right)\left(\frac{1}{1 + \frac{C_{et}}{K_{I,et}}}\right) \tag{12}$$

The calculation is performed by an elitist genetic algorithm implemented into the function 'gamultiobj' in MatLab R2017b. According the software documentation, the function is a variant of the 'non dominated sorting genetic algorithm II' (NSGA-II) [355] which has previously been used for optimizing operation parameters of mechanical machines [356].

4.3. Results and Discussion

This section starts with a description of the general distributions of the GWP, the EPC and the CAC obtained from the stochastic simulations of the three proposed process configurations. The latter assessment is followed by the sensitivity analysis using the Monte Carlo filtering method and ends with an elaboration on the results from the multi-objective optimizations.

4.3.1. Distribution trends in the performance indicators

Figure 4.3 shows boxplots with the distributions of the GWP, the EPC and the CAC for the three process configurations. The boxplots show the median values of the indicators, as well as the 5th, 25th, 75th and the 95th percentiles of their distributions. The trends obtained for the three process configurations are used to compare their performances between each configuration and with data reported in literature for second generation ethanol and for fossil-based ethanol and gasoline.

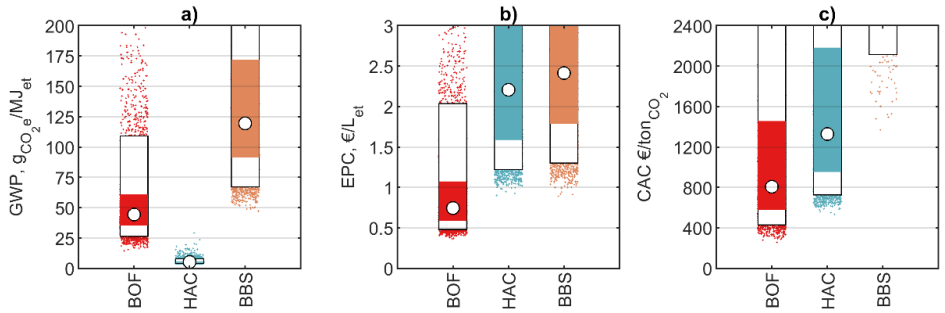

Figure 4.3. Distribution of the a) global warming potential, b) ethanol production costs and c) the relative CO_2 abatement costs from the stochastic simulations. On the boxplots: the colored vertical rectangles represent the extension of the 25th and 75th percentiles; the white vertical rectangles represent the extension of the 5th and 95th percentiles; the small colored dots represent the outliers; and the white circles represent the median values. The CAC plot was created neglecting the negative values obtained for the cases where the GWP was higher than that for fossil-based gasoline.

The results suggest that the ethanol produced from BOF off-gas and the H_2/CO_2 mixture has high probabilities of improving the GHG emissions related to the fossil-based ethanol [223] and gasoline [349] (GWP of 138 and 83.3 g_{CO2eq}/MJ, respectively). Ethanol produced from syngas has lower probabilities compared to the BOF and the HAC cases. However, only the BOF off-gas fermentation has a 25% probability of achieving production costs that are competitive with second generation ethanol (0.51 €/L [336]). In the BOF case, the EPC may even be lower (reaching a median of 0.45 €/L) if the production costs of the BOF off-gas were taken as the costs of the equivalent amount of coal needed by steel production to fill the gap left by diverting the BOF off-gas to the fermentation.

The large amounts of sensible heat available for integration in the BOF off-gas, added to the absence of gas production facilities, led this process configuration to achieve the lowest EPC of three process configurations (see Figure 4.4.b). Additionally, the base-case consideration that the carbon content in the BOF off-gas represents credits for the production of ethanol leaves the GWP of the process dependent only on the emissions generated by the consumption of the electric energy and the steam that is not be covered by heat integration. These two indicators altogether lead to the lowest CO_2 abatement costs of the three cases, becoming the only case with significant probabilities of competing with the CAC of second and first generation ethanol, 584 and 332 €/ton [338], respectively.

If alternatively, the GWP assigned to the BOF off-gas was taken as that of the extra energy inputs required to fill the energy gap left by the off-gas in the steel production process,

the final GWP of ethanol would be much higher than that estimated with the use of credits, *i.e.*, the ethanol GWP will reach median values of 498 and 914 g_{CO2eq}/MJ_{et} if the extra energy at steel production came from coal or electricity, respectively. This result suggests that the environmental impacts linked to ethanol produced from the BOF off-gas heavily depends on the modifications made at the steel production process. A potential feasible solution may be achieved by using a renewable and low-carbon source of electricity for steel production, for instance wind, which would bring the GWP of ethanol to a median of 53 g_{CO2eq}/MJ_{et}.

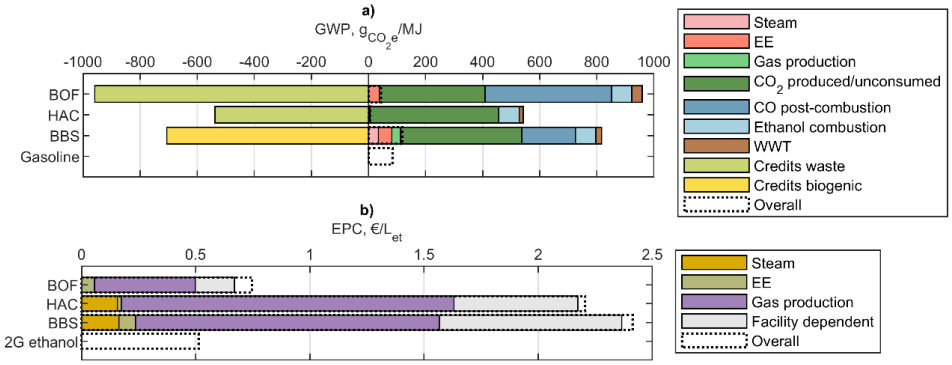

Figure 4.4. Median values of the itemized contributions for a) GWP and b) EPC for the three process configurations. Gasoline is given a GWP equal to 83.3 g_{CO2eq}/MJ, while 2G ethanol production costs are taken as 0.51 €/L [336].

The GWP and the EPC of the HAC case receive a similar benefit from the use of waste CO_2 compared to the BOF case *i.e.*, the GHG emissions are reduced by the use of credits; a similar result would be produced if the CO_2 was biogenic. However, the HAC case produced higher EPC's than the BOF case due to the costly production of H_2 and the capture of CO_2.

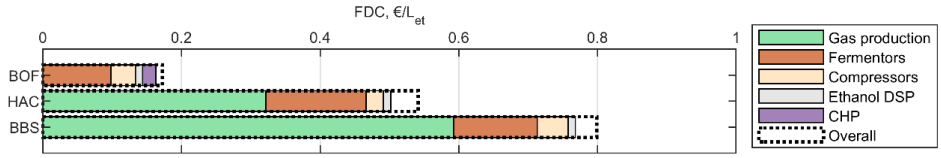

Figure 4.5. Median values of the itemized contributions to the facility dependent costs (FDC) of the three process configurations

The fermentation of the bio-based syngas produced the least promising results of the three considered process configurations. This result is derived mainly from the large costs of the gasification facilities (see Figure 4.5), which are also relatively expensive to operate

(see Figure 4.4) for producing a gas feedstock whose energy integration capabilities are limited by the temperature (lower than the BOF off-gas) and the steam requirements of the gasification process itself. If instead, bio-syngas was purchased as a utility, within a large industrial complex that benefits from the economy-of-scale, the EPC may be considerably lower than in Figure 4.4; an analysis of this possibility is shown in section 4.3.3.3.

Altogether, the BOF and the BBS cases have a similar cost distribution between fixed and variable costs as 2G ethanol production, where 30% corresponds to fixed costs and 70% to variable costs [337]. The gas production costs have a particularly large contribution on the HAC case, where it sums up 66% of the total EPC, while the fixed costs represent 25% of the EPC. The economic burden of the facility dependent costs would also be lower if the ethanol production throughput was larger (taking advantage of the economy-of-scale) than the 220 kton/y assumed in this study.

Moreover, it has been previously argued that ethanol produced from BOF off-gas and BBS fermentations would have GWP's of 31 and 12 $g_{CO2eq}/MJ_{ethanol}$, respectively [70]. Since no details are given in that study about the bioreactor configuration, ethanol yields, production of cells, acetate co-production or on GHG emissions during the gasification of lignocellulosic biomass, it is therefore not possible to draw comparisons with the present study from that technical perspective. However, the GHG emissions accounting in that study gives credits to the energy savings due to the heat integration with the combustion of biogas produced by the wastewater treatment process. If those specific GHG emissions credits were applied in the present study, the GWP of the BOF off-gas and the H_2/CO_2 cases would have had negative values within their distributions. That result could have been misleading since negative GHG emissions, or CO_2 sequestration, have only been acknowledged for the creation of grasslands, forests and geological formations, as well as for the use of enhanced agriculture management and the injection of CO_2 into the oceans in the form of carbonates [15]. Therefore, it may be presumed that if the GHG emission credits due to heat integration were not counted in [70], their results would have been comparable with the ones obtained in this study. That comparison may be used for further validating the accuracy of the estimations made by the gas fermentation model presented in [324].

Furthermore, since the end use of the produced ethanol is combustion, the GHG emissions from the process where the BOF off-gas is generated (steel manufacture) are not mitigated by ethanol production. The energy contained in the gas may instead receive a better use when producing ethanol than when producing electric energy after being combusted. If the ultimate use of the gas was powering electric vehicles, then the gas-to-wheel efficiencies may be used as comparison basis to determine if the production of

ethanol as fuel is worth the effort. For comparison, the analysis includes the HAC and BBS cases as well. The gas-to-fuel efficiency (η_{G-F} in equation 13) due to ethanol production can be as high as 56, 84 and 69% for the BOF, the HAC and the BBS cases, respectively; the latter efficiencies may represent an improvement from corn ethanol and may be competitive with cellulosic ethanol, butanol and Fischer-Tropsch-based diesel [357]. After ethanol is used in a hybrid electric vehicle (fuel-to-wheel efficiency of 31% [357]), the gas-to-wheel efficiencies become at most 17, 26 and 22% for the BOF, the HAC and the BBS cases, respectively. On the other hand, if the BOF off-gas and the syngas were instead used to produce electricity and then that electricity was used to power the vehicles, the gas-to-wheel efficiencies will be 24% (electricity production from gas combustion efficiency is 35% [70] while the energy efficiency of electric cars is 68% [357]), which is higher than that obtained by using the ethanol from the BOF off-gas and from syngas. A similar result is obtained if the H_2 was instead used directly by fuel-cell vehicles where the gas-to-wheel efficiency may reach 30%. Thus, the use of ethanol produced from the HAC case may lead to higher gas-to-wheel efficiencies than using electric cars powered by energy derived from the combustion of BOF off-gas and syngas, but it may not improve that efficiency of directly using H_2 in fuel-cell vehicles. However, the perceived risks on the transportation and storage of H_2 [358], traditional safety concerns about using H_2 in passenger vehicles [359], despite the development of new and safe technologies [360], could undermine its widespread use in the near future and give opportunities to ethanol instead.

$$\eta_{G-F} = \frac{NCV_{et}Q_{et}}{NCV_{gas\ feed}Q_{gas\ feed}}100\% \qquad (13)^{c}$$

4.3.2. Sensitivity analysis by the Monte Carlo filtering method

The Monte Carlo filtering method is applied to qualitatively assess the sensitivity of the global warming potential GWP, the EPC and the CAC to the model IV's. From the normalized maximum differences between the empirical cumulative distribution functions (ECDF) of the each IV in the behavioral and the non-behavioral Monte Carlo subsets, the level of sensitivity of the model OV's is classified into three categories: high, medium and low sensitivities, assumed when the normalized $d^{B-\bar{B}}$ > 0.30, when 0.29 > $d^{B-\bar{B}}$ > 0.16 and when $d^{B-\bar{B}}$ < 0.15, respectively. Table 4.5 shows the results of this classification, while Figure SI.4.2 shows the ECDF plots.

[c] NCV_{et} and $NCV_{gas\ feed}$ are the net calorific values of ethanol (1230 kJ/mol [28]) and the gas mixtures (284 and 242 kJ/mol of CO and H_2, respectively [28]), Q_{et} is the ethanol production rate in the bioreactor, and $Q_{gas\ feed}$ is the molar flow rate of CO and H_2 at the bioreactor gas inlet.

Table 4.5. Classification of sensitivity of the process performance indicators to each IV for the three process configurations

OV	Gas supply option	IV							
		T	p_t	f_{Dil}	C_{et}^{max}	h_L	f_{k_La}	f_{Ac^-}	ν_{sG}^c
GWP	BOF	0.41	0.25	0.42	-0.07	0.07	-0.41	0.26	0.24
	HAC	0.18	-0.23	n/a	-0.36	0.13	-0.17	0.77	0.09
	BBS	0.16	0.10	0.38	-0.17	-0.22	-0.32	0.52	0.33
EPC	BOF	0.10	0.12	0.34	-0.06	-0.50	-0.55	0.38	0.12
	HAC	-0.23	-0.21	n/a	-0.13	-0.37	-0.40	0.42	0.29
	BBS	-0.24	0.08	0.53	-0.07	-0.38	-0.36	0.34	0.29
CAC	BOF	0.07	0.05	0.05	-0.04	-0.04	-0.05	0.07	0.06
	HAC	-0.23	-0.21	n/a	-0.13	-0.36	-0.40	0.42	0.29
	BBS	0.10	0.07	0.40	-0.16	-0.28	-0.33	0.49	0.30

Note: The intensity of the blue color in the cells represents the level of the absolute sensitivity; the darker tones represent higher sensitivities while the lighter tones represent lower sensitivities. The signs + and - indicate whether the IV increases or decreases the value of the OV, respectively.

The following sections trace the causes of the resulting sensitivities of the model OV's to each IV, for the three gas supply options. Special attention is given to the effects of the estimated sensitivities on actual process development challenges.

4.3.2.1. Sensitivity of the global warming potential

The potential for energy integration of the different gas feedstocks determines the sensitivity of the GWP to the different IV's. Since the temperature and pressure of the gas feedstocks are different for the three process configurations, the GWP shows different sensitivity trends for the three gas-feed options. What can be generalized for the HAC and BBS cases is that the GWP directly depends on the IV's that influence the energy requirements of the gas compression and the distillation of ethanol, the two major requirements in the overall process. The shocks of the increases in energy requirements for the fermentation of the BOF off-gas are, differently than for the other gas feedstocks, buffered by the large amounts of energy available for integration in the gas feedstock. This feature of the BOF off-gas may be exceptionally beneficial since it causes a low sensitivity of the GWP to low ethanol concentrations and to low mass transfer coefficients, which in practice represent two relevant technological challenges of gas fermentations [122,307].

The power requirements for ethanol distillation are increased either when ethanol accumulations are low in the bioreactor or when most of the ethanol is withdrawn along

the liquid outflow. The co-production of acetic acid demands a large outflow rate from the bioreactor to avoid its accumulation; similarly, temperature exponentially rises the rates of microbial substrate consumption (see equation SI.4.4), which produces faster growth, and consequently demands higher liquid outflow rates from the bioreactor. Therefore, the GWP shows medium to high sensitivities to the T and the f_{Ac^-} for the three process configurations. The effect of increasing acetic acid co-production is particularly detrimental for the HAC case where biomass production rate is low, as well as the liquid outflow needed to withdraw the cells from the bioreactor; when f_{Ac^-} increases, the liquid outflow and the energy demands from the distillation increase largely (see Figures SI.4.7 –SI.4.9) due to a low concentration of ethanol in the bioreactor.

Increased temperatures may nevertheless be feasible if the biomass withdrawal from the bioreactor was decoupled from the fermentation broth outflow using unit operations such as filtration and centrifugation or other solutions like retaining cells within granular biofilms [279,299]. However, such solutions may only be feasible for fermentations of CO-rich gases because as the T increases, the threshold concentrations of CO, H_2 and CO_2 increase as well (see Figure SI.4.11). Considering that the threshold for H_2 is two orders of magnitude higher than that for CO, the thermodynamic feasibility of the catabolism of H_2 may represent a limitation for achieving high U_S with H_2-rich gases, since the partial pressures of the electron donors will be low at the top of the bioreactor.

Moreover, the power employed for gas compression will fall with lower gas flow rates to the bioreactor; that is the case when the mass transfer coefficients are high. Contrarily, increased top reactor pressures, liquid column heights and superficial gas velocities would, in general, involve higher energy demands for gas compression. However, the characteristics of the gas feedstocks cause the appearance of exceptions to the higher energy demands for gas compression, an effect that for instance, would be completely avoided if the gas feedstock was produced at high pressures, as in the HAC case; for that reason, the GWP of the HAC will fully benefit from the improvements on the ethanol productivity induced by the increased liquid column heights and top bioreactor pressures.

In the BOF case, the increases in the liquid column height would raise the GWP because the improved productivity ends in a reduced demand for gas inflow to the bioreactor, cutting the heat integration potential of this gas feedstock.

Moreover, the dilution of the gas feed will cause a drop on ethanol productivity in the bioreactor (see Figure SI.4.6) and therefore, although the absolute energy requirements remain unaffected when productivity falls, the requirements relative to ethanol produced increase with dilution (see Figure SI.4.9), and so does the GWP for the BOF and BBS cases.

The GWP in the HAC case is not affected because dilution is not considered an option because the gas feed composition can be finely adjusted.

4.3.2.2. Sensitivity of the ethanol production costs

The EPC in the three process configurations have a highly negative sensitivity to the IV's that influence the ethanol productivity in the bioreactor, variables that directly determine the number of bioreactors needed to achieve the desired ethanol throughput (see Figure SI.4.5.b). Thus, the EPC in the three process configurations is greatly reduced by increases in f_{k_La} and h_L; contrarily the EPC will expand by increases in the f_{Dil} and in the f_{Ac^-}.

One exceptional case is the effect of v_{sG}^c on the EPC. While increases in the v_{sG}^c will raise R_{et} (see Figure SI.4.6.a) and will therefore reduce the fixed costs related to the bioreactors (see Figure SI.4.5.b), it will also cause an increase on the size of the gas compressors (see Figure SI.4.5.c), ultimately rising the overall FDC. These effects of increasing v_{sG}^c are further aggravated by the higher costs related to the production of the gas feedstock and the higher energy demand for gas compression (see Figures SI.4.4.c and SI.4.4.d).

4.3.2.3. Sensitivity of the CO_2 abatements costs

Since the CO_2 abatement costs are calculated using the GWP and the EPC, the sensitivities of the latter parameters are partially transferred to the CAC. However, the large sensitivities on the cases where the EPC and the GWP have narrow distributions from the Mote Carlo simulation, are not transferred to the CAC. This is precisely the case for the CAC sensitivity on the H_2/CO_2 fermentation, which receives the sensitivity only from the EPC and not from the GWP, which for this process configuration is exceptionally low.

For the case of the BOF off-gas fermentation, the CAC is not sensitive to any of the IV's; the reason for this result is the generally low GWP values (as in the HAC case), and a cancelling effect produced by the combination between a highly negative with highly positive sensitivity observed for the increases in the liquid column height.

On the BBS case, the CAC is largely sensitive to T because it severely rises the already high value of the GWP, which for a large fraction of the Monte Carlo scenarios is higher than gasoline's GWP, thus making the CAC negative. The CAC's sensitivities for the rest of the IV's are the result of compensatory or additive effects between the sensitivity levels of GWP and EPC. In general, the CAC shows sensitivity to the IV's that affect the energy requirements for distillation and gas compression (p_t and h_L), the bioreactor productivity (f_{Dil}, h_L, f_{k_La} and f_{Ac^-}) and the demand of the gas feedstock (f_{Dil} and v_{sG}^c).

4.3.3. Multi-objective process optimizations

This section describes each optimized process configuration under the 'ideal' and the 'realistic' conditions; the description is made for each process configuration independently. Figure 4.6 and Figure 4.7 show the specific values of the IV's and OV's obtained for each optimized case, respectively.

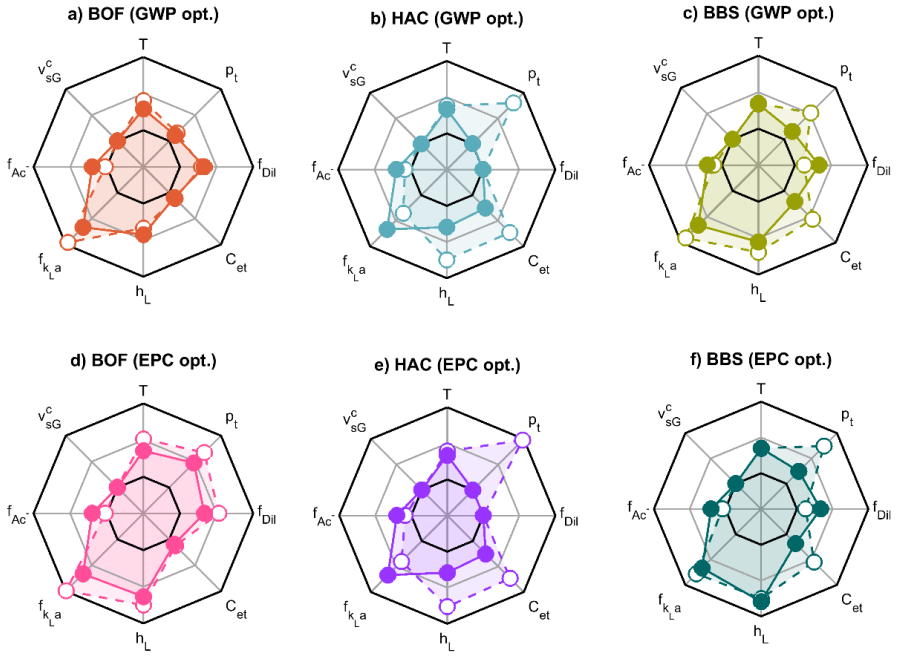

Figure 4.6. Combinations of IV's describing each optimized process configuration: a), b) and c) correspond to the BOF off-gas, H_2/CO_2 and the BBS cases, respectively, where the GWP is at the Pareto optimal; d), e) and f) correspond to the BOF off-gas, H_2/CO_2 and the BBS cases, respectively, where the EPC is at the Pareto optimal. The white and the fully colored circles represent the data for the optimized cases under the 'ideal' and the 'real' conditions, respectively.

4.3.3.1. The optimized BOF case

In general, the simultaneous optimization of the EPC and the GWP applied to the fermentation of BOF off-gas produced a system that minimizes the gas production costs and the facility dependent costs. The gas production costs are minimized by the maximization of gas utilization (U_S), while guaranteeing that the overall process steam requirements are covered by the heat integration with the minimized gas feedstock inflow to the bioreactor. The EPC is maximized only on the cases where the bioreactor productivity (R_{et}) is maximized. The higher R_{et} is translated to lower FDC, but it also

generates a higher demand of electric energy for the compression of higher gas flow rates, thus raising the GWP. This trend of the configuration of the Pareto frontier is seen in the optimizations under the 'ideal' and the 'realistic' conditions (see Figure 4.7.a and d).

As shown in Figure 4.6.a and d, the optimization under 'ideal' conditions favors the energy integration to compensate the higher steam demands caused by the higher ethanol productivities at the bioreactor. A gas feed dilution between 14 and 23% balances the energy that can be recovered from the gas feedstock with the R_{et} improved by a mass transfer coefficient factor at 2 and a temperature between 40 and 45 °C.

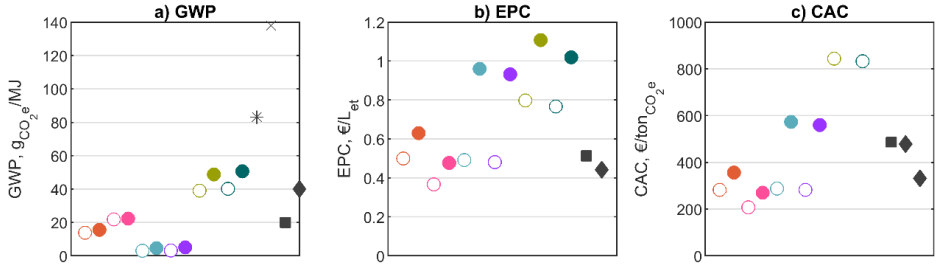

Figure 4.7. Pareto optimal OV's for each process configuration: a) global warming potential, b) ethanol production costs and c) the CO2 abatement costs. The white and the fully colored circles represent the data for the optimized cases under the 'ideal' and the 'real' conditions, respectively. The asterisk represents the GWP of fossil-based gasoline whereas the black squares and the black diamonds represent the performance of 2G and 1G ethanol, respectively. In the plots showing the IV's values, the black colored outer and inner radial axes represent the highest and the lowest values of the IV's as shown in Table 4.4. The specific data used to construct the plots is shown in Table SI.4.5 at the SI.

The Pareto frontier is formed by a balance between R_{et} and the steam requirements from the distillation of ethanol. In the bioreactor, there is a direct relation between R_{et} and the amount of ethanol that exits the bioreactor along the liquid outflow and consequently, the relationship extends to the steam requirements from the distillation. The top bioreactor pressure, the gas feed dilution and the height of the liquid column define the Pareto frontier *i.e.*, the p_t, the f_{Dil} and the h_L are at 0.9 atm, 14% and 33 m, respectively when the GWP is minimum, whereas p_t, the f_{Dil} and the h_L fall in 2.5 atm, 23% and 63 m, respectively when the EPC is minimum. For both configurations, the ethanol concentration in the bioreactor does not overpass 32 g/L; on the GWP Pareto optimum, due to the low pressure and on the EPC Pareto optimum, due to the high gas outflow rate from the bioreactor caused by the larger dilution of the gas feed. Overall, the two points (GWP, EPC) forming the 'ideal' Pareto frontier are (13.8, 0.50) and (21.9, 0.37) in units g_{CO2eq}/MJ_{et} and €/L_{et}, respectively (see Figure 4.7).

In the optimization under the 'realistic' conditions, R_{et} is highly affected by ethanol inhibition, however, this process configuration takes the advantage of the low contribution of the facility dependent costs to the overall EPC of the BOF case. One consequence of the reduced R_{et} is the reduced demand for gas feedstock, which contributes to keeping low costs related to the gas supply; other minor consequences are the reduced energy demand for gas compression and for the distillation of ethanol. Overall, the EPC climbs to 0.48 €/L_{et} in its Pareto optimum (see Figure 4.7.a).

The above mentioned 'realistic' EPC makes the BOF off-gas, the most economically attractive gas feedstock of the three considered in this study. However, the generation of the BOF off-gas in the world is limited by the steel throughput; approximately 217x10^9 L of ethanol could be produced per year if the BOF off-gas from all the steel production plants in the world was used (assuming that *i)* all these plants use the basic oxygen furnaces, *ii)* 65 m^3 of BOF off-gas is generated per ton of steel [330], *iii)* 0.5 m^3 of BOF off-gas is required per L of ethanol and considering that 1808 Mton of steel are produced in one year [361]). Such yearly production is equivalent to the 228% of the 2014 global production of ethanol [336] and is also equivalent to a 13.7% of the global consumption of gasoline and jet fuel during 2018 [362] (the fuel consumption data was corrected with the ratio between the lower heating values of ethanol and gasoline). Therefore, although the use of BOF off-gas to produce ethanol through its fermentation would have CO_2 abatement costs as low as 269 €/ton_{CO2} (see Figure 4.7.c), it would not completely displace the equivalent fossil-based fuels in the transportation sector due to a limitation on the availability of the feedstock.

4.3.3.2. The optimized HAC case

The optimization of EPC in the HAC case was solved for a bioreactor configuration that reduces the excessively high costs related to the production of the gas mixture and to the investment on the H_2 and CO_2 production facilities. Such performance is achieved by simultaneously maximizing R_{et} and U_S up to a point where the concentration of H_2 at the top of the bioreactor does not achieve its thermodynamic threshold. Here, the gas recycling scheme comes in handy because achieving U_S > 50% are not necessary, while it is for the other gas supply options to avoid wasting the valuable gas feedstock. At the same time, the already low GWP is minimized by reducing the energy demands of the distillation and those of the gas outflow compression (for gas recycle). The combinations between the IV's to achieve those performance trends depend on whether the optimization is made under the 'ideal' or the 'realistic' conditions. There are however, two common IV's for all the optimum points *i.e.*, a process temperature between 37 and 40 °C and a low superficial gas velocity between 4.2 and 6.8 m/s. Such T balances the potential gains in productivity with the consequential increases on steam requirements

by the distillation, while v_{sG}^{c} causes an improved gas utilization at low energy requirements for its compression.

The optimization under the 'ideal' conditions achieved an EPC between 0.48 and 0.49 €/L_{et} (see Figure 4.7); that is about 49% lower than the EPC estimated for the 'realistic' conditions. The potential economic gains of further research are thus large in this process configuration. The 'ideal' process conditions that may sustain the low EPC are two: the ethanol concentration of around 93 g/L and a top pressure between 2.9 and 3.4 atm. The high p_t allows the maximization of R_{et} while avoiding reaching H_2 threshold at the top of the bioreactor and takes advantage of the already pressurized gas feedstocks to avoid increases on costs and emissions due to gas compression. The high ethanol concentration, possible thanks to the low acetic acid co-production and the low biomass yield caused by H_2 catabolism, reduces the emissions at the distillation. Last, the optimized mass transfer coefficient factor is close to 1, implying that the ethanol productivity is maximized only by p_t and h_L, while the low f_{k_La} (along with the high p_t) assures that the H_2 threshold is not achieved at the top of the liquid column.

The optimization under 'realistic' conditions suffers from a very low ethanol productivity in the bioreactor (see Table SI.4.5), caused by the inhibitory effect of ethanol, whose concentration is estimated at 45 g/L. The main consequence of the low R_{et} is the doubling of the facility-dependent costs, compared to the 'ideal' optimization. To minimize costs and the GWP, the 30 m high bioreactor operates at a p_t of 0.5 atm to reduce U_S and allow higher gas outflow rates to remove larger amounts of ethanol from the liquid phase. This configuration reduces the burden on the distillation while increasing the energy demand for the compression of the gas recycle. The EPC thus falls between 0.93 and 0.96 €/L_{et} under the described configuration (see Figure 4.7).

To make the ethanol produced from the fermentation of H_2/CO_2 at the 'realistic' conditions able to compete with second generation ethanol (0.51 €/L [336]), large improvements on ethanol productivity may have to be achieved. The optimization suggests that the main objective of these improvements should be mitigating ethanol inhibition.

4.3.3.3. The optimized BBS case

Under the 'ideal' conditions, the bioreactor maximizes U_S by a tall liquid column of 60 m and a low superficial gas velocity of 6 cm/s (see Figure 4.6.c and f); R_{et} is on the other hand, maximized by a low dilution of the gas feedstock and a high mass transfer coefficient (see Figure 4.6.c and f). The Pareto frontier is formed, similar to the BOF case, by a balance between R_{et} and the energy requirements of the distillation. A p_t of 2.7 atm minimizes the EPC to 0.77 €/L_{et}, however, raising the costs related of the distillation. A p_t

of 2.0 atm reduces the load of the distillation columns, minimizing the GWP to 39 g_{CO2eq}/MJ_{et} but compromising the facility-dependent costs due to the reduction on R_{et}.

The severe reduction on productivity caused by the ethanol inhibition and the gas feed dilution in the optimization at 'realistic' conditions, increases the FDC by 50% compared to the optimization under 'ideal' conditions. Overall, a liquid column between 49 and 66 m, plus a superficial gas velocity of 8.5 cm/s aim to reduce the gas inflow rate, thus maintaining low gas production costs and low facility-dependent costs related to gas production. At the same time, the R_{et} reduced by ethanol inhibition and the low p_t (1.0 – 1.2 atm) increases the purchase costs of fermentors, but it also maintains low steam requirements at the distillation.

The EPC and the GWP estimated by the optimization of the BBS process under the 'realistic' conditions are 1.02 $€/L_{et}$ and 48.8 g_{CO2eq}/MJ (see Figure 4.7). With such performance, the ethanol may not be competitive with second generation ethanol unless further optimizations are made on the biomass supply chain and the gas production process, by far the major contributors to EPC. For instance, ethanol from BBS fermentation may compete with 2G ethanol if *i)* the syngas production costs were lowered by 60% to 0.51 $€/kg_{BBS}$ and *ii)* the investment for the gasification plant were also lowered 60% from what is reported in Table 4.3.

Lastly, using the results from the optimization at the 'realistic' conditions, the improvements derived from using wind energy and if the bio-syngas was purchased as a utility inside a large industrial complex (FDC cost of the gasification plant are passed as a 10% increase in the syngas production costs) are: *i)* a 25% reduction of the EPC to 0.76 $€/L_{et}$, *ii)* a 98% reduction of the GWP to 1.1 g_{CO2eq}/MJ_{et} and, *iii)* a 70% reduction on the CAC to 435 $€/ton_{CO2}$. These results bring the fermentation of BBS in line with the fermentation of H_2/CO_2 and suggest that the implementation of this process at industrial scale still depends on the overcoming of technological challenges delivered by the fermentation.

4.4. Conclusions

The analysis performed led to the acknowledgement that the selection of the gas production process is of paramount importance on the economic and environmental performances of the overall ethanol production process and its potential for replacing fossil-based transportation fuels and for competing with ethanol produced through other renewable pathways.

The fermentation of the steel manufacturing off-gas is the most economically robust process configuration of the three options analyzed over the main current technological limitations of the gas fermentation stage *i.e.*, low tolerance to ethanol, co-production of acetic acid and low mass transfer rates. Such robustness is given by *i)* the temperature at which the gas is generated, which allows the coverage of all the energy requirements for ethanol distillation, and *ii)* the low cost assigned to its production, which corresponds to the cost of replacing the energy provided by the BOF off-gas flaring in the steel production process. Moreover, the potential of this process configuration to lead the replacement of fossil-based fuels is constrained by the global throughput of steel and the fossil nature of the carbon used for its production.

On the other hand, the fermentation of H_2 produced from the electrolysis of water showed to have the lowest emissions of greenhouse gases, yet at prohibitive costs. Such environmental performance is the result of the fact that all energy of this process configuration is derived from low-carbon and renewable wind. In addition, the production of ethanol by this process configuration may improve the energy efficiency of using electricity to power passenger vehicles. The potential for this process configuration to lead the replacement of fossil-based fuels may depend on *i)* the development of less costly H_2 production technologies, and *ii)* the development of a microbial strain that tolerates ethanol concentrations above 50 g/L.

The environmental performance of the fermentation of bio-based syngas showed to be the lowest of the three process configurations analyzed. This result may be largely improved by factors external to the fermentation process, if *i)* bio-syngas was made a utility inside a large industrial complex, where harnessing the advantages of the economy-of-scale, the gas production costs are lowered, *ii)* if low-carbon and renewable source of energy was used for bio-syngas production and the fermentation process.

Lastly, even the smallest gains in raising the $k_L a$ inside the gas fermentor would bring significant benefits on the overall process environmental and economic performances; the same can be argued for the gains on increasing the bacterial tolerance to ethanol.

4.5. List of Symbols

BBS	Bio-based syngas	U_S	Gas utilization
BOF	Basic oxygen furnace	$\dot{V}$	Volumetric flow rate
CAC	CO_2 abatement costs	v_{sG}^{c}	Pressure corrected superficial gas velocity
C	Concentration in fermentation broth	y	Molar fraction in gas phase
C^*	Saturation concentration	$Y_{x/CS}$	Biomass yield
F	Molar flow rate	$\Delta G'$	Free Gibbs energy change at physiological conditions
f_{Dil}	Syngas dilution factor		
$f_{k_L a}$	Mass transfer coefficient factor	Subscripts	
f_{Ac^-}	Acetic acid co-production factor	cat	Catabolic

FDC	Facility-dependent costs	D	Electron donor of catabolism *i.e.,* CO, H_2
GHG	Greenhouse gases	et	Ethanol
GWP	Global warming potential	G	Gas
h_L	Height of the liquid column	i	Entering to the syngas fermentor
IV	Model input variable	L	Fermentation broth
k_H	Henry's coefficient	lm	Logarithmic mean
k_La	Gas-liquid mass transfer coefficient	o	Exiting the syngas fermentor
OV	Model output variable	S	Syngas components *i.e.,* CO, H_2, CO_2
p	Absolute pressure	x	Dry microbial biomass
q	Biomass specific production/consumption rate	Superscripts	
		max	Maximum
R	Volumetric productivity	met	Metabolic
T	Fermentation temperature		

Supplementary Information

SI.4.1 Lists of equations used within the bioreactor simulation algorithm

Table SI.4.1 List of equations used within the black-box model of bacterial reactions and the mass transfer model of the bubble column bioreactor (adapted from [324])

Equation	Additional information	# of equation
Black-box model of bacterial reactions		
$\Delta G_r' = \left[\frac{\Delta G_r^0}{298.15} + \Delta H_r^0\left(\frac{1}{T} + \frac{1}{298.15}\right)\right]T + \mathcal{R}T\sum_{j=1}^{m} v_j^r \ln C_j$		SI.4.1
$\Delta G_{dis} = 200 + 18(6-c)^{1.8} + \exp\left[\left(\left(3.8 - \frac{\gamma_{CS}}{c}\right)^2\right)^{0.16}(3.6 + 0.4c)\right]$	**S** / **c** / **γ_{CS} [mol$_{e^-}$/mol]**: CO / 1 / 2; CO_2 / 1 / 0	SI.4.2
$\frac{1}{Y_{x/CS}} = \frac{\Delta G_{dis}'}{\Delta G_{cat}^{0\prime}} + \frac{\gamma_x}{\gamma_D \nu_D^{an}}$		SI.4.3
$q_D^{max} = 3\exp\left[\frac{-69}{\mathcal{R}}\left(\frac{1}{T} + \frac{1}{298.15}\right)\right]\left(\frac{1}{\gamma_D}\right)$		SI.4.4
$q_D = q_D^{max}\left(\frac{C_D}{K_D + C_D}\right)$		SI.4.5
$\nu_j^{met} = \nu_j^{cat}\left(\frac{\Delta G_{dis}}{\Delta G_{cat}^{0\prime}}\right) + \nu_j^{an}\left(\frac{\gamma_x}{\gamma_D \nu_D^{an}}\right)$		SI.4.6
$q_j^{met} = q_D \frac{\nu_j^{met}}{\nu_D^{met}}$		SI.4.7
Mass transfer model of bioreactor		
$\overline{D}_{S,w} = 0.000000074\left[\frac{(2.6MW_w)^{0.5}T}{0.7{M_{V,S}}^{0.6}}\right]$	**S** / **M_V [L/mol]**: CO / 30.7; H_2 / 14.3; CO_2 / 34.0; O_2 / 25.6	SI.4.8
$k_L a_S = f_{k_L a_S} 0.32 {v_{sG}^C}^{0.7}\left[1.022^{(T-293.15)}\right]\left(\frac{\overline{D}_{S,w}}{\overline{D}_{O_2,w}}\right)$		SI.4.9
$p_b = p_t + g\rho_L h_L$	g is the acceleration of gravity (9.8 m/s^2) while ρ_L is the density of the fermentation broth (assumed 1000 kg/m^3)	SI.4.10
$\dot{V}_{G,ml}^0 = \frac{v_{sG}^C}{\left[\frac{\log\left(\frac{p_b}{p_t}\right)}{p_b - p_t}\right]} A_T$	A_T is the cross-sectional area of the bioreactor vessel.	SI.4.11
$p_{ml} = \frac{p_b - p_t}{\ln\left(\frac{p_b}{p_t}\right)}$		SI.4.12
$\dot{V}_{G,ml} = \dot{V}_{G,ml}^0\left(\frac{101325T}{p_{ml}273.15}\right)$	Assuming gas will behave as an ideal gas	SI.4.13
$F_{G,ml} = \frac{\dot{V}_{G,ml} p_{ml}}{1000\mathcal{R}T}$		SI.4.14

Equation	Additional information	# of equation
$k_{H,S} = a_S \exp\left[b_S\left(\frac{1}{T} - \frac{1}{298.15}\right)\right]$	S: CO; a_S [mol/L/atm]: 9.5E-4; b_S [K]: 1300 S: H_2; a_S [mol/L/atm]: 7.8E-4; b_S [K]: 500 S: CO_2; a_S [mol/L/atm]: 3.4E-2; b_S [K]: 2400	SI.4.15
$C^*_{S,t} = p_t y_{S,t} k_{H,S}$		SI.4.16
$C^*_{S,b} = (p_b - p_{mix}) y_{S,b} k_{H,S}$	Values used for $y_{S,b}$ can be seen at Table SI.4.8	SI.4.17
$C_{S,ml} = \frac{C_{S,b} - C_{S,t}}{\ln\left(\frac{C_{S,b}}{C_{S,t}}\right)}$		SI.4.18
$R_{et} = q_{et} C_x$		SI.4.19
$U_S = \frac{y_{D,i} F_{G,i} - y_{D,o} F_{G,o}}{y_{D,i} F_{G,i}}$		SI.4.20

Table SI.4.2 List of mass balance equations and constraints used for convergence of the bioreactor simulation (adapted from Supplementary Information of [324])

Equation	# of equation
Electron donor balance in the liquid phase $0 = k_L a_D (C^*_D - C_D) - q_D C_x - \dot{V}_{L,o} C_D$	SI.4.21
Electron donor balance in the gas phase $0 = F_{G,i} y_{D,i} - F_{G,o} y_{D,o} - k_L a_D (C^*_D - C_D) V_L$	SI.4.22
Overall CO_2 balance (used in CO fermentation) $0 = q_{CO_2} C_x V_L - F_{G,o} y_{CO_2,o} - \dot{V}_{L,o} C_{CO_2,ml}$	SI.4.23
CO_2 balance in the liquid phase (used in H_2/CO_2 fermentation) $0 = k_L a_{CO_2} (C^*_{CO_2} - C_{CO_2}) V_L - q_{CO_2} C_x V_L - \dot{V}_{L,o} C_{CO_2}$	SI.4.24
CO_2 balance in the gas phase (used in H_2/CO_2 fermentation) $0 = F_{G,i} y_{CO_2,i} - F_{G,o} y_{CO_2,o} - k_L a_{CO_2} (C^*_{CO_2} - C_{CO_2}) V_L$	SI.4.25
Overall ethanol balance $0 = q_{et} C_x V_L - F_{G,o} y_{et,o} - \dot{V}_{L,o} C_{et}$	SI.4.26
Overall acetic acid balance $0 = q_{Ac} C_{Ac} V_L - \dot{V}_{L,o} C_{et}$	SI.4.27
Molar fraction summation in off-gas $0 = 1 - y_{D,o} - y_{CO_2,o} - y_{et,o} - y_{w,o}$	SI.4.28
Definition of the mean log molar gas flow rate	SI.4.29
$0 = F_{G,ml} - \frac{\left\lvert F_{G,o} - \frac{F_{G,i}}{1 - \frac{p_{mix}}{p_b}} \right\rvert}{\left\lvert \ln\left(\frac{F_{G,o}}{\frac{F_{G,i}}{1 - \frac{p_{mix}}{p_b}}} \right) \right\rvert}$ Note: The correction $\frac{F_{G,i}}{1 - \frac{p_{mix}}{p_b}}$ was applied to the gas flow rate at the fermentor inlet to account for the amount of evaporated water/ethanol mixture at the bottom of the fermentor	SI.4.30
Overall water mass balance constraint (used in H_2 fermentation)	SI.4.31

$0 > q_w C_x V_L 3600 - F_{G,o} y_{w,o} - \frac{V_{L,o}(1 - C_{et} MW_{et})}{MW_w}$	

Table SI.4.3 List of equations used for calculation of energy requirements (adapted from Supplementary Information of [324])

Equation	Additional information	# of equation
Power for gas compression		
$Y_i = \frac{c_{P_{G,i}}}{c_{V_{G,i}}}$	S: Y_i — CO: 1.4; H_2: 1.4; CO_2: 1.3; Ethanol: 1.13; Water: 1.33	SI.4.32
$Y_o = \frac{c_{P_{G,o}}}{c_{V_{G,o}}}$		SI.4.33
$P_{com,i} = \left(\frac{Y_i}{Y_i - 1}\right) p_1 \dot{V}_{G,i} \left[\left(\frac{p_2}{p_1}\right)^{\left(\frac{Y_i - 1}{Y_i}\right)} - 1\right] \frac{1}{0.7}$	Adiabatic compression and a 70 % mechanical efficiency (η_C) are assumed for the calculations. Off-gas is compressed to 1.15 atm in all cases. p_1 and p_2 represent the inlet and outlet pressures of the compressors, respectively.	SI.4.34
$P_{com,o} = \left(\frac{Y_o}{Y_o - 1}\right) p_1 \dot{V}_{G,o} \left[\left(\frac{p_2}{p_1}\right)^{\left(\frac{Y_o - 1}{Y_o}\right)} - 1\right] \frac{1}{0.7}$		SI.4.35
Power for reactor cooling		
$P_{cool} = \Delta H_{met}^T [k_L a_D (C_D^* - C_D) V_L] + \left(\frac{p_{mix} F_{G,o}}{p_t}\right) \left[\lambda_w^T \left(\frac{y_{w,o}}{y_{w,o} + y_{et,o}}\right) + \lambda_{et}^T \left(\frac{y_{et,o}}{y_{w,o} + y_{et,o}}\right)\right]$	As reactor required cooling in all scenarios, its contribution to the total energy requirements is neglected and its calculation therefore is not reported in the main document. λ_w^T and λ_{et}^T were obtained from Perry's chemical engineer handbook [28].	SI.4.36
$\Delta H_{met}^T = \Delta H_{met}^0 + \int_{298.15}^{T} c_{P_m} dT$		SI.4.37
$c_{P_m} = \sum_{j=1}^{n} \nu_j^{met} c_{P_j}$		SI.4.38
Power for condensation of evaporated water/ethanol mixture		
$P_{cond} = \left[\lambda_w^{-6℃} \left(\frac{y_{w,o}}{y_{w,o} + y_{et,o}}\right) + \lambda_{et}^{-6℃} \left(\frac{y_{et,o}}{y_{w,o} + y_{et,o}}\right)\right] F_{G,o} \left(\frac{p_{mix}}{p_t}\right) \left(\frac{1}{3.7}\right)$	The operation is considered to happen isothermally at -6 °C. Coefficient of Performance of refrigeration is taken as 3.7.	SI.4.39
Power for distillation of ethanol in off-gas condensate		
$P_{dis,G} = 22.194 (100 x_{et}^G)^{-0.794} f_{et}^G$	Equation SI.4.43 was derived from fitting the data reported by Vane, 2008 [295].	SI.4.40
$f_{et}^G = \frac{y_{et,o} F_{G,o} 3600}{q_{et} C_x V_L}$		SI.4.41
$x_{et}^G = \frac{\left(\frac{y_{et,o}}{y_{w,o} + y_{et,o}}\right) MW_{et}}{\left[\left(\frac{y_{et,o}}{y_{w,o} + y_{et,o}}\right) MW_{et} + \left(\frac{y_{w,o}}{y_{w,o} + y_{et,o}}\right) MW_w\right]}$		SI.4.42
Power for distillation of ethanol in fermentation broth		
$P_{dis,L} = 22.194 (100 x_{et}^L)^{-0.794} f_{et}^L$		SI.4.43

Equation	Additional information	# of equation
$f_{et}^{L} = \frac{C_{et} F_{L,o} 3600}{q_{et} C_x V_L}$	Equation SI.4.43 was derived from fitting the data reported by Vane, 2008 [295].	SI.4.44
$x_{et}^{L} = \frac{C_{et} MW_{et}}{1000000}$		SI.4.45

SI.4.2 Process-level assignment of costs and emissions to the BOF off-gas

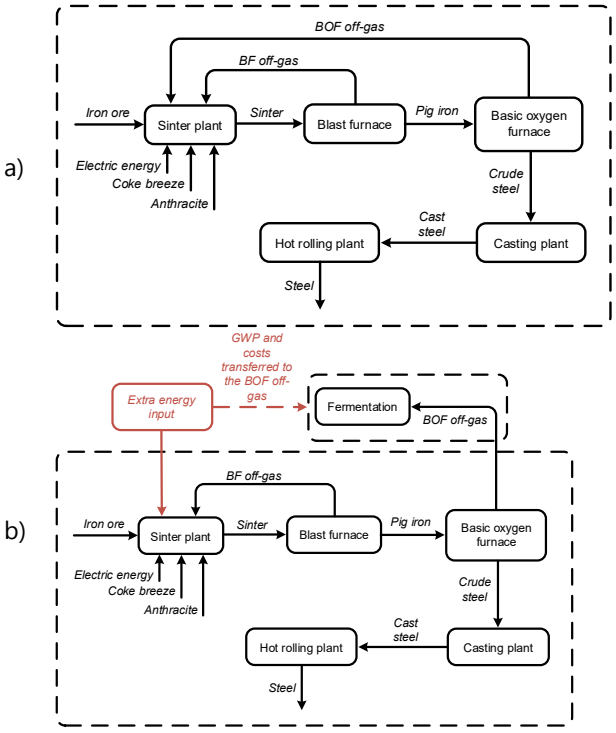

Figure SI.4.1. Schematic representation of a) steel production process and b) steel production process after deviating the BOF off-gas to the fermentation. The construction of the figure was based on the information reported by [339].

SI.4.3 Results from the sensitivity analysis

Figure SI.4.1 shows the empirical cumulative distribution functions (ECDF) of each IV in the behavioral (B) and the non-behavioral ($\bar{B}$) Monte Carlo subsets, for each process performance indicator and for each process configuration.

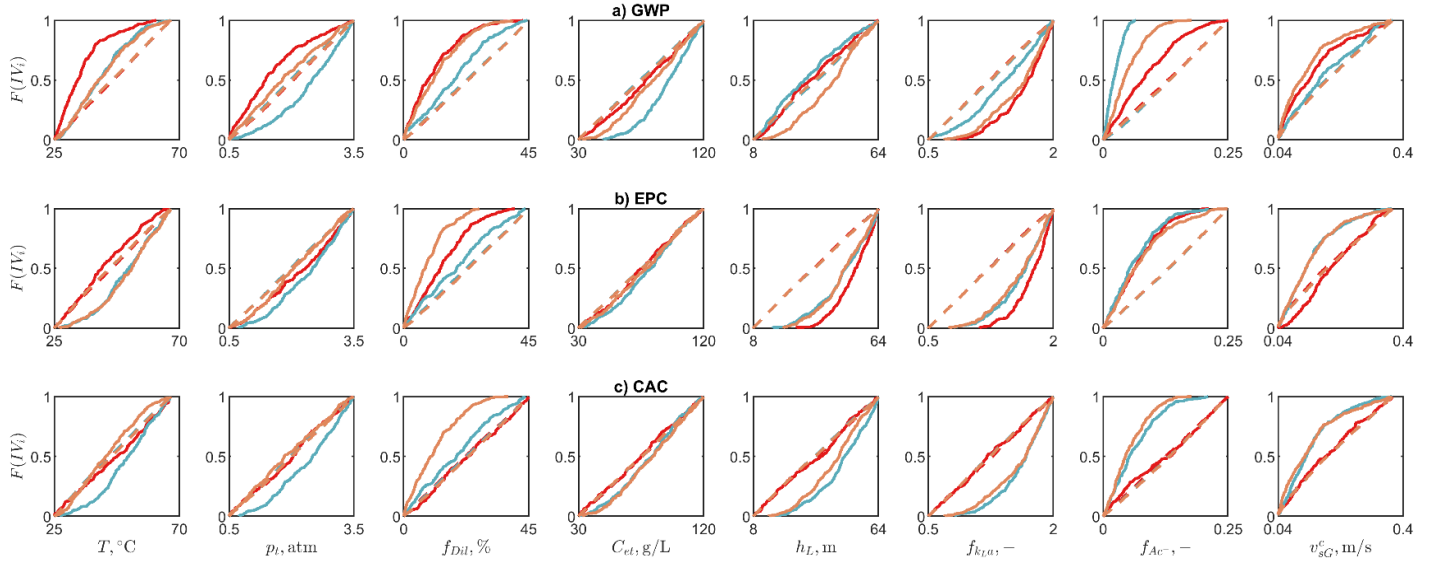

Figure SI.4.2 Difference between the ECDF of each IV on B and $\bar{B}$ for a) the overall global warming potential (GWP), b) the ethanol production costs (EPC) and c) the CO_2 abatement costs (CAC). Continuous lines show the ECDF of the behavioral subsets, while the dashed lines shows the ECDF of the non-behavioral subsets. The color coding used for the different process configurations is the same as that of Figure 4.2 *i.e.*, red for the BOF off-gas, blue for HAC and light orange for the BBS fermentation cases.

The Figures SI.4.3-SI.4.9 show also the empirical cumulative distribution functions of each IP in the behavioral and the non-behavioral Monte Carlo subsets constructed for different components of the GWP, the EPC, and the technical performance indicators of the bioreactors. The same color and line-style coding as in Figure SI.4.1 are used in the mentioned figures.

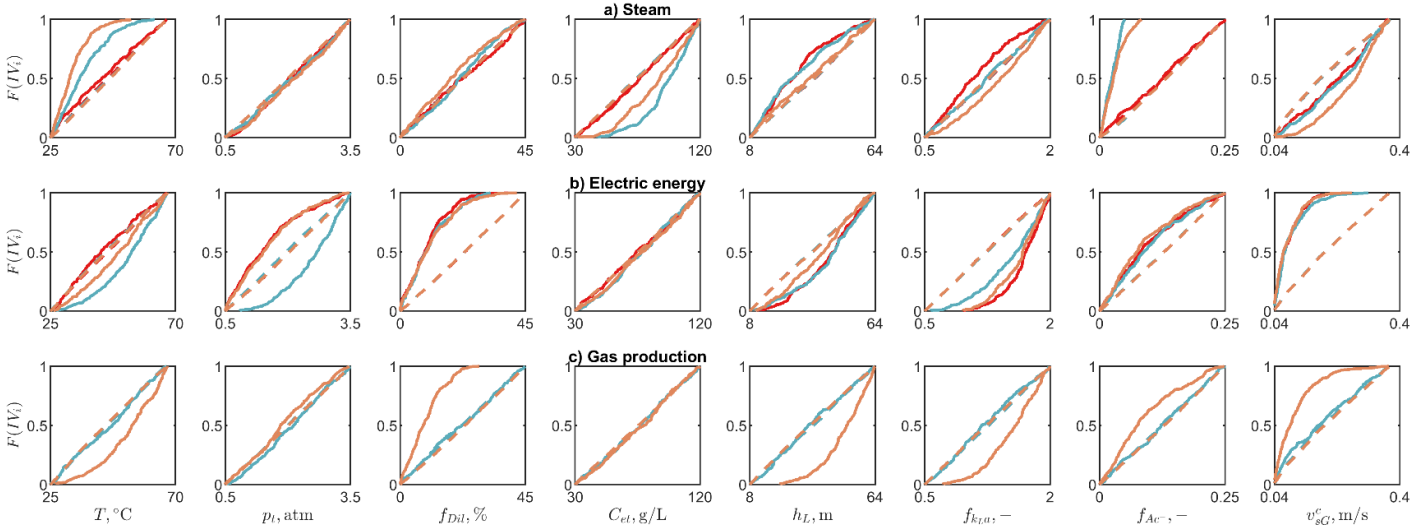

Figure SI.4.3 Difference between the ECDF of each IV on B and $\bar{B}$ for the contributors of the GWP: a) the GWP linked to the production of steam, b) the GWP linked to the production of electric energy and c) the GWP linked to the production of the gas feedstock.

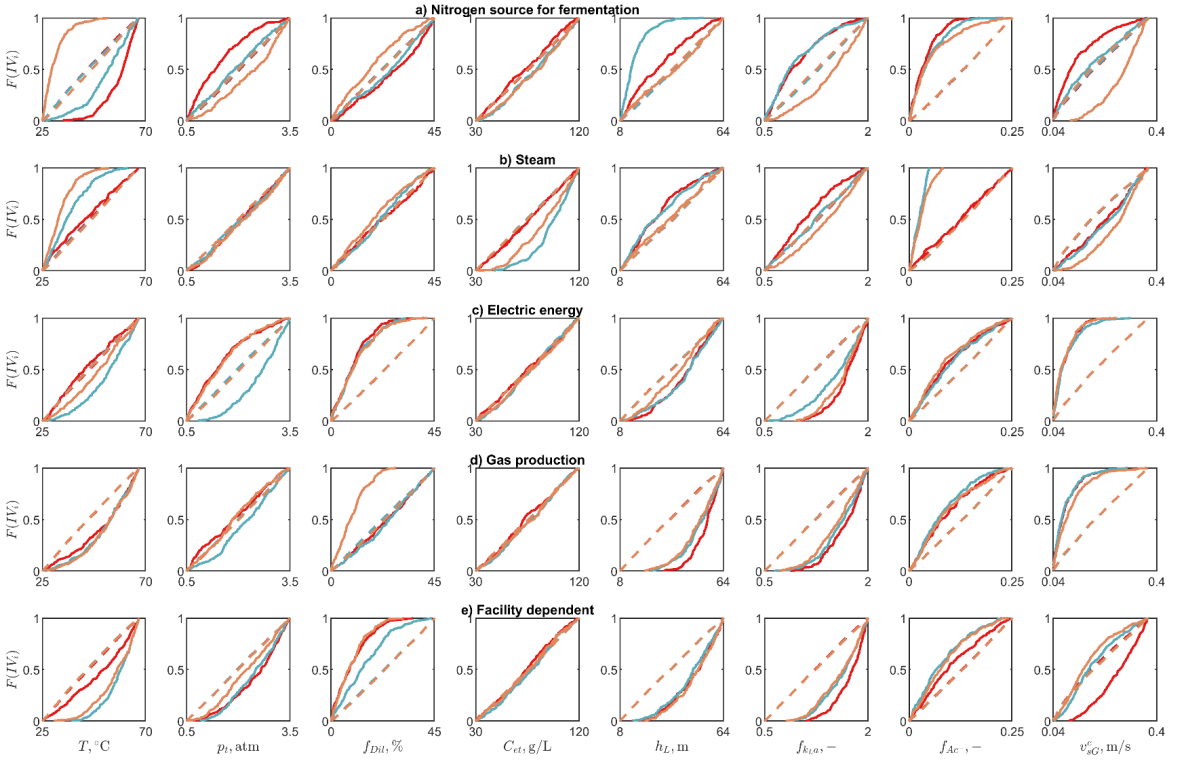

Figure SI.4.4 Difference between the ECDF of each IV on B and $\bar{B}$ for the contributors of the EPC: a) the EPC related to the fermentation nitrogen source, b) the EPC related to the production of steam, c) the EPC related to the production of electric energy, d) the EPC related to the production of the gas feedstock and e) the EPC related to the overall facility dependent costs.

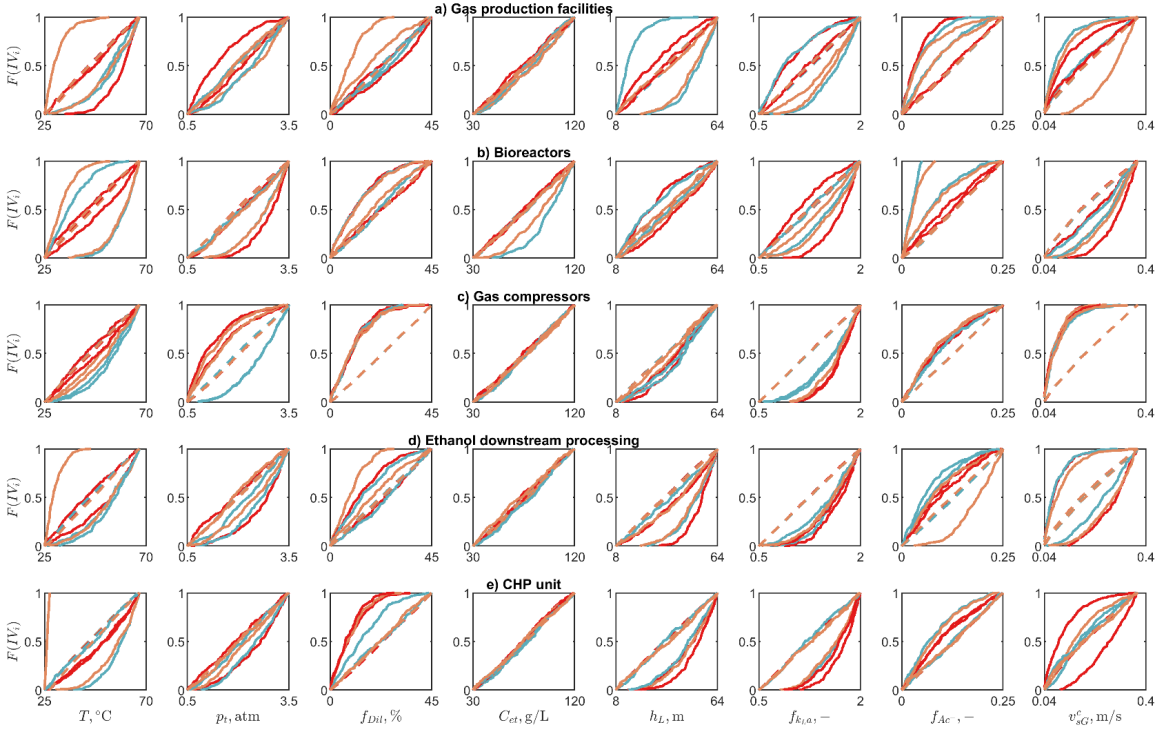

Figure SI.4.5 Difference between the ECDF of each IV on B and $\bar{B}$ for the contributors of the facility dependent costs (FDC): a) the FDC related to the gas production facilities, b) the FDC related to the bioreactors, c) the FDC related to the gas compressors, d) the FDC related to the downstream processing equipment and e) the FDC related to the combined heat and power unit.

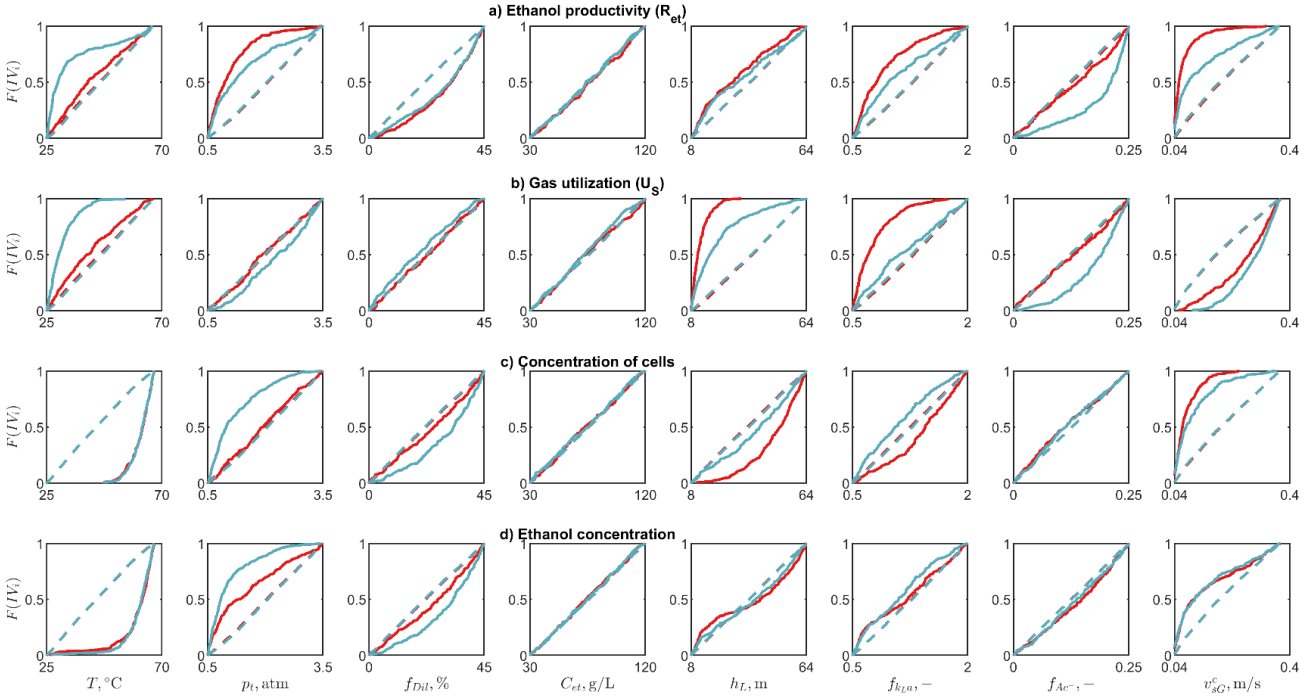

Figure SI.4.6 Difference between the ECDF of each IV on B and $\bar{B}$ for several indicators of the technical performance of the bioreactors: a) the volumetric ethanol productivity, b) the gas utilization, c) the concentration of cells inside the bioreactors and d) the concentration of ethanol inside the bioreactors. Only the results of the CO and the H_2/CO_2 fermentors are shown since the performance syngas fermentor was estimated indirectly (see section 4.2.1.1 in the main chapter content).

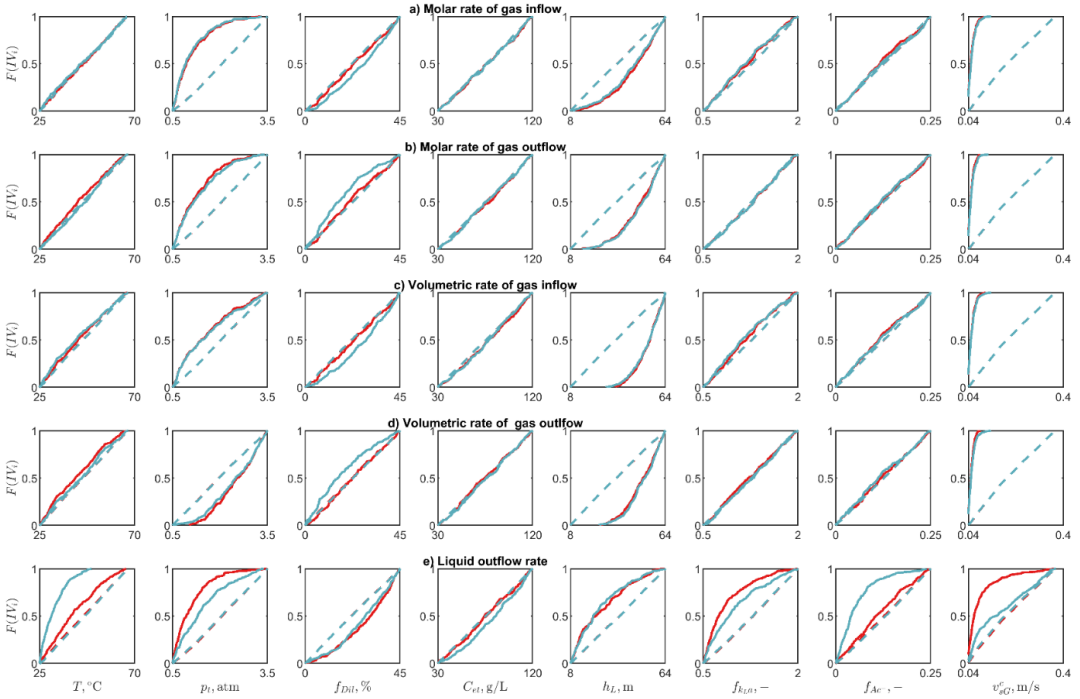

Figure SI.4.7 Difference between the ECDF of each IV on B and $\bar{B}$ for the main gas and liquid streams entering and leaving the bioreactors: a) the molar rate of gas inflow, b) the molar rate of gas outflow, c) the volumetric rate of gas inflow, d) the volumetric rate of gas outflow and e) the volumetric rate of liquid fermentation broth outflow. Only the results of the CO and the H_2/CO_2 fermentors are shown since the performance syngas fermentor was estimated indirectly (see section 4.2.1.1 in the main chapter content).

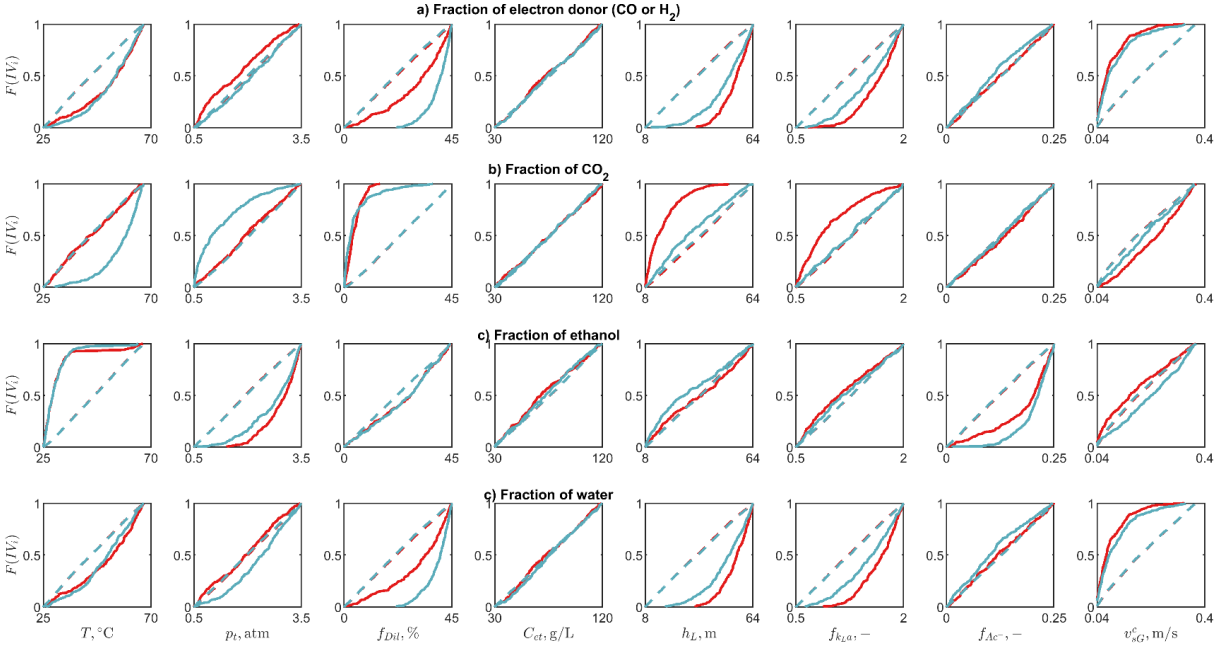

Figure SI.4.8 Difference between the ECDF of each IV on B and $\bar{B}$ for the molar fractions of the main off-gas components: a) the molar fraction of the electron donor (either CO or H_2), b) the molar fraction of CO_2, c) the molar fraction of ethanol and d) the molar fraction of water. Only the results of the CO and the H_2/CO_2 fermentors are shown since the performance syngas fermentor was estimated indirectly (see section 4.2.1.1 in the main chapter content).

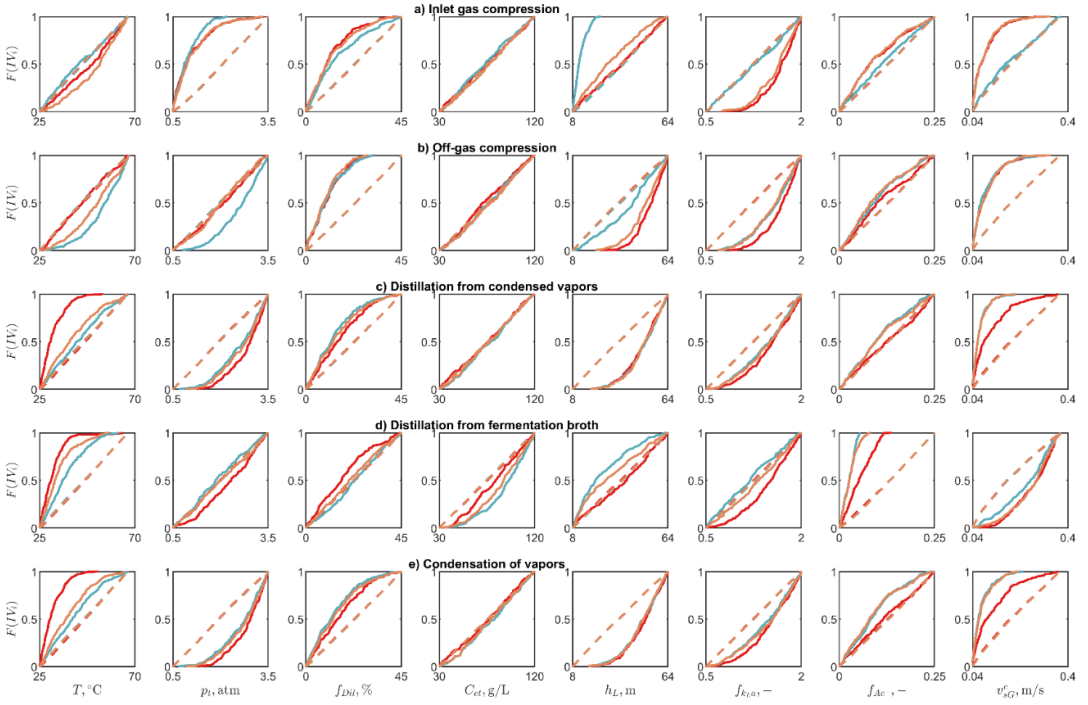

Figure SI.4.9 Difference between the ECDF of each IV on B and $\bar{B}$ for the main contributors to energy inputs of the overall ethanol production process: a) the power required by the compression of the inlet gas, b) the power required by the compression of the bioreactor off-gas, c) the power required by the distillation of ethanol from the condensed vapors, d) the power required by the distillation of ethanol from the fermentation broth and e) the power required by the condensation of vapors. See the median contribution of each of the previous processes to the overall energy requirements in Figure SI.4.8

SI.4.4 Results from the stochastic process simulations

Table SI.4.4. Distribution of the global warming potential, the ethanol production costs and the CO_2 abatement costs after the process stochastic simulations

Process performance Indicator	Gas supply option	Median	Percentiles				Min	Max
			5th	25th	75th	95th		
GWP, g_{CO2eq}/MJ_{et}	BOF	44.6	26.4	35.3	60.9	109.7	14.4	1365.6
	HAC	5.1	3.9	4.5	5.8	7.8	3.6	29.1
	BBS	119.9	67.2	91.7	172.7	319.0	47.3	1081.8
EPC, €/L_{et}	BOF	0.7	0.5	0.6	1.1	2.0	0.4	6.7
	HAC	2.2	1.2	1.6	3.6	8.4	0.9	45.6
	BBS	2.4	1.3	1.8	3.6	6.7	0.9	21.8
CAC, €/ton_{CO2eq}	BOF	807	430	581	1457	6554	259	$32.3x10^5$
	HAC	1328	727	954	2184	5128	534	$0.3x10^5$
	BBS	6536	2112	3647	15957	69459	1369	$137.0x10^5$

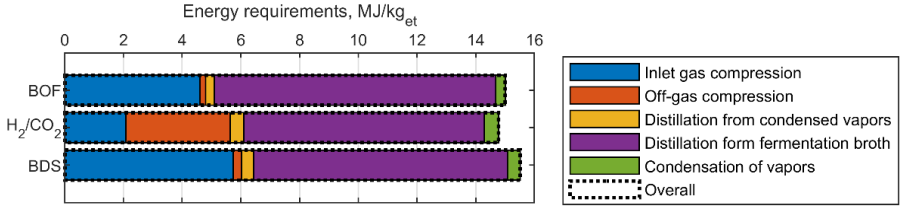

Figure SI.4.10 Composition of energy requirements

SI.4.5 Effects of temperature on the threshold concentrations of CO and H_2

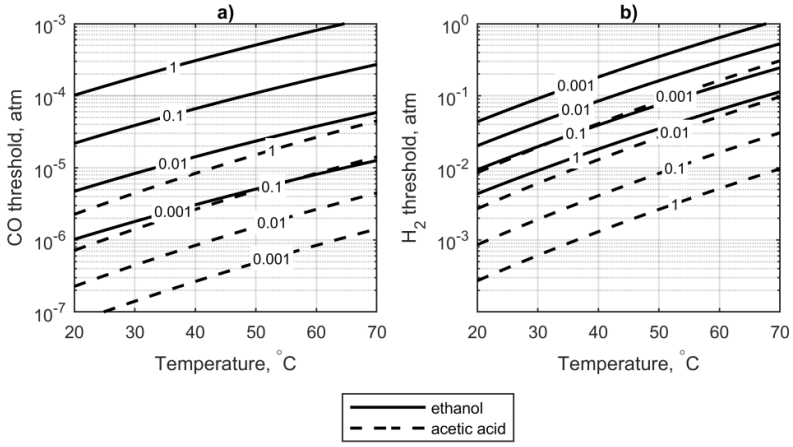

Figure SI.4.11 Variation of CO (a) and H_2 (b) threshold dissolved partial pressures as function of temperature and the CO_2 dissolved partial pressure for catabolic ethanol and acetic acid production. Each line corresponds to a fixed CO_2 dissolved partial pressure whose value is shown in front of each line in atmospheres. Solid lines are used for ethanol production (see equations 1 and 2 in the main document) while dashed lines represent acetic acid production (see equations 3 and 4 in the main chapter content)

SI.4.6 Results from the multi-objective optimizations

SI.4.6.1 Definition of the optimum cases through their IV's and OV's

The following table shows the specific data used to construct the plots shown in Figure 4.6 of the main chapter content.

Table SI.4.5 Combinations of IV's and resulting OV's describing each optimized process configuration

Gas supply option		**BOF**				**H_2/CO_2**				**BBS**			
Optimized case		**min GWP**		**min EPC**		**min GWP**		**min EPC**		**min GWP**		**min EPC**	
		Ideal	**Real**	**Ideal**	**Real**	**Ideal**	**Real**	**Ideal**	**Real**	**Ideal**	**Real**	**Ideal**	**Real**
IV's	T, °C	40.3	34.6	45.9	37.8	39.0	36.7	39.6	36.7	37.4	36.9	37.6	37.4
	p_t, atm	1.0	0.8	2.5	1.9	2.9	0.5	3.4	0.5	2.0	1.0	2.7	1.2
	f_{Dil}, %vol.	13	15	24	15	0	0	0	0	6	15	5	15
	C_{et}^{max}, g/L	31	30	32	29	93	45	93	45	75	41	75	38
	h_L, m	34	40	63	54	62	31	64	30	59	49	63	66
	f_{kLa}, -	1.9	1.5	2.0	1.5	1.0	1.5	1.1	1.5	1.9	1.5	1.7	1.5
	f_{Ac^-}, -	0.01	0.05	0.01	0.05	0.02	0.05	0.02	0.05	0.03	0.05	0.01	0.05
	v_{SG}^{c}, m/s	0.05	0.04	0.14	0.07	0.06	0.04	0.06	0.07	0.06	0.06	0.07	0.06
OV's	R_{et}, g/(L*h)	2.6	1.6	9.6	4.1	6.3	1.2	7.5	1.6	5.9	2.6	7.8	3.4
	U_S, %	63	61	78	67	45	37	46	34	87	78	85	85
	GWP, g_{CO2eq}/MJ_{et}	13.8	15.6	21.9	22.3	3.1	4.6	3.2	5.0	39.1	48.8	40.2	50.7
	EPC, €/L_{et}	0.50	0.63	0.37	0.48	0.49	0.96	0.48	0.93	0.80	1.11	0.77	1.02
	CAC, €/ton_{CO2eq}	282	356	208	270	289	574	282	559	844	1496	833	1458

Table SI.4.6 Detailed total purchase costs of equipment and plants considered part of the process configuration for each gas supply option. The data shown corresponds to the EPC Pareto minimum cases optimized under 'realistic' conditions

Equipment / plant	BOF			HAC			BBS		
	Capacity	Number	Total purchase cost, M€	Capacity	Number	Total purchase cost, M€	Capacity	Number	Total purchase cost, M€
Inlet compressors, kW	10337	2	9.44	n/a	n/a	n/a	8254	2	7.93
Outlet compressors, kW	698	1	0.58	13318	1	5.75	312	1	0.31
Bioreactors, m^3	506	14	53.79	509	34	130.63	511	17	65.31
Off-gas condensers, kW	3680	1	0.04	4028	1	0.04	994	1	0.02
Flash drum, m_{gas}^3/s	25.95	1	0.03	76.04	1	0.03	16.97	1	0.02
Distillation columns, kW	72174	1	0.28	32883	1	0.17	58746	1	0.24
Ethanol dehydration plant, kg_{etOH}/s	7.22	1	4.54	7.22	1	4.54	7.22	1	2.96
Heat recovery boiler, kg_{gas}/s	71.12	1	5.97	n/a	n/a	n/a	n/a	n/a	n/a
H_2 production plant, kg_{H2}/s	n/a	n/a	n/a	2.87	1	91.09	n/a	n/a	n/a
CO_2 capture plant, kg_{CO2}/s	n/a	n/a	n/a	20.90	1	70.47	n/a	n/a	n/a
Syngas production plant, kg_{syngas}/s	n/a	n/a	n/a	n/a	n/a	n/a	35.15	1	148.32

Note: As the reported purchase costs were gathered from techno-economic assessments made in different years, the costs were corrected with the CEPCI index for inflation and brought to year 2019.The CEPCI indexes used are shown in Table SI.4.7

Table SI.4.7 Used Chemical Engineering Plant Costs Indexes

Year	1998	2001	2006	2012	2014	2015	2017	2019
CEPCI	389.5	394.3	500.0	584.6	576.1	560.7	567.0	607.5

SI.4.6.2 Bioreactor performance in optimum cases

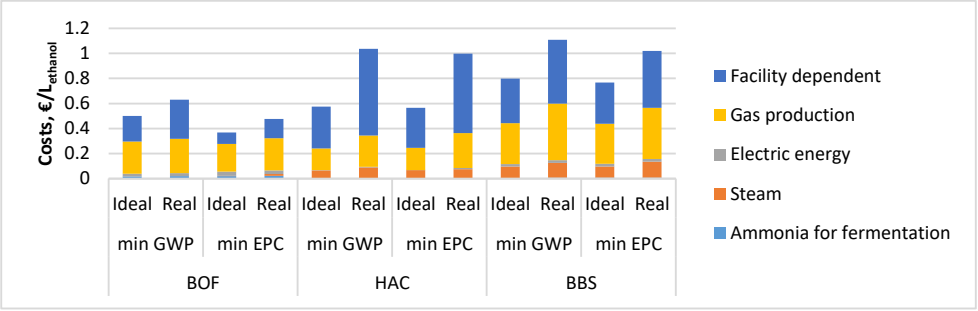

Figure SI.4.12 Composition of the ethanol production costs (EPC) of each optimized process configuration

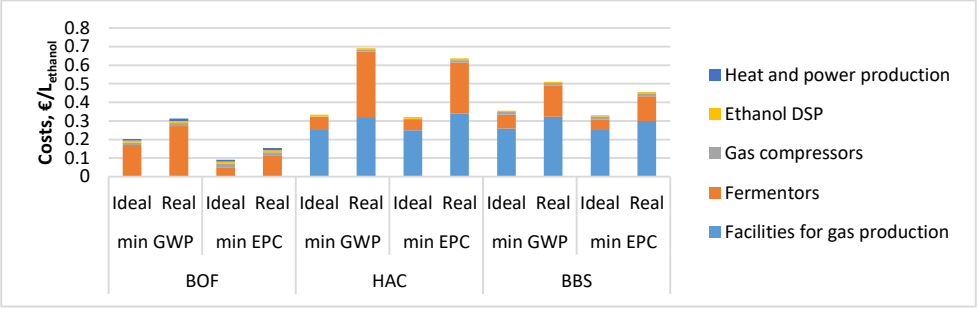

Figure SI.4.13 Composition of the facility dependent costs (FDC) of each optimized process configurations

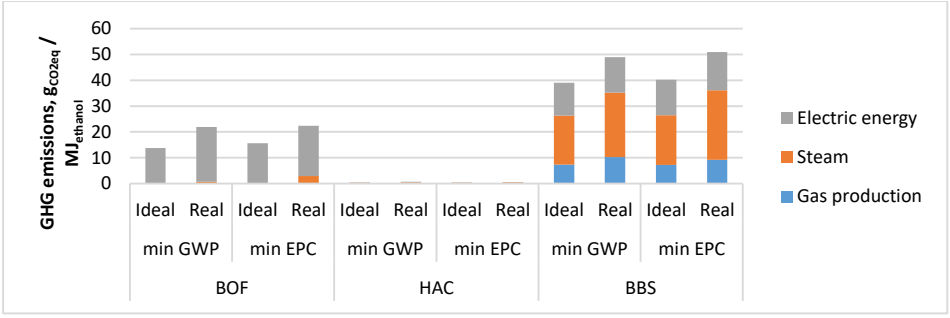

Figure SI.4.14 Composition of the global warming potential (GWP) of each optimized process configuration

SI.4.7 List of symbols

Table SI.4.8 List of the symbols used in this Supplementary Material section

Abbreviations		**Subscripts**	
A_T	Cross-sectional area of bioreactor, m	0	Standard conditions
C	Concentration in fermentation broth, mol/m^3	Ac	Acetic acid
C^*	Saturation concentration, mol/m^3	an	Anabolism
c_P	Heat capacity at constant pressure, kJ/mol/K	b	Fermentor bottom
c_V	Heat capacity at constant volume, kJ/mol/K	cat	Catabolism
$\overline{D}$	Film diffusion coefficient	$cond$	Condensation
f	Factor	$cool$	Cooling of fermentor contents
F	Molar flow rate, mol/s	CS	Carbon source
$\Delta G'$	Gibbs free energy change at physiological conditions, kJ/mol	com	Compression
		dis	Distillation
ΔG^0	Gibbs free energy change at standard conditions, kJ/mol	D	Electron donor of catabolism *i.e.,* CO, H_2
		et	Ethanol
ΔH^0	Standard enthalpy change, kJ/mol	G	Gas
h	Height, m	i	At syngas inlet
K	Half-saturation constant	L	Fermentation broth
k_La	Gas-liquid mass transfer coefficient, s^{-1}	m	Temperature averaged
MW	Molar mass, g/mol	max	Maximum
P	Specific power consumption, kJ/kg$_{ethanol}$	met	Metabolism
p	Absolute pressure, Pa	mix	Water-ethanol mixture at equilibrium with fermentation broth
q	Biomass specific production/consumption rate, mol/Cmol$_x$/h	ml	Logarithmic mean
$\mathcal{R}$	Ideal gas constant, 8.134 m^3*Pa/(mol*K)	o	At syngas outlet
R_{et}	Ethanol volumetric productivity in the bioreactor, mol/(m^3*s)	r	Reaction
		S	Components of fermentable gas, *i.e.,* CO, CO_2, H_2
T	Fermentation temperature, K	t	Fermentor top
U_S	Gas utilization in bioreactor	w	water
V	Volume, m^3	x	Dry microbial biomass
$\dot{V}$	Volumetric flow rate, m^3/s	**Superscripts**	
v_{sG}^c	Pressure-corrected superficial gas velocity, m/s		
x	Mass fraction in ethanol-water mixture	L	At the liquid phase
y	Molar fraction in gas phase	G	At the gas phase
Greek letters			
Υ	Heat capacity ratio		
λ	Latent heat, kJ/mol		
γ	Degree of reduction		
ν_j^r	Stoichiometric coefficient of substance j in reaction r		

Chapter 5

Modeling of syngas fermentation: integration of a Gibbs free energy-constrained black-box model and an ATP-constrained metabolic model

This chapter is the work of Eduardo Almeida Benalcázar, Sef Heijnen, Rubens Maciel Filho, John Posada and Henk Noorman. The study will be submitted to a journal in the future.

"*I don't know karate, but I know ka-razah*
(Yes we do)"

James Brown, *The payback*, 1973

5.1. Summary

This chapter presents the development of two models, a black-box and a metabolic model of the bacterium *Clostridium autoethanogenum*. The models are integrated for the simulation of ethanol, acetic acid and 2,3-butanediol production from the anaerobic fermentation of CO, H_2 and CO_2. Both models are aimed at reproducing common conditions by which ethanol production is favored over that of acetic acid, *i.e.*, low pH, high acetic acid concentration and use of H_2-rich gas mixtures.

Both models are calibrated using reconstructed steady state data gathered from 12 published continuous fermentations with *C. autoethanogenum* employing several ratios of CO and H_2 in the gas feed, several gas mass transfer rates and two dilution rates.

The modeling approach here presented contains three special features, *i)* it integrates black-box and metabolic models, *ii)* it considers cell growth under dual-limiting substrate conditions, where CO and the H_2/CO_2 pair are both limiting substrates, and *iii)* it uses the rates of Gibbs free energy production by metabolism and an ATP balance to derive information about the energy aspects of different intracellular processes, including growth, acetate export and acetic acid diffusion into the cells.

The model is used to *i)* extract design information from previously reported fermentations at pseudo steady state, *ii)* assess the relation between Gibbs free energy production and ATP production, *iii)* identify possible reasons behind the preference of CO and H_2 consumption when both electron donors are present in the gas feed, *iv)* assess the consequences of choosing different mechanisms for the active export of acetate, and *v)* evaluate the presence of a H_2 production and consumption futile cycle.

The integrated model is able to accurately reproduce common experimental observations where ethanol production is favored when pH is low, acetic acid concentration is high, and rate of H_2 uptake is faster than CO uptake.

5.2. Introduction

Acetogens are able to anaerobically convert H_2 and CO_2 into acetate through the Wood-Ljungdahl pathway [51,363], where CO_2 is used *i)* to reductively synthesize acetyl-CoA, *ii)* as the terminal electron acceptor in an energy-conserving process, and *iii)* to synthesize cell material [44]. Acetogens are also able to heterotrophically use several other carbon sources and electron donors (besides CO_2 and H_2) such as C1 compounds (CO, methanol and formate [56–58]), monosaccharides (hexoses and pentoses [47,55]), primary aliphatic alcohols (from C1 to C5 [59,60]), diols [60,61], and carboxylic acids [62] among other

substances [62,364,365]. Acetogens can further use other electron acceptors than CO_2, such as nitrate, protons, sulfate, nitrate and nitrite, fumarate, phenyl acrylates and perchlorate [44,61]. Due to this large metabolic flexibility, acetogens have a great potential for use in industrial applications.

So far, the most commonly researched products of acetogens are acetic acid [366], ethanol [48,67,68], 2,3-butanediol [367] and medium chain length alcohols and organic acids [63–65,368,369]. All these industrial applications aim to use gas mixtures containing CO, H_2 and CO_2 as sole energy and carbon sources. Such gas mixtures can be obtained from industrial off-gas streams and from lignocellulose via gasification [281,314]. For example, LanzaTech is the first company to have developed a successful commercial-scale ethanol production process using an off-gas mixture from the basic oxygen furnace often used in steel mills [370].

The current academic research efforts on gas fermentation are mostly focused on improving the gas/liquid mass transfer [307,321,368,371–373], controlling the selectivity between ethanol and acetic acid [72,75,374,375] and the expansion of the product portfolio of acetogens [376–380].

In literature, it is argued that the overall carbon distribution towards either acetic acid or ethanol production by acetogens could be divided into two different metabolic stages commonly found in ABE (acetone-butanol-ethanol) fermentations by *Clostridia*: acidogenesis and solventogenesis [381,382]. Experiments with batch and continuous fermentations have shown that ethanol production is favored when *i)* the pH is maintained below certain levels, *ii)* acetic acid concentration is kept above a threshold [72,73,75,248,285,383–389], *iii)* there is a sufficient presence of H_2 in the gas composition [74], and *iv)* cells multiply at a low rate [75]. Additionally, it is argued that solventogenesis is not linked to biomass growth (which is relatively fast during acidogenesis [72]) at low partial gas pressures [72,73,390,391] and that it could be induced by pH shifts [230,390,392], heat shocks [392] and increased presence of reducing agents [390]. However, since the reported results are diverse in literature, it is unclear how the combination of these factors influence the selectivity shift from acetate to ethanol, and whether this can be predicted and controlled.

The most commonly reported approaches used to understand the performance of microbial metabolism apply intracellular mass balances; this is the case for 'metabolic balance analysis' (MBA), which has already been applied to syngas fermentation since genome-scale models have been developed for both acetogenic bacteria *C. ljungdahlii* and *C. autoethanogenum* [105,393] among others [109]. In a set of reported experiments, MBA fed by steady state experimental data for syngas consumption and production of metabolites revealed that the enzyme activities and expression levels during acetic acid

production do not vary significantly from what is observed during predominant ethanol production [74,75]; similar result has so far not been published for the production of other products. Under both metabolic conditions (acidogenesis and solventogenesis), the level of expression and activities of key enzymes in the pathways leading to the synthesis of acetic acid and ethanol do not vary significantly [74,75]; this is different than in *Clostridia* performing ABE fermentations [394]. Therefore, it has been suggested that the product selectivity in acetogens could be driven by thermodynamic restrictions based on metabolite concentrations, rather than by enzyme levels based on genetic regulation [76]. One recent report claimed to have integrated thermodynamic restrictions in a stoichiometric genome-scale model for *C. autoethanogenum*, obtaining a good prediction of the biomass growth rate using only the CO uptake rate as input [114]. Lastly, the use of a genome-scale model for predicting the behavior of bacteria inside a large-scale bubble column bioreactor was limited by the lack of a proper link between the extra and the intracellular spaces [84].

However, the contribution of dynamic metabolic control as a driver for the selectivity between acetic acid and ethanol has so far not been assessed. The very large structure of the genome-scale models, which gives MBA a high level of resolution with respect to intracellular reactions, also becomes a limitation for dynamic simulations of metabolism, due to high computer power requirements and limited knowledge on in-vivo kinetic behavior of enzymes [94,395].

As a response to the mentioned practical limitations of genome-scale models, the current study presents an original model based on *i)* energetics and ATP-balancing and *ii)* dual substrate limited kinetics, leading to non-linear relations between net uptake/secretion rates and the intracellular reaction rates. Thus, the model is not only intended to serve as the basis for the development of kinetic metabolic models for *C. autoethanogenum*, but also to gain insights about the energetic regulations in acetogenic bacteria. The model is calibrated using reported experimental data and observations documented in literature at pseudo-steady state in chemostats. The model is here used to assess the influence of the extracellular concentrations of substrates, products and pH on the microbial selectivity for electron donor (CO and H_2) consumption and product (ethanol, acetic acid and 2,3-butanediol) generation. Lastly, the modeling framework here presented may also be extended to metabolic networks including the production of other metabolites such as acids and alcohols of larger chain lengths.

5.3. Model structure and development

The model here presented allows the estimation of the net conversion (uptake/secretion) rates and the fluxes of relevant intracellular metabolic reactions by establishing element and substance conservation constraints at the extra and the intracellular spaces (section 5.3.1). Section 5.3.2 describes the calculation of the Gibbs free energy of two relevant intracellular mechanisms. Section 5.3.3 describes the approach used to calibrate the model.

5.3.1. Structure of the conservation constraints

The model is designed in such a way that the concentrations of substrates and products in the bioreactor are the only variables needed to determine the values of the extra and intracellular rates of reaction. Thus, the approach presented idealizes cells as microbial industrial factories capable of responding to the changes in the extracellular environment (concentrations, pH and temperature) by adjusting their metabolic reaction rates (including growth rate), product assortment and the amount of Gibbs free energy harvested from catabolism (or ATP production). The environment is described specifically through the concentrations of *i)* the dissolved gases CO, H_2, CO_2, *ii)* the catabolic products acetic acid, ethanol and 2,3-butanediol, and *iii)* pH. The element balances are based on the net consumption and secretion reactions, which form the black-box description (section 5.3.1.1); similarly, the intracellular component balances are based on the intracellular reactions, which form the metabolic description (section 5.3.1.2).

All reactions used to construct the model are shown in Appendix A. The numbering of extracellular reactions is labelled as 'o#' while for intracellular reactions it is 'i#'; all the references to the reactions throughout the document use the mentioned format.

5.3.1.1. The black-box description

The black-box description of metabolism allows the calculation of the net consumption and secretion reaction rates based on the concentrations of several substances in the fermentation broth as inputs. The black-box description is formed by lumped catabolic (see reactions o1 – o6, Table A.1, Appendix A) and anabolic reactions (see reactions o7 and o8).

Overall, the black-box description contains 11 compounds, *i.e.*, CO, H_2, CO_2, ethanol, acetic acid, acetate, 2,3-butanediol, biomass ($CH_{1.75}O_{0.5}N_{0.25}$), water, ammonium ions as the nitrogen source and H^+. Their net reaction rates (commonly referred to as q-rates) are constrained by 4 elemental balances (C, H, O and N), plus an electrical charge balance and the pH-dependent equilibrium between acetate and acetic acid. These constraints

are the black-box conservation relations, and all are assembled into the 'black-box (BB) matrix' (see Appendix B). E is constructed according to the methodology outlined in [80]. The system of equations thus has 11 − 6 = 5 degrees of freedom and therefore, kinetic expressions must be specified for 5 q-rates. The remaining 6 q-rates can then be calculated from solving the linear relations based on the BB matrix.

Based on previous works [106,108], two kinetic expressions can be adopted for the uptake of CO and H_2, as modified hyperbolic rate equations (see equations 1 and 2); these equations are further described in section 5.3.1.1.1.

$$q_{co} = q_{CO}^{max}\left(\frac{C_{CO}}{K_{CO} + C_{CO} + \frac{{C_{CO}}^2}{K_I}}\right) \tag{1}$$

$$q_{H_2} = q_{H_2}^{max}\left(\frac{C_{H_2}}{K_{H_2} + C_{H_2}}\right)\left(\frac{1}{1 + \frac{C_{CO}}{K_{I,CO}}}\right) \tag{2}$$

In addition, the calculation of the biomass growth rate can be achieved using a Herbert-Pirt relation applied to the rate of microbial Gibbs energy production (q_G in equation 3). The first term in the equation ($a_G\mu$) represents the energy needed for growth, the second ($b_G r_{HAcD}$) the energy needed for the active export of acetate and H^+ ions needed to balance the passive diffusion of acetic acid into the cell, and the last term (m_G) counts the energy needed for maintenance. The methods used to calculate each of these terms are further introduced in section 5.3.1.1.2.

$$q_G = a_G\mu + b_G r_{HAcD} + m_G \tag{3}$$

The final two kinetic expressions needed to complete the black-box description outline the generation of two of the catabolic products. Such equations have not been previously proposed in literature. The last equations in the black-box description, proposed after numerous trials, relate the production rates of ethanol and 2,3-butanediol to other q-rates rates (see equations 4 and 5). Relating ethanol and 2,3-butanediol production to q_{e^-} and q_C (the rates of electrons and carbon uptake, see equations 6 and 7) implies directly relating the product generation rates, and μ indirectly, to the concentrations of two substrates, CO and H_2. Commonly, single-nutrient-limited conditions are used to relate substrate consumption, product generation and growth. In this study, CO and H_2 are both limiting nutrients, thus bacterial cells grow and produce under what may be called as dual-nutrient-limited conditions; this particular feature makes our approach exceptional and suitable in the field of kinetic modeling of microbial metabolism.

Both equations are explained further in section 5.3.1.1.3.

$$q_{Et} = e^{(a_1 q_{e^-} + b_1 q_C + c_1)} \quad (4)$$

$$q_{BDO} = a_2 q_{Et} \quad (5)$$

$$q_{e^-} = 2\left(q_{CO} + q_{H_2}\right) \quad (6)\ ^{d}$$

$$q_C = q_{CO} + q_{CO_2} \quad (7)\ ^{e}$$

5.3.1.1.1. CO and H_2 uptake

The CO and H_2 uptake equations are constructed based on the models proposed in [106,108]. The equations consider that the uptake rates of CO and H_2 are both inhibited by the concentration of CO in the liquid media. Find all the assumptions that have been made throughout this document conveniently consolidated in Appendix D.

The values for all the kinetic constants in equations 1 and 2 are estimated by adjusting the model to experimental data following the procedure detailed in section 5.3.3.

5.3.1.1.2. Biomass formation according to thermodynamics

The rate of Gibbs free energy production by the metabolism of bacteria (q_G) is considered as the energy needed for growth, maintenance and the uncoupling caused by the passive diffusion of acetic acid; these contributions are described by equation 3. q_G is the result of the multiplication (mathematically, the dot product) among the q-rates (organized within vector q) and the Gibbs free energies of formation under process conditions of each specie present in the black-box description (organized within vector G_j') (see equation 8). The Gibbs free energies of formation are corrected for the process conditions using equation 9; such conditions are: temperature of 310.15 K (correction made using the Gibbs – Helmholtz equation), the extracellular concentrations (C_j, in mol/L) for the dissolved, non-gaseous compounds, the dynamic partial pressures (p_j, in bar) for the dissolved gases and pH (in mol/L). For a compilation of all the symbols used in this document, see the list of symbols in section 5.6.

$$q_G = -q \cdot G_j' \quad (8)$$

[d] Applies if q_{H_2} is negative. If not, q_{H_2} should be zero in the equation.
[e] Applies if q_{CO_2} is negative. If not, q_{CO_2} should be zero in the equation.

$$G_j' = T\left[\frac{\Delta_f G_j^0}{T^0} + \Delta_f H_j^0\left(\frac{1}{T} - \frac{1}{T^0}\right)\right] + RT\ln(C_j) + RT\ln(p_j) \quad (9)$$

In equation 9, $\Delta_f G_j^0$ and $\Delta_f H_j^0$ are respectively the standard Gibbs free energy and enthalpy of formation of substance j, T^0 and T are the standard and process temperatures, respectively and R is the ideal gas constant equal to 0.008314 kJ/(mol*K).

The passive diffusion rate of acetic acid into the cells is described by equation 10, where k_{HAc} is the permeability coefficient, a_x is the molar surface area of cells (383 $m^2/Cmol_x$ [f]) and $C_{HAc,o}$ is the extracellular concentration of the undissociated acid. Equation 10 does not consider the intracellular concentration of acetic acid ($C_{HAc,i}$) since $C_{HAc,o} \gg C_{HAc,i}$ due to the pH gradient.

$$r_{HAcD} = k_{HAc} a_x C_{HAc,o} \quad (10)$$

The coefficient b_G in equation 3 does not need to be estimated because it can be deduced from the mechanism by which the diffused acetic acid is exported back to the extracellular space. Once one molecule of acetic acid diffuses into the cell, due to the neutral intracellular pH, it is split into acetate and one H^+. The acetate has to be exported as well as the H^+; depending on the specific mechanism, the export of acetate might channel none or one H^+ into the cell (for uniport and antiport, respectively). An assessment of the thermodynamic feasibility of different secondary translocation mechanisms for the export of acetate ions from the bacterial cells allowed the identification of uniport and antiport as mechanisms that are possibly used by acetogens. Based on the commonly reported extracellular concentrations of acetic acid, antiport would export acetate using a Gibbs free energy gradient while uniport would power the export using an electrochemical gradient. This assessment is further described in detail in section 5.3.2.1. Therefore, the energy cost of the diffusion of acetic acid would be equal to the energy needed to export the H^+ from the cell using the proton motive force (9.4 kJ/mol_{H+} [112] [g]). One or two H^+ ions would be extruded out if acetate was exported uniport or antiport, costing 9.4 or 18.8 kJ/mol_{HAc}, respectively.

[f] Number obtained assuming that a *C. autoethanogenum* cell is a cylinder that measures 2 µm of height by 1 µm of diameter, has a density of 1.1 g/mL and a molar mass of 25.25 $g_{DM}/Cmol_x$ (DM stands for dry matter). The dimensions are based on microscopic observations of *C. ljungdahlii* cells after an adaption period to CO that lasted 10 days in average. It is also assumed that the cell is composed by 30 % dry matter and 70 % water.

[g] That minimum energy quantum has been calculated by dividing a phosphorylation potential of 31 kJ/mol_{ATP}, reported for the acetogen *A. woodi* growing on CO and a H_2/CO_2 mixture [396], by a H^+/ATP stoichiometric ratio of 3.3 [112], assumed for the membrane based ATP-synthase.

Since the acetic acid diffusion rate is linked to b_G in equation 3, the deduction of b_G allows the estimation of the acetic acid permeability coefficient (see k_{HAc} in equation 8), together with the parameters a_G and m_G in equation 3, following the methodology detailed in section 5.3.3.

5.3.1.1.3. Product generation

Equations 4 and 5 were derived by fitting the model to experimental data reported in literature (see section 5.3.3). Equation 4 proposes that the rate of ethanol production is non-linearly related to the uptake rate of electrons (q_e-) from CO and/or H_2 (only when H_2 is consumed) and to the uptake rate of carbon (q_C) from CO and/or CO_2 (only when CO_2 is consumed). The exponent in equations 4 is used to avoid producing negative values of the ethanol production rate (q_{Et}). Equation 5 relates 2,3-butanediol production to q_{Et}. The kinetic parameters a_1, b_1, c_1 and a_2 are estimated by fitting the equations to experimental data (see section 5.3.3).

With the described equations, the black-box description can be used on its own, independently of any metabolic description.

5.3.1.2. The metabolic description

5.3.1.2.1. Structure of the metabolic description

Inside cells, conservation relations are established for the metabolites that belong to the ramified network harnessing carbon from CO and CO_2, and electrons from CO and H_2 to the three catabolic products and to cell material ($CH_{1.75}O_{0.5}N_{0.25}$). The structure of the metabolic network is schematized in Figure 5.1; the stoichiometry of each reaction is detailed in Table A.2 in Appendix A. The equations for all reactions were based on previous reports [50,53,105,112,363] and constructed such that carbon, hydrogen, nitrogen, oxygen and electrical charge balances close.

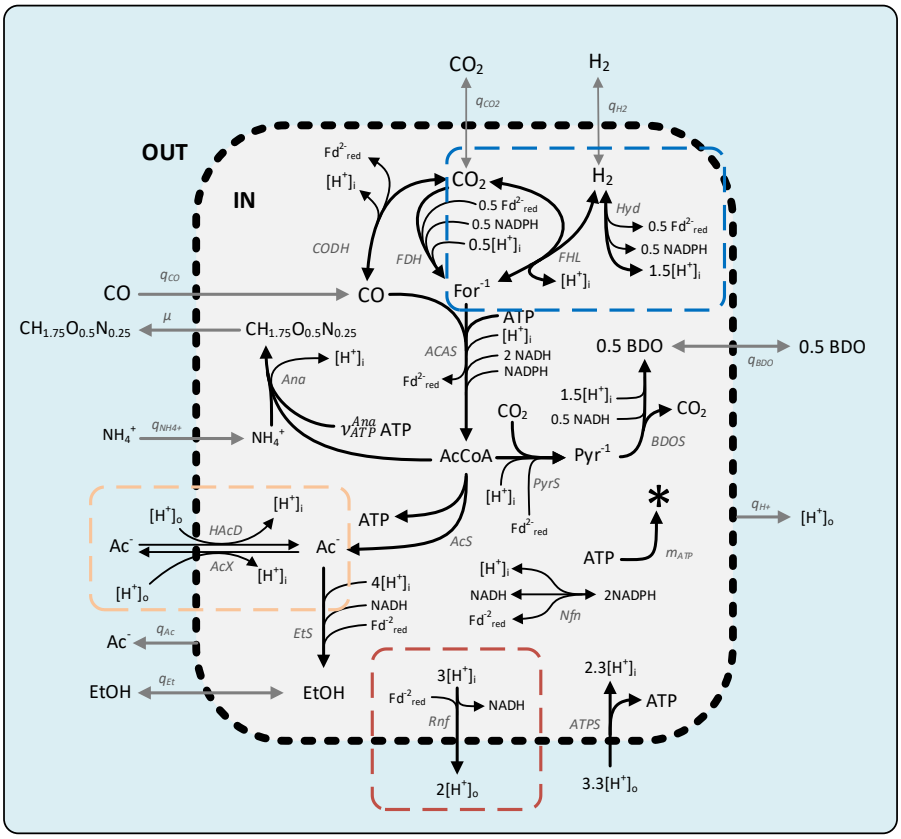

Figure 5.1. Schematic representation of the metabolic network of the acetogens *C. ljungdahlii* and *C. autoethanogenum*. The name of each reaction is shown with italic grey font. The thick dashed line resembles the bacterial membrane. For spacing and visibility concerns, the figure does not include the species NAD^+, $NADP^+$, Fd_{ox}, Pi, ADP, H_2O and H-CoA, although they were considered for the definition of the stoichiometry of each reaction (see Table A.2). The rectangles with dashed lines surrounding several reactions which are relevant to the energetic interactions within the cell; these mechanisms are referenced throughout the text. The figure is based on the stoichiometric information presented by [50,53,105,112,363].

Certain reactions within the metabolic network have been conveniently lumped to simplify the calculation of the intracellular rates of reaction. The lumped reactions are those that lead to the synthesis of acetyl-CoA through the Wood-Ljungdahl pathway (ACAS, reaction i2.a), the route from acetyl-CoA to acetate (AcS, reaction i5.a), the route from acetate to ethanol (EtS, reaction i6) and the route from pyruvate to 2,3-butanediol (BDOS, reaction i8). Anabolism (Ana, reaction i12.a) is also lumped into one reaction that starts off from acetyl-CoA as its carbon supplier.

The metabolic description also includes the reactions Nfn, Rnf and ATPS (reactions i9, i10 and i11.a, respectively), which form the characteristic energy conservation mechanism of acetogens [44]. The Rnf reaction transfers the highly energetic electrons from reduced ferredoxin (Fd_{red}^{2-}) to NADH while extruding H^+ ions (2 mol_{H+}/mol_{Fdred} [53]) to the extracellular space; those H^+ ions are channeled back into the cell by the ATPS reaction to produce ATP (3.3 mol_{H+}/mol_{ATP} [112]), in a process that is essentially ATP synthesis based on the high-energy electrons, a mechanism known as electron transport phosphorylation [71]. The Nfn reaction balances the electrons between the three redox carriers, NADH, NADPH and Fd_{red}^{2-}. Overall, these reactions describe the link between *i)* the electrons contained in NADH, NADPH and Fd_{red}^{2-} from the Wood-Ljungdahl pathway, *ii)* the proton motive force and *iii)* ATP production.

Acetic acid production is considered to be the result of two processes, the active export of acetate and the passive back-diffusion of the undissociated acid into the cell.

The synthesis of one mole of biomass is assumed to require an amount of $Y_{ATP/x}$ moles of ATP. A reaction is also included to take into account the ATP that is spent in un-specified and not-growth-related cellular processes, generalized as maintenance.

In the H_2 uptake region of the network, it is assumed that the electrons in H_2 are harvested by bacteria through a NADPH-dependent hydrogenase (r_{Hyd}, reaction i4). However, the existence of a H_2 futile cycle has been proposed to explain a high expression of the latter enzyme, as well as the presence of a formate hydrogen lyase (r_{FHL}, reaction i16) in *C. autoethanogenum* while growing on pure CO [53]. The characteristics of this cycle are further described in section 5.3.2.2 where the stoichiometric and energetic implications of its presence are further assessed.

The intracellular H^+ is also part of the metabolic description as a non-exchangeable compound, since *i)* it is poorly permeable through the bacterial membrane, *ii)* because cells carefully keep its concentration constant in the intracellular space and *iii)* because it plays a fundamental role in the proton motive force and the production of ATP.

For simplicity, the equilibrium reactions between CO_2 and HCO_3^-, and between acetate and acetic acid have been omitted from the metabolic description.

The information necessary for the construction of the conservation constraints for the metabolic description is contained within the metabolic (A) matrix which, parallel to the BB matrix (see section 5.3.1.1), is also constructed according to the methodology laid out by [80]. The columns and rows in the A matrix contain the reactions and the reacting species, respectively. The A matrix is formed by two parts that subdivide the intracellular reactions in *i)* those of which the rates are specified by the kinetic expressions (A_m), and

ii) the reactions of which the rates are calculated (A_c) from the linear relations specified in A. The A matrix and its parts are shown in Appendix B.

Matrix A_c was subjected to several assessments to prove the independency and consistency of its linear relations [80], as well as to assess whether the rates of the embedded reactions are calculable [397] from the rates present in A_m.

5.3.1.2.1. Solving the metabolic description

The substances that are part of the black-box description are considered the exchangeable compounds in the metabolic description; the intracellular undissociated acetic acid is excluded by the metabolic description because its presence in the intracellular space is minimal compared to that of acetate, due to the neutral intracellular pH. Besides the 11 compounds of the black-box description, the metabolic description includes 9 more, *i.e.*, acetyl-CoA, intracellular acetate, formate, pyruvate, H^+ ions, ATP, NADH, NADPH and Fd_{red}^{2-} as intracellular nodes or non-exchangeable compounds. Therefore, the system of equations contains 26 metabolic reactions and has 26 – 20 = 6 degrees of freedom, the same as the black-box description accommodating the Gibbs free energy balance.

The fluxes of all the reactions considered in the network could be readily determined using the kinetic equations 1, 2, 4 and 5; equation 3 is not necessary because the ATP balance is equivalent to the Gibbs free energy production. Yet, since the metabolic description offers more chances for finding relations between (reaction) rates, we took the advantage and propose here an empirical kinetic expression for estimating q_{AcT} (the measured total dissociated and undissociated acetic acid production rate, see equation 12). Equation 11 shows an expression designed for calculating the rate of acetate export from the cell, which was derived from fitting the model into the experimental data (as described in section 5.3.3). q_{AcT} is then the result of the difference between the rate of export of acetate and the rate of diffusion of the undissociated acetic acid into the cell (r_{HAcD} in equation 12). r_{HAcD} is calculated using equation 10.

$$r_{AcX} = \left(\frac{a_3 q_{CO}}{b_3 + q_{CO}}\right) + \left(\frac{r_{Nfn}}{c_3 + r_{Nfn}}\right) \tag{11}$$

$$q_{AcT} = r_{AcX} - r_{HAcD} \tag{12}$$

Equation 9 proposes that the rate of acetate export is co-related to the uptake rate of electrons from CO and H_2. However, this equation does not use q_{H_2} directly, but indirectly through the rate of the Nfn complex (r_{Nfn}). According to preliminary assessments r_{Nfn} is positive (NADPH production) when CO catabolism is predominant, and on the other

hand, r_{Nfn} becomes negative (NADPH consumption) when H_2 catabolism is predominant. q_{H_2} is not always negative; it can become positive when the gas feed contains only CO [74]. r_{Nfn} then correlates better the influence of q_{H_2} (when it is negative) into the equation.

The use of the ATP balance requires the introduction of a new equation, which strictly referring to known literature on bio-thermodynamics should be equivalent to equation 3. The production of Gibbs free energy is therefore equivalent to a net ATP production rate in the cell (r_{ATP}), which is the sum of the ATP produced by the ATPS and the AcS reactions minus the ATP consumed for the synthesis of acetyl-CoA by the ACAS reaction. This ATP production rate is then available for growth and maintenance. Equations 13 and 14 show the definition of r_{ATP} and the relation between r_{ATP} and equation 3. The coefficient $K_{G,ATP}$ (with units kJ/molATP) in equations 14 and 15 will be the slope of the line expected to describe the relation between q_G and r_{ATP} (equation 15), according to [101].

$$r_{ATP} = r_{AcS} + r_{ATPS} - r_{ACAS} \tag{13}$$

$$r_{ATP} = \frac{a_G}{K_{G,ATP}}\mu + \frac{m_G}{K_{G,ATP}} + \frac{b_G}{K_{G,ATP}} r_{HAcD} \tag{14}$$

$$q_G = K_{G,ATP} r_{ATP} \tag{15}$$

One last set of additional constraints is used for restricting the directions of several intracellular fluxes to only the positive direction, *i.e.*, r_{ACAS}, r_{AcS}, r_{EtS}, r_{PyrS}, r_{BDOS}, r_{Rnf}, r_{ATPS}, $r_{m_{ATP}}$ and r_{Ana}.

Summarizing, Table 5.1 shows the different equations used by the black-box and the metabolic descriptions.

Table 5.1. Summary of the equations used to solve the black-box and the metabolic models

Reaction rate	Black-box description	Metabolic description
CO consumption	Equation 1	Equation 1
H_2 consumption	Equation 2	Equation 2
Biomass growth	Equation 3	Equation 14
Ethanol production	Equation 4	Output of the model
2,3-butanediol production	Equation 5	Equation 5
Acetic acid production	Output of the model	Equation 12
Acetic acid diffusion	Equation 10	Equation 10
Number of calibrated parameters a	13	15

[a] See the complete list of parameters in section 5.3.3.

5.3.2. Structure of the thermodynamic assessment of the acetate export mechanism and the H_2 futile cycle

Acetate and the undissociated form of acetic acid are both part of a futile cycle in which the anion is exported (reaction i13) through active transport, while the undissociated acid passively diffuses back into the cell (reaction i14) due to a large concentration gradient between the extra and intracellular spaces [52,398]. The specific mechanism by which acetate is exported is relevant for measuring the impact of the acetic acid diffusion into the cells, as discussed in section 5.3.1.1.2. Therefore, the identification of the possible export mechanisms is also supported by an assessment of the Gibbs free energy linked to them.

Similarly, as stated in section 5.3.1.2, the existence of a H_2 futile cycle involving the Hyd and the FHL reactions (i4 and i16 in Table A.2, respectively, also enclosed by a rectangle with blue dashed lines in Figure 5.1) has been proposed elsewhere [53]. According to the idealized mechanism, H_2 may be produced by Hyd and consumed by FHL resulting in no or minimal net production of H_2. In those directions both reactions might be endergonic and may be used to avoid reaching overly reduced intracellular states [53]. An experimental finding that supports the existence of this endergonic mechanism is the small traces of H_2 found in the off-gas of a continuous CO fermentation [74]. Additionally, the expression levels of the enzymes catalyzing both reactions have also been found through transcriptomics [399,400] during the consumption of CO-rich and H_2-rich gas. Therefore, the Gibbs free energy of these two reactions is also calculated to support such assumption and assess its possible inclusion into the metabolic model.

The next subsections (5.3.2.1 and 5.3.2.2) describe how the Gibbs free energy of the two mentioned processes is calculated.

5.3.2.1. Active export of acetate ions

The reactions forming this mechanism are shown in Figure 5.1, surrounded by a rectangle with an orange dashed line.

In general, secondary transmembrane export of solutes in most prokaryotes (such as acetogenic bacteria) are electrochemically powered by the sum of *i)* gradients of the chemical potential of the transported solute, *ii)* the electrical potential gradient ($\Delta\psi$, calculated independently with equation 16) and *iii)* the chemical components of the proton motive force [52,71] (see the proton motive force enclosed within a red dashed rectangle in Figure 5.1).

Acetate is a solute that is likely exported through the stated form of active transport since it is electrically charged and thus poorly permeable in the bacterial membrane. Equations

16 and 17 are used to calculate the energy gradient for the acetate translocation reaction, where n represents the number of H^+ ions exported along with the carboxylate. n takes the value of 1, 0 or -1 when the transport mechanism is symport, uniport or antiport, respectively. The energy gradient is equaled to zero because the extra and intracellular concentrations of acetate are assumed to be at electrochemical equilibrium.

$$\Delta\psi = \frac{\Delta_r G_{pmf}}{F} + \frac{nRT\ln(10)\,(pH_i - pH_o)}{F} \tag{16}$$

$$\Delta_r G'_{Ac^-X} = 0 = RT\ln(10)\log\left(\frac{C_{Ac^-,o}}{C_{Ac^-,i}}\right) + nRT\ln(10)\,(pH_i - pH_o) - (n-1)F\Delta\psi \tag{17}$$

In equation 16, $\Delta_r G_{pmf}$ equals –9.4 kJ/mol of H^+ ions [112]; F represents the Faraday constant, 96.5 kC/mol. $C_{Ac^-,o}$ is calculated at pH 5 from the reported measured total concentrations of acetic acid (see data in section 5.3.3).

We assess the intracellular acetate concentrations that would be at equilibrium with the known extracellular concentrations of the anion when cells use symport, uniport or antiport transporters for the export of acetate. These results are presented in section 5.4.4.1.

5.3.2.2. The endergonic H_2 futile production and consumption cycle

The Gibbs free energy related to the H_2 cycle is calculated at physiological conditions using a similar approach as the one followed to calculate q_G. First, the Gibbs free energies of formation of the substances involved in the reactions are assembled into the vectors $G'_{j,Hyd}$ and $G'_{j,FHL}$ for the Hyd and the FHL reactions, respectively. These energies are corrected for physiological conditions using equation 9. Then, these vectors are multiplied by the vectors containing the reaction rates of the substances involved in the two reactions (r_{Hyd} and r_{FHL}). Equation 18 shows how the energy produced by the cycle is calculated.

$$r_{G,H_2\,cycle} = r_{Hyd} \cdot G'_{j,Hyd} + r_{FHL} \cdot G'_{j,FHL} \tag{18}$$

The calculation of $r_{G,H_2\,cycle}$ requires an assumption for the values of the intracellular concentrations of the substances involved. H_2 and CO_2 are assumed to be freely permeable across the cell membrane and thus their concentrations will be the same inside and outside the cells. On the other hand, formate ions, as well as the oxidized and reduced energy carriers participating in the Hyd reaction (ferredoxin and nicotinamide adenine dinucleotide phosphate), are poorly soluble in the membrane. Hence, their

concentrations are obtained from a stochastic minimization of the squared sum of the $\Delta_r G'$ of all intracellular reactions considered in the metabolic network. These concentrations are shown in Table E.3 in Appendix E. The minimization algorithm used the intracellular concentrations of all metabolites in the network as decision variables. More details about the methodology and data used for this calculation are shown in Appendix E.

5.3.3. Model calibration

The calibration of the black-box and the metabolic models is based on the minimization of the mismatch between the calculated and the experimental net conversion rates (q-rates) reported for 12 pseudo-steady states reached by continuous fermentations using 5 different gas compositions, 2 values of μ, 12 different combinations of q_{CO} and q_{H_2}, and one value of pH [74,75,401].

The first step for calibrating the model was preparing the set of experimental data to agree with element conservation relations and mass balances in the bioreactor. The complete procedure for preparing the experimental data is described in Appendix F. Unfortunately, we were unable to perform a reconciliation of the data because the number of equations (constraints) matched the number of calculated variables, among which were the net conversion rates, the concentrations of the dissolved gases in the liquid, the composition of the off-gas and the flow rates of gas and liquid entering and leaving the bioreactor. The reconstructed data and the process conditions used to characterize each experiment are shown in Table 5.2.

The calibration of the black-box model involved the estimation of the constants: q_{CO}^{max}, K_{CO} and K_I from equation 1, $q_{H_2}^{max}$, K_{H_2} and $K_{I,CO}$ from equation 2, a_G and m_G, from equation 3, a_1, b_1 and c_1 from equation 4, a_2 from equation 5 and k_{HAc} from equation 10. Since the term b_G in equation 3 can adopt two different values, depending on the mechanism by which acetate is exported, k_{HAc} can also have two different values depending on the export mechanism.

Besides the previously found constants for equations 1, 2, 3 and 10, the calibration of the metabolic model involved the estimation of the constants: a_3, b_3 and c_3 from equation 11, $K_{G,ATP}$ from equation 14 and $Y_{ATP/x}$ from the ATP requirements for the synthesis of biomass (reaction i12.a in Table A.2). Similar to k_{HAc}, the parameter $K_{G,ATP}$ can also have two different values depending on the acetate export mechanism.

Table 5.2. Relevant process conditions and experimental q-rates of the reports used for fitting the model

Variable/parameter	Case											
	1	**2**	**3**	**4**	**5**	**6**	**7**	**8**	**9**	**10**	**11**	**12**
Source of data	[74]		[75]					[74]		[401]		
Gas phase												
CO/H_2 at feed	100% CO		2.5 (CO-rich syngas)					0.3 (H_2-rich syngas)		0.03 (Low CO)		67% H_2, 23% CO_2
y_{CO}/y_D at feed	1.00		0.71					0.23		0.02		0.00
$F_{G,in}$, mL/min [a]	46.5	46.5	46.5	46.5	46.5	46.5	46.5	46.5	110.0	30.0	30.0	32.0
Liquid phase												
pH [a]	5.0											
C_X, g/L [a]	0.47	1.43	0.45	0.51	1.10	1.32	1.40	0.46	1.45	0.34	0.54	0.18
$C_{AT,o}$, mol/m^3 [a]	35.5	103.0	69.8	77.2	136.8	133.7	131.0	11.8	63.0	83.8	99.5	41.8
C_{et}, mol/m^3 [a]	13.7	82.2	11.5	13.1	62.0	111.7	122.0	97.0	250.0	104.1	210.7	51.3
C_{BDO}, mol/m^3 [a,b]	n.r.	2.6	0.0	0.0	0.43	2.4	2.2	n.r.	n.r.	n.r.	n.r.	n.r.
C_{CO}, mol/m^3 [c]	0.349	0.109	0.306	0.298	0.182	0.094	0.083	0.033	0.002	$1x10^{-10}$	0.009	$2x10^{-10}$
C_{H_2}, mol/m^3 [c]	0.002	0.006	0.092	0.087	0.040	0.039	0.031	0.234	0.233	0.348	0.318	0.405
C_{CO_2}, mol/m^3 [c]	1.09	5.03	5.57	5.69	8.14	10.39	10.72	0.19	0.51	4.17	4.62	5.22
q-rates, in mmol/Cmol$_X$/h [c]												
q_{CO}	-612	-817	-564	-555	-668	-800	-780	-616	-647	-111	-44	0
q_{H_2}	14	14	-355	-350	-347	-322	-323	-979	-857	-3071	-1740	-1422
q_{CO_2}	345	483	133	132	225	337	330	52	100	-1142	-626	-558
μ	42	42	42	42	43	43	43	42	43	43	22	20
q_{Et}	32	65	29	29	64	96	98	234	205	337	222	153
q_{HAc}	20	20	42	41	34	28	26	7	12	68	26	29
q_{Ac^-}	60	58	124	121	101	82	76	20	35	200	76	87
q_{BDO}	0	2	0	0	0	2	2	0	0	0	0	0
$q_{NH_4^+}$	-10	-11	-11	-11	-11	-11	-11	-10	-11	-11	-5	-5
q_{H_2O}	-292	-393	-83	-82	-139	-216	-206	202	126	1501	859	721
q_{H^+}	70	68	134	131	112	93	87	31	46	211	81	92
q_G, kJ/Cmol$_X$/h	25.2	28.8	26.4	25.8	27.6	30.1	28.8	32.0	26.8	41.3	24.5	21.3

[a] As reported in the sources. || [b] The abbreviation n.r. means not reported. || [c] Calculated as explained in Appendix F.

The final forms of equations 1, 2, 3, 4, 5, 10, 11 and 14 were parameterized (one by one and independently to each other) using MatLab's curve fitting toolbox which employs the minimization of squared differences as objective function; the tool provided the correlation coefficients as outputs.

5.4. Results and discussion

The construction of the model involved the systematic assembly of different pieces of conceptual interpretations laid out to summarize the complex responses of microbial metabolism to stimuli provided by the extracellular environment. Some of those pieces were gathered from different literature sources addressing other microorganisms than acetogenic bacteria, while other pieces are proposed in this study. Therefore, it is necessary to start the presentation and discussion of results by addressing *i)* the accuracy and conceptual soundness of the calibrated kinetic expressions; then the discussion focuses on assessing the information delivered individually by these conceptual packages and collectively by the whole assemblies: for *ii)* mass balances and *iii)* the Gibbs free energy balance of catabolism. As part of the assessment of the entire model assembly, we also present a description of the carbon and electron flows in the experimental cases listed in Table 5.2.

5.4.1. Results of the model calibration

This section shows and discusses the calibration results of the kinetic expressions for CO and H_2 uptake, biomass growth and the secretion of products. The resulting values for the calibrated parameters in the equations describing CO and H_2 uptake (equations 1 and 2 respectively), as well as those used calculate the biomass growth rate with the black-box and the metabolic model (from thermodynamics and the ATP balance, equations 3 and 14, respectively) and the production of ethanol, 2,3-butanediol and the export of acetate (equations 4, 5 and 11, respectively) are shown in Table 5.3.

Figure 5.2 shows the comparisons between the experimental q-rates for CO and H_2 uptake, as well as those for the production of biomass, ethanol, 2,3-butanediol and acetic acid, and the rates calculated with the black-box model. Figure 5.3 shows the same comparison but for the q-rates calculated with the metabolic model; the comparisons for q_{CO} and q_{H_2} were not included in Figure 5.3 because they are the same as those shown in Figure 5.2 (Table 5.1 summarizes which equations are used for each model).

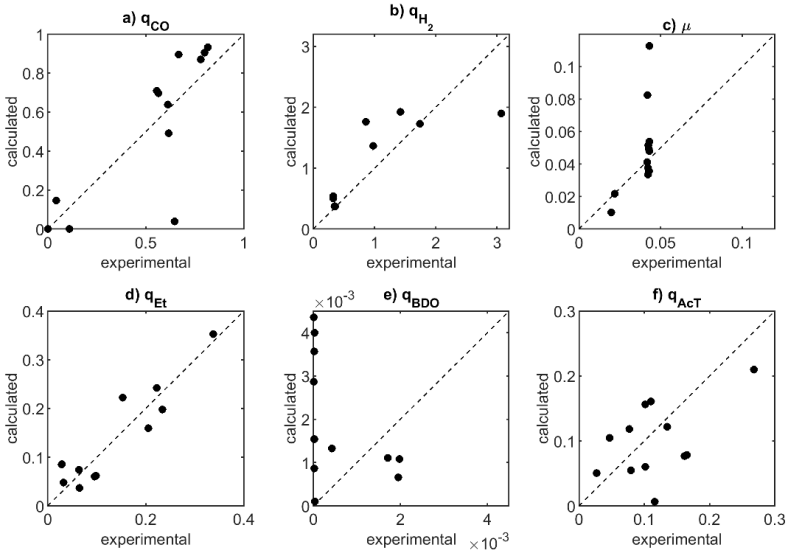

Figure 5.2. Comparison of the experimental q-rates and those calculated with the black-box model: a) equation 1, b) equation 2, c) equation 3, d) equation 4, e) equation 5 and f) an output of the whole model construct.

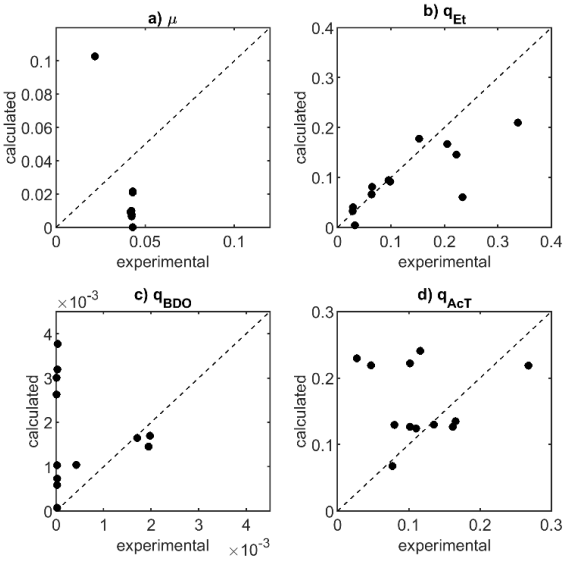

Figure 5.3. Comparison of the experimental q-rates and those calculated with the metabolic model: a) equation 14, b) an output of the whole model, c) equation 5 and d) equations 11 and 12.

Table 5.3. Results for calibrated parameters

Parameter	Units	Calibrated value	Initial guess	Lower bounds	Upper bounds	Used in equation	Used in model
CO uptake							
q_{CO}^{max}	mol/Cmol$_x$/h	-1.459	-4.4 [324]	-10	-0.1	1	Black-box and metabolic
K_{CO}	mol/m^3	0.042	0.012 [108]	0.005 [324]	1		
K_I	mol^2/m^6	0.246	0.1 [106]	0.001	10		
H_2 uptake							
$q_{H_2}^{max}$	mol/Cmol$_x$/h	-2.565	-4.4 [324]	-10	-0.1	2	Black-box and metabolic
K_{H_2}	mol/m^3	0.025	0.675 [108]	0.010	1		
$K_{I,CO}$	mol/m^3	0.025	0.827 [108]	0.001	10		
Biomass growth							
a_G	kJ/Cmol$_x$	170	1000 [263]	0	2000	3	Black-box and metabolic
m_G	kJ/Cmol$_x$/h	16.7	4.5 [263]	0	100		
$K_{G,ATP}$	kJ/mol$_{ATP}$	94.5 [a,c] 169.5 [a,d] 76.4 [a,e] 103.8 [b,c] 215.7 [b,d] 84.2 [b,e]	282 [101]	0	∞	14	Metabolic
$Y_{x/ATP}$	mol$_{ATP}$/Cmol$_x$	1.8 – 2.2 [a] 1.6 – 2.0 [b]	2.52	0	∞	Reaction 12.a in Table A.2	Metabolic
Acetic acid diffusion							
k_{HAc}	m/h	3.86x10^{-5} [a] 1.93x10^{-5} [b]	0	0	∞	10	Black-box and metabolic
Ethanol, 2,3-butanediol production and acetate export							
a_1	-	-0.729	0	-∞	∞	4	Black-box
b_1	-	2.752	0	-∞	∞		
c_1	-	-2.249	0	-∞	∞		
a_2	mol$_{BDO}$/mol$_{Et}$	0.018	0	-∞	∞	5	Black-box
a_3	-	28.65	0	-∞	∞	11	Metabolic
b_3	-	-21.8	0	-∞	∞		
c_3	-	-0.333	0	-∞	∞		

[a] Acetate is exported through uniport.
[b] Acetate is exported through antiport.
[c] Average for cases 1 – 12 (see Figure 5.6).
[d] For cases 1 – 7 only (see Figure 5.6).
[e] For cases 8 – 12 only (see Figure 5.6).

.

5.4.1.1. CO and H_2 uptake

Regarding the CO and H_2 uptake rate equations, the correlation between the equations 1 and 2 with the reconstructed experimental data was good for both cases (see Figure 5.2.a and b). This result comes surprisingly despite the impediment of reconciling the experimental data and the obligation of assuming the value assigned to the mass transfer

coefficient multiplier f_{broth}; as noted in Appendix E, the function of f_{broth} is to correct the mass transfer coefficient, calculated with a model developed for O_2 transfer to pure water, for effects of the actual broth composition and for possible bioreactor configuration differences. f_{broth} is here given a fixed value of 3, however, it is known that the mass transfer coefficient depends on the concentration of ethanol and acetic acid, and most significantly at their concentration ranges between 10 and 100 mol/m^3 [402,403]. Therefore, there is a large uncertainty linked to the calculated values of C_{CO} and C_{H_2}, and larger for the low concentrations which are more sensitive to small changes in q_{CO}, q_{H_2} and f_{broth}.

The estimated values of q_{CO}^{max} and $q_{H_2}^{max}$ suggest that the total electron uptake capacity of these microorganism is 7.37 $mol_{e^-}/Cmol_x/h$, a value 16% lower than a previous calculation [324]. Considering that the previous calculation used an equation based on a space limitation of the enzymes that collect the electrons from several substrates at the membrane of *E. coli* [233], our result suggests that such limitation may also be applicable for the acetogens that have the enzymes CO-dehydrogenase and the NADPH-Fd-specific hydrogenase dissolved in the cytoplasm.

The estimated value of the CO half-saturation constant (K_{CO}) is one order of magnitude higher than that suggested by thermodynamics [324] and similar to the value estimated by [108] using data from batch fermentations (see Table 5.3). As for K_{H_2}, the value estimated here is similar to the one suggested by thermodynamics [324] and one order of magnitude lower than an estimation made using batch fermentation data [108]. Such differences suggest that there cannot be an accurate estimation of the half-saturation constants as long as the procedure is not based on actual measurements of the dynamic dissolved concentrations of CO and H_2 in the fermentation media.

The forms used for equations 1 and 2 do not include the inhibitory effects of acetic acid nor ethanol concentrations as proposed by [108]. In preliminary assessments the experimental data used for the model calibration (shown in Table 5.2) did not produce any significant inhibitory effect that could be correlated.

5.4.1.2. Products secretion

The calculations of either the ethanol net production rate (with equation 4) or the acetate export rate (with equation 11) are key for the performance of both the black-box and the metabolic models. The forms of both equations are purely empirical and were found after extensive preliminary assessments. Moreover, in the development of equation 11, not only the accurate prediction of the acetic acid production rate was looked for, but also the applicability of the equation to large ranges of concentrations of CO, H_2, total acetic

acid and pH. Including the actual and currently un-known mechanisms of the export of acetate into the equation may be one of the next improvements for equation 11. Table 5.3 shows the calibrated values for the three parameters (a_3, b_3 and c_3); from the list in Table 5.3, these coefficients are the only ones that were sensitive to the initial guesses.

The poorest correlation quality was obtained for q_{BDO} (using equation 5, see Figure 5.2.e). Since 2,3-butanediol was only produced in minor amounts (between 1 and 2% of the carbon was directed to it) in the experimental cases in which it was actually detected at all, it was not possible to identify clearer correlations to derive a more accurate model.

5.4.1.3. Biomass growth from the perspectives of Gibbs free energy production and ATP production

Figure 5.4 shows the relation between the concentration of the undissociated acetic acid in the extracellular space (C_{HAc}) and the Gibbs free energy production rate (q_G) for the 12 experimental cases in Table 5.2. There is a direct relation between C_{HAc} and the Gibbs free energy production rate. As expected, the points for experiments 11 and 12, where the growth rate is about half compared to the rest of the experiments, have systematically lower values of q_G; also pointing to a direct relation between biomass growth rate and q_G. Therefore, equation 3 seems to appropriately describe the general trend, excluding the points obtained for experiments 8 and 10, which may be seen as outliers.

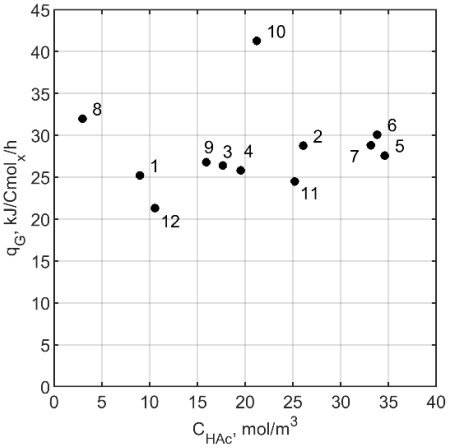

Figure 5.4. Relation between the extracellular concentration of undissociated acetic acid and the Gibbs free energy production rate for the 12 experimental cases (see Table 5.2).

Remarkably, the estimated value of a_G falls below of what would be expected according to [101], *i.e.*, if biomass is considered to be produced from CO and H_2, a_G should be close to 1000 kJ/$Cmol_x$, and if biomass is considered to be produced from a C2 metabolite, as

the acetyl component of acetyl-CoA, a_G should fall close to 500 kJ/Cmol$_x$. Instead, a_G is here estimated at 170 kJ/Cmol$_x$ (see Table 5.3). This result may suggest that the growth of *C. autoethanogenum* dissipates much less energy than other well-known microorganisms, suggesting a higher energy efficiency. The value of m_G is also significantly different from what would be expected. Previous estimations attributed a value of 4.5 kJ/Cmol$_x$/h to the m_G of *E. coli* growing at 25 °C feeding on different substrates [263]. In our case, m_G is estimated at 16.7 kJ/Cmol$_x$/h (see Table 5.3), higher than findings for *E. coli*, pointing to a possible advantage of *C. autoethanogenum* for its application in anaerobic industrial processes: less energy and hence less carbon is directed to growth, compared to other microorganisms. However, it is also possible that the used experimental dataset does not allow a reliable calibration of a_G and m_G; we therefore suggest pursuing such calibration using data from fermentations at steady state and at a wider range of dilutions rates, including values close to zero.

After applying the black-box model (equation 3) to each of the experimental cases, it is observed that the Gibbs free energy production due to the diffusion of acetic acid represents between 5 and 19% of q_G (see the breakdown of q_G for the 12 experimental cases in Figure 5.5, left y-axis). Such effect is supported by the large rate of acetic acid diffusion into the cell; r_{HAcD} is 1 to 5 times the value of q_{AcT} (Figure 5.5, right y-axis).

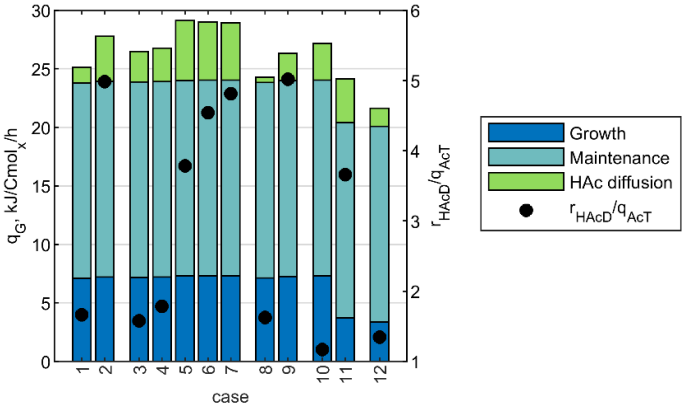

Figure 5.5. Breakdown of the Gibbs free energy production rate calculated for the 12 experimental cases using the black-box model. The ratio between the rates of acetic acid diffusion and the net production of acetic acid is shown at the right-hand side y-axis.

As introduced in section 5.3.1.1.2, the estimation of k_{HAc} depends on the specific acetate export mechanism. Both uniport and antiport are stoichiometrically feasible and produce lines that proportionally relate the net ATP production (r_{ATP}) and the rate of Gibbs free energy production (see Figure 5.6). The estimated k_{HAc} equals 3.86x10^{-5} or 1.93x10^{-5} m/h

if the export mechanism of acetate is uniport or antiport, respectively. Since the term b_G in equation 3 also changes for the different export mechanisms (9.4 kJ/mol$_{HAc}$ for uniport 18.8 kJ/mol$_{HAc}$ for antiport), the total rate of Gibbs free energy directed to the balancing of acetic acid diffusion (in units kJ/Cmol$_x$/h) is independent of the acetate export mechanism. Therefore, the effects of acetic acid diffusion should be included in future modeling strategies applied to *C. autoethanogenum* and possibly to other syngas-fermenting acetogens as well.

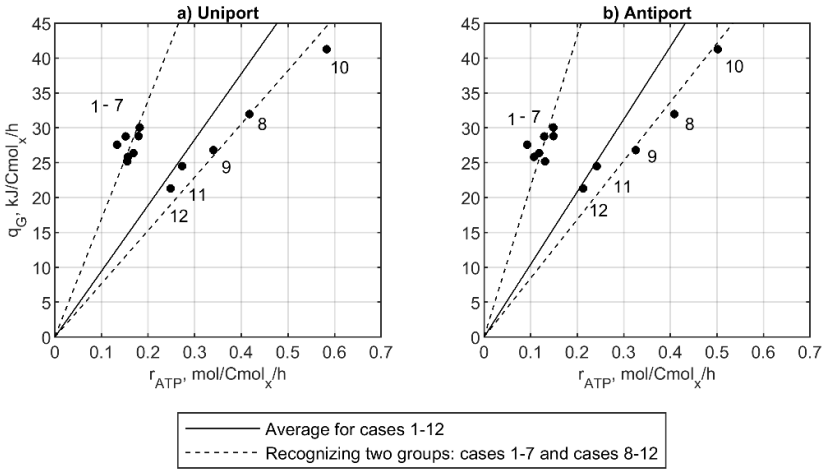

Figure 5.6. Relation between the net ATP production rate and the Gibbs free energy production rate calculated for the 12 experimental cases depending on the acetate export mechanism: a) uniport and b) antiport.

Further into the relation between r_{ATP} and q_G, two groups of data are identified in Figure 5.6.a and b: one group clustered at the left side of the plots and another cluster forming a line at the right side. The left-side group contains the results for the experimental cases 1 to 7, while the right-side group is formed by the cases 8 to 12 (challenging also our assumption that cases 8 and 12 are outliers for q_G). As shown in Figure 5.7, the group on the left directs most of the carbon to both CO_2 and acetic acid, and the electrons to acetic acid. The trend changes for experiments 8 to 12, where the carbon and the electrons are instead directed mostly to ethanol. Such different trends may lead to the question: could it be that the relation between q_G and r_{ATP} shows the two different metabolic states often regarded as acetogenesis and solventogenesis? It has elsewhere been hypothesized that ethanol production leads to higher ATP yields than acetic acid production [111], a behavior reflected in the two plots. No similar assessments have been made for the Gibbs free energy production rate, which according to our proposal through the black-box model, is only influenced by the rates of acetic acid diffusion and growth. Since the

production of Gibbs free energy and the production of ATP are two sides of the same coin, a deeper analysis of the stories told by both, based on more abundant steady state experimental data, remains to be seen. For now, the best approximation we have is one proportional relation between r_{ATP} and q_G (equation 15) and the exclusion of the experimental cases 8 and 12 in the parameterization of equation 3 from the black-box model.

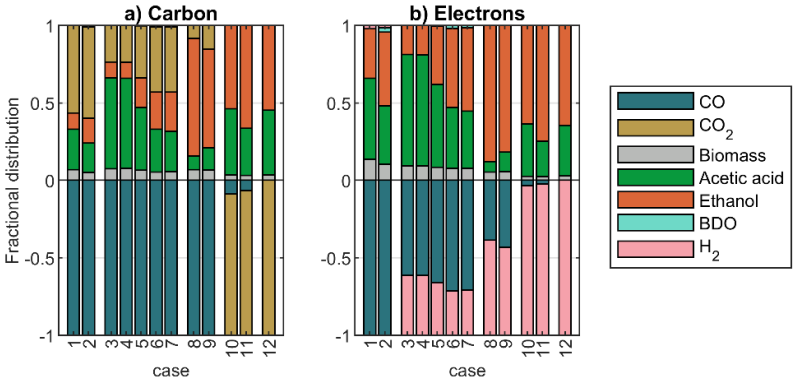

Figure 5.7. Distribution of carbon a) and electrons b) among substrates and products for the 12 experimental cases. On the y-axis, the negative values are for consumption, the positive for secretion.

Assuming one proportional relation between q_G and r_{ATP} for all the experimental points, the estimated average values of $K_{G,ATP}$ are 94.5 and 103.8 kJ/mol$_{ATP}$ if acetate is exported through uniport or antiport, respectively. Those values mean that the ATP requirements for the construction of biomass are 1.80 or 1.64 mol$_{ATP}$/Cmol$_x$, for the two cases. Both values challenge the well-known ATP requirements for biomass synthesis from C2 carbon sources, such as acetate or ethanol, which has been reported as 2.52 mol$_{ATP}$/Cmol$_x$ [44,101]. However, if two different groups of data are acknowledged in Figure 5.6, the group formed by experimental cases 8 – 12, and using uniport, have a $K_{G,ATP}$ of 76.4 kJ/mol$_{ATP}$ (see Table 5.3) which results in 2.23 mol$_{ATP}$/Cmol$_x$, the closest value to 2.52 mol$_{ATP}$/Cmol$_x$. The same group of experimental cases, using antiport have 2.02 mol$_{ATP}$/Cmol$_x$, a value that may also be consistent with literature. Therefore, both mechanisms are equally possible to be used by acetogens.

Although the estimated values for $K_{G,ATP}$ are lower that the average presented by [101] (283 kJ/mol$_{ATP}$), the estimated values are consistent with the ATP needs for cells production. Assuming only one proportional relation for the 12 experiments leads to large errors in the calculation of biomass growth rate. Therefore, in the current from, the metabolic model (equations 14 and 15) does not have an adequate prediction of biomass

growth rates. The two groups of data sets may be considered independently in future assessments.

5.4.2. Accuracy and applicability of the black-box and metabolic descriptions

This section presents an assessment of the accuracy of the predictions of biomass growth rate, product selectivity and all net consumption and secretion rates with the two models, the black-box and the metabolic model. In addition, a discussion is included on how applicable both models are for process simulations.

5.4.2.1. Biomass growth rate

Table 5.4 presents a comparison between the experimental biomass growth rates with those predicted by the black-box model (equation 3) and the metabolic model (equation 14). The predictions made by the metabolic model led to large errors when compared to most of the 12 experimental cases, excluding cases 6 and 7 and independently of the assumed acetate export mechanism. In the experimental cases 1 – 7, μ is underestimated with errors ranging from 26 to 93%; for cases 8 – 12, μ is largely overestimated by 2 to 8-fold. These deviations are visible in Figure 5.3.a and in Table 5.4. The errors are even larger if acetate is assumed to be exported through antiport.

Table 5.4. Comparison between the experimental and the predicted biomass growth rates

Experimental case	μ, $mCmol_x/Cmol_x/h$		
	Experimental	Calculated by	
		Black-box model	Metabolic model [a]
1	41.8	44.8	12.8
2	42.5	47.4	13.6
3	42.2	42.9	16.4
4	42.3	38.0	13.5
5	43.0	33.6	2.9
6	43.1	50.4	31.3
7	43.1	45.1	31.9
8	41.9	100.8	145.3
9	42.8	64.0	147.8
10	43.1	118.2	174.4
11	21.9	21.3	114.5
12	19.8	20.2	182.1

[a] Assuming acetate is exported through uniport

On the other hand, the predictions made by the black-box model lead to significantly smaller errors, ranging between 2 and 22%, with the exception of cases 8, 9 and 10 for which the error varies from 50 to 174% (see Figure 5.2.c and Table 5.4). The predictions of μ are highly accurate for the experimental cases where the q_{CO}/q_D ratio is either above 0.6 or below 0.02.

None of the approaches here presented produces accurate predictions of μ when a H_2-rich gas feed is supplemented with small amounts of CO (as in cases 8, 9, and 10). As discussed previously, more experimental data is needed to further develop the model.

To improve the predictive capacity of the metabolic model for calculating μ, the black-box and metabolic models can be hybridized, *i.e.*, taking ATP off the metabolic network and replacing it by a Gibbs free energy production. This change would lead to modifications of the stoichiometry of the metabolic reactions where ATP participates, and instead of using equation 14 to calculate μ, the hybridized model would use equation 3. Table A.2 shows the stoichiometry of the modified reactions (see reaction coded as i#.b); the modified version of the A matrix (called A_{hyrbid}) is also shown in Appendix C.

5.4.2.2. Product formation rates

Considering that the amount of carbon directed to biomass production represents between 3 and 8% of the carbon directed to acetic acid and ethanol, the inaccurate prediction of μ has a limited effect on ethanol and acetate production rates. However, the accuracy in the prediction of the net production rate of acetic acid improves with the metabolic model (see Figure 5.3.d) compared to the black-box model (see Figure 5.2.f). Such improvement is not due to an increase on the number of parameters (from 13 in the black-box model to 15 in the metabolic model, see Table 5.1), because the increase in the number of parameters focuses on the calculation for the biomass growth rate. The improvement is due to the increased number of possibilities for establishing correlations with the metabolic model.

As for the production of ethanol, the black-box model (equation 4) is more accurate than the whole metabolic model (see Figure 5.2.d and Figure 5.3.b). The better performance of the black-box model may be because q_{Et} is calculated directly (with equation 4), while in the metabolic model is a product of the whole construct.

5.4.2.3. Ethanol selectivity

Table 5.5 shows a comparison of the experimental and calculated ratios between the ethanol production rate and the sum of the ethanol and acetic acid production rates. The predictions made by the black-box (equation 4) and the metabolic (equation 9) models

are compared. The metabolic model is in general more accurate than the black-box model for predicting the ethanol selectivity. Excluding the experimental cases 1, 8 and 9, where predictions of both models overestimate ethanol selectivity by 10-fold or more (mainly due to the empirical forms of equations 4 and 11), the median errors are 38 and 16% for the black-box and the metabolic models, respectively. Therefore, the metabolic model offers not only the advantage of providing more options for establishing correlations than the black-box model, but also allows the improvement of its predictive capacity.

Table 5.5. Comparison of the ethanol selectivity for the experimental data and the predictions made by the models

Experimental case	$q_{Et}/(q_{AcT}+q_{Et})$, mol_{Et}/mol_{AcT+Et}		
	Experimental	Calculated by	
		Black-box model	Metabolic model
1	0.019	0.466	0.289
2	0.582	0.237	0.456
3	0.119	0.521	0.148
4	0.170	0.527	0.151
5	0.518	0.378	0.321
6	0.441	0.272	0.465
7	0.430	0.283	0.492
8	0.003	0.797	0.896
9	0.008	0.604	0.814
10	0.497	0.627	0.557
11	0.816	0.801	0.686
12	0.487	0.973	0.568

Figure 5.8 shows the selectivities of ethanol over acetic acid production predicted at different values of extracellular acetic acid concentration and pH, over wide ranges of CO and H_2 dissolved concentrations in the liquid phase. The figure was built using the hybridized model between the black-box and the metabolic model, as described at the end of section 5.4.2.1. The hybridized model predicts that the lowest selectivities for ethanol occur at low concentrations of the electron donors, depending on the extracellular concentration of acetic acid and pH (see Figure 5.8.a – c). The increase in C_{AcT} and the decrease in pH promote the selectivity for ethanol independently of the values of C_{CO} and C_{H_2}. This result is a consequence of the direct linkage between the rate of export of acetate (r_{AcX}), the net rate of CO uptake (q_{CO}) and the rate of the Nfn complex (r_{Nfn}). When either the pH is low or the total concentration of acetic acid (plus acetate) is high, the concentration of the undissociated form of acetic acid is also high and so is its

rate of diffusion across the bacterial membrane. q_{AcT}, as the result of $r_{AcX} - r_{HAcD}$, has an inverse relation with r_{HAcD}, and thus, when the latter is high, the product selectivity is directed to ethanol and 2,3-butanediol. This influence of r_{HAcD} over q_{AcT} is the reason why r_{AcX} was directly linked to q_{CO} and r_{Nfn} in equation 11. Such relation is founded on the assumption that bacteria do not directly control q_{AcT}, but only the export of carboxylate, which is likely an energy demanding task, since: *i)* acetate is a charged substance and therefore does not permeate into the membrane, and *ii)* there is a likely unfavorable concentration gradient. The energetics of this export mechanism are further assessed in section 5.4.4.1.

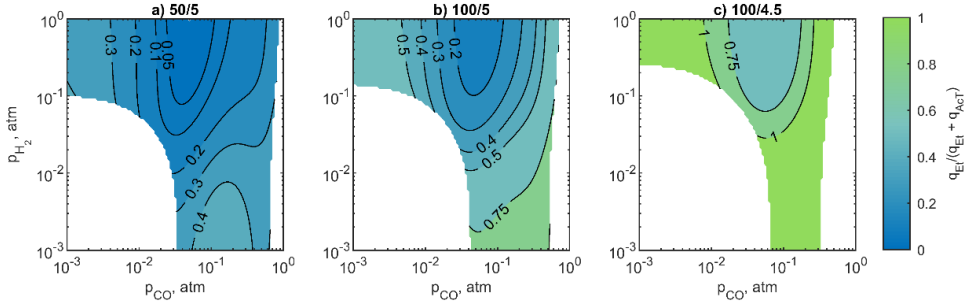

Figure 5.8. Relative selectivity of ethanol as a function of the concentrations of CO and H_2 from different combinations of total acetic acid plus acetate (C_{AcT}, in mM) and pH: a) 50 mM and pH 5, b) 100 mM and pH 5, and c) 100 mM and pH 4.5. For the three scenarios to be comparable, the plots were constructed for C_{Et} 100 mM and p_{CO_2} 0.2 atm. The white areas represent points where equations 1, 2, 3, 5, 9 conflicted with each other and produced solutions that did not fulfill the mass balances. The figures were built using the hybridized model between the black-box and the metabolic models (see section 5.4.2.1).

Therefore, the metabolic and the hybridized models are able to predict the enhanced selectivity of ethanol when either *i)* bacteria use H_2 as the dominant electron donor, *ii)* the extracellular concentration of acetic acid is high, or *iii)* the pH is low. These are prevalent trends in experimental reports for continuous and batch fermentations using different strains of acetogenic bacteria. This feature is therefore here regarded as a significant step forward in the understanding and accurate modeling of syngas fermentations.

Furthermore, when the diffusion rate of undissociated acetic acid exceeds the acetate export rate from the cell, the net production rate of acetate becomes lower than zero (meaning that acetate is consumed and consequently the selectivity for ethanol is higher than one, as shown by the light green-colored region in Figure 5.8.c). Such behavior has been reported for *i)* continuous fermentations, with *C. autoethanogenum* and *C.*

ljungdahlii, where the pH is lowered [72,230], and for *ii)* batch fermentations, with other acetogens, where ethanol titer increases at the same time that acetate concentration falls along with a pH rise (when pH is not controlled) [285,384,385]. Production of higher alcohols from their respective carboxylic acids has also been reported using *C. ljungdahlii* and *C. ragsdalei*, in batch fermentations, where the media was initially supplemented with butyric, valeric, caproic and isobutyric acids [387]. Hence, the model here presented may also be considered to be applied, after further adaptations, to simulate fermentations intended for the production of higher alcohols.

5.4.2.4. Accuracy and applicability of the whole model

The overall accuracy of the black-box and the metabolic models was explored in sections 5.4.2.1, 5.4.2.2 and 5.4.2.3. Summarizing, the black-box model has a higher accuracy for calculating ethanol production and biomass growth, while the metabolic model has a higher accuracy for acetic acid production and the ethanol selectivity. The accuracy for the uptake of CO and H_2, as well as for the production of 2,3-butanediol is the same for both models since they use the same equations (1, 2 and 5, respectively). Graphic comparisons between the mentioned uptake and secretion rates can be found in Figure 5.2 and Figure 5.3. One hybridized model could be also used, using the calculation method for μ from the black-box model (with q_G, equation 3) into the metabolic model (after taking ATP off its structure) for obtaining a somewhat improved overall accuracy.

Despite all the mentioned limitations of the metabolic and the hybridized models, the two have a reasonable accuracy for predicting the steady state ethanol selectivity by the acetogen *C. autoethanogenum*. To the best of our knowledge, such predictive capacity has not been previously reported in literature.

In addition, not only the black-box and the metabolic models are applicable for wide ranges of dissolved CO and H_2 concentrations, but also for commonly reported values of acetic acid, pH and CO_2 concentrations. This feature gives both models a high applicability for simulations of bacteria inside bioreactors at steady state. Considering that the turn-over times[h] for CO and H_2 range between 0.001 and 0.1 seconds in the experimental data set (see Table F.6 in Appendix F), it can be argued that inside large industrial bioreactors, bacteria will face significant gradients of CO and H_2 concentrations and therefore they will not be at steady state. To perform accurate simulations of large syngas fermentors, a metabolic model is needed which also describes intracellular kinetics.

[h] For example, the turn-over time for CO was calculated with the equation: $t_{CO} = C_{CO}/(-q_{CO}C_x)$.

5.4.3. Assessment of the distribution of electrons and energy production

To provide insights on how cells control selectivity on the electron donors and to identify possible reasons behind their choice, we first assess the routes taken by the electrons among the intracellular redox carriers, NADH, NADPH and reduced ferredoxin. Secondly, the energy dissipated by each of the experiments is related to the choice for CO or H_2 when both gases are fed at the same ratios, but they are consumed at different rates.

5.4.3.1. Following the electrons

Based on our model's results, we present a general overview of the role that the redox carriers have in the network depending on the electron source, for pure CO and the H_2/CO_2 mixture.

Reduced ferredoxin, the redox carrier that powers the proton motive force and hence the generation of ATP, is produced at different amounts depending on the electrons source, CO or H_2. H_2 uptake yields half as much reduced ferredoxin as CO uptake, according to the CODH and Hyd reactions (see equations i3 and i4 in Table A.2). This difference in the electrons uptake route has strong consequences for the energy conservation mechanisms.

When CO is the dominant electron donor (see Figure 5.9.a, b and c at the right of the x-axis), reduced ferredoxin (generated at the CODH reaction) powers the production of 100% of the cell's NADH and NADPH. The Rnf complex, where NADH is generated, oxidizes 75% of the cell's reduced ferredoxin (see Figure 5.9.a). The synthesis of formate and ethanol are other sinks of reduced ferredoxin, while NADH and NADPH (largely produced at the Nfn complex) are mainly needed for the synthesis of acetyl-CoA, the backbone of the catabolic route.

When H_2 is the dominant electron donor, the Rnf complex oxidizes only 50% of the cell's reduced ferredoxin (generated at the Hyd reaction) which has to power, in this case, the production of CO needed for the synthesis of acetyl-CoA (through the reversed CODH reaction). The Hyd reaction, besides producing most of the cells' reduced ferredoxin, also generates 100% of the cell's NADPH. When CO is the dominant electron donor, all the NADPH is produced at the Nfn complex instead. If the Nfn complex is assumed to be reversible, as it is the case in this study, the excess of NADPH generated at Hyd would produce small extra amounts of NADH and ferredoxin, at the Nfn complex. If the Nfn complex is instead assumed irreversible, as in [74,74], the excessive production of NADPH would be prevented by an alternate route for H_2 uptake, the formate-hydrogen lyase (or FHL in Table A.2) reaction. Through the FHL, CO_2 is fixed into formate using the electrons

directly from H_2; other effects that may result from including the FHL reaction in our model are further assessed in section 5.4.4.2.

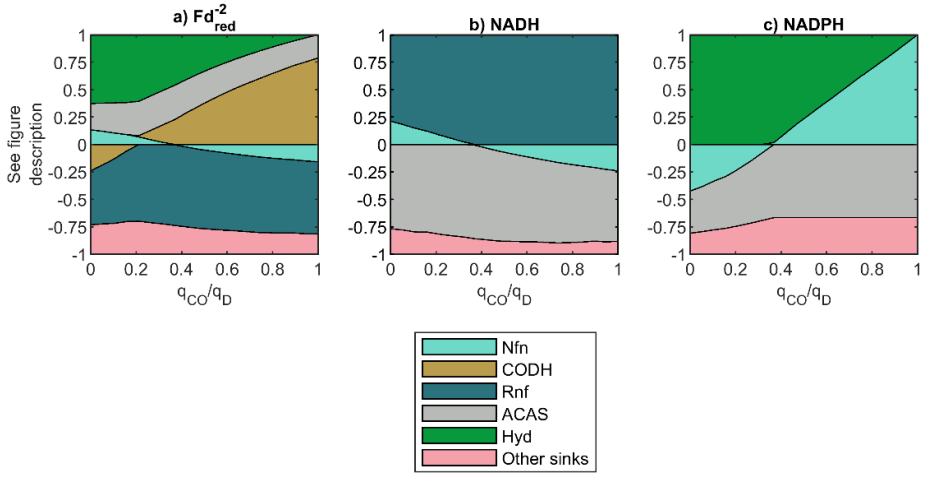

Figure 5.9. Fractional production and consumption rates of the redox carriers, based on the metabolic model, a) ferredoxin, b) NADH and c) NADPH as function of the fraction of CO uptake (q_{CO}) with respect to the total electron donor uptake ($q_D = q_{CO} + q_{H_2}$), *i.e.*, H_2 is the dominant electron donor at the left of the x-axis, while CO is the dominant electron donor at the right. Above the zero in the y-axis there is production of the redox carriers, while below the zero, there is consumption. The plots were constructed for C_{AcT} of 50 mM and a pH of 5.

It has been shown that ferredoxin plays a fundamental role in connecting the electron uptake reactions (the CODH and the Hyd reactions) with the energy conservation reactions (Rnf and Nfn). The relatively large amounts of the redox carriers produced and consumed within the latter connections suggest that the main roles of NADH, Fd_{red}^{2-} and NADPH are keeping the proton motive force active while guaranteeing a constant supply of acetyl-CoA. The reactions carrying out this connection are in fact, the fastest in the whole metabolic network (see Figure G.1 at Appendix G). However, it is unclear how the redox carriers influence the activity of other minor reactions, such as the production of ethanol or 2,3-butanediol. Reportedly, the production of ethanol through the acetaldehyde oxidoreductase (or AOR) route, here included within the EtS reaction, is close to equilibrium [113] . Such finding led to suggesting that the direction of the AOR route may be influenced by slight changes in the intracellular NADH, Fd_{red}^{2-} and acetate concentrations, which might be regulated by the connection between the CODH, the Hyd, the Rnf and the Nfn reactions [113]. Yet, to the best of our knowledge, no measurements of Fd_{red}^{2-} and intracellular acetate concentrations have been reported. Such

measurements are essential for drawing more solid conclusions about the role of the energy conservation mechanisms on the production of ethanol.

5.4.3.2. The choice of the electron donor

The fraction of CO in the gas feed is 0.71 for the experimental cases 3 to 7. These cases are the focus point of the present assessment since there are five points obtained with the same gas feed compositions and at different stirring speeds in the bioreactor.

Although the gas feed composition is constant for the mentioned experiments, their q_{CO} and q_{H_2} are not the same. In cases 3 and 4, where the stirring speed and C_x are the lowest between experiments 3 – 7 (see data in Table 5.2), bacteria preferably consume H_2 over CO, *i.e.*, q_{CO}/q_D equals 0.61 in both cases, while y_{CO}/y_D at the gas feed is 0.71 (see Table 5.6). As the overall mass transfer rate increases (implied by the higher stirring speed) along with increased concentration of cells (cases 5, 6 and 7), the amount of energy that cells are able to retrieve from the electron donors would fall as C_{CO} and C_{H_2} decrease, if the q_{CO}/q_D was not modified. However, q_G progressively increases for cases 5 to 7 (see Table 5.6) because of increased acetic acid concentration; the selectivity for also CO increases with the stirring speed. It is known that CO catabolism releases higher amounts of Gibbs free energy than H_2 [324] (see Table A.1 in Appendix A). Therefore, acetogens may regulate the amount of energy they harvest by controlling their selectivity for the electron donors, when CO and H_2 are both available in the gas feed.

Table 5.6. The energetic and metabolic effects of an increased selectivity for CO uptake

Experimental case	3	4	5	6	7
q_{CO}/q_D	0.61	0.61	0.66	0.71	0.71
q_G, kJ/Cmol$_x$/h	26.4	25.8	27.6	30.1	28.8
r_{Rnf}, mmol/Cmol$_x$/h	531.9	523.8	586.2	652.9	638.5
r_{ATPS}, mmol/Cmol$_x$/h	168.8	156.6	133.8	182.2	179.6
r_{HAcD}, mmol/Cmol$_x$/h [a]	260.9	288.5	511.3	499.7	489.6
r_{HAcD}, mmol/Cmol$_x$/h [b]	130. 5	144.3	255.7	249.9	244.8

[a] acetate exported through uniport
[b] acetate exported through antiport

Metabolically, an increased selectivity for the consumption of CO leads to a faster reduction of ferredoxin (CO uptake produces twice as much reduced ferredoxin as H_2 uptake). A faster production of reduced ferredoxin could be related to a higher activity of the Rnf complex (see r_{Rnf} in Table 5.6), which powers H^+ extrusion. The higher activity of the Rnf complex may also promote a faster production of ATP in the membrane-bound ATP-synthase, using the influx of H^+ (see r_{ATPS} in Table 5.6); the faster production of ATP

may be used for countering the effects of a faster diffusion of acetic acid into the cell (see r_{HAcD} in Table 5.6). This analysis may be equivalent to the one made in the previous paragraph and may explain, from the perspective of the metabolic model, why cells choose CO over H_2 when they face higher ATP (or energy) requirements.

5.4.4. Energetics of acetate export and the H_2 futile cycle

This section discusses the conditions under which the different acetate export mechanism are feasible as well as the reactions forming the H_2 futile cycle.

5.4.4.1. Active transport of acetate ions

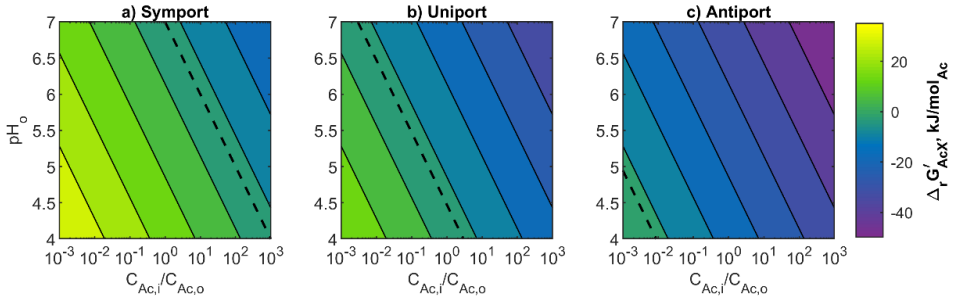

Figure 5.10. Gibbs free energy change for the export of acetate through a) symport, b) uniport and c) antiport transporters. The dashed line in b) represents $\Delta_r G'_{AcX}$ = 0 kJ/mol, where intra and extracellular concentrations of the anion will be at electrochemical equilibrium.

The active transport of ions across the bacterial membrane involves a Gibbs free energy gradient. The transport reaction is at energetic equilibrium ($\Delta_r G$ = 0, a condition often sought by microorganisms [52,99]) when the intracellular concentration of the ions are at electrochemical equilibrium with the extracellular concentration of the same ions. Figure 5.10.a, b and c show the pH-dependent acetate concentration ratios that would be at the said equilibrium for three different transport mechanisms, symport, uniport and antiport, respectively. If it is assumed that *C. autoethanogenum* seeks to achieve electrochemical equilibrium on the acetate export reaction (thus minimizing $\Delta_r G'_{AcX}$), the intracellular concentrations of the anion ($C_{Ac^-,i}$) would need to be in the order of 10000, 100 and 0.1 mM, when *i)* the export mechanisms are symport, uniport or anitport, respectively, and *ii)* the extracellular pH is 5 and $C_{Ac^-,o}$ is 100 mM (common conditions for the experimental cases in Table 5.2). A measurement of $C_{Ac^-,i}$ has so far not been reported for *C. autoethanogenum*, thus it is not possible to draw conclusions on which mechanism cells actually use. However from the presented analysis it can be concluded that symport is impossible (too high $C_{Ac^-,i}$ will be needed), while uniport is likely since $C_{Ac^-,i}$ has been

found to be in the order of 100 and 300 mM, in *E. coli* [404] and *C. acetobutylicum* [405], respectively. Nevertheless, antiport is also possible considering that the intracellular concentration of pyruvate and lactate have been measured in the order of 1 mM in *C. autoethanogenum* [113].

5.4.4.2. The endergonic H_2 futile cycle

Mathematically, including the formate hydrogen lyase reaction (or FHL) introduces a singularity into matrix A_c, since one of the two reactions forming the H_2 futile cycle (reactions i4 and i16) can be expressed as a linear combination of the other reactions in the system. In addition, since the two reactions are engrained with the intracellular nodes (formate and energy carriers) in the network, most of the rates contained in r_c have calculability issues after the inclusion of FHL. Several authors argue that one of the two reactions causing the singularity should be discarded, or otherwise the two reactions may be merged into one [79,80]. Another solution is to calculate the rates of reaction using an optimization where constraints can be applied [406]. Here, the latter option was used and the rate of the FHL reaction was maximized, while the direction of the reactions was constrained, Hyd to the direction of H_2 production and the FHL to the direction of H_2 uptake.

Metabolically, cells feeding on H_2 through the FHL and the Hyd reactions simultaneously produce less NADPH and Fd_{red}^{2-} as they would do when feeding only through the Hyd reaction. The presence of FHL in the network additionally, lowers the rate of the FDH reaction which produces formate at the expense of Fd_{red}^{2-} and NADPH. At the same time, formate is produced by FHL powered directly by H_2. Therefore, FDH buffers all the disturbances introduced by FHL when cells feed on H_2.

When CO is the only electron donor, the presence of FHL in the network forms the H_2 futile cycle, where Hyd generates H_2 and FHL consumes it. The futile cycle, therefore, drains NADPH and Fd_{red}^{2-} from the cell, which causes the rate of FDH to lower, and no other downstream (further than acetyl-CoA synthesis) consequences are foreseen. Therefore, the stoichiometric effects of including the FHL reaction do not pass from the reactions used for harvesting electrons towards the energy conservation reactions in the cell, or towards the product generation regions. Thus, FHL would only serve the cell to regulate the excess of reductive power introduced by the uptake of CO, as argued in [53].

Using the calculated values for the intracellular concentrations of formate, reduced and oxidized ferredoxin, the calculated values of H_2 and CO_2 (see Table 5.2), and the experimental values for $NADP^+$ and NADPH [74,257], the Gibbs free energies of reaction for Hyd and FHL were calculated at process conditions. The results are shown in Table 5.2.

Table 5.7. Data used for the thermodynamic assessment of the H_2 futile cycle

Variable	Unit	Experimental case (as in Table 5.2)				
		1	4	5	7	8
C_{H_2}	Atm	0.003	0.119	0.055	0.042	0.320
C_{CO_2}	Atm	0.044	0.229	0.327	0.431	0.008
C_{For^-}	mol/m^3	0.49	0.49	0.49	0.49	0.49
$C_{Fd^{2-}_{red}}$	mol/m^3	1.45	1.45	1.45	1.45	1.45
$C_{Fd_{ox}}$	mol/m^3	1.56	1.56	1.56	1.56	1.56
C_{NADPH}	mol/m^3	0.34	1.49	0.69	0.58	2.61
C_{NADP^+}	mol/m^3	6.81	8.73	6.12	7.60	15.6
$\Delta_r G'_{Hyd}$	kJ/mol$_{H2}$	-20.23	-28.37	-26.90	-26.75	-30.95
$\Delta_r G'_{FHL}$	kJ/mol$_{H2}$	-15.60	-29.99	-28.91	-28.96	-23.77
r_{Hyd}	mmol$_{H2}$/Cmol$_x$/h	-93	32	71	149	583
r_{FHL}	mmol$_{H2}$/Cmol$_x$/h	79	119	115	174	395
$r_{G_{Hyd}}$	kJ/Cmol$_x$/h	1.88	-0.90	-1.90	-3.98	-18.05
$r_{G_{FHL}}$	kJ/Cmol$_x$/h	-1.23	-3.58	-3.32	-5.03	-9.39
$r_{G_{H2-cycle}}$	kJ/Cmol$_x$/h	0.65	-4.48	-5.22	-9.01	-27.45

The results suggest that the only case where the H_2 futile cycle might require the input of the energy from the cell (0.65 kJ/mol$_x$/h) is on case 1, where there is a net production of H_2 (see Table 5.2). In comparison to the value of q_G for case 1 (25 kJ/Cmol$_x$/h), the energy needed for the H_2 futile cycle is small and its effect is not significant. The energy required by the Hyd reaction to produce H_2 will increase with a higher H_2 partial pressure. However, a 10-fold increase in the H_2 partial pressure in case 1 will rise the energy needed by the H_2 futile cycle to 1.2 kJ/Cmol$_x$/h.

5.5. Conclusions

The black-box and the metabolic models allow a reasonable prediction of the product selectivity between ethanol and acetate as a function of the extracellular CO, H_2 and acetic acid concentrations as well as the pH. Similar to common experimental findings, the model predicts that ethanol selectivity is promoted when cells consume an H_2-rich gas, when the concentration of acetic acid is high, and the pH is low. The modeling structure facilitating this estimation may also be applied to the simulation of the production of higher alcohols by acetogens.

The study of the Gibbs free energy production rate led to the estimation of the permeability rate of acetic acid in the membranes of *C. autoethanogenum*, which proved

to be 1 – 5 times faster than the rate net acetic acid production rate. Such fast diffusion has a limited but significant effect on the Gibbs free energy production rate. In addition, the same assessment allows the identification of Gibbs free energy production constants for growth and maintenance, which remarkably differ from well-known microorganisms. The combined assessment between the Gibbs free energy production rate and the rate of ATP production led to the estimation of the ATP requirements for the production of cells.

The model was also used to gather insights about the distribution of the electrons among redox carriers. Such distribution plays an important role in the production of ATP. CO is preferred when cells need to counter the effects of acetic acid diffusion, while producing Gibbs free energy at higher rates.

Moreover, uniport and antiport are equally plausible mechanisms that cells could use to export acetate to the extracellular space. The use of both mechanisms produces consistent results rearding the relation between the production of Gibbs free energy and ATP. The only difference between the two mechanisms relies on the intracellular concentrations of acetate that would be maintained, in the order of 100 and 0.1 mM for uniport and antiport respectively. Uniport would maintain the intra and extracellular concentrations of acetate at electrochemical equilibrium, while antiport would generate sufficient thermodynamic driving force to export the acetate against a concentration gradient.

The presence of a futile H_2 production and consumption cycle is feasible thermodynamically and stoichiometrically only for the experimental cases where there is a net production of H_2. The futile cycle may be used by cells to maintain a high intracellular H_2 partial pressure to fine-tune the amount of energy harvested by the uptake of CO. However, the amount of energy needed represents only a 2.5% of the total energy produced by the cell.

Lastly, the assessment of the model results led to the identification of a relevant knowledge gap about the metabolic regulations surrounding the two divergent trends obtained for the relation between the Gibbs free energy production rate and the net ATP production rate.

These insights could, in principle, already be used in an integrated metabolic-hydrodynamic model to be deployed in further development and commercialization of syngas fermentation processes. However, more biochemical evidence is required from dedicated experiments to substantiate the model and turn it into a reliable, predictive design tool for biochemical engineers.

5.6. List of symbols

Latin letters	
a_G	Gibbs free energy needed for growth
a_x	Molar surface area of cells
$a_\#$	Correlation coefficient in equation 4, 5, and 9
b_G	Gibbs free energy needed to balance the diffusion of acetic acid
$b_\#$	Correlation coefficient in equation 4 and 9
C	Concentration
$c_\#$	Correlation coefficient in equation 4 and 9
F	Faraday's constant
G'	Gibbs free energy at physiological conditions
k_{HAc}	Permeability coefficient of acetic acid
K_{CO}	Half saturation constant for CO uptake
$K_{G,ATP}$	Slope of the line relating q_G with r_{ATP}
K_{H_2}	Half saturation constant for H_2 uptake
K_I	Inhibition constant for CO uptake
$K_{I,CO}$	CO Inhibition constant for H_2 uptake
m	Maintenance
n	Number of H^+ ions exported along acetate
q	Biomass specific reaction rate
r	Biomass specific reaction rate of intracellular reaction
R	Ideal gas constant
R^2	Coefficient of determination
T	Temperature
Y	Yield
y	Molar fraction in the gas phase
z	Charge

Greek letters	
$\Delta_f H^0$	Enthalpy change of formation at standard conditions
$\Delta_f G^0$	Gibbs free energy of formation at standard conditions
$\Delta_r G'$	Gibbs free energy change of reaction at physiological conditions
μ	Biomass growth rate
$\Delta\psi$	Electrical potential gradient
Subscripts	
Ac^-	Acetate (dissociated form)
BDO	2,3-butanediol
cat	In catabolism
C	Carbon
D	Electron donor
e^-	Electron
Et	Ethanol
G	Gibbs free energy
HAc	Acetic acid (undissociated)
i	At the intracellular space
j	For any *j-th* substance
o	At the extracellular space
pmf	Proton motive force
x	Cell biomass
Superscripts	
max	Maximum
'	At physiological conditions

Appendix A

Lists of extra and intracellular reactions

Table A.1 Bacterial reactions considered from the extracellular space

Part of metabolism	Electron donor	Product	Reaction equation	$\Delta_r G^0$ [a]		Rx. nr.
				kJ/mol$_{product}$	kJ/mol$_{electrons\ in\ product}$	
Catabolism	CO	Acetate	$-4CO - 2H_2O + Ac^- + H^+ + 2CO_2$	-135.0	-16.87	(o1)
		Acetic acid	$-4CO - 2H_2O + HAc + 2CO_2$	-162.0	-20.25	(o2)
		Ethanol	$-6CO - 3H_2O + Et + 4CO_2$	-224.5	-18.71	(o3)
		2,3-butanediol	$-11CO - 5H_2O + BDO + 7CO_2$	-387.7	-17.62	(o4)
	H_2/CO_2	Acetate	$-4H_2 - 2CO_2 + Ac^- + H^+ + 2H_2O$	-55.0	-6.87	(o5)
		Acetic acid	$-4H_2 - 2CO_2 + HAc + 2H_2O$	-81.8	-10.22	(o6)
		Ethanol	$-6H_2 - 2CO_2 - Et + 3H_2O$	-104.5	-8.71	(o7)
		2,3-butanediol	$-11H_2 - 4CO_2 + BDO + 6H_2O$	-167.7	-7.62	(o8)
Anabolism	CO/NH_4^+	Cells	$-2CO - \frac{1}{4}NH_4^+ - \frac{1}{2}H_2O + CH_{7/4}O_{1/2}N_{1/4} + CO_2 + \frac{1}{4}H^+$	-48.6	-12.15	(o9)
	$H_2/CO_2/NH_4^+$		$-2H_2 - CO_2 - \frac{1}{4}NH_4^+ + CH_{7/4}O_{1/2}N_{1/4} + \frac{3}{2}H_2O + \frac{1}{4}H^+$	-8.6	-2.15	(o10)

[a] The complete list of standard Gibbs free energies of formation for all the substances above are shown in Table E.2 in Appendix E.

Note: From the calculated values of $\Delta_r G^0$, it is clear that CO use yields about 10 kJ/molelectrons in product higher than H_2 use.

Table A.2 List of reactions considered for the metabolic network

Name	Abb. [a]	Equation [b,c]	Rx. nr.
Formate dehydrogenase	FDH	$-2CO_2 - [H^+]_i - Fd_{red}^{2-} - NADPH + 2For^- + Fd_{ox} + NADP^+$	(i1)
Acetyl-CoA synthesis [d]	ACAS	$-For^- - CO - [H^+]_i - ATP - 2NADH - NADPH - H\text{-}CoA - Fd_{ox} + C_2H_3O\text{-}CoA + H_2O + ADP + Pi^- + Fd_{red}^{2-} + 2NAD^+ + NADP^+$	(i2.a)
		$-For^- - CO - 2[H^+]_i - 2NADH - NADPH - H\text{-}CoA - Fd_{ox} + C_2H_3O\text{-}CoA + 2H_2O + Fd_{red}^{2-} + 2NAD^+ + NADP^+$	(i2.b)
CO-dehydrogenase	CODH	$-CO - H_2O - Fd_{ox} + CO_2 + [H^+]_i + Fd_{red}^{2-}$	(i3)
Fd-NADPH-Hydrogenase	Hyd	$-2H_2 - NADP^+ - Fd_{ox} + 3[H^+]_i + NADPH + Fd_{red}^{2-}$	(i4)
Acetate synthesis [d]	AcS	$-C_2H_3O\text{-}CoA + ADP + Pi^- + Ac^- + ATP + H\text{-}CoA$	(i5.a)
		$-C_2H_3O\text{-}CoA - H_2O + Ac^- + H\text{-}CoA + [H^+]_i$	(i5.b)
Ethanol synthesis	EtS	$-Ac^- - 4[H^+]_i - NADH - Fd_{red}^{2-} + Et + H_2O + NAD^+ + Fd_{ox}$	(i6)
Pyruvate synthesis	PyrS	$-CO_2 - C_2H_3O\text{-}CoA - [H^+]_i - Fd_{red}^{2-} + Pyr^- + H\text{-}CoA + Fd_{ox}$	(i7)
2,3-butanediol synthesis	BDOS	$-2Pyr^- - 3[H^+]_i - NADH + BDO + 2CO_2 + NAD^+$	(i8)
Nfn complex	Nfn	$-[H^+]_i - Fd_{red}^{2-} - NADH - 2NADP^+ + 2NADPH + Fd_{ox} + NAD^+$	(i9)
Rnf complex	Rnf	$-3[H^+]_i - Fd_{red}^{2-} - NAD^+ + Fd_{ox} + NADH + 2[H^+]_o$	(i10)
ATP-synthase [d]	ATPS	$-3.3[H^+]_o + ADP + Pi^- + ATP + H_2O + 2.3[H^+]_i$	(i11.a)
		$-3.3[H^+]_o + 3.3[H^+]_i$	(i11.b)
Anabolism [d]	Ana	$-\frac{1}{2}C_2H_3O\text{-}CoA - {NH_4}^+ - Y_{ATP/x}(ATP + H_2O) + CH_{\frac{7}{4}}O_{\frac{1}{2}}N_{\frac{1}{4}} + H\text{-}CoA + \frac{1}{4}[H^+]_i + Y_{ATP/x}(ADP + Pi^- + [H^+]_i)$	(i12.a)

Name	Abb. [a]	Equation [b,c]	Rx. nr.
		$-\frac{1}{2}C_2H_3O\text{-}CoA - NH_4^+ + CH_{7/4}O_{1/2}N_{1/4} + H\text{-}CoA + \frac{1}{4}[H^+]_i$	(i12.b)
ATP dissipation	m_{ATP}	$-ATP - H_2O + ADP + Pi^- + [H^+]_i$	(i13)
Acetate export [e]	AcX	$-[Ac^-]_i + \left(n - (1 - x_{Ac^-})\right)[H^+]_o + x_{Ac^-}[Ac^-]_o + (-n)[H^+]_i + (1 - x_{Ac^-})[HAc]_o$	(i14)
Acetic acid passive diffusion	HAcD	$-x_{Ac^-}[Ac^-]_o - x_{Ac^-}[H^+]_o - (1 - x_{Ac^-})[HAc]_o + [Ac^-]_i + [H^+]_i$	(i15)
Formate hydrogen lyase	FHL	$-H_2 - CO_2 + For^- + [H^+]_i$	(i16)

[a] Abbreviations

[b] For substances that dissociate depending on the pH, the reactions only depict their most abundant form within the cells. Matrix A was constructed however, considering all the relevant forms of each substance. The stoichiometric coefficient of water was determined such that the oxygen balance closes; similarly, the amount of H^+ was defined such that the hydrogen balance closes. See Tables E.1 and E.2 for the dissociation constants and the thermodynamic data, respectively.

[c] The sub-fixes i and o after brackets containing the chemical species denotes the location of the protons: inside or outside the cells, respectively.

[d] These reactions have two different versions a and b: the first with ATP and the second without ATP (hybridized model as explained in section 5.4.2.1), respectively. The later versions form the metabolic description that uses the Gibbs free energy balance to calculate the biomass yield. ATP dissipation is not considered in the metabolic network when the Gibbs free energy balance is used.

[e] n is the number of H^+ ions exported along acetate. x_{Ac^-} is the concentration of acetate over the sum of the acetate and acetic acid concentrations at the extracellular space:

$$x_{Ac^-} = \frac{10^{(pH_o - pK_a)}}{1 + 10^{(pH_o - pK_a)}}.$$

Appendix B

Black-box (BB) and metabolic (A) matrixes

$$BB = \begin{array}{c} \begin{matrix} q_{CO} & q_{H_2} & q_{CO_2} & q_{HAc} & q_{Ac^-} & q_{Et} & q_{BDO} & \mu & q_{H_2O} & q_{H^+} & q_{NH_4^+} & q_G & q_H \end{matrix} \\ \begin{bmatrix} 1 & 0 & 1 & 2 & 2 & 2 & 4 & 1 & 0 & 0 & 0 & 0 & 0 \\ 0 & 2 & 0 & 4 & 3 & 6 & 10 & 7/4 & 2 & 1 & 4 & 0 & 0 \\ 1 & 0 & 2 & 2 & 2 & 1 & 2 & 1/2 & 1 & 0 & 0 & 0 & 0 \\ 0 & 0 & 0 & 0 & 0 & 0 & 0 & 1/4 & 0 & 0 & 1 & 0 & 0 \\ 0 & 0 & 0 & 0 & -1 & 0 & 0 & 0 & 0 & 1 & 1 & 0 & 0 \\ 0 & 0 & 0 & 10^{(pH-pK_a)} & -1 & 0 & 0 & 0 & 0 & 0 & 0 & 0 & 0 \\ G'_{CO} & G'_{H_2} & G'_{CO_2} & G'_{HAc} & G'_{Ac^-} & G'_{Et} & G'_{BDO} & G'_x & G'_{H_2O} & G'_{H^+} & G'_{NH_4^+} & 1 & 0 \\ H^0_{CO} & H^0_{CO} & H^0_{CO} & H^0_{CO} & H^0_{CO} & H^0_{CO} & H^0_{CO} & H^0_{CO} & H^0_{CO} & H^0_{CO} & H^0_{CO} & 0 & 1 \end{bmatrix} \end{array} \begin{array}{l} C-balance \\ H-balance \\ O-balance \\ N-balance \\ z-balance \\ Ac^- - HAc\ equilibrium \\ Gibbs\ free\ energy \\ Enthalpy \end{array}$$

$$A_c = \begin{bmatrix}
0 & -1 & -1 & 0 & 0 & 0 & 0 & 0 & 0 & 0 & 0 & 0 & 0 & 0 & 0 & 0 & 0 & 0 & 0 & 0 \\
0 & 0 & 0 & -2 & 0 & 0 & 0 & 0 & 0 & 0 & 0 & 0 & 0 & 0 & 0 & 0 & 0 & 0 & 0 & 0 \\
0 & 0 & 0 & 0 & 0 & 0 & 0 & 0 & 0 & 0 & 0 & 1 & 0 & 0 & 0 & 0 & 0 & 0 & 0 & -1 \\
0 & 0 & 0 & 0 & 0 & 0 & 0 & 0 & 0 & 0 & 0 & 0 & 0 & 0 & 0 & 0 & 0 & 0 & -1 & 0 \\
0 & 0 & 0 & 0 & 0 & 0 & 0 & 0 & 0 & 0 & 0 & 0 & 0 & 0 & 0 & 0 & 0 & -1 & 0 & 0 \\
0 & 0 & 0 & 0 & 0 & 0 & 0 & 1 & 0 & 0 & 0 & 0 & 0 & 0 & 0 & 0 & 0 & 0 & 0 & 0 \\
0 & 0 & 0 & 0 & 0 & 1 & 0 & 0 & 0 & 0 & 0 & 0 & 0 & -1 & 0 & 0 & 0 & 0 & 0 & 0 \\
-1 & 0 & 1 & 0 & 0 & 0 & -1 & 2 & 0 & 0 & 0 & 0 & -1 & 0 & 0 & 0 & 0 & 0 & 0 & 0 \\
0 & 1 & -1 & 0 & 0 & 1 & 0 & 0 & 0 & 0 & 0 & -Y_{ATP/x} & 0 & 0 & -1 & 0 & 0 & 0 & 0 & 0 \\
0 & 0 & 0 & 0 & 0 & 0 & 0 & 0 & 0 & 2 & -3.3 & 0 & 0 & 0 & 0 & -1 & 0 & 0 & 0 & 0 \\
0 & 0 & 0 & 0 & 0 & 0 & 0 & 0 & 0 & 0 & 0 & -0.25 & 0 & 0 & 0 & 0 & -1 & 0 & 0 & 0 \\
0 & 1 & 0 & 0 & -1 & 0 & -1 & 0 & 0 & 0 & 0 & -0.5 & 0 & 0 & 0 & 0 & 0 & 0 & 0 & 0 \\
0 & 0 & 0 & 0 & 1 & -1 & 0 & 0 & 0 & 0 & 0 & 0 & 0 & 0 & 0 & 0 & 0 & 0 & 0 & 0 \\
1 & -1 & 0 & 0 & 0 & 0 & 0 & 0 & 0 & 0 & 0 & 0 & 0 & 0 & 0 & 0 & 0 & 0 & 0 & 0 \\
0 & 0 & 0 & 0 & 0 & 0 & 1 & -2 & 0 & 0 & 0 & 0 & 0 & 0 & 0 & 0 & 0 & 0 & 0 & 0 \\
-0.5 & -1 & 2 & 3 & 0 & -4 & -1 & -3 & -1 & -3 & 2.3 & 0.25 + Y_{ATP/x} & 0 & 0 & 0 & 0 & 0 & 0 & 0 & 0 \\
0 & -2 & 0 & 0 & 0 & -1 & 0 & -1 & -1 & 1 & 0 & 0 & 0 & 0 & 0 & 0 & 0 & 0 & 0 & 0 \\
-0.5 & -1 & 0 & 1 & 0 & 0 & 0 & 0 & 2 & 0 & 0 & 0 & 0 & 0 & 0 & 0 & 0 & 0 & 0 & 0 \\
-0.5 & 1 & 1 & 1 & 0 & -1 & -1 & 0 & -1 & -1 & 0 & 0 & 0 & 0 & 0 & 0 & 0 & 0 & 0 & 0 \\
0 & -1 & 0 & 0 & 1 & 0 & 0 & 0 & 0 & 0 & 1 & -Y_{ATP/x} & 0 & 0 & 0 & 0 & 0 & 0 & 0 & 0
\end{bmatrix}
\begin{matrix}
\mathrm{CO} \\ H_2 \\ x \\ [Ac^-]_o \\ HAc \\ BDO \\ Et \\ CO_2 \\ H_2O \\ [H^+]_o \\ NH_4^+ \\ AcCoA \\ [Ac^-]_i \\ For^- \\ Pyr^- \\ [H^+]_i \\ NADH \\ NADPH \\ Fd_{red}^{2-} \\ ATP
\end{matrix}
\qquad r_c = \begin{bmatrix}
r_{FDH} \\ r_{ACAS} \\ r_{CODH} \\ r_{Hyd} \\ r_{AcS} \\ r_{EtS} \\ r_{PyrS} \\ r_{BDOS} \\ r_{Nfn} \\ r_{Rnf} \\ r_{ATPS} \\ r_{Ana} \\ q_{CO_2} \\ q_{Et} \\ q_W \\ q_{H^+} \\ q_{NH_4^+} \\ q_{HAc} \\ q_{Ac^-} \\ \mu
\end{bmatrix}$$

$$A_m = \begin{bmatrix} -1 & 0 & 0 & 0 & 0 & 0 \\ 0 & -1 & 0 & 0 & 0 & 0 \\ 0 & 0 & 0 & 0 & 0 & 0 \\ 0 & 0 & 0 & -x_{Ac^-} & x_{Ac^-} & 0 \\ 0 & 0 & 0 & -(1-x_{Ac^-}) & (1-x_{Ac^-}) & 0 \\ 0 & 0 & -1 & 0 & 0 & 0 \\ 0 & 0 & 0 & 0 & 0 & 0 \\ 0 & 0 & 0 & 0 & 0 & 0 \\ 0 & 0 & 0 & 0 & 0 & 1 \\ 0 & 0 & 0 & -x_{Ac^-} & n-(1-x_{Ac^-}) & 0 \\ 0 & 0 & 0 & 0 & 0 & 0 \\ 0 & 0 & 0 & 0 & 0 & 0 \\ 0 & 0 & 0 & 1 & -1 & 0 \\ 0 & 0 & 0 & 0 & 0 & 0 \\ 0 & 0 & 0 & 0 & 0 & 0 \\ 0 & 0 & 0 & 1 & -n & 1 \\ 0 & 0 & 0 & 0 & 0 & 0 \\ 0 & 0 & 0 & 0 & 0 & 0 \\ 0 & 0 & 0 & 0 & 0 & 0 \\ 0 & 0 & 0 & 0 & 0 & -1 \end{bmatrix} \begin{matrix} \mathrm{CO} \\ H_2 \\ x \\ [Ac^-]_o \\ HAc \\ BDO \\ Et \\ CO_2 \\ H_2O \\ [H^+]_o \\ NH_4^+ \\ AcCoA \\ [Ac^-]_i \\ For^- \\ Pyr^- \\ [H^+]_i \\ NADH \\ NADPH \\ Fd_{red}^{2-} \\ ATP \end{matrix} \qquad r_c = \begin{bmatrix} q_{CO} \\ q_{H_2} \\ q_{BDO} \\ r_{HAcD} \\ r_{AcX} \\ r_{m_{ATP}} \end{bmatrix}$$

$$x_{Ac^-} = \frac{10^{(pH_o - pK_a)}}{1 + 10^{(pH_o - pK_a)}}$$

Appendix C

Hybrid metabolic (A_{hybrid}) matrix using Gibbs free energy production rate to calculate biomass growth rate

$$[A_c]_{hybrid} = \begin{bmatrix}
0 & -1 & -1 & 0 & 0 & 0 & 0 & 0 & 0 & 0 & 0 & 0 & 0 & 0 & 0 & 0 & 0 & 0 & 0 \\
0 & 0 & 0 & -2 & 0 & 0 & 0 & 0 & 0 & 0 & 0 & 0 & 0 & 0 & 0 & 0 & 0 & 0 & 0 \\
0 & 0 & 0 & 0 & 0 & 0 & 0 & 0 & 0 & 0 & 1 & 0 & 0 & 0 & 0 & 0 & 0 & 0 & -1 \\
0 & 0 & 0 & 0 & 0 & 0 & 0 & 0 & 0 & 0 & 0 & 0 & 0 & 0 & 0 & 0 & 0 & -1 & 0 \\
0 & 0 & 0 & 0 & 0 & 0 & 0 & 0 & 0 & 0 & 0 & 0 & 0 & 0 & 0 & 0 & -1 & 0 & 0 \\
0 & 0 & 0 & 0 & 0 & 0 & 0 & 1 & 0 & 0 & 0 & 0 & 0 & 0 & 0 & 0 & 0 & 0 & 0 \\
0 & 0 & 0 & 0 & 0 & 1 & 0 & 0 & 0 & 0 & 0 & 0 & 0 & -1 & 0 & 0 & 0 & 0 & 0 \\
-1 & 0 & 1 & 0 & 0 & 0 & -1 & 2 & 0 & 0 & 0 & 0 & -1 & 0 & 0 & 0 & 0 & 0 & 0 \\
0 & 2 & -1 & 0 & -1 & 1 & 0 & 0 & 0 & 0 & 0 & 0 & 0 & 0 & -1 & 0 & 0 & 0 & 0 \\
0 & 0 & 0 & 0 & 0 & 0 & 0 & 0 & 0 & 2 & -3.3 & 0 & 0 & 0 & 0 & -1 & 0 & 0 & 0 \\
0 & 0 & 0 & 0 & 0 & 0 & 0 & 0 & 0 & 0 & 0 & -0.25 & 0 & 0 & 0 & 0 & -1 & 0 & 0 \\
0 & 1 & 0 & 0 & -1 & 0 & -1 & 0 & 0 & 0 & 0 & -0.5 & 0 & 0 & 0 & 0 & 0 & 0 & 0 \\
0 & 0 & 0 & 0 & 1 & -1 & 0 & 0 & 0 & 0 & 0 & 0 & 0 & 0 & 0 & 0 & 0 & 0 & 0 \\
1 & -1 & 0 & 0 & 0 & 0 & 0 & 0 & 0 & 0 & 0 & 0 & 0 & 0 & 0 & 0 & 0 & 0 & 0 \\
0 & 0 & 0 & 0 & 1 & 0 & 1 & -2 & 0 & 0 & 0 & 0 & 0 & 0 & 0 & 0 & 0 & 0 & 0 \\
-0.5 & -2 & 2 & 3 & 0 & -4 & -1 & -3 & -1 & -3 & 3.3 & 0.25 & 0 & 0 & 0 & 0 & 0 & 0 & 0 \\
0 & -2 & 0 & 0 & 0 & -1 & 0 & -1 & -1 & 1 & 0 & 0 & 0 & 0 & 0 & 0 & 0 & 0 & 0 \\
-0.5 & -1 & 0 & 1 & 0 & 0 & 0 & 0 & 2 & 0 & 0 & 0 & 0 & 0 & 0 & 0 & 0 & 0 & 0 \\
-0.5 & 1 & 1 & 1 & 0 & -1 & -1 & 0 & -1 & -1 & 0 & 0 & 0 & 0 & 0 & 0 & 0 & 0 & 0 \\
0 & 0 & 0 & 0 & 0 & 0 & 0 & 0 & 0 & 0 & 0 & 0 & G'_{CO_2} & G'_{Et} & G'_{W} & G'_{H^+} & G'_{NH_4^+} & G'_{HAc} & G'_{Ac^-} & G'_{x}
\end{bmatrix}
\begin{matrix}
\mathrm{CO} \\ H_2 \\ x \\ [Ac^-]_o \\ HAc \\ BDO \\ Et \\ CO_2 \\ H_2O \\ [H^+]_o \\ NH_4^+ \\ AcCoA \\ [Ac^-]_i \\ For^- \\ Pyr^- \\ [H^+]_i \\ NADH \\ NADPH \\ Fd_{red}^{2-} \\ Gv_{H_4^+}^{c}
\end{matrix}$$

$$[r_c]_{hybrid} = \begin{bmatrix}
r_{FDH} \\ r_{ACAS} \\ r_{CODH} \\ r_{Hyd} \\ r_{AcS} \\ r_{EtS} \\ r_{PyrS} \\ r_{BDOS} \\ r_{Nfn} \\ r_{Rnf} \\ r_{ATPS} \\ r_{Ana} \\ q_{CO_2} \\ q_{Et} \\ q_{W} \\ q_{H^+} \\ q_{NH_4^+} \\ q_{HAc} \\ q_{Ac^-} \\ \mu
\end{bmatrix}$$

$$[A_m]_{hybrid} = \begin{bmatrix} -1 & 0 & 0 & 0 & 0 & 0 \\ 0 & -1 & 0 & 0 & 0 & 0 \\ 0 & 0 & 0 & 0 & 0 & 0 \\ 0 & 0 & 0 & -x_{Ac^-} & x_{Ac^-} & 0 \\ 0 & 0 & 0 & -(1-x_{Ac^-}) & (1-x_{Ac^-}) & 0 \\ 0 & 0 & -1 & 0 & 0 & 0 \\ 0 & 0 & 0 & 0 & 0 & 0 \\ 0 & 0 & 0 & 0 & 0 & 0 \\ 0 & 0 & 0 & 0 & 0 & 0 \\ 0 & 0 & 0 & -x_{Ac^-} & n-(1-x_{Ac^-}) & 0 \\ 0 & 0 & 0 & 0 & 0 & 0 \\ 0 & 0 & 0 & 0 & 0 & 0 \\ 0 & 0 & 0 & 1 & -1 & 0 \\ 0 & 0 & 0 & 0 & 0 & 0 \\ 0 & 0 & 0 & 0 & 0 & 0 \\ 0 & 0 & 0 & 1 & -n & 0 \\ 0 & 0 & 0 & 0 & 0 & 0 \\ 0 & 0 & 0 & 0 & 0 & 0 \\ 0 & 0 & 0 & 0 & 0 & 0 \\ G'_{CO} & G'_{H_2} & G'_{BDO} & 0 & 0 & 1 \end{bmatrix} \begin{matrix} \mathrm{CO} \\ H_2 \\ x \\ [Ac^-]_o \\ HAc \\ BDO \\ Et \\ CO_2 \\ H_2O \\ [H^+]_o \\ NH_4^+ \\ AcCoA \\ [Ac^-]_i \\ For^- \\ Pyr^- \\ [H^+]_i \\ NADH \\ NADPH \\ Fd_{red}^{2-} \\ Gv_{H_4^+}^c \end{matrix} \quad [r_c]_{hybrid} = \begin{bmatrix} q_{CO} \\ q_{H_2} \\ q_{BDO} \\ r_{HAcD} \\ r_{AcX} \\ q_G \end{bmatrix}$$

$$x_{Ac^-} = \frac{10^{(pH_o - pK_a)}}{1 + 10^{(pH_o - pK_a)}}$$

Appendix D

List of assumptions

For calculating the q_{CO} and q_{H_2} uptake rates:

- The equations for the uptake of CO and H_2 are combinations of two models:

$$q_{CO} = \frac{q_{max} p_{CO}}{K_p + p_{CO} + \frac{{p_{CO}}^2}{K_I}} \quad [106]$$

$$v_{CO} = -\frac{v_{max,CO} C_{L,CO}}{K_{S,CO} + C_{L,CO}} \left(\frac{1}{1 + \frac{C_{L,EtOH}}{K_{IE}}}\right)\left(\frac{1}{1 + \frac{C_{L,HAc}}{K_{IA}}}\right)$$

$$v_{H_2} = -\frac{v_{max,H_2} C_{L,H_2}}{K_{S,H_2} + C_{L,H_2}} \left(\frac{1}{1 + \frac{C_{L,EtOH}}{K_{IE}}}\right)\left(\frac{1}{1 + \frac{C_{L,HAc}}{K_{IA}}}\right)\left(\frac{1}{1 + \frac{C_{L,CO}}{K_{I,CO}}}\right) \quad [108]$$

- The space occupied by the enzymes that harvest the electrons, from CO (CO dehydrogenase) and H_2 (hydrogenases) in the cell, is the same for both.

For the concentrations in the intracellular space:

- CO, H_2, CO_2, ethanol and 2,3-butanediol are assumed to be permeable to the cell membrane, therefore, their intracellular and extracellular concentrations are the same.
- The intracellular pH is neutral.

Assumptions regarding biomass formation:

- The cell is composed by 30 % dry matter plus 70 % water.
- The chemical formula for cellular biomass is $CH_{1.75}O_{0.5}N_{0.25}$, hence its molar weight is 25.25 g/$Cmol_x$.

Conformation of the metabolic network:

- The H^+/ATP stoichiometric ratio for the membrane-based ATP-synthase is of 3.3.
- The Nfn complex is reversible.
- All the electrons in H_2 are harvested by bacteria through the NADPH-dependent hydrogenase.

Thermodynamics:

- Catabolism should at least generate -9.4 kJ per mole of H^+ ions exported by the Rnf reaction.

Appendix E

Calculation of intracellular concentrations of metabolites

The values of the intracellular concentrations of all metabolites present in reactions i1 – i16 (Table A.2, Appendix A) were defined using a stochastic simulation. The calculation used $1x10^6$ different combinations of the concentrations of the 17 metabolites (extra and intracellular H^+ ions are not included in the calculation) to calculate the Gibbs free energy of each metabolic reaction at physiological conditions. The pH-dependent levels of ionization and the respective concentrations of each species of the acetic acid, coenzyme-A, CO_2 and phosphoric acid, as well as ammonium were considered in the calculation (see Table E.1), along with their respective energies of formation (see Table E.2). The dissociation constants that are shown in E.1 were corrected for the temperature and the ionic strength as explained in [407]. The minimization consisted in choosing the combinations of concentrations that produced the 1% overall lowest values of the Gibbs free energy change of all the reactions in the metabolic network.

Table E.3 shows the median intracellular concentrations of the j-th metabolites ($C_{j,i}$) considered for the metabolic network calculated by the stochastic simulation along the 95% confidence range (5 and 95 percentiles) for each concentration. Table E.3 also shows the lower and upper bounds between which the concentrations of all substances are varied during the stochastic simulation. Table E.4 shows the calculated Gibbs free energies of the reaction in the network, as well as their 95% confidence range.

Table E.1 Dissociation constants of the substances involved in the metabolic reactions

Substance	K_1	K_2	**Ref.** [a]
Acetic acid	$1.778x10^{-5}$	-	1
H_2CO_3	$4.266x10^{-7}$	$5.012x10^{-11}$	1
Coenzyme-A	$4.169x10^{-9}$	-	1
Formic acid	$1.774x10^{-4}$	-	2
Ammonia	$5.623x10^{-10}$	-	1
Phosphoric acid (Pi) [b]	$6.026x10^{-8}$	-	1
Pyruvate	$3.236x10^{-3}$	-	1

[a] References: 1: [407]; 2: [408].

[b] Only the equilibrium between HPO_4^{-2} and $H_2PO_4^-$ is considered due to the intracellular pH of 7.

Table E.2 Standard Gibbs free energy and enthalpy of formation and charges of the substances involved in the proposed metabolic network

Substance	$-\Delta_f G^0$, kJ/mol	$-\Delta_f H^0$, kJ/mol	z [a]	Ref. [b]	Substance	$-\Delta_f G^0$, kJ/mol	$-\Delta_f H^0$, kJ/mol	z	Ref.
2,3-butanediol	321.8	544.8	0	1,2	Formic acid	371.8	425.3	0	5
Acetyl-CoA	188.5	0.00	0	3	$Formate^-$	351.0	425.6	-1	3
Acetic acid	396.5	485.8	0	3	H^+	0.0	0.0	1	3
$Acetate^-$	369.3	486.0	-1	3	H_2 (g)	0.0	0.0	0	3
ADP	1972.0	2638.5	0	3	H_2O	237.2	285.8	0	3
ATP	2838.2	3627.9	0	3	Lactic acid	538.5	686.2	0	5,6
Cells	67.0	91.0	0	4	$Lactate^-$	516.7	686.6	-1	3
CO_2 (g)	394.4	393.5	0	3	NAD^-	0.0	0.0	-1	3
H_2CO_3	623.1	699.6	0	3	$NADH^{-2}$	-22.7	31.94	-2	3
HCO_3^-	586.8	692.0	-1	3	$NADP^{-3}$	835.2	0.0	-3	3
CO_3^{-2}	527.8	677.1	-2	3	$NADPH^{-4}$	809.2	29.18	-4	3
HCoA	47.8	0.0	0	3	NH_3	26.5	80.3	0	3
CoA^-	0.0	0.0	-1	3	NH_4^+	79.3	132.5	1	3
Ethanol	181.6	288.3	0	3	$H_2PO_3^-$ (Pi)	1137.3	1302.6	-1	3
Ferredoxin (oxidized)	0.0	0.0	-2	3	HPO_3^{-2} (Pi)	1096.1	1299.0	-2	3
Ferredoxin (reduced)	-38.1	0.0	-2	3	$Pyruvate^-$	472.3	596.2	-1	3

[a] Charge.

[b] References: 1: [409]; 2 [410]; 3: [407]; 4: [263]; 5: [408]; 6: [411].

Table E.3 Calculated intracellular concentrations of metabolites

Substance	$C_{j,i}$, mol/m³				
	Median	95% confidence range		Bounds used during stochastic simulation	
		Lower	Upper	Lower	Upper
2,3-butanediol	1.76	0.08	43.4	0.06	55.48
Acetyl-CoA	1.49	0.03	11.4	0.01	13.10
Acetic acid	0.23	0.01	11.95	0.01	50
ADP	7.58	0.84	38.3	0.42	42.3
ATP	4.08	1.23	50.5	1.04	104.4
CO [a]	$3.7x10^{-3}$	$1.0x10^{-5}$	$6.5x10^{-1}$	$6.2x10^{-6}$	1.0
CO_2 [a]	$5.4x10^{-2}$	$1.4x10^{-3}$	$8.4x10^{-1}$	$1.0x10^{-5}$	1.0
Coenzyme A	0.14	0.04	2.13	0.04	3.63
Ethanol	16.6	0.29	428.7	0.22	652.2
Ferredoxin (oxidized)	1.56	0.02	36.34	0.01	50.0

Substance	$C_{j,i}$, mol/m³				
	Median	95% confidence range		Bounds used during stochastic simulation	
		Lower	Upper	Lower	Upper
Ferredoxin (reduced)	1.45	0.02	29.02	0.01	50.0
Formate	0.49	0.03	8.91	0.01	50.0
H_2 [a]	$9.2x10^{-2}$	$6.0x10^{-4}$	$7.6x10^{-1}$	$5.5x10^{-5}$	1.0
NAD^+	10.7	0.81	54.2	0.64	64.0
NADH	0.47	0.07	5.44	0.06	6.49
$NADP^+$	1.43	0.20	13.9	0.16	15.9
NADPH	0.52	0.10	5.76	0.08	7.27
NH_4^+	0.27	0.01	7.45	0.01	10.0
Phosphoric acid	1.90	0.05	8.38	0.01	10.0
Pyruvic acid	0.03	0.00	10.8	0.00	45.9
H^+ ions [b]	$1.0x10^{-4}$	n/a	n/a	n/a	n/a

[a] The values are partial pressures in atm.

[b] The intracellular pH is equal to 7 and constant. n/a means not applicable.

Note: The shown concentrations for CO_2, acetic, formic, pyruvic and phosphoric acids, as well as for coenzyme A and NH_4^+ represent the sum of their dissociated forms

Experimental NADPH and $NADP^+$ concentrations [74,75,113] fall within the confidence range here calculated. The intracellular concentration of formate has not been reported for acetogens, yet the estimations fall in the same order of magnitude as lactate and pyruvate concentrations in *C. autoethanogenum* [74,75].

Table E.4 Calculated Gibbs free energy change in the intracellular reactions during the stochastic minimization

Reaction	$\Delta_r G'$, kJ/mol			Reaction	$\Delta_r G'$, kJ/mol		
	Median	95% confidence range			Median	95% confidence range	
		Lower	Higher			Lower	Higher
FDH	18.9	8.5	35.2	PyrS	55.3	36.0	78.1
CODH	-55.7	-78.0	-34.1	BDOS	-50.4	-82.3	-24.5
Hyd	-36.6	-56.4	-11.7	AcX	2.2	-4.4	10.5
FHL	1.3	-5.4	12.7	Nfn	44.1	26.0	63.0
ACAS	-92.8	-118.9	-67.7	Rnf	-40.1	-57.1	-26.7
AcS	4.7	-3.2	32.0	ATPS	158.9	151.3	171.0
EtS	66.7	45.8	89.0	Ana	-189.1	-221.4	-166.1

Appendix F

Calculation of experimental net conversion rates and reconstruction of relevant experimental variables

The information provided by the reports which served as sources of experimental data is incomplete for our analysis. Based on the concentrations data that is provided in the source reports we re-calculate the experimental net conversion rates, although some of them are indeed reported. This is done to check the consistency of the reported rates and to produce a data set that is consistent with mass balances of species in the gas and liquid phases of the bioreactor, gas-liquid equilibrium relations and with element conservation relations. The calculation is also done with the objective of reconstructing the dissolved gas concentrations in the liquid, variables not provided by the experimental source reports, which are essential to the proposed kinetic and thermodynamic analysis of the fermentation process. In addition, the composition of the off-gas, as well as the liquid and gas outflow rates are also calculated.

A last remark is made of the signs of the net conversion rates: the rates are negative when the specie is consumed by bacteria and positive when the specie is produced.

Table F.1 shows all the equations used in this process:

Table F.1 System of equations used to calculate net conversion rates and reconstruct un-reported experimental data

Mass balances in the liquid phase. Units are [mol/h] for all equations except equations F.9, where the units are [kg/h].		
CO in the liquid phase	$0 = q_{CO}C_xV_L + k_La_{CO}(C^*_{CO} - C_{CO})V_L - C_{CO}\frac{F_{L,out}}{\rho_L}$	(F.1)
H_2 in the liquid phase	$0 = q_{H_2}C_xV_L + k_La_{H_2}(C^*_{H_2} - C_{H_2})V_L - C_{H_2}\frac{F_{L,out}}{\rho_L}$	(F.2)
CO_2 in the liquid phase	$0 = q_{CO_2}C_xV_L + k_La_{CO_2}(C^*_{CO_2} - C_{CO_2})V_L - C_{CO_2}\frac{F_{L,out}}{\rho_L}$	(F.3)
Ethanol in the liquid phase	$0 = q_{Et}C_xV_L + k_La_{Et}(C^*_{Et} - C_{Et})V_L - C_{Et}\frac{F_{L,out}}{\rho_L}$	(F.4)
Total acetic acid in the liquid phase	$0 = q_{AcT}C_xV_L - C_{AcT}\frac{F_{L,out}}{\rho_L}$	(F.5)
2,3-butanediol in the liquid phase	$0 = q_{BDO}C_xV_L - C_{BDO}\frac{F_{L,out}}{\rho_L}$	(F.6)
Cells in the liquid phase	$0 = \mu C_xV_L - C_x\frac{F_{L,out}}{\rho_L}$	(F.7)
H^+ balance in liquid	$0 = C_{T,in}\frac{F_{T,in}}{\rho_T} - q_{H^+}C_xV_L$	(F.8)

Total liquid phase balance	$0 = F_{L,in} - F_{L,out} + k_L a_{CO}(C^*_{CO} - C_{CO})V_L MW_{CO} + k_L a_{H_2}(C^*_{H_2} - C_{H_2})V_L MW_{H_2} + k_L a_{CO_2}(C^*_{CO_2} - C_{CO_2})V_L MW_{CO_2} + k_L a_{Et}(C^*_{Et} - C_{Et})V_L MW_{Et} - y_{W,out}F_{G,out}MW_W + F_{T,in}$	(F.9)
Mass balances in the gas phase. Units are [mol/h] for all equations except equation F.16, which is dimensionless.		
CO in the gas phase	$0 = F_{G,in}y_{CO,in} - F_{G,out}y_{CO,out} - k_L a_{CO}(C^*_{CO} - C_{CO})V_L$	(F.10)
H_2 in the gas phase	$0 = F_{G,in}y_{H_2,in} - F_{G,out}y_{H_2,out} - k_L a_{H_2}(C^*_{H_2} - C_{H_2})V_L$	(F.11)
CO_2 in the gas phase	$0 = F_{G,in}y_{CO_2,in} - F_{G,out}y_{CO_2,out} - k_L a_{CO_2}(C^*_{CO_2} - C_{CO_2})V_L$	(F.12)
Ethanol in the gas phase	$0 = F_{G,in}y_{Et,in} - F_{G,out}y_{Et,out} - k_L a_{Et}(C^*_{Et} - C_{Et})V_L$	(F.13)
Inert gas in the gas phase	$0 = F_{G,in}y_{inert,in} - F_{G,out}y_{inert,out}$	(F.14)
Total gas phase balance	$0 = F_{G,in} - F_{G,out} - k_L a_{CO}(C^*_{CO} - C_{CO})V_L - k_L a_{H_2}(C^*_{H_2} - C_{H_2})V_L - k_L a_{CO_2}(C^*_{CO_2} - C_{CO_2})V_L - k_L a_{Et}(C^*_{Et} - C_{Et})V_L + y_{W,out}F_{G,out}$	(F.15)
Summation relation	$0 = 1 - y_{CO,out} - y_{H_2,out} - y_{CO_2,out} - y_{Et,out} - y_{W,out} - y_{inert,out}$	(F.16)
Equilibrium relations. Units are [mol/(Cmol$_x$*h)] for equations F.17 – F.18 and [mol/m^3] for equations F.19 – F.22.		
Total acetic acid in the liquid phase	$q_{AcT} = q_{Ac^-} + q_{HAc}$	(F.17)
Acetic acid equilibrium	$\frac{q_{Ac^-}}{q_{HAc}} = 10^{(pH - pK_a)}$	(F.18) [a]
CO saturation	$C^*_{CO} = k_{H,CO}y_{CO,out}p$	(F.19)
H_2 saturation	$C^*_{H_2} = k_{H,H_2}y_{H_2,out}p$	(F.20)
CO_2 saturation	$C^*_{CO_2} = k_{H,CO_2}y_{CO_2,out}p$	(F.21)
Ethanol saturation	$C^*_{Et} = k_{H,Et}y_{Et,out}p$	(F.22)
Relations for conservation of the elements. Units are [mol/(Cmol$_x$*h)].		
Carbon conservation	$0 = q_{CO} + q_{CO_2} + 2q_{Ac^-} + 2q_{HAc} + 2q_{Et} + 4q_{BDO} + \mu$	(F.23)
Hydrogen conservation	$0 = 2q_{H_2} + 3q_{Ac^-} + 4q_{HAc} + 6q_{Et} + 10q_{BDO} + \frac{7}{4}\mu + 4q_{NH_4^+} + 2q_W + q_{H^+}$	(F.24)
Oxygen conservation	$0 = q_{CO} + 2q_{CO_2} + 2q_{Ac} + 2q_{HAc} + q_{Et} + 2q_{BDO} + \frac{1}{2}\mu + q_W$	(F.25)
Nitrogen conservation	$0 = \frac{1}{4}\mu + q_{NH_4^+}$	(F.26)
Charge conservation	$0 = -q_{Ac^-} + q_{NH_4^+} + q_{H^+}$	(F.27)

[a] Equations is derived from the assumption that the molar concentrations of the two forms of acetic acid are at equilibrium, *i.e.*, the activity coefficients of the two species equal one.

In the inventory of equations there are 27 parameters of which the value is calculated, *i.e.*, 12 net conversion rates (q_{CO}, q_{H_2}, q_{CO_2}, q_{AcT}, q_{Ac^-}, q_{HAc}, q_{Et}, q_{BDO}, μ, q_W, $q_{NH_4^+}$ and q_{H^+}), the concentrations for the dissolved gases in the liquid phase (C_{CO}, C_{H_2} and C_{CO_2}), the saturation concentrations of the substances for which mass transfer rates are quantified (C_{CO}^*, $C_{H_2}^*$, $C_{CO_2}^*$ and C_{Et}^*), the mole fractions of these four substances in the off-gas plus the fraction of the inert gas ($y_{CO,out}$, $y_{H_2,out}$, $y_{CO_2,out}$, $y_{Et,out}$ and $y_{inert,out}$), the molar flow rate of the off-gas ($F_{G,out}$), the mass flow rate of the liquid outflow ($F_{L,out}$) and mass input of the titrant solution ($F_{T,in}$).

The information provided by the reports which were source of the experimental data [74,75,401] are the concentrations of ethanol, total acetic acid (in dissociated and undissociated forms), 2,3-butanediol and cells in the liquid phase (C_{Et}, C_{Ac}, C_{BDO} and C_x, respectively). In addition, the volume of the liquid broth (V_L), the liquid and gas inflows ($F_{G,in}$), the concentration of the titrant NH_4OH ($C_{T,in}$), the composition of the gas inflow ($y_{CO,in}$, $y_{H_2,in}$, $y_{CO_2,in}$ and $y_{inert,in}$) and the process pressure (p) are also explicitly provided. The dilution rate is also a variable provided in those reports, which is here used to calculate the rate of liquid inflow to the bioreactor ($F_{L,in}$). Table F.2 shows the values of the parameters provided by the data source reports, which are used to solve the system of equations.

Table F.2 also contains the net-conversion rates reported for CO, H_2, CO_2, total acetic acid, ethanol and in some cases 2,3-butanediol. The carbon and electron balance gaps calculated for the average values of the reported conversion rates are also included in the table. The carbon gaps reach 20% for cases 1, 3, 4, 8 and 9; yet, for the other cases the gaps are significantly lower. The presence of carbon and electron gaps larger than 5 – 10% would commonly lead to the assessment of the possible presence of un-measured substances in the experiments. Here, we assumed that this is not that case, instead we assumed that the reported conversion rates were calculated through inaccurate mass balances. Therefore, we solved the system equations above to obtain, as stated in [412], "true and accurate rate-values", besides calculating the other mentioned un-measured or un-reported data.

The density of the liquid broth (ρ_L) is assumed to be 1000 kg/m^3, whereas the density of the titrant solution (ρ_T) was found to be approximately 1100 kg/m^3 as function of the concentration (5 M as provided in the sources reports) in physical properties tables in [28]. The Henry's coefficients for equations F.17 – F.20 are 0.803, 0.731, 24.9, 65372 mol/(m^3*atm) [292] for CO, H_2, CO_2 and ethanol, respectively. Since equation F.9 uses units kg/h, the molecular weights of the substances involved in the equation are used in units mol/kg to convert moles into mass units.

Table F.2 Experimental data provided in the data source reports

Variable/parameter		Case											
		1	**2**	**3** [a]	**4** [a]	**5** [a]	**6** [b]	**7** [a]	**8**	**9**	**10**	**11**	**12**
Source of data		[74]		[75]					[74]		[401]		
Concentrations in the liquid phase													
Gas inflow rate	mL/min	46.5	46.5	46.5	46.5	46.5	46.5	46.5	46.5	110	30	30	32
	mol/h	0.110	0.110	0.110	0.110	0.110	0.110	0.110	0.110	0.259	0.071	0.071	0.075
Molar fractions at gas inlet	CO	0.60	0.60	0.50	0.50	0.50	0.50	0.50	0.15	0.15	0.02	0.02	0.00
	H_2	0.00	0.00	0.20	0.20	0.20	0.20	0.20	0.45	0.45	0.65	0.65	0.67
	CO_2	0.00	0.00	0.20	0.20	0.20	0.20	0.20	0.00	0.00	0.23	0.23	0.23
	Inert gas	0.40	0.40	0.10	0.10	0.10	0.10	0.10	0.40	0.40	0.00	0.00	0.00
Concentrations in the liquid phase [c]													
Volume of liquid, m^3 ($x10^{-3}$)		0.75	0.75	0.75	0.75	0.75	0.75	0.75	0.75	0.75	0.75	0.75	0.75
Dilution rate, 1/h		0.042	0.042	0.042	0.042	0.042	0.042	0.042	0.042	0.042	0.042	0.021	0.020
Liquid inflow rate, kg/h ($x10^{-2}$)		3.13	3.13	3.13	3.13	3.13	3.13	3.13	3.13	3.13	3.13	1.56	1.47
pH		5.0	5.0	5.0	5.0	5.0	5.0	5.0	5.0	5.0	5.0	5.0	5.0
C_x, mol/m^3		18.6±1.3	56.6±4.3	17.8±0.3	20.2±0.3	43.6±3.8	52.3	55.4±0.6	18.2±1.7	57.4±2.6	13.5±0.8	21.4±0.4	7.1±0.8
$C_{AT,o}$, mol/m^3		35.5±3.0	103.0±9.2	69.8±2.6	77.2±4.1	136.8±7.8	133.7	131.0±6.6	11.8±1.5	63.0±6.2	83.8±5.7	99.5±16.3	41.8±7.0
C_{Et}, mol/m^3		13.7±1.6	82.2±5.6	11.5±1.1	13.1±2.6	62.0±11.6	111.7	122.0±5.6	97.0±9.3	250±10.9	104.1±9.3	210.7±8.5	51.3±5.7
C_{BDO}, mol/m^3 [d]		n.r.	2.6±0	0.0	0.0	0.43±0.16	2.4	2.2±0.8	n.r.	n.r.	n.r.	n.r.	n.r.
Titrant feed concentration, mol/m^3		5000	5000	5000	5000	5000	5000	5000	5000	5000	5000	5000	5000
Stirring speed, 1/s		8.5	11.1	8.3	8.3	9.7	10.8	10.8	10.8	16.7	20.0	13.3	8.3

Variable/parameter	Case											
	1	2	3 [a]	4 [a]	5 [a]	6 [b]	7 [a]	8	9	10	11	12
Reported net conversion rates, mmol/(Cmol$_x$*h) [c]												
q_{CO}	-551±12	-778±24	-487±13	-462±13	-621	-798	-747±25	-508±31	-520±21	-94±0	-38±0	0
q_{H_2}	13±0	13±0	-328±10	-308±10	-316	-311	-290±10	-838±77	-748±43	-2754±61	-1652±28	-1202±167
q_{CO_2}	418±6	534±12	144±3	141±3	220	326	308±8	54.8±4	111±1	-1002±22	-568±22	-495±72
q_{AT}	81±5	79±3	167	154	131	106	99	27±3	48±4	256±17	96±16	119±10
q_{Et}	32±1	65±2	30	30	63	93	96	229±5	200±13	322±28	207±9	148±12
μ	42	42	42	42	42	42	42	42	42	42	21	20
q_{BDO} [d]	n.r.	2.2±0	0	0	0.3	2.3	2.3	n.r.	n.r.	n.r.	n.r.	n.r.
Carbon balance gap [e], %	24.4	12.1	19.0	19.2	4.8	2.9	0.2	19.8	24.8	9.3	3.4	11.8
Electron balance gap [e], %	11.2	6.2	14.3	14.2	5.5	1.7	4.2	16.3	16.4	6.7	1.3	16.7

[a] The errors in the net conversion rates for these cases were not reported in a table or figure; the errors were only mentioned in the text of the article.

[b] Only one data point was reported, therefore, the calculation of errors was not possible.

[c] The data points where the error is 0 correspond to data gathered from figures where the error was too small to be perceived.

[d] n.r. means 'not reported'.

[e] Calculated from the provided average experimental net conversion rates.

The calculation of the mass transfer coefficients ($k_L a$) required making several assumptions about the fermentation broth, the dimensions of the bioreactor vessel and the dimensions of the stirrer; the assumptions are listed in Table F.3. The assumptions were necessary since such details were not reported in none of the sources of experimental data shown in Table F.2; the relevant details that were reported are the total vessel volume of 1.4 L, the liquid volume of 0.75 L, the stirring speeds and the gas inflow rates for all the experiments, as shown in Table F.2. Furthermore, the calculation of $k_L a$ was based on the power input by the stirrer (P_S in equation F.26) and by the gas sparging. The power input by the gas sparging is quantified using the average superficial gas velocity, considering that the gas in and out flows ($F_{G,in}$ and $F_{G,out}$, respectively) are different. The stirrer power input is not corrected for the effect of the gas sparging since its effect is negligible due to the very low gas flow rate in the experiments. Moreover, $k_L a$ is also corrected for the process temperature and the film diffusivity (Đ) of the gases in pure water compared to that of O_2 (see equation F.27), because equation F.27 was developed and parameterized for O_2 transfer to pure water.

$$P_S = N_P \rho N^3 {D_S}^5 \tag{F.26}$$

$$k_L a_j = f_{broth}\left[1.022^{(T-293.15)}\right]\left[0.002\left(\frac{P_{sG}}{V_L}\right)^{0.7} {v_{Gs}^c}^{0.2}\right]\left(\frac{Đ_j}{Đ_{O_2}}\right)^{0.5} \tag{F.27}$$

Table F.3 Assumptions made for the calculation of mass transfer coefficients

Item	Units	Value
Fermentation broth		
Density of the fermentation broth (ρ)	kg/m^3	1000
Coalescence characteristics of the fermentation broth	-	Non-coalescent
Bioreactor vessel		
Height-to-diameter ratio of the bioreactor vessel	-	1.5
Stirrer		
Vessel diameter to stirrer diameter (D_s) ratio	-	3
Type of impeller	-	Six flat blades (Rushton)
Stirrer diameter to height of blade (H_s) ratio	-	5
Stirrer power number (N_P)	-	5

Equation F.27 contains a correction factor for the mass transfer coefficient (f_{broth}); it includes corrections due to the differences between the experimental set-up and the case for which the model was constructed and parametrized; this means that f_{broth} considers the effects of the likely different dimensions of the bioreactor and internals and the effects of the components of the liquid media that affect mass transfer, *e.g.*, salts, acetic acid and ethanol. The value of f_{broth} is 3, a value chosen based on a sensitivity analysis, where

f_{broth} was varied from 1.5 to 3. The value of f_{broth} was selected based on the calculated dissolved concentrations of CO and H_2, *i.e.*, values lower than 3 produced negative concentrations of CO and H_2, mainly in two of the experimental cases (see Figures F.1 and F.2). The obtained large enhancement on the mass transfer coefficient may be sustained on the expected inhibition of coalescence due to the presence of ethanol, acetic acid and salts in the fermentation media [403,413,414]. In addition, Table F.4 shows the driving forces for mass transfer calculated in the sensitivity analysis.

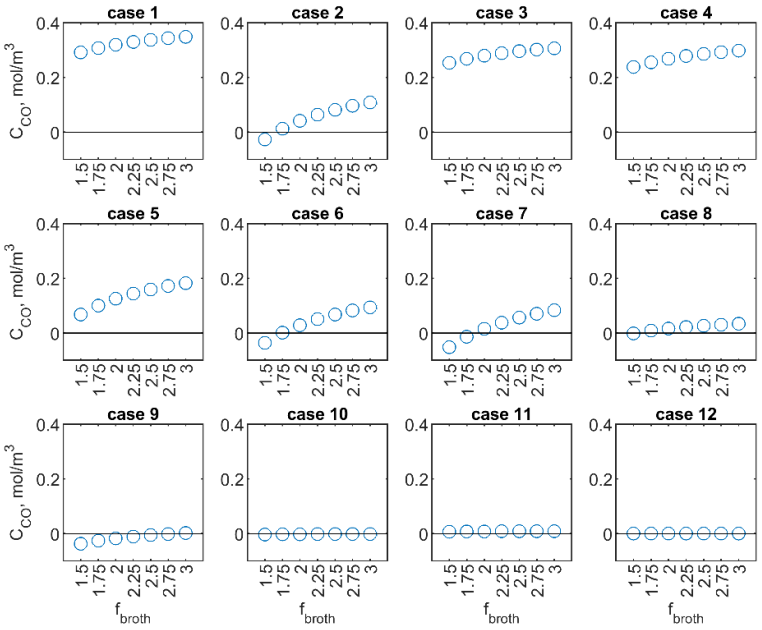

Figure F.1 CO concentration in the liquid calculated using different values of f_{broth}

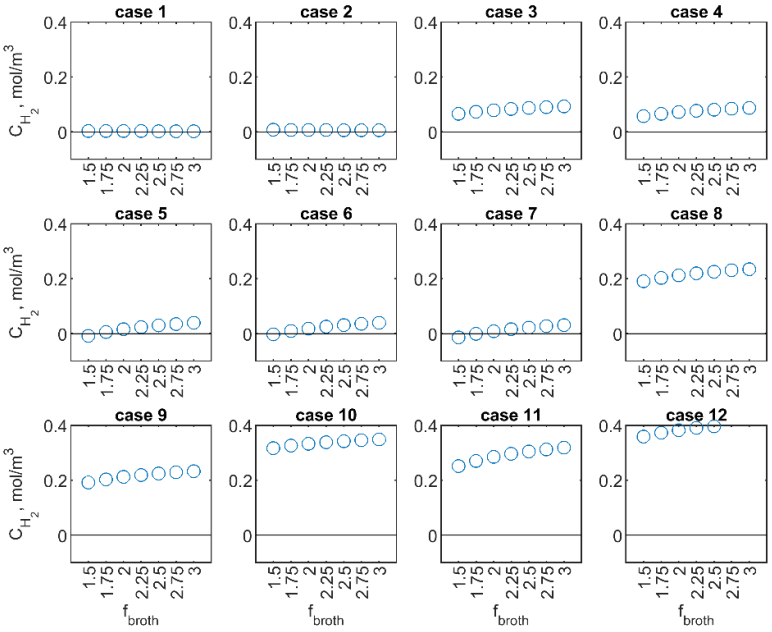

Figure F.2 H_2 concentration in the liquid calculated using different values of f_{broth}

In Table F.4, the cases where the driving force is close to one are far from equilibrium and mass transfer rate is close to its maximum. The cases where the driving force is higher than one are obtained when the calculated dissolved concentrations of the gases were lower than zero. For case 10, the CO concentration was never higher than zero, not even after a small test where f_{broth} was increased to 5; this could mean that there are measurement errors on the concentrations of other substances which make q_{CO} fall into a value that does not allow the calculation of a positive C_{CO}. Lastly, the driving forces close to zero, especially for CO_2 and ethanol, represent cases where the dissolved concentration close to equilibrium with the gas phase.

Table F.5 shows the summary of the results obtained from solving the system of equations (from F.1 to F.25) using the values of concentrations shown in Table F.2 as inputs. Only the average concentrations were used in the calculation.

Table F.4 Driving force for CO, H_2, CO_2 and ethanol mass transfer at different values of f_{broth}

Substance	f_{broth}	$\left(\frac{C^* - C}{C^*}\right)$											
	Case	1	2	3	4	5	6	7	8	9	10	11	12
CO	1.5	0.283	1.109	0.297	0.334	0.773	1.163	1.240	1.017	1.888	309.191	0.386	0.000
	1.75	0.243	0.950	0.254	0.286	0.662	0.997	1.063	0.872	1.618	265.021	0.331	0.000
	2	0.213	0.832	0.222	0.250	0.580	0.872	0.930	0.763	1.416	231.894	0.289	0.000
	2.25	0.189	0.739	0.198	0.222	0.515	0.775	0.827	0.678	1.258	206.128	0.257	0.000
	2.5	0.170	0.665	0.178	0.200	0.464	0.698	0.744	0.610	1.133	185.515	0.231	0.000
	2.75	0.155	0.605	0.162	0.182	0.422	0.634	0.676	0.555	1.030	168.650	0.210	0.000
	3	0.142	0.554	0.148	0.167	0.386	0.581	0.620	0.509	0.944	154.596	0.193	0.000
H_2	1.5	-1.657	-0.867	0.448	0.511	1.089	1.033	1.178	0.315	0.302	0.170	0.350	0.205
	1.75	-1.420	-0.743	0.384	0.438	0.934	0.886	1.010	0.270	0.259	0.145	0.300	0.176
	2	-1.243	-0.650	0.336	0.383	0.817	0.775	0.884	0.236	0.226	0.127	0.262	0.154
	2.25	-1.105	-0.578	0.299	0.341	0.726	0.689	0.786	0.210	0.201	0.113	0.233	0.137
	2.5	-0.994	-0.520	0.269	0.307	0.654	0.620	0.707	0.189	0.181	0.102	0.210	0.123
	2.75	-0.904	-0.473	0.244	0.279	0.594	0.564	0.643	0.172	0.165	0.093	0.191	0.112
	3	-0.828	-0.434	0.224	0.256	0.545	0.517	0.589	0.158	0.151	0.085	0.175	0.103
CO_2	1.5	-0.063	-0.033	-0.004	-0.005	-0.009	-0.011	-0.011	-0.032	-0.025	0.007	0.014	0.009
	1.75	-0.054	-0.028	-0.004	-0.004	-0.008	-0.009	-0.009	-0.028	-0.021	0.006	0.012	0.008
	2	-0.047	-0.025	-0.003	-0.004	-0.007	-0.008	-0.008	-0.024	-0.019	0.006	0.010	0.007
	2.25	-0.042	-0.022	-0.003	-0.003	-0.006	-0.007	-0.007	-0.021	-0.017	0.005	0.009	0.006
	2.5	-0.038	-0.020	-0.003	-0.003	-0.006	-0.006	-0.006	-0.019	-0.015	0.004	0.008	0.006
	2.75	-0.034	-0.018	-0.002	-0.003	-0.005	-0.006	-0.006	-0.018	-0.014	0.004	0.007	0.005
	3	-0.032	-0.017	-0.002	-0.002	-0.005	-0.005	-0.005	-0.016	-0.012	0.004	0.007	0.005
Ethanol	1.5	-3.6×10^{-5}	-1.9×10^{-5}	-3.5×10^{-5}	-3.5×10^{-5}	-2.2×10^{-5}	-1.6×10^{-5}	-1.6×10^{-5}	-1.8×10^{-5}	-1.4×10^{-5}	-0.2×10^{-5}	-0.5×10^{-5}	-2.5×10^{-5}
	1.75	-3.1×10^{-5}	-1.6×10^{-5}	-3.0×10^{-5}	-3.0×10^{-5}	-1.9×10^{-5}	-1.4×10^{-5}	-1.4×10^{-5}	-1.6×10^{-5}	-1.2×10^{-5}	-0.2×10^{-5}	-0.4×10^{-5}	-2.1×10^{-5}

Substance	f_{broth}	$\left(\frac{C^* - C}{C^*}\right)$											
	Case	1	2	3	4	5	6	7	8	9	10	11	12
	2	-2.7x10^{-5}	-1.4x10^{-5}	-2.6x10^{-5}	-2.6x10^{-5}	-1.7x10^{-5}	-1.2x10^{-5}	-1.2x10^{-5}	-1.4x10^{-5}	-1.1x10^{-5}	-0.1x10^{-5}	-0.4x10^{-5}	-1.9x10^{-5}
	2.25	-2.4x10^{-5}	-1.2x10^{-5}	-2.3x10^{-5}	-2.3x10^{-5}	-1.5x10^{-5}	-1.1x10^{-5}	-1.1x10^{-5}	-1.2x10^{-5}	-0.9x10^{-5}	-0.1x10^{-5}	-0.3x10^{-5}	-1.7x10^{-5}
	2.5	-2.1x10^{-5}	-1.1x10^{-5}	-2.1x10^{-5}	-2.1x10^{-5}	-1.3x10^{-5}	-1.0x10^{-5}	-1.0x10^{-5}	-1.1x10^{-5}	-0.8x10^{-5}	-0.1x10^{-5}	-0.3x10^{-5}	-1.5x10^{-5}
	2.75	-1.9x10^{-5}	-1.0x10^{-5}	-1.9x10^{-5}	-1.9x10^{-5}	-1.2x10^{-5}	-0.9x10^{-5}	-0.9x10^{-5}	-1.0x10^{-5}	-0.8x10^{-5}	-0.1x10^{-5}	-0.3x10^{-5}	-1.4x10^{-5}
	3	-1.8x10^{-5}	-0.9x10^{-5}	-1.7x10^{-5}	-1.7x10^{-5}	-1.1x10^{-5}	-0.8x10^{-5}	-0.8x10^{-5}	-0.9x10^{-5}	-0.7x10^{-5}	-0.1x10^{-5}	-0.2x10^{-5}	-1.2x10^{-5}

Table F.5 Results from the calculation of dissolved gas concentrations and the reconstruction of off-gas composition

Variable/parameter		Case											
		1	2	3	4	5	6	7	8	9	10	11	12
Detailed gas phase description													
y_{in} [a]	CO	0.60	0.60	0.50	0.50	0.50	0.50	0.50	0.15	0.15	0.02	0.02	0.00
	H_2	0.00	0.00	0.20	0.20	0.20	0.20	0.20	0.45	0.45	0.65	0.65	0.67
	CO_2	0.00	0.00	0.20	0.20	0.20	0.20	0.20	0.00	0.00	0.23	0.23	0.23
	Inert gas	0.40	0.40	0.10	0.10	0.10	0.10	0.10	0.40	0.40	0.00	0.00	0.00
y_{out}	CO	0.51	0.30	0.45	0.45	0.37	0.28	0.27	0.08	0.05	0.00	0.01	0.00
	H_2	0.002	0.006	0.16	0.16	0.12	0.11	0.10	0.38	0.37	0.52	0.53	0.62
	CO_2	0.04	0.20	0.22	0.23	0.33	0.42	0.43	0.01	0.02	0.17	0.19	0.21
	Ethanol	0.000	0.001	0.000	0.000	0.001	0.002	0.002	0.001	0.004	0.002	0.003	0.001
	Inert gas	0.39	0.43	0.10	0.11	0.12	0.13	0.13	0.46	0.49	0.25	0.21	0.11
	Water	0.06	0.06	0.06	0.06	0.06	0.06	0.06	0.06	0.06	0.06	0.06	0.06
$F_{G,in}$, mol/h [a]		0.110	0.110	0.110	0.110	0.110	0.110	0.110	0.110	0.259	0.071	0.071	0.075
$F_{G,out}$, mol/h		0.113	0.102	0.106	0.104	0.089	0.084	0.082	0.095	0.213	0.029	0.034	0.069
Detailed liquid phase description													
C_x, mol/m^3 [a]		18.6	56.6	17.8	20.2	43.6	52.3	55.4	18.2	57.4	13.5	21.4	7.1

$C_{AT,o}$, mol/m^3 [a]	35.5	103.0	69.8	77.2	136.8	133.7	131.0	11.8	63.0	83.8	99.5	41.8
$C_{HAc,o}$, mol/m^3 [b]	9.0	26.1	17.7	19.5	34.6	33.8	33.2	3.0	15.9	21.2	25.2	10.6
$C_{Ac^-,o}$, mol/m^3 [b]	26.5	76.9	52.1	57.7	102.2	99.9	97.8	8.8	47.1	62.6	74.3	31.2
C_{et}, mol/m^3 [a]	13.7	82.2	11.5	13.1	62.0	111.7	122.0	97.0	250	104.1	210.7	51.3
C_{BDO}, mol/m^3 [a]	0.01	2.6	0.01	0.01	0.43	2.4	2.2	0.01	0.01	0.01	0.01	0.01
C_{CO}, mol/m^3	0.349	0.109	0.306	0.298	0.182	0.094	0.083	0.033	0.002	$1x10^{-10}$	0.009	$2x10^{-10}$
C_{H_2}, mol/m^3	0.002	0.006	0.092	0.087	0.040	0.039	0.031	0.234	0.233	0.348	0.318	0.405
C_{CO_2}, mol/m^3	1.09	5.03	5.57	5.69	8.14	10.39	10.72	0.19	0.51	4.17	4.62	5.22
$F_{L,in}$, kg/h ($x10^{-2}$) [c]	3.13	3.13	3.13	3.13	3.13	3.13	3.13	3.13	3.13	3.13	1.56	1.47
$F_{L,out}$, kg/h ($x10^{-2}$)	3.14	3.18	3.17	3.17	3.23	3.23	3.23	3.15	3.21	3.23	1.64	1.49
$F_{T,in}$, kg/h ($x10^{-3}$)	0.22	0.64	0.39	0.44	0.80	0.80	0.79	0.09	0.43	0.47	0.29	0.11
*Calculated net conversion rates, mmol/($Cmol_x$*h)*												
q_{CO}	-612	-817	-564	-555	-668	-800	-780	-616	-647	-111	-44	0
q_{H_2}	14	14	-355	-350	-347	-322	-323	-979	-857	-3071	-1740	-1422
q_{CO_2}	345	483	133	132	225	337	330	52	100	-1142	-626	-558
μ	42	42	42	42	43	43	43	42	43	43	22	20
q_{Et}	32	65	29	29	64	96	98	234	205	337	222	153
q_{HAc}	20	20	42	41	34	28	26	7	12	68	26	29
q_{Ac^-}	60	58	124	121	101	82	76	20	35	200	76	87
q_{BDO}	0	2	0	0	0	2	2	0	0	0	0	0
$q_{NH_4^+}$	-10	-11	-11	-11	-11	-11	-11	-10	-11	-11	-5	-5
q_{H_2O}	-292	-393	-83	-82	-139	-216	-206	202	126	1501	859	721
q_{H^+}	70	68	134	131	112	93	87	31	46	211	81	92

[a] Data provided in the source reports, see Table F.1.

[b] Calculated from equilibrium relations (equations F.17 and F.18).

[c] Calculated from provided dilution rates, see Table F.1.

Table F.6 Turn-over times of CO and H_2

Case	1	2	3	4	5	6	7	8	9	10	11	12
Turn-over times, s [a]												
CO	0.110	0.008	0.110	0.096	0.023	0.008	0.007	0.011	0.000	0.000	0.034	n.a.
H_2	n.a.	n.a.	0.053	0.044	0.009	0.008	0.006	0.047	0.017	0.030	0.031	0.144

[a] n.a. means not applicable.

As suspected, there are differences between the in and out flows of the gas and the liquid phases. Assuming the liquid outflow is the same as the inflow would not produce significant errors as their difference is 5 % at most (in case 11). However, for the gas phase, the difference between the in and outflow is generally much higher than that for the liquid, especially on the cases where H_2 content in the gas feed is high (cases 10 to 12) where the gas flow rate is reduced by 51 and 59 %. That is because the major components of the gas feed (H_2 and CO_2) are both consumed. On the cases where CO is dominant over H_2 in the gas feed, CO_2 is produced as CO is consumed, thus the variation in the gas flow rates is small.

The components and final results of the calculation of the mass transfer coefficients are shown in Table F.7.

Table F.7 Results from the calculation of mass transfer coefficients

Variable/parameter	Case											
	1	2	3	4	5	6	7	8	9	10	11	12
Stirring speed, 1/s	8.5	11.1	8.3	8.3	9.7	10.8	10.8	10.8	16.7	20.0	13.3	8.3
P_{SG}/V_L, W/m^3	225	498	212	212	330	465	465	465	1693	2926	867	212
v_{Gs}^c, m/s (x10^{-5})	7.7	7.7	7.7	7.7	7.7	7.7	7.7	7.7	18.3	5.0	5.0	5.3
$k_L a_{CO}$, 1/h	164	287	158	158	215	274	274	274	804	909	388	146
$k_L a_{H_2}$, 1/h	207	361	198	198	271	344	344	344	1011	1143	488	184
$k_L a_{CO_2}$, 1/h	160	279	153	153	209	265	265	265	779	881	376	142
$k_L a_{Et}$, 1/h	108	188	103	103	141	179	179	179	526	594	254	96

Table F.8 shows the energy changes for all experimental cases. The Gibbs free energy of the reaction is calculated at process conditions, *i.e.*, includes corrections for the extracellular concentrations of the 10 substances involved in the reaction. For the highly soluble species the concentrations are supplied in units mol/L; for the gases CO, H_2 and CO_2, their partial pressures in atm are used. No concentration corrections are applied for water and cells because they form the matrix where the process reaction takes place. For NH_4^+ ions the concentration is assumed to be 0.1 mol/L and for H^+ ions 1x10^{-5} mol/L (experimental pH 5). Lastly, the contributions of the different forms of acetic acid (dissociated and undissociated) were included in the calculation, assuming that the pKa of acetic acid is 4.53 at 37 °C. The standard Gibbs free energy of formation of the

undissociated acetic acid ($\Delta_f G_{HAc}$) was calculated through equation F.28 provided the standard Gibbs free energy of formation of acetate ($\Delta_f G_{Ac^-}$) is -369.31 kJ/mol. Figure F.3 shows the Gibbs free energy production at standard and process conditions.

$$\Delta_f G_{HAc} = \Delta_f G_{Ac^-} - \ln(10) RT\, pK_a \tag{F.28}$$

Table F.8 Energy production in the metabolic reactions for the different experimental cases

Variable		q_{G^0}, kJ/(Cmol$_x$*h)	$q_{G^{pH5}}$, kJ/(Cmol$_x$*h)	$q_{G^{process\ conditions}}$, kJ/(Cmol$_x$*h)	q_{H^0}, kJ/(Cmol$_x$*h)	q_{S^0}, J/(K*Cmol$_x$*h)
Case	**1**	20.9	23.0	25.2	35.6	47.3
	2	28.6	30.6	28.8	47.3	60.5
	3	24.9	28.8	26.4	57.5	105.1
	4	24.5	28.4	25.8	56.6	103.4
	5	28.8	32.1	27.6	62.0	106.9
	6	33.5	36.3	30.1	67.4	109.2
	7	32.9	35.4	28.8	66.0	106.9
	8	38.8	39.7	32.0	93.4	175.9
	9	37.7	39.0	26.8	88.5	163.8
	10	54.4	60.7	41.3	196.5	458.3
	11	30.6	33.0	24.5	108.7	252.0
	12	23.3	26.0	21.3	87.8	207.8

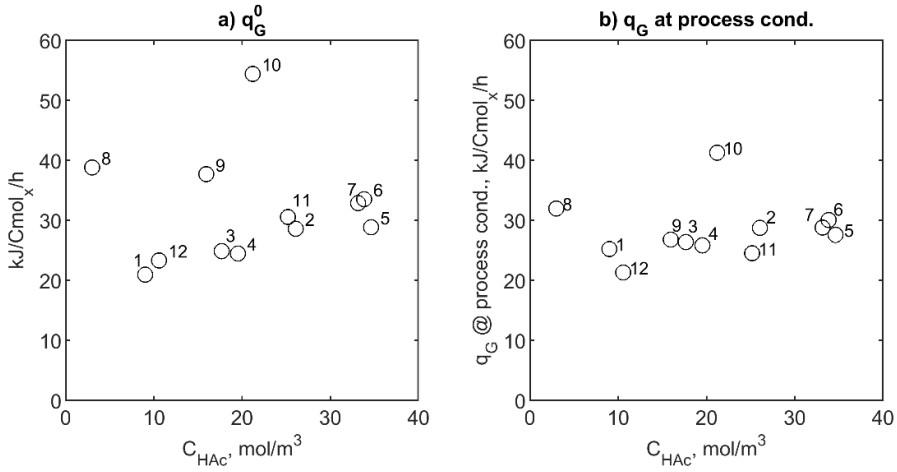

Figure F.3 Production of Gibbs free energy at standard conditions and at process conditions for the 12 experimental cases

Lastly, Table F.9 shows a comparison between the reported average net conversion rates and those calculated by solving the system of equations (from F.1 to F.25). The table bring

the data reported in Table F.2 and in Table F.5 into one table where the reported and calculated rates can be compared to each other.

Table F.9 Comparison between reported and calculated q-rates

Substance	Case											
	1		2		3		4		5		6	
	Rep	Est	Rep	Est	Rep	Est	Rep	Est	Rep	Est	Rep	Est
CO	-551	-612	-778	-817	-487	-564	-462	-555	-621	-668	-798	-800
H_2	13	14	13	14	-328	-355	-308	-350	-316	-347	-311	-322
CO_2	418	345	534	483	144	133	141	132	220	225	326	337
Biomass	42	42	42	42	42	42	42	42	42	43	42	43
Ethanol	32	32	65	65	30	29	30	29	63	64	93	96
Total acetic acid	81	80	79	77	167	165	154	162	131	135	106	110
Undissociated acetic acid	n.r.	20	n.r.	20	n.r.	42	n.r.	41	n.r.	34	n.r.	28
Acetate	n.r.	60	n.r.	58	n.r.	124	n.r.	121	n.r.	101	n.r.	82
2,3-butanediol	n.r.	0	2	2	0	0	0	0	0	0	2	2
NH_4^+	n.r.	-10	n.r.	-11	n.r.	-11	n.r.	-11	n.r.	-11	n.r.	-11
Water	n.r.	-292	n.r.	-393	n.r.	-83	n.r.	-82	n.r.	-139	n.r.	-216
H^+	n.r.	70	n.r.	68	n.r.	134	n.r.	131	n.r.	112	n.r.	93
Substance	**Case**											
	7		8		9		10		11		12	
	Rep	Est	Rep	Est	Rep	Est	Rep	Est	Rep	Est	Rep	Est
CO	-747	-780	-508	-616	-520	-647	-94	-111	-38	-44	0	0
H_2	-290	-323	-838	-979	-748	-857	-2754	-3071	-1652	-1740	-1202	-1422
CO_2	308	330	55	52	111	100	-1002	-1142	-568	-626	-495	-558
Biomass	42	43	42	42	42	43	42	43	21	22	20	20
Ethanol	96	98	229	234	200	205	322	337	207	222	148	153
Total acetic acid	99	102	27	27	48	47	256	268	96	102	119	116
Undissociated acetic acid	n.r.	26	n.r.	7	n.r.	12	n.r.	68	n.r.	26	n.r.	29
Acetate	n.r.	76	n.r.	20	n.r.	35	n.r.	200	n.r.	76	n.r.	87
2,3-butanediol	2	2	n.r.	0	n.r.	0	n.r.	0	n.r.	0	n.r.	0
NH_4^+	n.r.	-11	n.r.	-10	n.r.	-11	n.r.	-11	n.r.	-5	n.r.	-5
Water	n.r.	-206	n.r.	202	n.r.	126	n.r.	1501	n.r.	859	n.r.	721
H^+	n.r.	87	n.r.	31	n.r.	46	n.r.	211	n.r.	81	n.r.	92

Notes: n.r., Rep., and Est., stand for 'not reported', 'reported' and 'calculated', respectively. The q-rates are reported in units mmol/$Cmol_x$/h.

Table F.10 shows the percent changes in the q-rates for CO, H_2, CO_2, biomass growth, ethanol and acetic acid production. The table also includes information about the initial carbon and electron gaps calculated for the crude experimental data reported in the data sources. Lastly, the table also includes the calculated variations between the gas and liquid in and outflow rates.

Table F.10 Differences in q-rates and flow rates after data reconstruction

Item	Experimental case											
	1	2	3	4	5	6	7	8	9	10	11	12
Percent differences between the reconstructed and reported q-rates												
q_{CO}	11.0	5.0	15.7	20.2	7.5	0.2	4.4	21.3	24.4	18.6	15.6	0.0
q_{H_2}	6.4	4.6	8.1	13.5	9.7	3.6	11.3	16.8	14.5	11.5	5.3	18.3
q_{CO_2}	17.4	9.6	7.5	6.6	2.3	3.5	7.0	4.4	9.7	14.0	10.2	12.7
μ	0.4	1.9	1.4	1.6	3.3	3.3	3.3	0.7	2.6	3.3	4.9	1.2
q_{Et}	1.5	0.5	4.5	3.9	1.3	2.8	2.5	2.0	2.5	4.8	7.3	3.2
q_{AcT}	1.5	2.3	0.9	5.0	3.1	3.9	2.8	0.6	2.3	4.7	5.9	2.3
Initial carbon and electron gaps, plus calculated differences between the liquid and gas in and outflow rates. Units are %.												
C gap	24.4	12.1	19.0	19.2	4.8	2.9	0.3	19.8	24.8	9.3	3.4	11.8
e^- gap	11.2	6.2	14.3	14.2	5.5	1.7	4.2	16.3	16.4	6.7	1.3	16.8
ΔF_G	3.1	6.8	15.2	15.0	16.8	17.0	16.7	13.8	17.9	58.4	50.9	8.3
ΔF_L	0.2	1.7	1.2	1.4	3.1	3.2	3.2	0.5	2.5	3.2	5.1	1.1

As conclusion of the experimental data reconstruction process, the largest corrections in the q-rates are not related to large carbon and electron gaps but also to the consideration that the gas and liquid in and outflow rates are equal. In further experiments at steady-state, such assumptions must be avoided and even more informatively, measured and reported.

Appendix G

Summary of the reaction rates calculated for the whole metabolic network

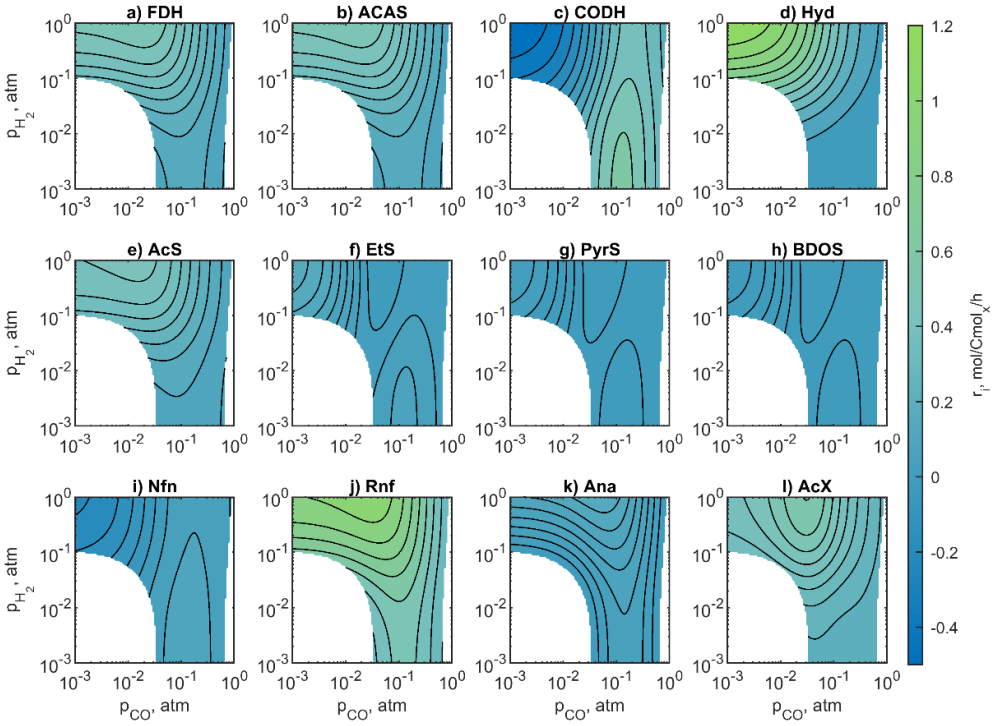

Figure G.1 Reaction rates of all the intracellular reactions as function of p_{CO} and p_{H_2}. The plots were constructed for C_{AcT} of 50 mM, C_{Et} 100 mM, p_{CO_2} 0.2 atm, and pH 5. The white areas represent points where the solutions of the systems of equations did not fulfill equation 3.

Chapter 6

Applying linlog approximative kinetics to anaerobic syngas fermentation: experimental data processing and early-stage metabolic kinetic model design and parameterization

This chapter is the work of Eduardo Almeida Benalcázar, Peter Verheijen, Henk Noorman, Rubens Maciel Filho and John Posada. The study will be submitted to a journal in the future.

"Grab a calculator and fix yourself"

Nicolas Jaar, *Space is only noise*, 2011

6.1. Summary

This chapter presents the design and parameterization of a kinetic metabolic model of the bacterium *Clostridium autoethanogenum*. Since the kinetic model is based on the metabolic network presented in Chapter 5, which contains several lumped reactions, an approximative kinetic format was chosen for building the kinetic model. The kinetic model uses the following inputs: the extracellular concentrations of CO, H_2, CO_2, acetate, undissociated acetic acid, ethanol, 2,3-butanediol and pH, as well as the intracellular concentrations of NADH, acetyl-CoA, NADPH, reduced ferredoxin, formate and acetate.

The kinetic expressions for 11 intracellular reactions were designed and parameterized using data from a published experiment where metabolic oscillations are provoked in a continuous fermentation with *C. autoethanogenum*. During those oscillations, the net conversion rates of the main electron and carbon substrates and products change.

The parameterization of the model was based on the minimization of the mismatch between the experimental net conversion rates and those predicted by the model. A sequence of minimizations was used to estimate the values of *i)* the model's kinetic parameters, *ii)* the reference concentrations of un-measured intracellular concentrations, and *iii)* the initial concentrations supplied to the solver of the differential equations. The series of sequential minimizations were used to guarantee that the estimated sets of parameters are consistent with each other while exploring the vast solutions space using stochastic and iterative minimization algorithms.

The parameterized model successfully reproduced the experimental oscillations, suggesting that the linlog format holds potential for describing the dynamic behavior of *C. autoethanogenum*. However, an average error of 15% between the calculated and the experimental concentrations, reveals that the model still needs improvements. Different targets for possible improvements were identified and described.

The analysis of the parameterized model revealed that the NADH pool is highly sensitive to changes in the metabolic network, while wielding a significant influence on the kinetics of the carbon and electron routes. The control that NADH exerts over the catabolism of *C. autoethanogenum* should be further explored with detail.

6.2. Introduction

Disregarding the specific product of an industrial fermentation, whether it is an intracellular or extracellular metabolite, cells, or a converted substrate, controlling the mechanisms influencing the metabolic generation of this product is one of the key

objectives of fermentation process development. The design of the bioreactor vessel must enable the controlled overproduction of the microbial product through *i)* providing sufficient carbon and electron sources (*e.g.*, glucose, or in the case of syngas fermentation CO, H_2 and CO_2), as well as nutrients to the microorganisms, and *ii)* preventing the harmful accumulation of products. An optimal fermentation process in terms of yield, productivity, product titer, downstream efficiency, operation costs, environmental impacts and ease of operation depends on establishing a common ground between the two perspectives, the bioreactor dynamics and the microorganism regulation [118]. Any reactor design, *e.g.* for scaling, should secure that the operating conditions are maintained within specified ranges.

Large industrial-scale bioreactors, with volumes of tens, hundreds and even thousands of cubic meters, are dynamic systems, where unavoidable gradients of (limiting) substance concentrations are present [415,416]. Such gradients are induced basically by differences between conversion rates and transport rates [118,415]. Conversion rates are dominated by the microorganisms while transport rates are governed mainly by mixing, mass and heat transfer, pressure, scale, reactor geometry and rheology of the fermentation broth [415]. The cyclic circulation of microorganisms through these gradients may cause changes in the product yield, productivity and product quality compared to the performance observed in the lab-scale fermentations, where gradients are less prominent or virtually absent [415]. Therefore, the relevance of the data gathered from a chemostat for predicting microorganisms' behavior inside a large-scale bioreactor becomes insufficient.

The dynamic behavior of the large bioreactor can be partially recreated in the laboratory using down-scaled environments, where the lab-scale fermentation is kept "within the same operating regimes and the same rate-limiting mechanisms" as the large-scale [417]. Mixing, mass and heat transfer, CO_2 removal and gas-liquid separation at the head-space are the most common limiting steps in large-scale fermentations [417]. When the large-scale bioreactor is under design, the rate-limiting mechanisms are identified using a regime analysis [418] from the information obtained from detailed simulations of the bioreactor (*e.g.*, using compartment models [85,416] or simulations based on computational fluid dynamics (CFD) [419]). The scale-down approach aids in the recreation of a dynamic environment in the laboratory where cells are subjected to the same gradients of substance concentrations, temperatures, pH and shear rates [417] as they would be inside the large-scale bioreactor. The gradients are recreated through pulses [420] or step-changes [421] in the feed rate of a relevant substance, temperature or shear rate. Gradients induced through repetitive cyclic changes in the relevant variable are used to assess the adaptation of cells to the dynamic environment [420,422], whereas

one-time changes allow performing kinetic studies of the metabolic response to the dynamic environment [421].

Under either steady state or dynamic scaled-down environments the intracellular space is revealed through mathematical descriptions of the metabolic networks. Large genome-scale models, comprising hundreds of reactions and metabolites, are useful to predict the consequences of overexpressing or suppressing the activities of certain enzymes that may lead to the overproduction of a certain metabolite of commercial interest [87]. Due to the mathematical complexity of genome-scale models and the often limiting computing power, simpler models, comprising complete pathways lumped onto few reactions, are used to study the influence of the large-scale bioreactor dynamics on the dynamics of microbial metabolic reactions [88]. Formulating and parameterizing mechanistic equations to describe the kinetic properties of such lumped reactions or complete pathways may represent a challenge [89,94,423]. Mechanistic equations describe the kinetic properties of enzymes for large ranges of concentrations of the substances involved in the reactions; in the heavily regulated intracellular space, the concentrations of metabolites vary within rather narrow ranges [90], due to homeostasis. In response, approximative kinetic formats have been developed [94,424], which describe the kinetic properties of a reaction using a comparison between the current state of the system and a reference steady state. The linlog [95] is an approximative format which gathers useful features: *i)* it reproduces the non-linear, downward concave behavior of conversion rates with respect to increasing metabolite concentrations, *ii)* it reproduces the proportional relation between enzyme levels and the reaction rates, *iii)* the number of kinetic parameters is lower than those of mechanistic approaches, *iv)* it allows analytical solutions of the intracellular mass balances, and *v)* the analytical solutions are consistent with experimental evidence [95]. The linlog format is also compatible with metabolic control analysis [425,426] and has been used for the redesign of primary metabolic routes [96].

The application of the described systematic approach to the development of the anaerobic conversion of CO, H_2 and CO_2 mixtures by *Clostridia* into value-added products, such as ethanol, may be done stepwise. The first step is the development of the black-box and metabolic models for the study of the microorganisms at steady-state [324,427], followed by the development of mass transfer models for the study of the large-scale bioreactor [428]. The work developed in this study is a subsequent step, *i.e.*, it explores the applicability of the linlog kinetic format to describe the still unraveled *in vivo* intracellular kinetics of the acetogen *Clostridium autoethanogenum*. To achieve the mentioned objective, this study presents procedures for the processing of experimental data, *i.e.*, *i)* the reconciliation of experimental net conversion rates and *ii)* the reconstruction of the un-measured dissolved CO, H_2 and CO_2 concentrations. In addition, systematic approaches are presented for the development and the parameterization of

the kinetic model, and for the assessment of the estimated kinetic parameters' quality. This work provides advice for future experimental studies and modelling approaches, in search of an appropriate coupling between the needs of the microorganism and the conditions governed by the bioreactor vessel.

6.3. Methodology

This section presents the structure of the kinetic model and describes the parameterization process including the preparation of the experimental data. The preparation of the experimental data comprises the *i)* reconciliation of the net uptake and secretion rates (q-rates), *ii)* the reduction of noise and reconstruction of missing points in the raw experimental concentration data, and *iii)* the reconstruction of un-measured concentrations of the dissolved gases.

6.3.1. Structure of the kinetic model

The model is designed to deliver the transient rates of the intracellular reactions and the q-rates from the following data as inputs:

- Extracellular concentrations of CO, H_2, CO_2, ethanol, acetic acid, 2,3-butanediol and cells.
- Intracellular concentrations of formate, acetyl-CoA, acetate, NADH, NADPH and reduced ferredoxin.

The metabolic network is formed by lumped reactions that describe the pathways followed by both the carbon atoms (starting from CO and CO_2) and the electrons (originating from CO and H_2) towards the extracellular products: acetate, ethanol, 2,3-butanediol and cells. Figure 6.1 shows a schematic representation of the metabolic network. The stoichiometry of each reaction is shown in Table A.1 in Appendix A.

The possible routes of the carbon atoms consist of:

- The reversible production of CO_2 from CO (reaction CODH).
- The production of formate from the reduction of CO_2 (reaction FDH).
- The lumped Wood-Ljungdahl pathway ending in the synthesis of acetyl-CoA (AcCoA) using CO and formate (reaction ACAS) as starting points.
- The synthesis of acetate from AcCoA (reaction AcS).
- The export of acetate ions into the extracellular space (reaction AcX).
- The passive diffusion of the undissociated acetic acid from the extracellular space towards the inside of the cell (reaction HAcD).
- The lumped production of ethanol from acetate (reaction EtS).

- The lumped production of 2,3-butanediol from AcCoA (reaction BDOS).
- The lumped anabolism or production of cell material from AcCoA (reaction Ana).

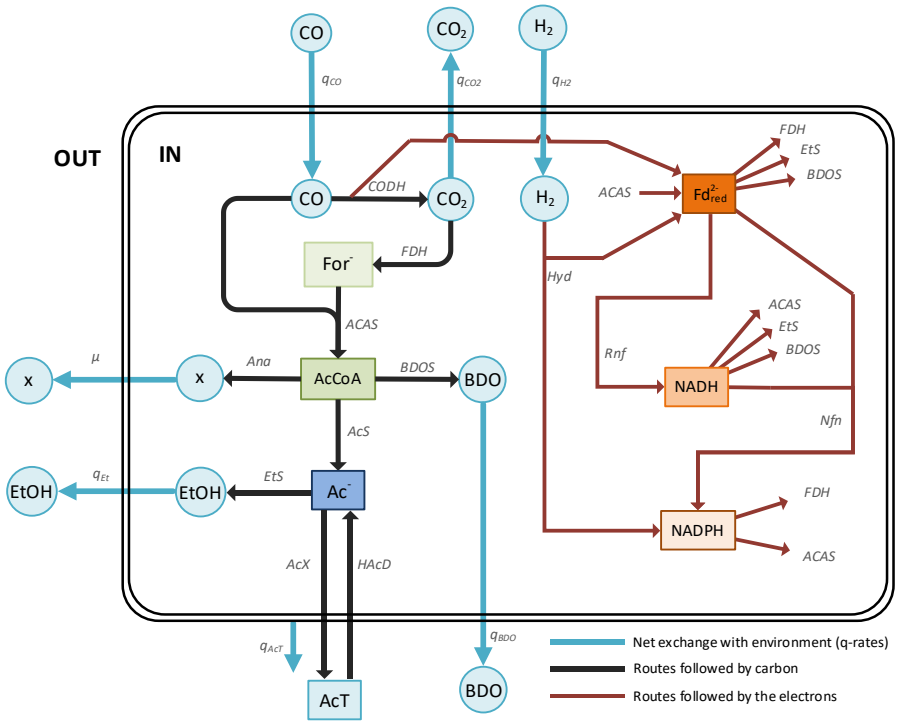

Figure 6.1. Schematic representation of the main metabolite pools and the routes followed by the carbon and the electrons in the cell of *C. autoethanogenum*. The exchangeable compounds are contained within blue circles, while the non-exchangeable compounds are contained within squares of different colors (one color for each substance). Only the dissociated form of acetic acid (acetate) is considered to be present in the cell due to the assumed neutral intracellular pH; acetate and acetic acid are considered for the extracellular space and lumped as AcT.

Similarly, the possible routes for the electrons include:

- The harvest of the electrons from CO (reaction CODH) into ferredoxin.
- The harvest of the electrons from H_2 (reaction Hyd) into ferredoxin and NADPH.
- The oxidation and reduction of the electron carriers (NADH, NADPH and ferredoxin) within the carbon route.
- The transfer of electrons from ferredoxin to NADH at the Rnf complex (reaction Rnf).
- The transfer of electrons between NADPH, NADH and ferredoxin at the Nfn complex (reaction Nfn).

The q-rates are the result of the contributions of the intracellular reactions (see the light-blue lines in Figure 6.1). Only in the case of acetic acid production, its net production rate is equal to the rate of acetate export (r_{AcX}) minus the rate of acetic acid back-diffusion into the cell (r_{HAcD}); the latter are exchange reactions between the intra and extracellular spaces.

With the proposed structure, the network contains the three characteristic traits of acetogens according to [51,363], which are based on the use of CO_2 for three main purposes: *i)* to reductively synthesize acetyl-CoA, *ii)* as the terminal electron acceptor in an energy-conserving process, and *iii)* to synthesize cell material.

To calculate the transient rates of the i number of reactions in the metabolic network (J_i), this study uses equation 1, where r_i^0 is a vector that contains the rates of reaction at a reference state, while r_i^{ll} may be considered as a correction factor that introduces the influence of the concentrations of metabolites to the reactions' kinetics.

$$J_i = r_i^0 \times r_i^{ll} \tag{1}$$

By definition, the reference state is defined by a fixed set of reaction rates and metabolites concentrations [95]. The reference state in this study is taken from a set of experimental data, which is introduced in section 6.3.2.

The term r_i^{ll} in equation 1 follows an approximative kinetic model previously presented as the linlog format [90,95] and shown by equation 2.

$$r_i^{ll} = 1 + \varepsilon \times \ln\left(\frac{C_j}{C_j^0}\right) \tag{2}$$

The linlog approach incorporates the influence of the concentrations of a j number of metabolites (C_j) through the deviation of those concentrations from a reference value (C_j^0). The terms C_j and C_j^0 in equation 2 are vectors, while the term ε is a $n \times m$ matrix that contains the so-called elasticity coefficients (ε_{ij}) and where n is the number of reactions and m is the number of compounds. The terms in ε convert the deviation on each j-th substance concentration from the reference state into a change in the rate of each i-th reaction. The terms in ε can be positive, negative or equal to 0, depending on whether the influence of the concentration deviation is inhibitory ($\varepsilon_{ij} < 0$), promoting ($\varepsilon_{ij} > 0$), or not influential ($\varepsilon_{ij} = 0$), respectively.

In its original source [90], equation 2 also considers the contribution of the concentrations of enzymes, however since enzyme concentrations remained constant throughout the oscillations [113], the respective term in equation 2 was neglected in our study.

Since the linlog format is conceptualized as an approximative approach, the metabolites used to define r_i^{ll} do not necessarily intervene in the reaction as substrates or products. Therefore, the linlog format is able to simulate indirect kinetic effects such as, for instance, allosteric regulations [95].

6.3.2. Source of the experimental data and definition of the reference state

The reference state is taken from a set of time-dependent experimental data. The data reported by Mahamkali and colleagues [113] was used to define the reference state in our model and also for its parameterization. The mentioned report comprises two experimental replicate runs of continuous fermentations using *C. autoethanogenum*. During these experiments, after a steady-state was reached (reported elsewhere [75]), the stirring speed was increased from 650 to 800 rpm (at an un-specified rate); this change triggered metabolic oscillations on the bacteria. The uptake rates of CO and H_2 as well as the production rates of ethanol, acetic acid, 2,3-butanediol and biomass vary during the oscillations, revealing dynamic links with *i)* the rates of electron uptake (from CO and H_2), *ii)* the specific source of the electrons at certain moments, *iii)* the distribution of these electrons among the redox carriers, *iv)* the cell growth rate and *v)* the distribution of the carbon and electrons among the products. The oscillatory behavior is reportedly maintained for 330 hours until the gas feed is depleted in the source cylinders; it is therefore unknown if the oscillations could have been maintained for a longer period of time.

Although the dynamic conditions in the experiment are not the product of a systematic scale-down design, the oscillations are highly suitable for the parameterization of a kinetic metabolic model since dynamic regulations within the central carbon and electrons routes are stimulated.

The reference state is then chosen as the experimental point whose rates of reaction and metabolites concentrations are closest to the median values of the rates and the concentrations, meaning, that the reference state is regarded as the most common state of the bacteria during the oscillations.

The reference rates of the intracellular reactions are calculated using the reconciled net conversion rates of CO, H_2, CO_2, acetic acid, ethanol, 2,3-butanediol and biomass as inputs for the matrix A (see Appendix A) which contains the stoichiometric information of the metabolic network. A description of the reconciliation process is given in section 6.3.4.1.1.

The reference extracellular concentrations of ethanol, acetic acid, 2,3-butanediol and the intracellular concentrations of NADH, NADPH and acetyl-CoA are directly taken from

[113]. The dissolved concentrations of CO, H_2, CO_2 were calculated from the reported gas composition data, as explained in section 6.3.4.1.2. The reference concentrations of formate, intracellular acetate, and reduced ferredoxin were estimated as part of the parameterization process, as explained in section 6.3.4.

6.3.3. Design of the elasticities (ε) matrix

According to mass-action kinetics, the rate of a chemical reaction is a function of the concentration of its reactants and its products. This approach was initially followed to define the substances that would influence each reaction of the network. Also, based on knowledge about the metabolic system, additional elasticity coefficients were added to selected reactions to account for possible indirect effects of metabolites that do not directly intervene in the reactions; this process obeyed to different criteria which are described for each specific case, as follows:

- The participation of the three redox carriers NADH, NADPH and reduced ferredoxin in the anabolic reaction (Ana) because ATP is not included as a metabolite in the network.
- The elasticity coefficients of CO_2 and formate in the Hyd reaction which collects the electrons from H_2 into ferredoxin and NADPH; CO_2 and formate were included to simulate the possible effects of bacteria using an alternative route for the uptake of H_2 and CO_2 to synthesize formate which is in reality catalyzed by the formate-hydrogen lyase enzyme [53].

The final locations of the elasticity coefficients that are not equal to zero in the ε matrix are shown with a number 1 in Table 6.1; those are the elasticity coefficients estimated in the model parameterization (further described in section 6.3.4).

As an illustrative example, the equation for calculating the rate of the CODH reaction, formed by the combination of equations 1 and 2 and the information in Table 6.1 is presented by equation 3.

$$J_{CODH} = r^0_{CODH}\left[1 + \varepsilon_{CO,CODH}\ln\left(\frac{C_{CO}}{C^0_{CO}}\right) + \varepsilon_{CO_2,CODH}\ln\left(\frac{C_{CO_2}}{C^0_{CO_2}}\right) + \varepsilon_{Fd^{2-}_{red},CODH}\ln\left(\frac{C_{Fd^{2-}_{red}}}{C^0_{Fd^{2-}_{red}}}\right)\right] \quad (3)$$

From the list of 14 reactions in Table A.1, there are three that have not been included in the formulation of the ε matrix (thus have not been assigned elasticity coefficients). These reactions are the H^+ influx (reaction i11) because its rate is determined by mass balances, the diffusion of acetic acid (reaction i13) because its rate is defined by a mechanistic equation (see note *b* in Table 6.2) and the formate-hydrogen lyase (reaction i14) because

in this study we make an initial exploration about the need for this reaction's inclusion in the model.

Table 6.1. Locations of the estimated elasticity coefficients in the ε matrix

		i											
		CO	H_2	CO_2	$[Ac^-]_o$	Et	BDO	$AcCoA$	$NADH$	$[Ac^-]_i$	For^-	$NADPH$	Fd_{red}^{2-}
j	FDH	0	0	1	0	0	0	0	0	0	1	1	1
	ACAS	1	0	0	0	0	0	1	1	0	1	1	1
	CODH	1	0	1	0	0	0	0	0	0	0	0	1
	Hyd	0	1	1	0	0	0	0	1	0	1	1	1
	AcS	0	0	0	0	0	0	1	0	1	0	0	0
	EtS	0	0	0	0	1	0	0	1	1	0	0	1
	BDOS	0	0	1	0	0	1	1	1	0	0	0	1
	Nfn	0	0	0	0	0	0	0	1	0	0	1	1
	Rnf	0	0	0	0	0	0	0	1	0	0	0	1
	Ana	0	0	0	0	0	0	1	1	0	0	1	1
	AcX	0	0	0	1	0	0	0	0	1	0	0	0

6.3.4. Model Parameterization

Since the elasticity coefficients are linear in equation 2, ideally, they can be calculated by simply solving equation 2. However, such methodology was not followed in this study. That is because the metabolic network considers intracellular balances for substances for which no experimental data was gathered by [113], *i.e.*, reduced ferredoxin (Fd_{red}^{2-}), formate and acetate ions. This partial incompatibility between the model's structure and the available experimental data prevents finding the complete set of experimental J_i in equation 1. Thus, the elasticity coefficients (in the ε matrix) are estimated through the minimization of the squared errors between the concentrations calculated by the model and those reported in [113]. The reference concentrations of intracellular formate, acetate and Fd_{red}^{2-} are also estimated during the model's parameterization because there is no experimental data for them.

The reported concentrations that were used from [113] are *i)* those of acetic acid, ethanol, 2,3-butanediol and biomass in the extracellular liquid phase, *ii)* acetyl-CoA, NADH and NADPH in the intracellular liquid phase, and *iii)* CO and H_2 molar fractions in the bioreactor off-gas. Hence, the 9 substances and the 21 time-points of the experiment provided 180 experimental points (excluding 9 points where the acetyl-CoA concentrations are reported as below detection limits and are therefore assumed as absent data) for comparison.

Although the intracellular concentrations of the oxidized redox carriers NAD^+ and $NADP^+$ were reported by [113], they were not used in this study due to the lack of a kinetic model that describes the production of nicotinamide adenine dinucleotide and nicotinamide adenine dinucleotide phosphate in the cell. Those kinetic expressions are seen as possible

improvements of the model here presented since, the summed concentrations of the reduced and oxidized redox carriers are not constant throughout the oscillations.

The system of mass balance equations shown in Table 6.2 describes the behavior of the substances considered at the intracellular space, the extracellular liquid and the bioreactor off-gas. Section 6.6 contains the list of the symbols used throughout this chapter. The net q-rates are constructed with equations 4 – 13 using the intracellular rates calculated with equations 1 and 2. The concentrations of ethanol, acetic acid, 2,3-butanediol and biomass in the extracellular liquid phase are calculated with equations 17 – 20. Equations 26 and 27 calculate the molar fractions of CO and H_2 in the gas phase. The intracellular concentrations of acetyl-CoA, NADH and NADPH are calculated with equations 32, 33 and 34.

Table 6.2. System of mass balance equations

Specification	Equation	Units	Nr.
Equalities for the construction of the net q-rates [a]			
CO	$-q_{CO} = J_{ACAS} + J_{CODH}$	mol/(Cmol$_x$*h)	(4)
H_2	$-q_{H_2} = 2J_{Hyd}$	mol/(Cmol$_x$*h)	(5)
CO_2	$q_{CO_2} = J_{CODH} - J_{FDH}$	mol/(Cmol$_x$*h)	(6)
Ethanol	$q_{Et} = J_{EtS}$	mol/(Cmol$_x$*h)	(7)
Acetic acid [b]	$q_{AcT} = J_{AcX} - r_{HAcD}$	mol/(Cmol$_x$*h)	(8)
2,3-butanediol	$q_{BDO} = J_{BDOS}$	mol/(Cmol$_x$*h)	(9)
Biomass	$\mu = J_{Ana}$	mol/(Cmol$_x$*h)	(10)
Water	$q_W = 2J_{ACAS} - J_{CODH} - J_{AcS} + J_{EtS}$	mol/(Cmol$_x$*h)	(11)
H^+ ions [c]	$q_{H^+} = 2J_{Rnf} - J_{H^+,in} - J_{HAcD}$	mol/(Cmol$_x$*h)	(12)
Ammonium ions	$q_{NH_4^+} = -\frac{\mu}{4}$	mol/(Cmol$_x$*h)	(13)
Balances in the extracellular liquid phase [d]			
CO	$\frac{dC_{CO}V_L}{dt} = q_{CO}C_xV_L + k_La_{CO}(C^*_{CO} - C_{CO})V_L - C_{CO}\frac{F_{L,o}}{\rho_L}$	mol/h	(14)
H_2	$\frac{dC_{H_2}V_L}{dt} = q_{H_2}C_xV_L + k_La_{H_2}(C^*_{H_2} - C_{H_2})V_L - C_{H_2}\frac{F_{L,o}}{\rho_L}$	mol/h	(15)
CO_2	$\frac{dC_{CO_2}V_L}{dt} = q_{CO_2}C_xV_L + k_La_{CO_2}(C^*_{CO_2} - C_{CO_2})V_L - C_{CO_2}\frac{F_{L,o}}{\rho_L}$	mol/h	(16)
Ethanol	$\frac{dC_{Et}V_L}{dt} = q_{Et}C_xV_L + k_La_{Et}(C^*_{Et} - C_{Et})V_L - C_{Et}\frac{F_{L,o}}{\rho_L}$	mol/h	(17)
Total acetic acid (acetate plus acetic acid)	$\frac{dC_{AcT}V_L}{dt} = q_{AcT}C_xV_L - C_{AcT}\frac{F_{L,o}}{\rho_L}$	mol/h	(18)

Specification	Equation	Units	Nr.
2,3-butanediol	$\frac{dC_{BDO}V_L}{dt} = q_{BDO}C_xV_L - C_{BDO}\frac{F_{L,o}}{\rho_L}$	mol/h	(19)
Biomass	$\frac{dC_xV_L}{dt} = \mu C_xV_L - C_x\frac{F_{L,o}}{\rho_L}$	mol/h	(20)
Total balance	$0 = F_{L,i} - F_{L,o} + k_La_{CO}(C^*_{CO} - C_{CO})m_{CO}V_L + k_La_{H_2}(C^*_{H_2} - C_{H_2})m_{H_2}V_L + k_La_{CO_2}(C^*_{CO_2} - C_{CO_2})m_{CO_2}V_L + k_La_{Et}(C^*_{Et} - C_{Et})m_{Et}V_L - y_WF_{G,out}m_W$	kg/h	(21)
Gas-liquid equilibrium relations			
CO	$C^*_{CO} = k_{H,CO}y_{CO}p$	mol/m³	(22)
H_2	$C^*_{H_2} = k_{H,H_2}y_{H_2}p$	mol/m³	(23)
CO_2	$C^*_{CO_2} = k_{H,CO_2}y_{CO_2}p$	mol/m³	(24)
Ethanol	$C^*_{Et} = k_{H,Et}y_{Et}p$	mol/m³	(25)
Balances in the gas phase [e]			
CO	$0 = F_{G,i}y_{CO,i} - F_{G,o}y_{CO} - k_La_{CO}(C^*_{CO} - C_{CO})V_L$	mol/h	(26)
H_2	$0 = F_{G,i}y_{H_2,i} - F_{G,o}y_{H_2} - k_La_{H_2}(C^*_{H_2} - C_{H_2})V_L$	mol/h	(27)
CO_2	$0 = F_{G,i}y_{CO_2,i} - F_{G,o}y_{CO_2} - k_La_{CO_2}(C^*_{CO_2} - C_{CO_2})V_L$	mol/h	(28)
Ethanol	$0 = -F_{G,o}y_{Et,o} - k_La_{Et}(C^*_{Et} - C_{Et})V_L$	mol/h	(29)
Inert gas component	$0 = F_{G,i}y_{Inert,i} - F_{G,o}y_{Inert}$	mol/h	(30)
Balances in the intracellular liquid phase (for non-exchangeable substances) [f,g]			
Formate	$\frac{dC_{For^-}}{dt} = (J_{FDH} - J_{ACAS})\frac{1}{V_x} - \mu C_{For^-}$	mol/(m^3_{cell}*h)	(31)
Acetyl-CoA	$\frac{dC_{AcCoA}}{dt} = \left(J_{ACAS} - J_{AcS} - 2J_{BDOS} - \frac{1}{2}J_{Ana}\right)\frac{1}{V_x} - \mu C_{AcCoA}$	mol/(m^3_{cell}*h)	(32)
NADH	$\frac{dC_{NADH}}{dt} = \left(J_{Rnf} - 2J_{ACAS} + J_{EtS} - \frac{1}{2}J_{BDOS} - J_{Nfn}\right)\frac{1}{V_x} - \mu C_{NADH}$	mol/(m^3_{cell}*h)	(33)
NADPH	$\frac{dC_{NADPH}}{dt} = \left(J_{Hyd} + 2J_{Nfn} - \frac{1}{2}J_{FDH} - J_{ACAS}\right)\frac{1}{V_x} - \mu C_{NADPH}$	mol/(m^3_{cell}*h)	(34)
Fd_{red}^{2-}	$\frac{dC_{Fd^{2-}_{red}}}{dt} = \left(-\frac{1}{2}J_{FDH} + J_{ACAS} + J_{CODH} + J_{Hyd} - J_{EtS} - J_{BDOS} - J_{Nfn} - J_{Rnf}\right)\frac{1}{V_x} - \mu C_{Fd^{2-}_{red}}$	mol/(m^3_{cell}*h)	(35)
Intracellular acetate	$\frac{dC_{[Ac^-]_i}}{dt} = (J_{AcS} + J_{HAcD} - J_{EtS} - J_{AcX})\frac{1}{V_x} - \mu C_{Ac^-,IC}$	mol/(m^3_{cell}*h)	(36)

[a] The rates of diffusion of CO, H_2, CO_2, ethanol, 2,3-butanediol and water across the bacterial membrane are assumed to be much faster than the intracellular rates of reaction. This assumption

also causes that the differences between the intra and extracellular concentrations of these substances are very small and, therefore, neglected.

[b] The net production rate for acetic acid is the difference between the rate of acetate export and that of acetic acid diffusion. The rate of acetic acid diffusion does not follow the linlog approach; instead, it is simulated using the equation $r_{HAcD} = a_x k_{HAcD} C_{HAc,o}$, where a_x is the surface area of cells (321 $m^2/Cmol_x$), k_{HAcD} is the diffusivity of acetic acid across the membrane (3.85x10^{-5} m/h) and $C_{HAc,o}$ is the pH-dependent extracellular concentration of the undissociated acetic acid. The equation and the values of the parameters in it were obtained from Chapter 5 of this dissertation.

[c] The net conversion rate of H^+ ions only consider the intracellular reactions which involve an exchange of the ions with the extracellular space.

[d] The volume and the density of the bioreactor's liquid phase are assumed constant. In consequence, the volume of the gas phase is also constant.

[e] Since the pressure was likely controlled during the experiment, no accumulation of substances was considered in the gas phase and thus it assumed to be at steady state. The concentration of water in the gas phase is considered constant. The effects of dispersion are also neglected in the gas phase and therefore the concentrations of the gas components in the off-gas are equal to those in the reactor's headspace.

[f] V_x represents the molar volume of bacteria, equal to 5.89x10^{-5} $m^3/Cmol_x$. That value is calculated assuming that *i)* the cell is formed by 30 % dry mass plus 70 % water (approximated from [429]), and that *ii)* the molar mass of dry biomass is 25.25 $g_{DM}/Cmol_x$.

[g] The intracellular concentration of H^+ ions is assumed constant and equal to 1x10^{-7} mol/L (pH 7), therefore the balance of this specie is not considered in the system of equations.

To facilitate solving the ordinary differential equations from Table 6.2, the initial concentrations of the 13 species that are not at steady state are also estimated in the parameterization. Those species are CO, H_2, CO_2, ethanol, acetic acid, 2,3-butanediol and biomass in the extracellular liquid phase (see equations 14 - 20), and formate, acetate, acetyl-CoA, NADH, NADPH and Fd_{red}^{2-} in the intracellular liquid phase (see equations 31 - 36).

Summarizing the parameters estimated in the model's parameterization are *i)* the 41 elasticity coefficients, *ii)* the 3 reference concentrations for the intracellular metabolites (formate, acetate and Fd_{red}^{2-}) and *iii)* the 13 initial concentrations for the species listed in the previous paragraph.

Further, section 6.3.4.1 describes how the experimental data were processed to obtain both the complete set of reference concentrations and the intracellular reaction rates. Section 6.3.4.2 describes the steps followed to adjust the values of the elasticity coefficients.

6.3.4.1. Processing of experimental data

The reference concentrations and reaction rates were calculated using the following data available in [113]: *i)* the extracellular concentrations of ethanol, acetate, 2,3-butanediol and cells, *ii)* the intracellular concentrations of AcCoA, NADH, NADPH *iii)* the uptake rates

of CO and H_2, and *iv)* the molar fractions of CO and H_2 in the off-gas (available for only one of the two experimental runs). Hence, to obtain a full set of data needed for the parameterization of the kinetic model, the following data were calculated: *i)* the reconciled (see section 6.3.4.1.1) set of net consumption and secretion rates for CO, H_2, ethanol, acetic acid, 2,3-butanediol, biomass, CO_2, water, H^+ ions and the nitrogen source (assumed to be NH_4^+ ions), and *ii)* the concentrations of dissolved CO, H_2 and CO_2 (see section 6.3.4.1.2).

The reported intracellular metabolite concentrations were converted from μmol/g_{DM} into mol/m^3 of intracellular liquid for their use in the present study. Such conversion was done assuming that 30% of the cells total weight corresponds to dry matter and the remaining 70% to water, and also assuming the metabolites are contained only in the water phase of the cell. Therefore, the unit conversion was done by multiplying the reported values by the factor 3/7.

Since the gas composition data were reported for only one of the two replicate experiments in [113], the parameterization of our model used only the data from that experimental run. That experiment will be referred to as "experiment 1", while the data of the other experiment (experiment 2) was used to compare trends of certain concentrations and as reference for the formulation of the optimization problem (see section 6.3.4.2).

6.3.4.1.1. Reconciliation of the net consumption and secretion rates

The un-reported q-rates for ethanol, acetate, 2,3-butanediol and biomass were initially approximated using the mass balance equations 17 – 20 and using their reported concentrations as base [113]. The concentration differentials in those equations were calculated assuming them equal to the experimental gradients; the gradients were estimated using forward, backward and central derivation for the first, last and middle points within the experimental time span, respectively. Table 6.3 shows the equations used to calculate the concentration differentials.

Table 6.3. Equations used for the calculation of the concentration gradients with the experimental data

Type of differentiation	Equation	nr.
Central	$\frac{\mathrm{d}C_j}{\mathrm{d}t} \approx \frac{\Delta C_j}{\Delta t} = \frac{C_{t+1} - C_{t-1}}{2 \cdot \Delta t}$	(37)
Forward	$\frac{\mathrm{d}C_j}{\mathrm{d}t} \approx \frac{\Delta C_j}{\Delta t} = \frac{C_{t+1} - C_t}{\Delta t}$	(38)
Backward	$\frac{\mathrm{d}C_j}{\mathrm{d}t} \approx \frac{\Delta C_j}{\Delta t} = \frac{C_t - C_{t-1}}{\Delta t}$	(39)

The obtained q-rates were then reconciled in a process that also allowed the calculation of the q-rates for CO_2, water, NH_4^+ and H^+ ions. The reconciliation process was based on the minimization of the mismatch between the reconciled data and the raw experimental data (objective function) while closing the carbon, hydrogen, oxygen, nitrogen elemental balances as well as the charge balances (constraints) [79]. Therefore, the q-rates for CO, H_2, CO_2, acetate, ethanol, 2,3-butanediol, biomass growth, water, nitrogen source and H^+ ions were used as decision variables. The sum of the squared residuals between the reconciled and the experimental data was the objective function. The reconciliation was further constrained by closing the ethanol mass balance since its presence in the gas phase was included. Consequently, the complete gas composition and the gas outflow rate were also calculated from the reconciliation.

6.3.4.1.2. Calculation of dissolved gas concentrations

The mass balances for CO, H_2 and CO_2 in the liquid phase (equations 14 – 16) and their equilibrium with the gas phase (equations 22 – 24), together with their data for the off-gas composition that was given in [113] for experiment 1 only, were used in this calculation. The concentration gradients were calculated using equations (37 – 39) in Table 6.3. The coefficients ($k_{H,CO}$, k_{H,H_2} and k_{H,CO_2}) for the equilibrium relations were gathered from [292]. The calculation of the mass transfer coefficients ($k_L a$) required making several assumptions for the fermentation broth, the dimensions of the bioreactor vessel and the dimensions of the stirrer; these assumptions are listed in Table 6.4. The assumptions were necessary since in [113], such details were not reported, and involved the introduction of the correction factor f_{broth} in equation 40. f_{broth} includes corrections for the composition of the liquid media, and for the internal configuration of the bioreactor. The value of f_{broth} was defined such that the estimated concentrations of CO and H_2 (C_{CO} and C_{H_2}, respectively) are not negative at any point during the experiment.

$$k_L a_j = f_{broth}\left[1.022^{(T-293.15)}\right]\left[0.002\left(\frac{P_S}{V_L}\right)^{0.7} {v_{Gs}^c}^{0.2}\right]\left(\frac{Đ_{O_2}}{Đ_j}\right)^{0.5} \quad (40)$$

$$P_S = N_P \rho_L N^3 {D_S}^5 \quad (41)$$

Furthermore, the calculation of $k_L a$ was based, in principle, on the power input by the stirrer (P_S in equations 40 and 41) and by gas sparging, and was also corrected for *i)* the process temperature and *ii)* the film diffusivity (Đ) of CO and H_2 in pure water compared to that of O_2, because the model used was developed for O_2 transfer to pure water at 20 °C. The correction of the power input by the stirrer due to the effects of gas sparging (proposed by [430]) was not taken into account since the experimental gas flow rate was too low for the model to be applicable.

Table 6.4. Assumptions made for the calculation of the mass transfer coefficients

Item	Units	Value
Fermentation broth		
Density of the fermentation broth (ρ)	kg/m^3	1000
Coalescence characteristics of the fermentation broth	-	Non-coalescent
Bioreactor vessel		
Total volume of the bioreactor vessel	mL	1000
Height-to-diameter ratio of the bioreactor vessel	-	1
Stirrer		
Vessel diameter to stirrer diameter (D_s) ratio	-	3
Type of impeller	-	Six flat blades (Rushton)
Stirrer power number (N_P)	-	5

6.3.4.2. Formulation of the optimization problem

The parameterization of the model was done step-wise because of *i)* the large number of unknown elasticity coefficients, *ii)* the partial compatibility between the model's structure and the concentrations data reported by [113], and *iii*) the simultaneous estimation of the 3 reference concentrations along with the initial concentrations of the 17 species in the system of ode's. The three sets of estimated parameters are given the following abbreviations: ε_{ij} for the elasticity coefficients, C_j^0 for the unknown reference concentrations of acetate, formate and Fd_{red}^{2-}, and $C_{j,0}$ for the intial concentrations of the 13 species whose concentrations vary with time.

The steps followed to parameterize the model are described in the following lines. The details of all the steps are summarized in Table 6.5.

In the first step, ε_{ij} and C_j^0 are estimated while $C_{j,0}$ is fixed at the reported experimental values or at the calculated values for the un-reported substances. That is done to avoid possible interferences of $C_{j,0}$ with the estimation of ε_{ij}, witnessed during preliminary trials. The initial guesses for all ε_{ij} are set at 0.1, the upper and lower bounds are set to 1 and -1, respectively. The initial guesses for C_j^0 are 0.1, the upper and lower bounds are 100 mol/m^3 for acetate and 10 mol/m^3 for formate and Fd_{red}^{2-}, and the lower bounds are 1x10^{-5} mol/m^3 for the three substances.

Two sequential minimization algorithms are applied in this and in all the subsequent steps of the model parameterization, *i.e.*, a stochastic particle swarm algorithm immediately followed by an iterative minimization using MatLab's 'fmincon' function using the 'interior point' algorithm. The first algorithm explores the vast solutions space while the second minimization refines the solution delivered by the first algorithm.

The objective function of the minimization is shown by equation 42, where $C_{k,exp}$, $C_{k,cal}$ and δ_k are vectors containing the experimental concentrations, the calculated

concentrations and the errors expected in the experimental measurements, respectively; the subscript k stands for ethanol, acetic acid, 2,3-butanediol and biomass in the extracellular liquid, CO and H_2 in the gas phase, and for acetyl-CoA and NADH in the intracellular liquid.

$$f = \sum \left(\frac{C_{k,exp} - C_{k,cal}}{\delta_k} \right)^2 \quad (42)$$

The terms in δ_k are the absolute errors expected in the experimental measurements; the errors were assumed to be 10% for the measurements in both, the extra and the intracellular spaces, and 5% for the measurements in the gas phase.

The elements in $C_{k,cal}$ are obtained from solving the ordinary differential equations (ode), using MatLab's function 'ode15s'.

However, equation 42 is only one part of the objective function used within each minimization. More often at the early iterations, the 'ode' solver finds solutions of concentrations that are either negative or too high compared to the experimental data. When such concentrations are calculated, the 'ode' solver is stopped by an event function programmed into the solver [i] and the objective function is penalized with a value equal to the ratio between the time at which the event was produced and the time of the last experimental data point multiplied by 10^6. This causes the objective function to have two main structures: *i)* a plateau at very high values (higher than 10^6) where negative or too high concentrations are calculated and *ii)* deep valleys where the integration timespan is covered without the events being met, and where the objective function is produced by equation 42 and therefore, where the parameterization solutions are found.

In a second minimization step, $C_{j,0}$ is estimated while keeping ε_{ij} and C_j^0 at the values found in the first step. The initial guesses for $C_{j,0}$ are taken from the experimental and the reconstructed experimental data. The upper bounds are equal to 5 times the experimental value and lower bounds equal the experimental values divided by 5 (see Table 6.5). The number 5 was chosen arbitrarily after preliminary trials where the optimization algorithm estimated values for $C_{j,0}$ that diverged largely from the experimental values.

In a third step, ε_{ij}, C_j^0 and $C_{j,0}$ are all estimated simultaneously.

The proposed structure of the objective function (plateau and deep valleys) might lead to the finding of local minima after the three sequential steps. To further explore the

[i] The exact constraints programmed into the event function are: *i)* $C_j < 5C_j^0$, *ii)* $C_j > 10^{-5}$, *iii)* the time the ODE solver takes should not surpass the 5 seconds (constraint imposed to prevent the ODE solver to use extremely small time-steps).

solution space five iterations of the three sequential minimization steps are followed in total.

Table 6.5. Description of the sequence of minimizations followed during the first round of optimization

Iteration	Step	Algorithm [a]	Decision variables	Initial guesses	Bounds [b]
1	1	PS	ε_{ij} and C_j^0	0.1 for ε_{ij}. 0.1 for C_j^0.	-1 and 1 for $\varepsilon_{i,j}$. 100 for $C_{Ac_i^-}^0$ and 10 for $C_{For^-}^0$, C_{NADPH}^0 and $C_{Fd_{red}^{2-}}^0$.
		IP		From previous solution	Unchanged
	2	PS	$C_{j,0}$	The experimental values for $C_{j,0}$. C_j^0 from previous solution.	Same as above for C_j^0. 5 and 1/5 times the experimental value for $C_{j,0}$.
		IP		From previous solution	Unchanged
	3	IP	ε_{ij}, C_j^0 and $C_{j,0}$	From previous solution	Unchanged
2	1	PS	ε_{ij} and C_j^0	From previous solution	-20 and 20 for ε_{ij}. Unchanged for C_j^0 and $C_{j,0}$.
		IP		From previous solution	Unchanged
	2	PS	$C_{j,0}$	From previous solution	Unchanged
		IP		From previous solution	Unchanged
	3	IP	ε_{ij}, C_j^0 and $C_{j,0}$	From previous solution	Unchanged
3 to 5	1	PS	ε_{ij} and C_j^0	From previous solution	Unchanged
		IP		From previous solution	Unchanged
	2	PS	$C_{j,0}$	From previous solution	Unchanged
		IP		From previous solution	Unchanged
	3	IP	ε_{ij}, C_j^0 and $C_{j,0}$	From previous solution	Unchanged

[a] PS means 'particle swarm' and IP means the 'interior point' method in MatLab's 'fmincon' function.
[b] 'Unchanged' means that the lower and upper bound take the last values that were specified.

After the first iteration, the upper and lower bounds for $\varepsilon_{i,j}$ are opened to 20 and -20, respectively. This strategy was implemented because the optimization algorithm fixed the values of certain elements of ε to the lower or upper bounds (-1 and 1).

The results obtained after the five iterations are reproducible.

The optimizations were run using parallel computing in a computer with two AMD EPYC processors, with 24 CPU cores each.

6.4. Results and discussion

The results section is divided into two main parts. The first part shows the results obtained from the reconciliation of the net conversion rates and the reconstruction of the un-

measured concentrations of dissolved CO and H_2. The second part describes the model parameterization results by exploring the errors linked to the estimated parameters and the deviation of the calculated reaction rates with respect to the reconciled rates. A final part explores the possible implications of the results on the levels of control that the different metabolites appear to exert over the metabolic network.

6.4.1. Data processing

6.4.1.1. Reconciliation of q-rates

After the reconciliation of the net conversion rates, the largest changes are observed for q_{CO} and q_{CO_2}, as shown in Figure 6.2. The corrections in the mentioned rates range from 2 to 26%, and coincide, partly, with the size of the carbon gap (in the mass balances) in the data points (10 – 20%, see Table B1 in Appendix B). For the whole experimental run, the carbon gap reveals that carbon is missing at the uptake side, meaning that there is more carbon going out as a product than it is entering the cell. The presence of carbon gaps could suggest that there are un-measured substances in the experiments. Since no other carbon source can be acknowledged from what is reported in [113], and no yeast extract is used as fed in the fermentation broth composition, it may be assumed that the reported conversion rates were calculated through incomplete mass balances.

A more robust reconciliation process, based on dynamic mass balances was, unfortunately, unsuccessful in preliminary trials since the time interval between the experimental data points was significantly large to allow an accurate calculation of the concentration differentials of all species present in the system. For future experiments, where metabolic oscillations are witnessed, we recommend to increase the frequency of sampling; if the oscillations were faster than in [113], it could also be recommended to consider possible effects of dispersion of the gas within the bioreactor headspace and avoid assuming that the off-gas composition is the same as that in the headspace, as described in [422].

Lastly, Figure 6.2.g and h show that the rate of ethanol production has a linear relation with the total uptake rate of electrons (q_{e^-}) from CO and H_2, while the rate of acetic acid production does not depend on q_{e^-}. Those relations may suggest that the faster the electrons are consumed by cells, the faster they secrete ethanol. This result is relevant for understanding what would happen inside a large-scale syngas fermentor, where the concentrations of the electron donors are the highest at the bottom and the lowest at the top (or in the downcomer of a gas lift bioreactor, where gas is fed from the bottom of the riser [431]). It could be speculated that ethanol would mostly be produced at the bottom of the column while the acid will be produced during starvation.

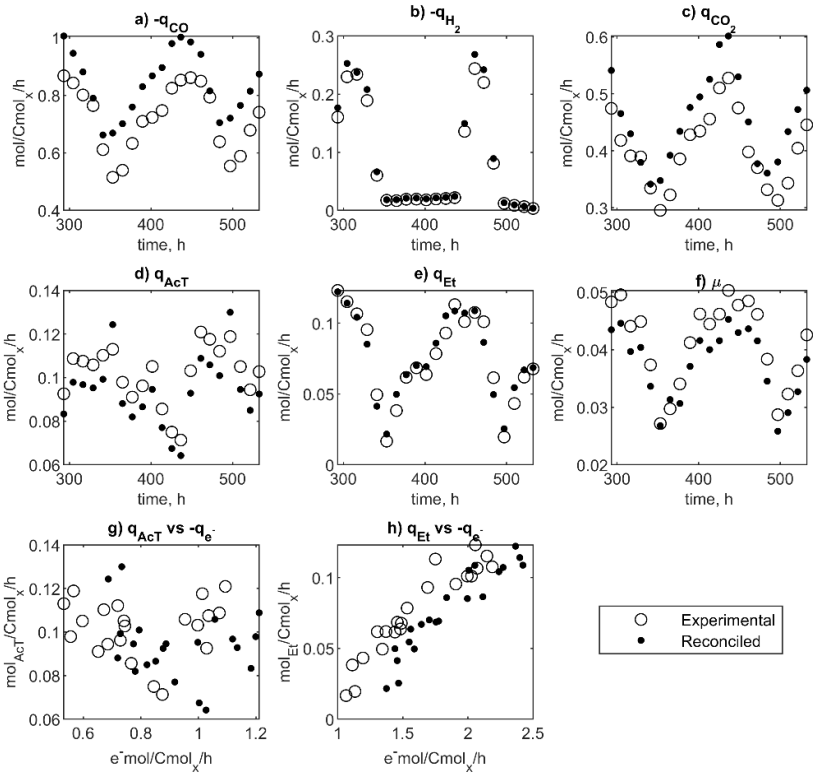

Figure 6.2. Comparison between the reported and reconciled values for the uptake rates of a) CO and b) H_2, and the production rates of c) CO_2, d) acetic acid, e) ethanol and f) biomass. The figure also includes the dependencies of g) acetic acid and h) ethanol production on the total uptake rates of electrons (q_e-).

6.4.1.2. Concentrations of dissolved CO and H_2

Relevant assumptions were necessary to calculate the mass transfer coefficient of the bioreactor used by [113] given the limited details about the bioreactor's internal configuration were reported. Unfortunately, in general, such useful details are rarely given in scientific reports describing anaerobic syngas-based fermentation experiments with acetogens. The correction factor f_{broth} was introduced to overcome these information gaps and also the possible effects of the broth composition. However, the introduction of such factor brings considerable uncertainties to the estimated C_{CO} and C_{H_2}, variables that are essential for the parameterization, use and interpretation of the kinetic model, as well as for the fundamental understanding of the syngas fermentation technology. Therefore, to reduce uncertainties on the internal performance of the syngas-fermenting

acetogens, we recommend implementing methods that allow measuring the dynamic concentrations of the dissolved gases during the fermentation experiments -in real time- such as the case of the broadly popular dissolved oxygen. Measuring C_{H_2} can already be achieved by changing the polarization voltage of a Clark electrode [432,433]; C_{CO} may also be measured using tubes made of materials permeable to CO, which are submerged in the fermentation broth during the experiment, as proposed by [434]. It may be expected than in the coming years, reports of the application of those or similar techniques in syngas fermentations will be published.

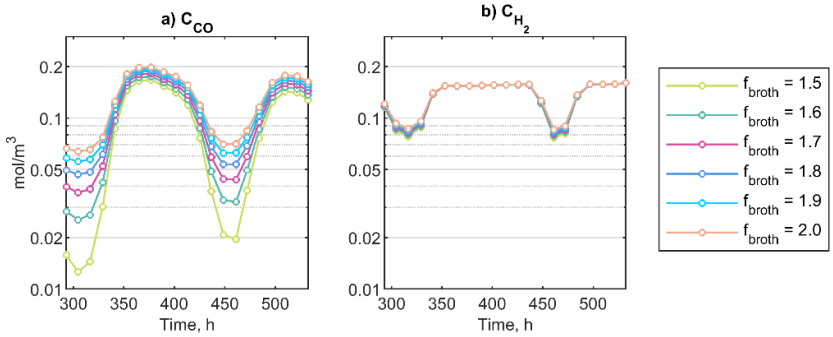

Figure 6.3. Effect of f_{broth} on the estimated concentrations of the electron donors, a) CO and b) H_2.

Figure 6.3 shows the dependency of the calculated C_{CO} and C_{H_2} for different values of f_{broth}, ranging between 1.5 and 2. Those values mean that the experimental $k_L a$ obtained by [113] falls between a 50 and 100% higher than that obtained in a bioreactor with the configuration details presented in Table 6.4. Depending on the value of f_{broth}, C_{CO} can range between 0.06 and 0.006 mM when q_{CO} is largest throughout the oscillations; that is an uncertainty of one order of magnitude. When the uptake rates are low, such as for the lowest values of q_{CO} and all the values of q_{H_2}, there is a significantly lower uncertainty derived from the value of f_{broth}. Therefore, the calculated dissolved concentrations of H_2 are in general more reliable than that of CO.

For the subsequent steps in this study, a value of 1.6 is taken for f_{broth} because it delivers C_{CO} values that range between 0.2 and 0.02 mM throughout the oscillations (see Figure 6.3). That is a change of one order of magnitude, a similar change calculated by CFD-based simulations of the large-scale bioreactor [428]. Moreover, the significant enhancements of mass transfer due to the presence of ethanol in the fermentation media [413,414] also give realism to the assumed f_{broth}. Therefore, the choice of f_{broth} is not only useful for testing the potential of the kinetic model's application within a bioreactor model (where the concentrations gradients vary by one order of magnitude), but it may

also be reasonable, since the presence of salts, ethanol and acetic acid in the liquid media inhibit the coalescence of bubbles [403,413,414,435]. Consequently, the mass transfer coefficient can be expected to be significantly higher in syngas fermentations than that obtained with oxygen transfer to pure water. More solid basis would be provided to the analysis of the model if the impact of f_{broth} would be evaluated more deeply. However, such assessment would diverge from the scope of the present study.

6.4.2. Model Parameterization

This section describes the results obtained from the parameterization of the model by exploring the errors linked the estimated parameters, the deviation of the calculated reaction rates with respect to the reconciled rates and the possible causes of the deviations.

Overall, the summed squared errors relative to the experimental concentrations equals 3.50; considering the number of degrees of freedom in the parameterization (180 – 61 = 119), the value of the objective function returns an average error of 15.0% for the model predictions compared to the experimental concentrations used to construct the objective function. The error is higher than the experimental error (expectedly around 10 – 5% [436]), therefore, further improvements are still required in the model.

6.4.2.1. The estimated elasticity coefficients and their uncertainty

The uncertainty of the estimated parameters was inspected using the jacobian (Jac) matrix, one of the outputs of MatLab's 'lsqnonlin' function; in this study the 'lsqnonlin' function was only used for estimating the jacobian by setting the maximum number of iterations to zero. Through the jacobian matrix, the variances of the parameters were estimated. The covariance matrix (σ^2) was calculated using equation 43, where the numbers 180 and 61 represent the number of experimental data-points (concentrations) available for comparison and the number of parameters estimated by the model parameterization, respectively. The relative error ($error$) of all the parameters equal to the squared root of the diagonal of σ^2.

$$\sigma^2 = \frac{\text{pinv}(Jac^T \times Jac) * f}{180 - 61} \tag{43}$$

Table 6.6. shows the estimated elasticity coefficients next to the relative errors calculated for each coefficient. Assuming a perfect fit, any parameter with a relative error higher than half of its value (or $\left|\varepsilon_{ij}/error\right| < 2$) could have a value of zero. In our case, the fit is far

from perfect, therefore all the parameters that were estimated in the parameterization have high levels of uncertainty.

The obtained values of the elasticity coefficients are, in general, highly uncertain. In the above, the error analysis is based on the measurement of the uncertainty. However, there is also parameter ambiguity derived from three features of our parameterization methodology: *i)* it is unknown whether the solution we found corresponds to a local (most likely) or to a global minimum, *ii)* considering that the experimental data set is incomplete (certain concentrations were not measured, see section 6.3.2) it does not allow the elasticities of some reactions to be determined, and *iii)* the choice of elasticities can inadvertently introduce these ambiguities between the parameters *i.e.*, one or more combinations of parameters could produce the same result. Therefore, the solution reported here should be considered with care.

An interpretation of the results is presented as follows as an example of the relevance of performing a kinetic model parameterization and also the usefulness of the approach for advancing on the fundamental understanding of syngas-fermenting acetogenic bacteria.

Starting with the formate dehydrogenase reaction (FDH): it is kinetically promoted mainly by the electron carriers participating in it, NADPH and Fd_{red}^{2-}; CO_2 and formate may influence the rates of FDH only slightly, if at all. The acetyl-CoA synthesis (ACAS reaction) may be promoted by CO (the substrate), Fd_{red}^{2-} and NADH, while inhibited by acetyl-CoA (the product) and NADPH. Furthermore, the rate of the CODH reaction may be promoted by CO but inhibited by Fd_{red}^{2-}. Such dependencies may agree with the hypothesis that CO consumption can lead to an excessively reduced intracellular state [53], and the way cells prevent such state is by Fd_{red}^{2-} inhibition, which is externally seen as CO inhibiting its own consumption [106].

The results obtained for the Hyd reaction (which collects the electrons from H_2) were unexpected, *i.e.*, H_2 inhibits the reaction while the effect of Fd_{red}^{2-}, NADPH and CO_2 is null due to the high error in ε. Formate, a substance added to the kinetic expression of Hyd due to the possible presence of the H_2-futile cycle (introduced in section 6.3.3) has an inhibitory effect on Hyd. The inhibition exerted by formate and H_2 may support the hypothesis of the existence of a reaction producing H_2 and another producing formate, within a possible futile cycle. Lastly, NADH, a substance which was considered for the construction of the kinetic expression for Hyd while not being directly part it also appears to inhibit its rate. The existence of an active NADH-ferredoxin-dependent hydrogenase has not yet been proven even though it has been looked for [53]; our result suggest that the search of such enzyme or other regulatory mechanisms of NADH over Hyd should still continue.

Table 6.6. Estimated elasticity coefficients and their errors

i	j	ε_{ij}	$error$	$\left\|\frac{\varepsilon_{ij}}{error}\right\|$	i	j	ε_{ij}	$error$	$\left\|\frac{\varepsilon_{ij}}{error}\right\|$
FDH	CO_2	0.16	5.3	0.03	EtS	Et	-0.51	1.5	0.33
	For	-0.15	1.9	0.08		NADH	1.41	9.5	0.15
	NADPH	1.11	7.5	0.15		$[Ac^-]_i$	0.07	1.4	0.05
	Fd_{red}^{2-}	0.98	6.2	0.16		Fd_{red}^{2-}	-0.77	5.0	0.15
ACAS	CO	0.49	4.0	0.12	BDOS	CO_2	0.70	4.5	0.16
	AcCoA	-0.47	3.3	0.14		BDO	1.66	9.5	0.17
	NADH	3.81	25	0.15		AcCoA	-0.46	4.9	0.09
	For	-0.004	0.7	0.01		NADH	10.2	56	0.18
	NADPH	-0.57	4.4	0.13		Fd_{red}^{2-}	1.08	7.7	0.14
	Fd_{red}^{2-}	0.45	6.7	0.07	Nfn	NADH	-0.89	1.9	0.46
CODH	CO	0.26	0.9	0.29		NADPH	0.07	0.6	0.12
	CO_2	0.02	4.6	0.00		Fd_{red}^{2-}	0.01	0.7	0.02
	Fd_{red}^{2-}	-0.45	2.1	0.21	Rnf	NADH	-0.81	1.9	0.43
Hyd	H_2	-0.96	8.1	0.12		Fd_{red}^{2-}	-0.37	1.6	0.23
	CO_2	-0.11	7.6	0.01	Ana	AcCoA	-0.01	0.8	0.01
	NADH	-0.65	3.9	0.17		NADH	0.50	5.0	0.10
	For	-0.97	7.9	0.12		NADPH	0.79	2.8	0.28
	NADPH	0.02	14	0.00		Fd_{red}^{2-}	-0.81	3.8	0.21
	Fd_{red}^{2-}	-0.08	5.5	0.01	AcX	AcT	0.99	1.8	0.56
AcS	AcCoA	0.60	6.2	0.10		$[Ac^-]_i$	0.13	1.6	0.08
	$[Ac^-]_i$	0.980	8.8	0.11					

The kinetics of acetate synthesis (AcS reaction) may be promoted by acetyl-CoA and interestingly by acetate, the product of the reaction. Further downstream, ethanol synthesis may be kinetically promoted by NADH while being inhibited by Fd_{red}^{2-} and ethanol. The synthesis of 2,3-butanediol is promoted by NADH, Fd_{red}^{2-}, CO_2 and ethanol whereas acetyl-CoA inhibits the reaction.

Regarding the rate of the lumped anabolic reaction (Ana reaction), its rate depends only slightly on the substrate assigned in the network, acetyl-CoA. The rate of biomass synthesis appears to instead depend mostly on the concentrations of the redox carriers, *i.e.*, promoted by NADH and NADPH while inhibited by Fd_{red}^{2-}. Such result is however not surprising since in reality, the synthesis of cell material is much more complex than the proposed lumped reaction.

Lastly, the rate of acetate export may be promoted by the summed extracellular concentrations of acetic acid and acetate. Such effect is not surprising and logical since

the rate of the diffusion of the undissociated acetic acid into the cell is one to five times larger than the net rate of acetate production (see section 5.4.1.3). Acetic acid diffusion therefore brings enormous amounts of acetate into the cell and causes pressure to export the acetate again to maintain homeostasis.

The Rnf reaction appears to be inhibited by both, its substrate: Fd_{red}^{2-} and its product: NADH; such effect may suggest a careful control of the proton motive force and thus of *i)* NADH production (the Rnf complex is the only source of NADH in the network) and also *ii)* ATP production at the membrane-based ATP-synthase (not included in the network). Lastly, NADH also inhibits the rate of the Nfn complex; since the only source of NADPH is the Nfn complex, NADH controls the production of NADPH from the substrate side. The effect of Fd_{red}^{2-} on the Nfn complex may be small compared to that of NADH and NADPH.

To close this sub-section, it is worth mentoning that further efforts should be implemented to prove the finding of a global minimum during the parameterization and to find experimental evidence such that the veracity of the previous discussion is determined.

6.4.2.2. The estimated reference and initial concentrations

The values of the reference rates of reaction and concentrations are shown in Table 6.7. The reference intracellular concentrations for acetate, formate and Fd_{red}^{2-} (all contained in C_j^0) were estimated as part of the model parameterization process. The estimated reference concentrations for Fd_{red}^{2-} and formate fall within the range of the concentrations calculated from solving the system of differential equations (see Figure 6.4.b and c). Therefore, in future explorations with the model's parameterization, their values may be fixed to reduce the number unknown parameters. On the other hand, the reference intracellular concentration of acetate falls below the range of the calculated concentrations for intracellular acetate (see Figure 6.4.a); the reference intracellular concentration of acetate should still be considered within the list of the parameters estimated in the model parameterization, if no experimental information is made available.

Figure 6.4.b shows that the dynamic oscillations of the intracellular formate concentration ranges from very low values (in the order of 10^{-9} mol/m^3) to 15 mol/m^3. By definition, the linlog format is only applicable for small variations of the substance concentrations. Thus, the results obtained for formate suggest that *i)* there is another solution possible in a potential global minimum and/or *ii)* the intracellular concentration of the carboxylate may be regulated by mechanisms that were neglected in the construction of this work. Considering that formic acid can also be produced by acetogens feeding on syngas [311],

a cycle similar to the proposed for acetic acid (export plus back-diffusion) may also be implemented for formate in improved versions of the model here presented.

Table 6.7. Values of the reference rates of reaction (r_i^0) and concentrations (C_j^0)

Reaction	r_i^0, mol/Cmol$_x$/h	Specie	C_j^0, mol/m^3
FDH	0.182	CO	0.157
ACAS	0.182	H_2	0.155
CODH	0.686	CO_2	9.21
Hyd	0.010	AcT	110
AcS	0.160	Et	63.4
EtS	0.078	BDO	1.28
BDOS	0.003	AcCoA	0.210
Nfn	0.131	NADH	0.011
Rnf	0.575	NADPH	0.184
Ana	0.039	$[Ac^-]_i$	34.8
AcX	0.426	For^-	18.6
		Fd_{red}^{2-}	9.13

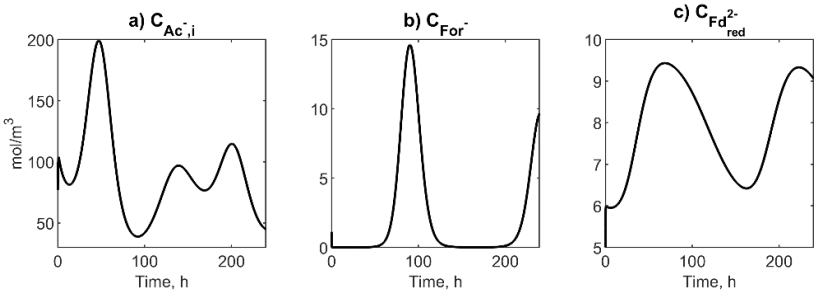

Figure 6.4. Calculated concentrations of the un-measured intracellular and non-exchangeable metabolites, *i.e.*, a) acetate, b) formate and c) Fd_{red}^{2-}.

Table 6.8. Comparison between the experimental initial concentrations and those estimated in the parameterization ($C_{j,0}$)

Concentration	Unit	Estimated	Experimental	Deviation, %
C_{AcT}	mol/m^3	88.4	94.0	6.0
C_{Et}	mol/m^3	119.7	113.8	5.1
C_{BDO}	mol/m^3	3.2	3.2	1.3
C_x	mol/m^3	50.7	51.6	1.8
y_{CO}	-	0.269	0.271	0.6
y_{H_2}	-	0.189	0.189	0.0
C_{AcCoA}	mol/m^3	0.041	0.041	1.1
C_{NADH}	mol/m^3	0.010	0.010	0.1
C_{NADPH}	mol/m^3	0.133	0.132	0.8

Table 6.8 presents a comparison between the experimental and the estimated initial concentrations of the substances considered for solving the systems of differential equations. Mostly small deviations are produced, lower than the 5% expected error in the experimental measurements [436]. The only exceptions are the deviations of 5 and 6% found for ethanol and total acetic acid concentrations in the liquid phase, respectively.

6.4.2.3. Accuracy of the kinetic model's predictions

Figure 6.5 shows a comparison between the reported and the calculated concentrations of the extra and intracellular metabolites that were used for the construction of the minimization's objective functions. The model succeeds in reproducing the oscillatory behavior of the experimental data, suggesting that the linlog format may be applied to simulate the dynamic behavior of *C. autoethanogenum*. The oscillatory behavior of the concentrations of extracellular products and cells are comparable to those of the experimental data, yet with lower amplitude in the oscillation for ethanol, and an offset for biomass. The concentrations of CO and H_2 in the gas phase, as well as intracellular NADH also present offsets. The possible causes for the low accuracy in some of the mentioned concentrations are traced in the following discussion.

Figure 6.6 shows the comparisons between the experimental and the calculated q-rates for CO, H_2, CO_2, acetic acid, ethanol, 2,3-butanediol, biomass growth and water. The calculated low amplitude in y_{CO} (see Figure 6.5.e) is caused by a partial adjustment of the oscillations amplitude of the net CO uptake rate (see Figure 6.6.a). q_{CO} is formed by the contributions of the intracellular reactions CODH and ACAS; CODH collects the electrons from CO into Fd_{red}^{2-} and produces CO_2, while ACAS lumps the methyl branch of the Wood-Ljungdahl pathway [363]. Between the CODH and ACAS reactions, the CODH is the fastest and consequently the largest contributor the q_{CO}. The influence of the CODH reaction is also seen at the partial adjustment of q_{CO_2}, especially in the low q_{CO_2} values (see Figure 6.6.c). Thus, improving the kinetic expression for CODH (considering also that the elasticity coefficients of the CODH reaction contained large errors, see Table 6.6) may lead to not only a better reproduction of the peaks in q_{CO} and q_{CO_2}, but also to better predictions of the flow of carbon into the metabolic network and the flow of electrons through Fd_{red}^{2-}. Fd_{red}^{2-} powers the production of NADH as well as the proton motive force (by the Rnf reaction) and the synthesis of NADPH (by the Nfn reaction). The intracellular reaction rates contributing to the formation and depletion of the pools of Fd_{red}^{2-}, NADH and NADPH, are shown in Figure 6.7. The pool of Fd_{red}^{2-} is the fastest of the three and CODH produces the largest flow into that pool. This is another point that would benefit from further assessment of the kinetics of CODH and from actual measurements of the intracellular concentration of Fd_{red}^{2-}.

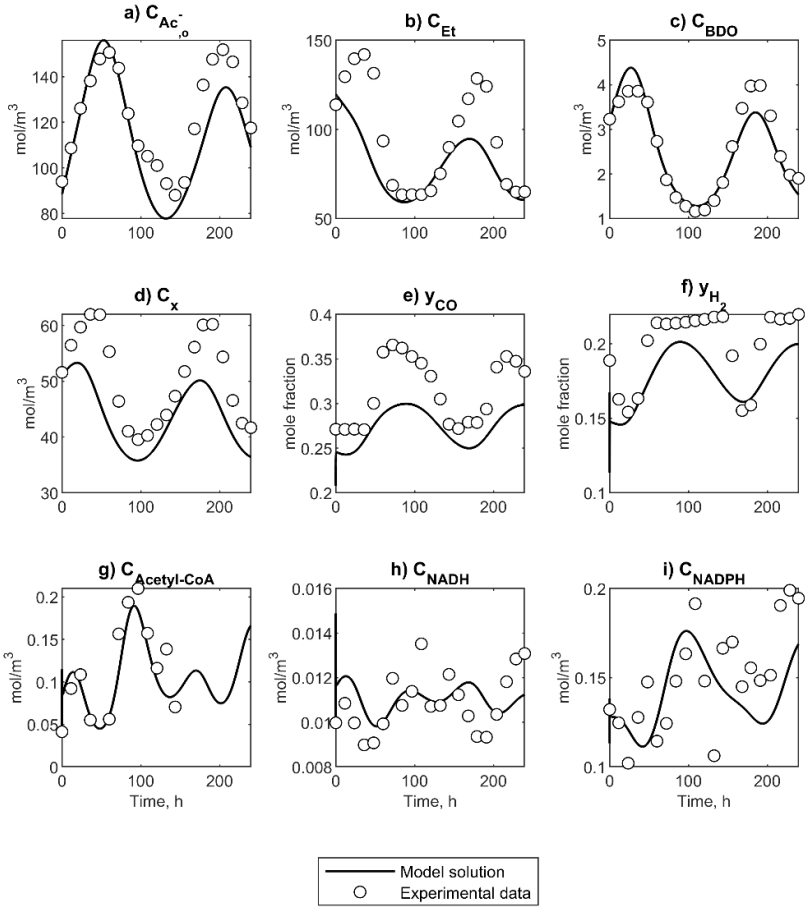

Figure 6.5. Comparison between the reported and the calculated concentrations of extra and intracellular metabolites, cells and CO and H_2 in the gas phase.

Moreover, the calculated H_2 uptake rate forms an oscillatory trend (see Figure 6.6.c), while the experimental data shows that H_2 is consumed by pulses. As discussed in section 6.4.2.1, considering that two reactions are involved in the uptake of H_2 may improve the predictive capacity of the present model. Such consideration should be backed up by a study of the conditions under which the two reactions are carried out simultaneously during the fermentation of CO/H_2 mixtures and during the fermentation of pure CO.

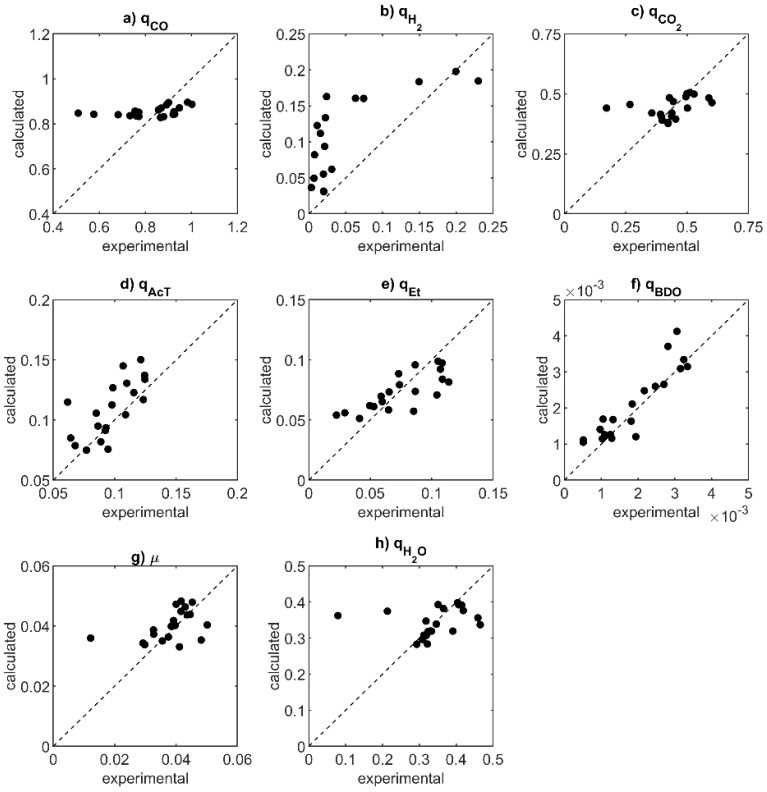

Figure 6.6. Correlation between the experimental q-rates and those calculated with the kinetic model.

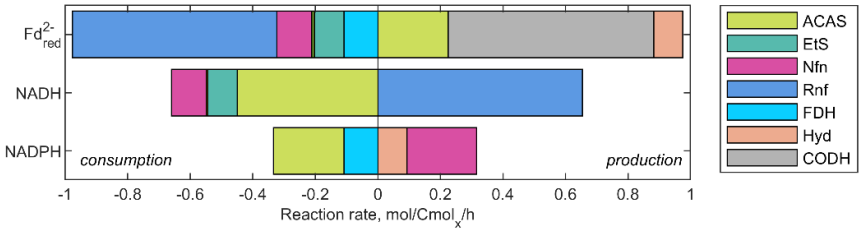

Figure 6.7. Reaction rates of the components influencing the metabolic pools of a) Fd_{red}^{2-}, b) NADH and c) NAPH. The values shown are the median values calculated for the experimental run 1.

6.4.3. The turnover frequencies of the metabolic pools

Figure 6.8 shows the turnover frequencies of all the metabolic pools considered in the intra and extracellular liquid phases. The turnover frequencies were calculated dividing

the sum of the reaction rates feeding or depleting the pools by their respective sizes (metabolite concentrations). The frequencies give an idea of how fast the metabolic pools can change their sizes. The NADH pool is the fastest, followed by that of CO, H_2, acetyl-CoA and that of NADPH. The list is tailed by the extracellular acetic acid pool.

From the estimated values of the elasticity coefficients (see Table 6.6.), it is clear that NADH may play a major role influencing the fluxes in the carbon and the electron routes, including electron harvest from H_2, synthesis of acetyl-CoA, ethanol and 2,3-butanediol, the proton motive force (Rnf reaction) and the Nfn complex. Adding to the previous, NADH has the highest turnover frequency. Therefore, besides NADH being influential in the rates of reaction in key parts of the metabolic network, it is also a pool whose size changes with a frequency of 261 s^{-1}; or in other words, the NADH pool can be depleted in 3.8 ms. The two findings about NADH suggest that this redox carrier plays a fundamental role in the control of the fluxes in the proposed metabolic network. To quantify such control, we recommend that metabolic flux control analysis (such as that presented by [426]) should be another subsequent step to be taken to advance the fundamental understanding of *C. autoethanogenum*.

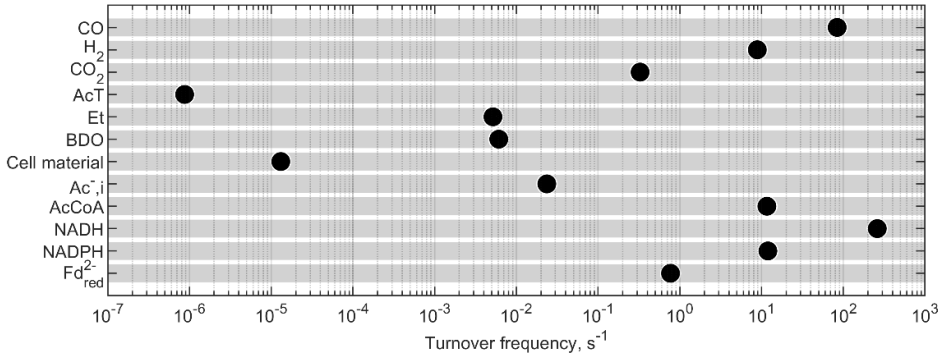

Figure 6.8. Turnover frequencies calculated for the for the substance pools in the extra and intracellular liquid phases. Only the median values are shown.

It has been argued (and supported by extensive experimental evidence) that the production of acetic acid is linked to growth of acetogens. The analysis of the turnover frequencies may provide extra evidence, since the low turnover frequency of the extracellular acetic acid pool approaches the value of the growth rate of *C. autoethanogenum* during the experiment.

6.5. Conclusions and recommendations

Two main conclusions can be drawn from the presented study:

- The linlog format was applied to a set of experimental data where metabolic oscillations were observed in a continuous fermentation with *C. autoethanogenum* and reported by [113]. Using the linlog format, we were able to reproduce the dynamic behavior of the extracellular concentrations of acetic acid, ethanol, 2,3-butanediol, cells, CO, H_2 and CO_2, as well as the intracellular concentration of NADH, acetyl-CoA and NADPH.
- The reconciled reaction rates showed that the synthesis of ethanol responds linearly to the influx of electrons from CO and H_2, under the dynamic oscillatory state of *C. autoethanogenum*. The model reproduces this relation.

The predictive capacity of the current version of the model is still constrained by the non-reliability of the estimated elasticity coefficients. Further improvements are required on the parameterization methodology such that a global minimum is found. The parameterization should also be based on more extensive data to improve the reliability of the estimated parameters.

Moreover, further improvements are required on the kinetic model structure. The inclusion of ATP into the metabolic network may be the most urgent improvement to make. Another improvement should consider that H_2 uptake is performed by two separate reactions. These reactions are catalyzed by not only the ferredoxin-NADPH-dependent hydrogenase (as in this study), but also by a formate-hydrogen-lyase. The indirect and possibly direct influence of NADH in the uptake of H_2 should also be explored.

To deploy the potential of the proposed kinetic model for simulating syngas fermentation in a large-scale bioreactor, the model should be parameterized using experimental data gathered from scaled-down fermentations. Such experiments should be based on oscillations of the CO and H_2 concentrations with a frequency in the order of one per minute. The scaled-down experiments must employ experimental techniques for *i)* in-line measurements of CO and H_2 dissolved concentrations, *ii)* the measurement of the mass transfer coefficient, and *iii)* the measurement of the intracellular concentrations of formate, acetate and in the best case, Fd_{red}^{2-}.

6.6. List of abbreviations and symbols

Abbreviations		
Abbreviation	**Meaning**	
$[Ac^-]_i$	Intracellular acetate	
HAcD	Extracellular undissociated acetic acid	
AcT	Extracellular total acetic acid (dissociate plus undissociated forms)	
AcCoA	Acetyl coenzyme A	
BDO	2,3-butanediol	
DM	Dry mass	
Et	Ethanol	
For^-	Formate	
Fd_{red}^{2-}	Reduced ferredoxin	
Fd_{ox}^-	Oxidized ferredoxin	
NADH	Reduced nicotinamide adenine dinucleotide	
NAD^+	Oxidized nicotinamide adenine dinucleotide	
NADPH	Reduced nicotinamide adenine dinucleotide phosphate	
$NADP^+$	Oxidized nicotinamide adenine dinucleotide phosphate	
x	Cells	
W	Water	
Symbols		
Symbol	**Meaning**	**Unit**
C_j	Concentration of substance *j*	mol_j/m^3
C_j^0	Reference concentration of substance *j*	mol_j/m^3
C_j^*	Saturation concentration of substance *j*	mol_j/m^3
$Đ_j$	Film diffusivity of substance *j* in pure water	m^2/h
D_S	Diameter of stirrer	m
$F_{G,i}$	Gas inflow rate from the bioreactor	mol/h
$F_{G,o}$	Gas outflow rate from the bioreactor	mol/h
$F_{L,i}$	Liquid inflow rate from the bioreactor	kg/h
$F_{L,o}$	Liquid outflow rate from the bioreactor	kg/h
f	Objective function	-
H	Hessian matrix	-
J_i	Transient flux of the reaction *i*	$mol/Cmol_x/h$
$k_{H,j}$	Henry's coefficient of substance *j*	$mol/m^3/bar$
$k_L a_j$	Mass transfer coefficient of substance *j*	h^{-1}
m_j	Molar mass of substance *j*	g/mol
N_P	Power number is bioreactor stirrer	-
N	Stirring speed	s^{-1}
n_G	Number of moles of the gas phase in the bioreactor's headspace	mol
P_S	Power delivered by the stirrer	W
p	Pressure in the bioreactor headspace	bar
q	Net uptake/secretion rate	$mol/Cmol_x/h$
r_i^{ll}	Linlog correction applied to the rate of reaction *i*	-
r_i^0	Reference rate of the reaction *i*	$mol/Cmol_x/h$
T	Temperature	K
t	Time	h
V_L	Volume of liquid in the bioreactor	m^3
V_x	Molar volume of cells	$m^3/Cmol_x$
v_{GS}^c	Superficial gas velocity	m/s
y_j	Molar fraction of substance *j* in the gas phase	-
ε	Elasticity matrix	-

ε_{ij}	Elasticity coefficient of substance j for reaction i	-
ρ_L	Density of the liquid in the bioreactor	kg/m^3

Appendix A

Stoichiometry of the metabolic network and assembly of the A matrix

Table A.1 List of reactions considered for the metabolic network. Matrix adapted from [427].

Name	Abb. [a]	Equation [b,c]	Rx. nr.
Formate dehydrogenase	FDH	$-\mathrm{CO_2} - 0.5[\mathrm{H^+}]_\mathrm{i} - 0.5\mathrm{Fd}_\mathrm{red}^{2-} - 0.5\mathrm{NADPH} + \mathrm{For}^- + 0.5\mathrm{Fd}_\mathrm{ox} + 0.5\mathrm{NADP^+}$	(i1)
Acetyl-CoA synthesis	ACAS	$-\mathrm{For}^- - \mathrm{CO} - 2[\mathrm{H^+}]_\mathrm{i} - 2\mathrm{NADH} - \mathrm{NADPH} - \mathrm{H\text{-}CoA} - \mathrm{Fd}_\mathrm{ox} + \mathrm{C_2H_3O\text{-}CoA} + 2\mathrm{H_2O} + \mathrm{Fd}_\mathrm{red}^{2-} + 2\mathrm{NAD^+} + \mathrm{NADP^+}$	(i.2)
CO-dehydrogenase	CODH	$-\mathrm{CO} - \mathrm{H_2O} - \mathrm{Fd}_\mathrm{ox} + \mathrm{CO_2} + 2[\mathrm{H^+}]_\mathrm{i} + \mathrm{Fd}_\mathrm{red}^{2-}$	(i3)
Fd-NADPH-Hydrogenase	Hyd	$-2\mathrm{H_2} - \mathrm{NADP^+} - \mathrm{Fd}_\mathrm{ox} + 3[\mathrm{H^+}]_\mathrm{i} + \mathrm{NADPH} + \mathrm{Fd}_\mathrm{red}^{2-}$	(i4)
Acetate synthesis	AcS	$-\mathrm{C_2H_3O\text{-}CoA} - \mathrm{H_2O} + \mathrm{Ac}^- + \mathrm{H\text{-}CoA} + [\mathrm{H^+}]_\mathrm{i}$	(i5)
Ethanol synthesis	EtS	$-\mathrm{Ac}^- - 4[\mathrm{H^+}]_\mathrm{i} - \mathrm{NADH} - \mathrm{Fd}_\mathrm{red}^{2-} + \mathrm{Et} + \mathrm{H_2O} + \mathrm{NAD^+} + \mathrm{Fd}_\mathrm{ox}$	(i6)
2,3-butanediol synthesis	BDOS	$-\mathrm{C_2H_3O\text{-}CoA} - \frac{5}{2}[\mathrm{H^+}]_\mathrm{i} - \frac{1}{2}\mathrm{NADH} - \mathrm{Fd}_\mathrm{red}^{2-} + \frac{1}{2}\mathrm{BDO} + \frac{1}{2}\mathrm{NAD^+} + \mathrm{Fd}_\mathrm{ox} + \mathrm{H\text{-}CoA}$	(i7)
Nfn complex	Nfn	$-[\mathrm{H^+}]_\mathrm{i} - \mathrm{Fd}_\mathrm{red}^{2-} - \mathrm{NADH} - 2\mathrm{NADP^+} + 2\mathrm{NADPH} + \mathrm{Fd}_\mathrm{ox} + \mathrm{NAD^+}$	(i8)
Rnf complex	Rnf	$-3[\mathrm{H^+}]_\mathrm{i} - \mathrm{Fd}_\mathrm{red}^{2-} - \mathrm{NAD^+} + \mathrm{Fd}_\mathrm{ox} + \mathrm{NADH} + 2[\mathrm{H^+}]_\mathrm{o}$	(i9)
Anabolism	Ana	$-\frac{1}{2}\mathrm{C_2H_3O\text{-}CoA} - \mathrm{NH_4}^+ + \mathrm{CH_{7/4}O_{1/2}N_{1/4}} + \mathrm{H\text{-}CoA} + \frac{1}{4}[\mathrm{H^+}]_\mathrm{i}$	(i10)
Proton influx	$\mathrm{H^+}$,i	$-[\mathrm{H^+}]_\mathrm{o} + [\mathrm{H^+}]_\mathrm{i}$	(i11)
Acetate export [d]	AcX	$-[\mathrm{Ac}^-]_\mathrm{i} + [\mathrm{Ac}^-]_\mathrm{o}$	(i12)
Acetic acid passive diffusion	HAcD	$-[\mathrm{HAc}]_\mathrm{o} + [\mathrm{Ac}^-]_\mathrm{i} + [\mathrm{H^+}]_\mathrm{i}$	(i13)
Formate hydrogen lyase	FHL	$-\mathrm{H_2} - \mathrm{CO_2} + \mathrm{For}^- + [\mathrm{H^+}]_\mathrm{i}$	(i14)

[a] Abbreviations

[b] The stoichiometric coefficient of water was determined such that the oxygen balance closes; similarly, the amount of $\mathrm{H^+}$ was defined such that the hydrogen balance closes. This applies for the whole metabolic network.

[c] The sub-fixes i and o after the brackets containing the chemical species denotes the location of the protons: inside or outside the cells, respectively.

[d] The assumed mechanism of acetate transport is uniport [427].

The metabolic matrix (A)

$$A = \begin{bmatrix}
0 & -1 & -1 & 0 & 0 & 0 & 0 & 0 & 0 & 0 & 0 & 0 & 0 & 0 & 0 & 0 & 0 & 0 & 0 & -1 & 0 & 0 \\
0 & 0 & 0 & -2 & 0 & 0 & 0 & 0 & 0 & 0 & 0 & 0 & 0 & 0 & 0 & 0 & 0 & 0 & 0 & 0 & -1 & 0 \\
0 & 0 & 0 & 0 & 0 & 0 & 0 & 0 & 0 & 1 & 0 & 0 & 0 & 0 & 0 & 0 & 0 & 0 & 0 & -1 & 0 & 0 \\
0 & 0 & 0 & 0 & 0 & 0 & 0 & 0 & 0 & 0 & 0 & 1 & -1 & 0 & 0 & 0 & 0 & 0 & -1 & 0 & 0 & 0 \\
0 & 0 & 0 & 0 & 0 & 0 & 0.5 & 0 & 0 & 0 & 0 & 0 & 0 & 0 & 0 & 0 & 0 & 0 & 0 & 0 & 0 & -1 \\
0 & 0 & 0 & 0 & 0 & 1 & 0 & 0 & 0 & 0 & 0 & 0 & 0 & 0 & -1 & 0 & 0 & 0 & 0 & 0 & 0 & 0 \\
-1 & 0 & 1 & 0 & 0 & 0 & 0 & 0 & 0 & 0 & 0 & 0 & 0 & -1 & 0 & 0 & 0 & 0 & 0 & 0 & 0 & 0 \\
0 & 2 & -1 & 0 & -1 & 1 & 0 & 0 & 0 & 0 & 0 & 0 & 0 & 0 & 0 & -1 & 0 & 0 & 0 & 0 & 0 & 0 \\
0 & 0 & 0 & 0 & 0 & 0 & 0 & 0 & 2 & 0 & -1 & 0 & -1 & 0 & 0 & 0 & -1 & 0 & 0 & 0 & 0 & 0 \\
0 & 0 & 0 & 0 & 0 & 0 & 0 & 0 & 0 & -0.25 & 0 & 0 & 0 & 0 & 0 & 0 & 0 & -1 & 0 & 0 & 0 & 0 \\
0 & 1 & 0 & 0 & -1 & 0 & -1 & 0 & 0 & -0.5 & 0 & 0 & 0 & 0 & 0 & 0 & 0 & 0 & 0 & 0 & 0 & 0 \\
0 & 0 & 0 & 0 & 1 & -1 & 0 & 0 & 0 & 0 & 0 & -1 & 1 & 0 & 0 & 0 & 0 & 0 & 0 & 0 & 0 & 0 \\
1 & -1 & 0 & 0 & 0 & 0 & 0 & 0 & 0 & 0 & 0 & 0 & 0 & 0 & 0 & 0 & 0 & 0 & 0 & 0 & 0 & 0 \\
-0.5 & -2 & 2 & 3 & 1 & -4 & -2.5 & -1 & -3 & 0.25 & 1 & 0 & 1 & 0 & 0 & 0 & 0 & 0 & 0 & 0 & 0 & 0 \\
0 & -2 & 0 & 0 & 0 & -1 & -0.5 & -1 & 1 & 0 & 0 & 0 & 0 & 0 & 0 & 0 & 0 & 0 & 0 & 0 & 0 & 0 \\
-0.5 & -1 & 0 & 1 & 0 & 0 & 0 & 2 & 0 & 0 & 0 & 0 & 0 & 0 & 0 & 0 & 0 & 0 & 0 & 0 & 0 & 0 \\
-0.5 & 1 & 1 & 1 & 0 & -1 & -1 & -1 & -1 & 0 & 0 & 0 & 0 & 0 & 0 & 0 & 0 & 0 & 0 & 0 & 0 & 0
\end{bmatrix}
\begin{matrix}
\mathrm{CO} \\ H_2 \\ x \\ [Ac^-]_o \\ BDO \\ Et \\ CO_2 \\ H_2O \\ [H^+]_o \\ NH_4^+ \\ AcCoA \\ [Ac^-]_i \\ For^- \\ [H^+]_i \\ NADH \\ NADPH \\ Fd_{red}^{2-}
\end{matrix}
\qquad
r = \begin{bmatrix}
r_{FDH} \\ r_{ACAS} \\ r_{CODH} \\ r_{Hyd} \\ r_{AcS} \\ r_{EtS} \\ r_{BDOS} \\ r_{Nfn} \\ r_{Rnf} \\ r_{Ana} \\ r_{H^+,i} \\ r_{AcX} \\ r_{HAcD} \\ q_{CO_2} \\ q_{Et} \\ q_W \\ q_{H^+} \\ q_{NH_4^+} \\ q_{Ac^-} \\ \mu \\ q_{CO} \\ q_{H_2} \\ q_{BDO}
\end{bmatrix}$$

Appendix B

Carbon and electron gaps

Table B.1 Carbon and electron gaps in the experimental q-rates for the Experiment 1 in [113]

Time, h	Carbon gap, %	Electrons gap, %
293	11	20
305	10	18
317	9	15
329	11	17
341	14	24
353	13	15
365	16	24
377	15	25
390	13	22
402	14	22
414	12	20
426	9	15
437	12	25
449	10	16
461	8	16
472	9	19
484	14	28
497	12	17
510	15	27
522	12	22
533	13	24

Chapter 7

Conclusions and outlook

"The better is the enemy of the good"

Henk Noorman, *Personal exchanges between Henk and Eduardo, 2021 – 2022*

This chapter is divided into two parts, one for the conclusions and another for the outlook.

7.1. Conclusions

This section reflects on how the overall research question was answered. As presented in Chapter 1, the question was: for the industrial fermentation of CO, H_2 and CO_2 gas mixtures, *i)* how does the selection of the product, the feedstock, the bioreactor operation conditions and the energy sources impact on the overall process economic and environmental performances, and *ii)* what dependencies are there among the environmental conditions given by a large-scale bioreactor and the growth of cells, their uptake of the gases, and the selectivity among the catabolic products?

Four sub-questions were designed to answer the research question:

i) Is the production of ethanol, 2,3-butanediol and hexanoic acid from lignocellulosic biomass-based syngas fermentation economically feasible and what are the environmental impacts related to their production?

ii) How reliable are the results from the simulation of bacteria with a black-box model and what can we learn about the operation of the syngas fermentor with such model?

iii) What are the impacts of the gas feedstock selection, and the bioreactor operation conditions on the economic and environmental performances of a syngas fermentation-based ethanol production process?

iv) How do the concentrations of substrates and products, pH and temperature in the bioreactor influence on growth, substrate uptake and product secretion by *C. autoethanogenum* developing under steady state and under dynamic conditions?

Overall, the answering of the research questions involved the development of mathematical tools to enable the simulation of syngas-fermenting microorganisms *i)* using gas feedstocks with different compositions, ranging from pure CO to the mixture of H_2 and CO_2, *ii)* at different temperatures, *iii)* pH and *iv)* concentrations of the main products, acetic acid and ethanol. The conclusions section follows the storyline of the development of those mathematical tools and the findings gathered along the way.

The models served as conceptual platforms that allowed linking into one common framework and interpreting the evidence obtained from a vast diversity of reported experimental conditions, *i.e.*, microbial strains, temperatures, values of pH, bioreactor internal configurations and operation modes, headspace pressures and scales of the fermentation process [54,57,72,73,127,230,285,298,299,311]. With such features, the

mathematical models allow describing the main observable phenomena taking place in the fermentation process, all leading to an enhanced understanding of the whole system.

7.1.1. The first black-box model

The first version of the black-box model was developed and used in the three first research chapters of this dissertation (Chapters 2, 3 and 4).

7.1.1.1. Structure

The simplest of the developed tools is the black-box model using single combinations of electron donor and catabolic product. This type of model is used in this dissertation, for sizing the bioreactors and assessing the performance (through productivity, gas utilization and energy use) of the syngas fermentation technology at the industrial scale. The black-box model considers cells as black boxes where substrates go in and products come out; any relevance of the intracellular processes is disregarded. The anaerobic catabolism is lumped in a reaction that describes the collection of electrons from the electron donors (CO and H_2) and the carbon from the carbon sources (CO and CO_2) as well as the production of the catabolic products. According to extensive experimental evidence published in literature, acetic acid, ethanol and 2,3-butanediol are the most common native catabolic products in the most studied syngas-fermenting microorganisms, or acetogens [72,74,106,257].

The black-box model allows the calculation of the Gibbs free energy of the catabolic reactions. Such metric is important for *i)* assessing the feasibility of the reaction at process conditions, and for *ii)* calculating the biomass yield, which is the link between catabolism and anabolism.

The black-box model initially considers the consumption of only one electron donor at a time and the production of only one catabolic product. The number of degrees of freedom in such systems is two, therefore, a Herbert-Pirt expression and a kinetic expression describing electron donor uptake produce the necessary information to kinetically link the microbial reaction with other dynamic processes occurring in the large bioreactor at steady state, *i.e.*, the most relevant being mass transfer due to the low solubilities of CO and H_2 in the fermentation broth. Initially, the kinetic parameters needed to establish the mentioned linkage (*i)* the maximum substrate uptake rate, *ii)* the half-saturation constant, *iii)* the biomass yield and *iv)* the maintenance requirements) were calculated using thermodynamics [183]. Such approach had not been previously presented for syngas fermentation.

We used the linkage between the black-box and the mass transfer model to size the large-scale syngas fermentor, at conditions where the concentrations of CO and H_2 are

enough to support a thermodynamically feasible catabolic reaction. The coupling of the bioreactor model with other (less detailed) models of the unit operations adjacent to the bioreactor (see the processes configurations in sections 2.2.1, 3.4.3 and 4.2.1), allowed us to calculate fixed and variable costs, and the greenhouse gas (GHG) emissions related to the overall production process.

7.1.1.2. Application of the model for early-stage process designs

Chapter 2 shows a first application of the introduced modelling approach, at this point built in Microsoft Excel. We assessed the individual production of three different products of commercial interest: ethanol, 2,3-butanediol and hexanoic acid (this product is formed after a subsequent anaerobic fermentation fed by ethanol and acetic acid from the syngas fermentation). The feedstock was syngas produced through the gasification of four types of lignocellulosic biomass, including agricultural residues and wood residues. The gasification process was also simulated in detail using AspenPlus.

From the simulation of syngas production (gasification) we learned that the largest contributors to the gas production costs are the production of lignocellulose, the transportation of biomass to the processing plant and the oxidative agent for gasification (in our case, steam). Steam is also the largest contributor to the CO_2 emissions related to the gas production (60 – 80%). An assessment of the costs related to the transportation of biomass to another continent (from America to Europe) may increase syngas production costs by 30 to 80%. Therefore, the location of the gasification-syngas fermentation plant should be close to where the biomass is produced.

In the overall production process, the largest contributor to the fixed costs is the fermentation unit (bioreactor plus the gas compressor, 50 – 80% of the total fixed costs), while the largest operation costs (and the largest GHG emissions) originate from the compression of the gas feedstock (40 – 60%). An additional high contribution to the production costs comes from the production and transportation of the lignocellulosic biomass (20 – 40%). Comparing with sugar-based fermentation processes, syngas fermentation uses a feedstock with a lower cost but needs an expensive production plant where the capital expenses are significantly higher.

Assessing the competitiveness of the syngas fermentation-based products, in terms of GHG emissions, the production of the three products improved the environmental performance of their fossil-based counterparts. In economic terms, 2,3-butanediol showed to be the most promising product, while the feasibility of ethanol still depended on potential improvements to be made on the process designs (*e.g.*, definition of fermentor operation conditions that improve productivity, gas utilization and

identification the more promising gas feedstocks, see conlcusions for Chapters 3 and 4) and on the reduction on the costs of lignocellulose production/recollection and transportation.

At the end, the results from the economic analysis were deemed highly uncertain due to the lack of data about commercial-scale projects that could serve as reference for cost-related data in order to validate our results.

7.1.1.3. Assessment of the accuracy and applicability of the black-box model

Guided by the search of validation and to implement potential improvements in the design of the process, we focused our analysis on the bioreactor since it is the unit operation with the highest uncertainty regarding its performance and also the most influential unit on variable and fixed costs. To explore the potential improvements while having comparable reference points of process performance, we chose to study the production of ethanol. Ethanol is the first commercialized product of the anaerobic syngas fermentation, by LanzaTech, the global pioneer company of this technology at industrial scale [437]; there are also a significant amount of scientific publications dealing with ethanol production from experimental and process design perspectives. However, before assessing any potential process improvements, we needed to assess the accuracy and applicability of the predictions delivered by the black-box model of microbial reactions.

In the work presented in **Chapter 3**, we systematically compared each of the stoichiometric and kinetic parameters delivered by thermodynamics to experimental evidence reported by different research groups, which used different bacterial strains, syngas compositions (going from pure CO to a mixture of H_2 and CO_2), pH, stirring speeds, fermentation broth compositions, under batch and continuous operation, among other process conditions [54,57,72,73,127,230,285,298,299]. In this sense, we found that the black-box model is a useful and sufficiently accurate tool to gain insights into the performance of experimental trials and to point out possible targets of improvement (*e.g.*, CO and H_2 uptake rates may be higher than those reported until the time when the study was made).

In **Chapter 3** we also presented a detailed description of the input and output variables of a simulation of the large-scale bubble column bioreactor, fed by either pure CO or a mixture of H_2 and CO_2. At this point of the project, the black-box model as well as the simulation of the bioreactor and the adjacent unit operations (see process configuration in section 3.4.3) were implemented in MatLab.

We assessed the dependencies between ethanol productivity, gas utilization in the bioreactor and energy consumption of the process, as functions of CO and H_2 specific uptake rates (q_{CO} and q_{H_2}, respectively), always guaranteeing the thermodynamic feasibility of the catabolic reaction. We identified two regions of operation of the bioreactor: a suboptimal and an optimal region. The suboptimal region is found where q_{CO} and q_{H_2} are closer to their maximum values and mass transfer is driven by small concentration gradients; such operation results in a low ethanol productivity and gas consumption and may be expected during bioreactor start-up. The opposite was found for the optimal region, where q_{CO} and q_{H_2} are lower than the 70% of their maximum values and mass transfer is driven by large concentration gradients. In the optimal region, high ethanol productivity and gas utilization are maintained until q_{CO} and q_{H_2} reach their minimum values where the concentrations of the dissolved electron donors reach their thermodynamic thresholds; the thresholds are the concentrations below which the catabolic reaction is not thermodynamically feasible, for CO two orders of magnitude lower than H_2, suggesting that CO fermentation may support higher concentrations of cells in a continuous fermentation.

The use of H_2 as the electron donor in the gas feed may provide higher productivities than CO (5.1 and 4.3 g/L/h for H_2 and CO, respectively) due to H_2's higher mass transfer coefficient. Such performance may be possible only if *i)* H_2 does not reach low concentrations at the top of the vessel that can render catabolism thermodynamically unfeasible, *ii)* CO consumption is not inhibited at the bottom of the bioreactor and if *iii)* biomass withdrawal from the bioreactor was decoupled from the fermentation broth removal.

The estimated gas utilization was, however, still poor (between 17 and 21%) with our initial assumptions for the fermentation process conditions. A sensitivity analysis suggested that increasing mass transfer coefficients would return higher ethanol productivities and increased gas utilization. This quick analysis led to the design of the following study.

7.1.1.4. Assessment of the impact of the bioreactor operation conditions on process performance

In a subsequent study, presented in **Chapter 4**, we assessed the influence of eight fermentation process variables that command the fermentation process, on the overall economic and environmental performance of the whole ethanol production process. The eight variables are: *i)* temperature, *ii)* pressure, *iii)* dilution of the gas feed with inert gaseous components (*e.g.*, N_2 or excess CO_2), *iv)* ethanol concentration, *v)* height of the liquid column, *vi)* gas-to-liquid mass transfer coefficient, *vii)* superficial gas velocity, and

viii) acetic acid co-production. In addition, three different gas production processes were included within the process battery limits, *i.e.*, *i)* the CO-rich off-gas from the steel production process' basic oxygen furnace, the first route commercialized by LanzaTech, *ii)* a mixture of electrolytic H_2 and CO_2 captured from a generic combustion process, and *iii)* syngas produced by the gasification of lignocellulosic biomass.

We used Monte Carlo simulations of the three production processes to gather data for performing a sensitivity analysis of the ethanol production costs (including fixed costs), the global warming potential and the CO_2 abatement costs. The Monte Carlo simulations varied the eight process conditions generating 5000 scenarios for each of the three gas feedstocks. In addition, the Monte Carlo simulations also served for testing and refining the stability of the MatLab code in which the simulation of the bioreactor was carried out. Such testing and refining was done by trial and error by assessing the model output variables at every scenario.

From the sensitivity analysis we learned that the selection of the gas production process is of paramount importance for the economic and environmental performances of the syngas-fermentation-based ethanol production process. The two most relevant features of the gas production processes are:

- If the gas production process uses renewable energy with a low global warming potential, the probability of achieving significant reductions on GHG emissions related to the production and use of the fermentation product is very high.
- If the gas is a waste from another (upstream) process and if it is available at high temperatures (around 1000°C), then the energy requirements of the gas-fermentation process plus ethanol downstream processing may be covered by heat integration, thus giving its economic performance great chances for being competitive with first and second-generation ethanol, and with fossil-based gasoline.

The latter result gives a possible explanation to the success of LanzaTech's process fed by the basic-oxygen furnace off-gas, a waste of steel production and available at high temperatures. Lignocellulosic biomass-based syngas was the least promising feedstock due to the high costs of the biomass and the gas production processes. The use of biomass or other carbonaceous wastes may be valuable if, after their combustion, for *e.g.*, energy production, the CO_2 generated is coupled to electrolytic H_2 and fed to the fermentation.

To further assess the potential benefits of directing research towards overcoming current technological constraints, we performed two multi-objective optimizations for each process configuration. One of the optimizations used wide ranges of the eight parameters

commanding the fermentation, while the second, constrained the possible solutions to current technical limitations observed in syngas fermentation reports. The multi-objective optimizations were based on the construction of Pareto frontiers using the global warming potential and the production costs of ethanol as simultaneous objective functions. As result, significant improvements may be expected on the economic and environmental performances if the rate of mass transfer and the bacterial tolerance to ethanol are both enhanced in the bioreactor. If such challenges are addressed, the ethanol produced from the BOF off-gas, from the H_2/CO_2 mixture and the bio-mass based syngas may cost 0.37, 0.48 and 0.77 €/L, respectively; ethanol production from the same three gas feedstocks may also generate 14, 3 and 40 g of CO_2 equivalents per MJ of combusted ethanol, respectively.

Once the relations between the choice of the gas feedstock, bioreactor operation and the overall process' economic and environmental performances were understood, it was time to inquire about the factors influencing ethanol production by acetogens. Ethanol was assumed to be the main product in all the simulations run up to this point. However, acetic acid is, in fact, the main product of acetogens; ethanol is only produced under certain circumstances, still not clearly understood. High concentrations of acetic acid in the fermentation broth, low pH and a dominant presence of H_2 over CO in the gas feed are three commonly reported promoters of ethanol production by acetogens [72,74,230,257]. Therefore, we designed three other mathematical models that allow the calculation of the fluxes on the main carbon and electron routes within the metabolism of acetogenic bacteria, two of the models were developed for steady state (one further improved version of the black-box model and one metabolic model) and the third model was dynamic (a kinetic metabolic model). The models were designed for *Clostridium autoethanogenum*, one of the two most studied acetogens for syngas fermentation.

7.1.2. A further improved black-box model and a metabolic model

One of the models at steady state is a more sophisticated form of the first black-box model (which, in the following paragraphs, we call IBB model – standing for improved black-box model). The new form of the model was designed to simulate the simultaneous uptake of the electron donors, CO and H_2, the simultaneous production of acetic acid, ethanol and 2,3-butanediol and cell growth, depending on temperature and the extracellular concentrations of substrate and products, and pH. This improved black-box description uses five kinetic expressions to calculate the values of the net uptake and secretion rates of 11 substances, CO, H_2, CO_2, acetate, acetic acid (undissociated form), ethanol, 2,3-butanediol, cells, water, nitrogen source and H^+. The forms of the kinetic expressions for the uptake of CO and H_2 were adapted from works presented in literature

[106,108], while the remaining three (*i.e.*, for cell growth, ethanol and 2,3-butanediol production) were designed for this study, which is reported in **Chapter 5**.

The proposed equations for ethanol and 2,3-butanediol production are functions of the uptake rates of both CO and H_2. This approach is not common in literature where product secretion rates are functions of only one limiting substrate. Our study considers that cells grow under dual-substrate-limited conditions (see section 5.3.1.1). Moreover, the equation used to calculate the biomass growth rate is based on thermodynamics, specifically on a Gibbs free energy balance. According to that equation, the total rate of Gibbs free energy production is the sum of the energy needed for growth, maintenance and the energy needed to balance the passive diffusion of acetic acid into the cell, of which the rate was found to be significantly faster than the net rate of acetic acid production (see section 5.3.1.1.2). This IBB model was able to reproduce the three common experimental conditions under which ethanol production is enhanced at steady state, *i.e.*, *i)* low pH, *ii)* high acetic acid concentration, and *iii)* the use of H_2-rich syngas as feedstock (see section 5.4.2.3).

In addition to the IBB model, a metabolic model (M model) was also developed for the same study. The M model has the same objective as the IBB for simulating growth and the simultaneous uptake and secretion of substrates and products, depending on temperature, pH and the concentrations of substrates and products in the fermentation broth. One of the pillars of metabolic modeling is the metabolic network [79], which organizes the stoichiometry of the reactions constituting the main routes for carbon and electrons inside cells. The network was designed to contain the three characteristic traits of acetogenic bacteria, by which they are able to use CO_2 *i.e.*, *i)* to reductively synthesize acetyl coenzyme A, *ii)* as electron acceptor in an energy-conserving process, and *iii)* to synthesize cell material [44].

The metabolic network was also designed such that the rates of all the reactions are linearly calculable using five kinetic expressions, the same number as the IBB model. Contrary to the IBB model, the M model used an ATP balance to calculate the biomass growth rate. In addition, using the higher flexibility of the metabolic model for finding correlations among reaction rates (the metabolic model contains 23 reactions while the black-box, only 11), we derived one kinetic expression to calculate the rate of acetate export from the intracellular space; the net acetic acid production rate is thus the difference between the rates of acetate export and that of the acetic acid back-diffusion into the cell. Such strategy allowed us to leave the rate of ethanol production as one of the outputs of the M model and, remarkably, to increase the accuracy in the prediction of ethanol selectivity.

Both, the IBB and the M models were parameterized by fitting to published experimental data obtained from 12 continuous fermentations at steady-state that use *i)* two dilution rates, *ii)* five different gas feed compositions, ranging from pure CO to a mixture of H_2 and CO_2, *iii)* two dilution rates, *iv)* different stirring speeds (which determine the rate of gas-to-liquid mass transfer), and *v)* one value of pH [74,75,401]. The experimental net uptake and secretion rates were calculated from the reported concentration data. The calculation was based on mass balances established for the liquid and gas phases, and the exchange of compounds between both phases. The un-reported compositions of the off-gas (and its flow rate), as well as the un-measured concentrations of dissolved CO, H_2 and CO_2 were also estimated by the same calculation.

The connection of both mathematical frameworks (the IBB and the M models) through the rates of ATP and Gibbs free energy production allowed us to identify:

- Two equally possible mechanisms for the active export of acetate, *i.e.*, uniport and antiport.
- The stoichiometric and thermodynamic feasibility of a H_2 production / consumption cycle, previously hypothesized to explain the production of H_2 in fermentations using pure CO [53]. However, the cycle has a low impact on the total energy production rate by the cells.
- A possible differentiation between two metabolic states, often regarded as acetogenesis and solventogenesis. The differentiation was seen in the different ratios between the ATP and Gibbs free energy production rates, *i.e.*, for the experimental cases where acetic acid production is dominant the mentioned ratio is higher, while for the other group where ethanol is the dominant product, the ratio is lower. The 12 experimental cases organize in two clearly separated clusters.
- The acetogen *C. autoethanogenum* chooses CO over H_2 uptake when it needs a faster production of ATP and Gibbs free energy.

Considering the low solubility of CO and H_2 in the fermentation broth, one can expect that the large-scale bioreactor will have significant CO and H_2 concentration gradients. According to a computational fluid dynamics-based simulation, in a parallel project in our department [431,435], the concentrations of CO and H_2 may vary by one order of magnitude between the bottom and the top of the large-scale bioreactor. Therefore, we started working towards the construction of a kinetic metabolic model that can simulate the effects of such changes in the intracellular metabolite pools.

7.1.3. The metabolic kinetic model

The metabolic network built in **Chapter 5** is the base for the construction of a kinetic metabolic model. Since the metabolic network contains several lumped reactions, an approximative kinetic format was chosen for building the kinetic metabolic model, as shown in **Chapter 6**. The linlog format uses the deviations of the concentrations of intra and extracellular metabolites from fixed reference concentrations to determine the variation of a reaction rate from a reference rate. Our kinetic model uses as inputs: the concentrations of CO, H_2, CO_2, acetate, undissociated acetic acid, ethanol, 2,3-butanediol and pH at the extracellular space, as well as the intracellular concentrations of NADH, acetyl-CoA, NADPH, reduced ferredoxin, formate and acetate. The kinetic expressions for 11 intracellular reactions were designed and parameterized using data from a published experiment where metabolic oscillations are provoked in a continuous fermentation, with the acetogen *C. autoethanogenum* [113]. During those oscillations, the rates of CO and H_2 uptake vary, as well as the production rates of the three catabolic products, acetic acid, ethanol and 2,3-butanediol, and also biomass growth.

The design of the kinetic equations was mostly based on the stoichiometry of the metabolic reactions, except for two:

- In the uptake of H_2, although the model did not include the possible production / consumption cycle, the kinetic expression included all the substances participating in the cycle.
- Although the lumped anabolic reaction in the network uses acetyl-CoA and NH_4^+ as substrates, the construction of cell material in reality is far more complex. Therefore, the kinetic expression for anabolism included the influence of the redox carriers NADH, NADPH and reduced ferredoxin.

The reference state for the kinetic equations was defined from the time-point where the concentrations of the substances are closest to the most common concentrations during the whole experimental run. The reference concentrations for dissolved CO, H_2 and CO_2 which were not measured in the experiment were reconstructed from the reported off-gas analysis data using mass balances; the calculation required making several assumptions (see section 6.4.1.2) to estimate the values of the mass transfer coefficients for the three gases. The reference reaction rates were calculated from reconciled net conversion rates assuming a metabolic steady-state.

The search for relations between the reconciled net uptake and secretion rates allowed us to identify one correlation that bears significant relevance regarding the possible behavior of bacteria inside a large-scale bioreactor. The rate of ethanol production responds linearly to the total uptake rate of electrons from CO and H_2. Such relation may

suggest that in the large-scale bioreactor, ethanol production is promoted at regions where the uptake of the gases is fast; possibly the points where the gas feedstock is sparged into the bioreactor.

The parameterization of the kinetic model was based on a sequence of minimizations that estimated the values of *i)* the model's kinetic parameters (called elasticity coefficients), *ii)* the reference concentrations of the un-measured intracellular concentrations, and *iii)* the initial concentrations supplied to the solver of the differential equations. The three sets of unknown parameters were estimated in different minimization runs, *i.e.*, one minimization used one set of parameters as the decision variables while keeping the other two sets as constant. Series of sequential minimizations were used to guarantee that the estimated sets of parameters are consistent with each other. Several loops with the previous sequence were used for exploring the vast solutions space. Lastly, two different minimization algorithms were used: a stochastic particle swarm to explore the solutions space of the elasticity parameters and an iterative algorithm to refine the solutions delivered by the stochastic algorithm.

The parameterized model successfully reproduced the experimental oscillations for the extracellular concentrations of CO, H_2, CO_2, acetic acid, ethanol, 2,3-butanediol and biomass, as well as those of the intracellular concentrations of NADH, NADPH and acetyl-CoA. That result allowed us to conclude that the linlog format holds a potential of describing the dynamic (transient) behavior of *C. autoethanogenum*. However, there was an average error of 15% between the calculated and the experimental concentrations, therefore, the model still needs improvements before use in bioreactor simulations.

The analysis of the Hessian matrix, one of the outputs of one of the minimization algorithms, allowed us to calculate the errors linked to the estimated parameters. Based on those errors and the mismatch between the experimental and calculated concentrations, we argued that:

- ATP needs to be included as another metabolite in the metabolic network.
- Formic acid may be simulated as part of a cycle similar to the one used for acetic acid, *i.e.*, export of the carbolxylate and back-diffusion of the acid.
- The kinetic expression for the enzyme CO-dehydrogenase should reviewed and improved.
- The uptake of H_2 should be simulated as a two-reaction cycle where H_2 is simultaneously produced and consumed. A possible indirect influence of NADH on the uptake of H_2 should also be explored.

The elasticity parameters estimated for NADH were not close to zero in any reaction where it participated; that result is special among the metabolites in the network. In

addition, the turnover frequency of the NADH pool was the fastest in the network. The combination of those two results suggests that the size of the NADH pool is very sensitive to changes in the network and it also wields a significant influence on the carbon and the electron routes fluxes. Therefore, the control that NADH exerts over the catabolism of *C. autoethanogenum* should be further explored with detail.

With the described knowledge that was gathered up to this point, the project was concluded.

The future improvement and use of all the models constructed as part of the present project is strongly encouraged, since *i)* the product portfolio of acetogenic bacteria is wide, and *ii)* the potential of the industrial syngas fermentation for lowering the emissions of greenhouse gases related to the production of chemicals is large. Recommendations about the development of experiments as well as ideas for further applications of the models are given in section 7.2.

7.2. Outlook

The models developed during this project are tools that may return valuable insights for *i)* process design (as shown in Chapters 2, 3 and 4), *ii)* the fundamental understanding of acetogenic bacteria (as shown in Chapters 5 and 6), and *iii)* for the future development and scale-up of the syngas fermentor. However, all the models remain partly incomplete since they are not all sustained by data gathered from focused experiments, also acknowledging that the used experimental datasets are incomplete and partly inconsistent (*i.e.,* not fulfilling mass conservation constraints). Therefore, the main recommendation is to dedicate efforts on *i)* the experimental validation of the four models, where experimental designs are strongly guided by the models, and further *ii)* retrofit the experimental results to improve the predictive capabilities of the models, such that they are useful for a systematic scalling-up of the synas fermentation process while expanding their product portfolio and the variety of gas compositions fed to it (including higher amounts of H_2).

Continuous fermentations will be the basis for the models' validation process because such operation guarantees the achievement of pseudo-steady states where all cells in the bioreactor have almost the same metabolic states. To draw reliable data, several recommendations are here given for any planned continuous fermentation experiment:

- Conventionally, the concentration of cells is measured from samples withdrawn from the bioreactor. The point of sampling is especially important as it has been proven that cells may distribute unevenly in the bioreactor due to stirring and gas sparging.

Therefore, the measurement of biomass concentrations should be supported by the understanding of the distribution of microbial cells within the bioreactor and the careful choice of the sampling point [438].

- Efforts should be made to guarantee the precise measurement of the total mass of the bioreactor contents, for instance using scales. Such strategy may reduce the effects of unknown density of the fermentation broth, which may change during experiments where the concentrations of microbial products are high and when the gas hold-up is significant.

In addition to the mentioned general recommendations for any type of continuous fermentations, other recommendations, specific for the study of syngas fermentations, are provided as well. The measurement of the concentrations of dissolved CO and H_2 in the fermentation broth is of paramount importance for *i)* the calibration of all the kinetic expressions here presented, *ii)* to reduce the uncertainties faced during the calculation of the Gibbs free energy production by cells, and *iii)* to draw clear comparisons between the conditions offered by the large-scale bioreactor (regarding mass transfer and the dissolved gas concentration gradients) and the effects that such conditions have on the metabolism of bacteria growing in it. Two methods have been reported for directly measuring the dissolved concentrations of CO and H_2 [432,434]. Alternatively, the dissolved concentrations can also be calculated based on the off-gas composition data. Such calculation should be done if *i)* the mass transfer coefficient has been measured in the actual fermentation broth, at different concentrations of ethanol and acetic acid, and *ii)* the effects of dispersion of the gas in the bioreactor headspace have been considered.

The construction of reliable kinetic expressions for the uptake of CO and H_2, should also be based on the assessment of the inhibitory effects of acetic acid, ethanol and possibly CO_2 [439]. Such considerations would make any sizing of the bioreactor and consequently, the economic assessment of the entire process, more accurate.

Several process design options were also left un-assessed by our studies. Due to their low costs, the use of municipal solid wastes for the production of either CO_2 (for forming a mixture with electrolytic H_2) or syngas should be assessed. It could be expected that the gas cleaning requirements would be higher compared to lignocellulose-based syngas, but there could be a balance between the costs reduced in the feedstock supply and the costs increased for its cleaning.

Moreover, a reliable calculation of the rate of Gibbs free energy production by cells, coupled to the calculation of the rate of ATP production inside cells may also help to understand if there is, in fact, a distinction between acetogenesis and solventogenesis; such knowledge would lead to the understanding of how to go from one metabolic state

to the other. The methods for calculating the Gibbs free energy production, could also be validated by the experimental use of calorimetry [440]. Experiments using more abundant values of the growth rate of cells and pH will also be useful for improving our understanding of the allocation of the Gibbs free energy (and ATP) production between growth, maintenance and for balancing the effects of the passive diffusion of carboxylic acids into the cell (where formic acid, as well as acids of longer carbon chains may also be included).

The parameterization of the kinetic metabolic model faced many challenges due to the partial compatibility of the model with the experimental data. Besides using measurements of the dissolved gas concentrations, efforts should also be taken to develop experimental techniques to measure the intracellular concentrations of formate, acetate and ferredoxin (in both, oxidized and reduced forms). Efforts should also be made to understand how reliable are the measurements of the metabolome, considering the effects of quenching on bacterial cells [441].

A step forward from the construction of the kinetic metabolic model would be to dedicate efforts on the development of perturbation experiments, where the gradients of CO and H_2 concentrations are simulated in a laboratory set-up. Such gradients may be recreated using a feast/famine approach, where the gases are fed (at high concentrations in the gas feed) to the bioreactor during a period of time, and then the feeding stops (the gas feed may also contain an inert gas to wash-out CO and H_2 from the headspace) for another period of time. Alternatively, the stirring speed could be varied, paying attention to possible effects of changing shear rates on bacteria. The frequency and the duration of each cycle, as well as the sizes of the gas concentration gradients should be determined through simulations of the large-scale bioreactor based on computational fluid dynamics. The structure of the metabolic kinetic model developed in this study could already be applied in such simulations. The data from the perturbations experiment can then be used to improve the predictive capacity of the kinetic metabolic model.

The development and scale-up of the syngas fermentor should be made using an iterative process, where down-scaled experiments and bioreactor simulations retrofit with information exchange in both directions. The strategies for the optimization of the microorganisms' metabolism should also be included in the iterative process.

Lastly, the deployment of syngas fermentation in industry will not only be based on the bioreactor design, but also on the careful choice of the gas feedstock, such that the process is economically feasible, and the production of the product involves the generation of low impacts to the environment and benefits society.

Chapter 8

References

1. Earth System Research Laboratories, Global Monitoring Laboratory. Trends in Atmospheric Carbon Dioxide [Internet]. Earth Syst. Res. Lab. [cited 2022 Dec 4]. Available from: https://www.esrl.noaa.gov/gmd/ccgg/trends/global.html

2. Lüthi D, Le Floch M, Bereiter B, Blunier T, Barnola J-M, Siegenthaler U, et al. High-resolution carbon dioxide concentration record 650,000–800,000 years before present. Nature. 2008;453:379–82.

3. Schilt A, Baumgartner M, Blunier T, Schwander J, Spahni R, Fischer H, et al. Glacial–interglacial and millennial-scale variations in the atmospheric nitrous oxide concentration during the last 800,000 years. Quat Sci Rev. 2010;29:182–92.

4. Spahni R, Chappellaz J, Stocker T, Loulergue L, Huasammann G, Kawamura K. Atmospheric methane and nitrous oxide of the late pleistocene from antarctic ice cores. Science. 2005;310:1317–21.

5. Fischedick M, Roy J, Abdle-Aziz A, Acquaye A, Allwood J, Ceron J-P, et al. Industry. Clim Change 2014 Mitig Clim Change Contrib Work Group III Fifth Assess Rep Intergov Panel Clim Change. Cambridge, United Kingdom and New York, NY, USA: Cambridge University Press; 2014.

6. European Commission. Causes of climate change [Internet]. Eur. Comm. 2020 [cited 2020 May 4]. Available from: https://ec.europa.eu/clima/change/causes_en

7. Pörtner H-O, Roberts D, Tignor M, Poloczanska E, Mintenbeck K, Alegría A, et al. Summary for Policymakers. Switzerland: Intergovernmental Panel on Climate Change; 2022. Available from: https://www.ipcc.ch/report/ar6/wg2/downloads/report/IPCC_AR6_WGII_SummaryForPolicymakers.pdf

8. Edenhofer O, Pichs-Madruga R, Sokona Y, Minx J, Farahani E, Kadner S, et al., editors. Climate change 2014: mitigation of climate change: Working Group III contribution to the Fifth Assessment Report of the Intergovernmental Panel on Climate Change. New York, NY: Cambridge University Press; 2014.

9. Ritchie H, Roser M. CO_2 and Greenhouse Gas Emissions [Internet]. Our World Data. 2020 [cited 2020 May 4]. Available from: https://ourworldindata.org/co2-and-other-greenhouse-gas-emissions

10. Mann M. Radiative forcing [Internet]. Britannica. Available from: https://www.britannica.com/science/radiative-forcing

11. Mander S, Anderson K, Larkin A, Gough C, Vaughan N. The Climate-Change Mitigation Challenge. In: Clair G, Patricia T, Sarah M, Naomi V, Temitope F, editors. Biomass Energy Carbon Capture Storage BECCS Unlocking Negat Emiss [Internet]. Chichester, UK: John Wiley & Sons, Ltd; 2018 [cited 2020 May 4]. p. 187–203. Available from: http://doi.wiley.com/10.1002/9781119237716.ch9

12. Clark B, York R. Carbon metabolism: Global capitalism, climate change, and the biospheric rift. Theory Soc. 2005;34:391–428.

13. Koch M. Climate Change, Capitalism and Degrowth Trajectories to a Global Steady-State Economy. Int Crit Thought. 2015;5:439–52.

14. Bajželj B, Allwood JM, Cullen JM. Designing Climate Change Mitigation Plans That Add Up. Environ Sci Technol. 2013;47:8062–9.

15. Majumdar A, Deutch J. Research opportunities for CO_2 utilization and negative emissions at the gigatonne scale. Joule. 2018;2:805–9.

16. Kapetaki Z, Miranda Barbosa E. Carbon Capture Utilisation and Storage Technology Development Report 2018 [Internet]. Luxembourg: European Commission; 2019. Report No.: EUR 29909 EN. Available from: https://publications.jrc.ec.europa.eu/repository/bitstream/JRC118297/jrc118297_1.pdf

17. Beck L. Carbon capture and storage in the USA: the role of US innovation leadership in climate-technology commercialization. Clean Energy. 2020;4:2–11.

18. Jiang K, Ashworth P, Zhang S, Liang X, Sun Y, Angus D. China's carbon capture, utilization and storage (CCUS) policy: A critical review. Renew Sustain Energy Rev. 2020;119:109601.

19. Iglesias A, Podestá F. Photosynthate Formation and Partitioning in Crop Plants. In: Pessarakli M, editor. Handb Photosynth. 2nd ed. Boca Raton, FL: Taylor & Francis; 2005. p. 524.

20. Gabrielli P, Gazzani M, Mazzotti M. The Role of Carbon Capture and Utilization, Carbon Capture and Storage, and Biomass to Enable a Net-Zero-CO_2 Emissions Chemical Industry. Ind Eng Chem Res. 2020;59:7033–45.

21. Posada JA, Osseweijer P. Socio-economic and environmental considerations for sustainable supply and fractionation of lignocellulosic biomass in a biorefinery context. Biomass Fractionation Technol Lignocellul Feedstock Based Biorefinery. 1st ed. Mussatto SL; 2016. p. 674.

22. Chen H. Chemical Composition and Structure of Natural Lignocellulose. Biotechnol Lignocellul [Internet]. Dordrecht: Springer Netherlands; 2014 [cited 2023 Feb 10]. p. 25–71. Available from: http://link.springer.com/10.1007/978-94-007-6898-7_2

23. Mussatto SI, Bikaki N. Technoeconomic Considerations for Biomass Fractionation in a Biorefinery Context. Biomass Fractionation Technol Lignocellul Feedstock Based Biorefinery [Internet]. Elsevier; 2016 [cited 2023 Feb 10]. p. 587–610. Available from: https://linkinghub.elsevier.com/retrieve/pii/B9780128023235000256

24. Efe Ç, van der Wielen LAM, Straathof AJJ. Technical and economical feasibility of production of ethanol from sugar cane and sugar cane bagasse [Internet]. Delft: Delft University of Technology; 2005. Available from: https://repository.tudelft.nl/islandora/object/uuid%3A5f3b7381-0da3-4d26-b334-9b4856ecacda

25. OECD. Biofuel projections: Ethanol [Internet]. 2015. Available from: https://www.oecd-ilibrary.org/content/component/agr_outlook-2015-table66-en

26. Renewable Fuels Association. Annual ethanol production [Internet]. ethanolrfa.org. 2022 [cited 2023

Oct 2]. Available from: https://ethanolrfa.org/markets-and-statistics/annual-ethanol-production

27. Indexmundi. Motor Gasoline Consumption by Country [Internet]. Indexmundi.com. 2023 [cited 2023 Oct 2]. Available from: https://www.indexmundi.com/energy/?product=gasoline&graph=consumption&display=rank

28. Perry RH, Green DW, editors. Perry's chemical engineers' handbook. 7th ed., internat. ed., [Nachdr.]. New York: McGraw-Hill; 2003.

29. Alonso Pippo W, Luengo CA, Alonsoamador Morales Alberteris L, Garzone P, Cornacchia G. Energy Recovery from Sugarcane-Trash in the Light of 2nd Generation Biofuels. Part 1: Current Situation and Environmental Aspects. Waste Biomass Valorization. 2011;2:1–16.

30. Almeida Benalcázar E, Gevers-Deynoot B, Noorman H, Osseweijer P, Posada JA. Production of bulk chemicals from lignocellulosic biomass via thermochemical conversion and syngas fermentation: a comparative techno-economic and environmental assessment of different site-specific supply chain configurations: Techno-economic and environmental assessment of bulk chemicals production though biomass gasification and syngas fermentation. Biofuels Bioprod Biorefining [Internet]. 2017 [cited 2017 Aug 15]; Available from: http://doi.wiley.com/10.1002/bbb.1790

31. Hein L, Leemans R. The Impact of First-Generation Biofuels on the Depletion of the Global Phosphorus Reserve. AMBIO. 2012;41:341–9.

32. Leal MRLV, Horta Nogueira LA, Cortez LAB. Land demand for ethanol production. Appl Energy. 2013;102:266–71.

33. Jorissen T, Oraby A, Recke G, Zibek S. A systematic analysis of economic evaluation studies of second-generation biorefineries providing chemicals by applying biotechnological processes. Biofuels Bioprod Biorefining. 2020;bbb.2102.

34. European Commission. Directorate General for Research and Innovation. Bioeconomy: the European way to use our natural resources : action plan 2018. [Internet]. LU: Publications Office; 2018 [cited 2021 Oct 6]. Available from: https://data.europa.eu/doi/10.2777/79401

35. Rosales-Calderon O, Arantes V. A review on commercial-scale high-value products that can be produced alongside cellulosic ethanol. Biotechnol Biofuels. 2019;12:240.

36. Kirkels AF, Verbong GPJ. Biomass gasification: Still promising? A 30-year global overview. Renew Sustain Energy Rev. 2011;15:471–81.

37. Molino A, Larocca V, Chianese S, Musmarra D. Biofuels Production by Biomass Gasification: A Review. Energies. 2018;11:811.

38. Bertuccioli L, Chan A, Hart D, Lehner F, Madden B, Standen E. Development of water electrolysis in the European Union [Internet]. E4tech Sàrl with Element Energy Ltd.; 2014 Feb. Available from: https://www.fch.europa.eu/sites/default/files/study%20electrolyser_0-Logos_0_0.pdf

39. IEA. The future of hydrogen. Seizing today's opportunities. Paris: International Energy Agency; 2019.

40. Cetinkaya E, Dincer I, Naterer GF. Life cycle assessment of various hydrogen production methods. Int J Hydrog Energy. 2012;37:2071–80.

41. Huang Z, Grim RG, Schaidle JA, Tao L. The economic outlook for converting CO_2 and electrons to molecules. Energy Environ Sci. 2021;14:3664–78.

42. De Luna P, Hahn C, Higgins D, Jaffer SA, Jaramillo TF, Sargent EH. What would it take for renewably powered electrosynthesis to displace petrochemical processes? Science. 2019;364:eaav3506.

43. Bushuyev OS, De Luna P, Dinh CT, Tao L, Saur G, van de Lagemaat J, et al. What Should We Make with CO2 and How Can We Make It? Joule. 2018;2:825–32.

44. Drake HL. Acetogenesis, acetogenic bacteria, and the acetyl-CoA "Wood/Ljungdahl" pathway: past and current perspectives. In: Drake HL, editor. Acetogenesis. London, Great Britain: Chapman & Hall; 1994. p. 1–62.

45. Wieringa KT. Over het verdwijnen van waterstof en koolzuur onder anaerobe voorwaarden: Voortzetting van een onderzoek van wijlen Prof. Dr. Ir. N. L. Söhngen. Antonie Van Leeuwenhoek. 1936;3:263–73.

46. Fischer F, Lieske R, Winzer K. Biologische Gasreaktionen. II. Über die Bildung von Essigsäure bei der biologischen Umsetzung von Kohlenoxyd und Kohlensäure mit Wasserstoff zu Methan. Biochem Z. 1932;245:2–12.

47. Fontaine FE, Peterson WH, McCoy E, Johnson MJ, Ritter GJ. A new type of glucose fermentation by *Clostridium thermoaceticum*. J Bacteriol. 1942;43:701–15.

48. Daniell J, Köpke M, Simpson S. Commercial Biomass Syngas Fermentation. Energies. 2012;5:5372–417.

49. Diekert G, Wohlfarth G. Energetics of acetogenesis from C1 units. In: Drake HL, editor. Acetogenesis. London, Great Britain: Chapman & Hall; 1994. p. 157–79.

50. Latif H, Zeidan AA, Nielsen AT, Zengler K. Trash to treasure: production of biofuels and commodity chemicals via syngas fermenting microorganisms. Curr Opin Biotechnol. 2014;27:79–87.

51. Ljungdahl L. The autotrophic pathway of actetate synthesis in acetogenic bacteria. Annu Rev Microbiol. 1986;40:415–50.

52. van Maris AJA, Konings WN, van Dijken JP, Pronk JT. Microbial export of lactic and 3-hydroxypropanoic acid: implications for industrial fermentation processes. Metab Eng. 2004;6:245–55.

53. Wang S, Huang H, Kahnt J, Mueller AP, Kopke M, Thauer RK. NADP-specific electron-bifurcating [FeFe]-hydrogenase in a functional complex with formate dehydrogenase in *Clostridium autoethanogenum* grown on CO. J Bacteriol. 2013;195:4373–86.

54. Drake HL, Gößner AS, Daniel SL. Old Acetogens, New Light. Ann N Y Acad Sci. 2008;1125:100–28.

55. Karlsson JL, Volcani BE, Barker HA. The nutritional requirements of *Clostridium aceticum*. J Bacteriol. 1948;56:781–2.

56. Diekert GB, Thauer RK. Carbon monoxide oxidation by *Clostridium thermoaceticum* and *Clostridium formicoaceticum*. J Bacteriol. 1978;136:597–606.

57. Savage MD, Wu ZG, Daniel SL, Lundie LL, Drake HL. Carbon monoxide-dependent chemolithotrophic growth of *Clostridium thermoautotrophicum*. Appl Environ Microbiol. 1987;53:1902–6.

58. Drake HL, Daniel SL, Küsel K, Matthies C, Kuhner C, Braus-Stromeyer S. Acetogenic bacteria: what are the *in situ* consequences of their diverse metabolic versatilities? BioFactors. 1997;6:13–24.

59. van der Meijden P, van der Drift C, Vogels GD. Methanol conversion in methanogenic and acetogenic bacteria. Antonie Van Leeuwenhoek. 1985;51:454–454.

60. Eichler B, Schink B. Oxidation of primary aliphatic alcohols by *Acetobacterium carbinolicum* sp. nov., a homoacetogenic anaerobe. Arch Microbiol. 1984;140:147–52.

61. Schuchmann K, Schmidt S, Martinez Lopez A, Kaberline C, Kuhns M, Lorenzen W, et al. Nonacetogenic growth of the acetogen *Acetobacterium woodii* on 1,2-propanediol. Metcalf WW, editor. J Bacteriol. 2015;197:382–91.

62. Schuchmann K, Müller V. Energetics and application of heterotrophy in acetogenic bacteria. Stams AJM, editor. Appl Environ Microbiol. 2016;82:4056–69.

63. Datta R, Enzien M, Xu J, Do YS, Levinston WE. Method for production of n-propanol and other C3-containing products from syngas using membrane supported bioreactor. 2014.

64. Enzien M, Datta R, Tobey R. Method for production of n-butanol from syngas using syntrophic co-cultures of anaerobic microorganisms. 2014.

65. Levinston WE. Butyrate Producing Clostridium Speccies, *Clostridium pharus*. 2014.

66. Harmon L, Hallen R, Lilga M, Heijstra B, Palou-Rivera I, Handler R, et al. A Hybrid Catalytic Route to Fuels from Biomass Syngas [Internet]. 2017 Dec. Report No.: DOE-LanzaTech--EE0005356, 1423741. Available from: http://www.osti.gov/servlets/purl/1423741/

67. Simpson SD, Tizard H. Alcohol production process. 2010.

68. Gaddy J, Arora D, Ko CW, Phillips JR, Basu R, Wikstrom C, et al. Methods for increasing the production of ethanol from microbial fermentation. 2003.

69. Haynes C. DOE BETO Advancing the bioeconomy: from waste to conversion-ready feedstocks [Internet]. 2020 [cited 2020 May 14]. Available from: https://www.energy.gov/sites/prod/files/2020/03/f72/beto-20-msw-wkshp-feb-2020-haynes_0.pdf

70. Handler RM, Shonnard DR, Griffing EM, Lai A, Palou-Rivera I. Life Cycle Assessments of Ethanol Production via Gas Fermentation: Anticipated Greenhouse Gas Emissions for Cellulosic and Waste Gas Feedstocks. Ind Eng Chem Res. 2016;55:3253–61.

71. Thauer RK, Jungermann K, Decker K. Energy conservation in chemotrophic anaerobic bacteria. Bacteriol Rev. 1977;41:100–80.

72. Richter H, Martin M, Angenent L. A two-stage continuous fermentation system for conversion of syngas into ethanol. Energies. 2013;6:3987–4000.

73. Kundiyana DK, Huhnke RL, Wilkins MR. Syngas fermentation in a 100-L pilot scale fermentor: Design and process considerations. J Biosci Bioeng. 2010;109:492–8.

74. Valgepea K, de Souza Pinto Lemgruber R, Abdalla T, Binos S, Takemori N, Takemori A, et al. H_2 drives metabolic rearrangements in gas-fermenting *Clostridium autoethanogenum*. Biotechnol Biofuels. 2018;11:55.

75. Valgepea K, de Souza Pinto Lemgruber R, Meaghan K, Palfreyman RW, Abdalla T, Heijstra BD, et al. Maintenance of ATP homeostasis triggers metabolic shifts in gas-fermenting acetogens. Cell Syst. 2017;4:505-515.e5.

76. Richter H, Molitor B, Wei H, Chen W, Aristilde L, Angenent LT. Ethanol production in syngas-fermenting *Clostridium ljungdahlii* is controlled by thermodynamics rather than by enzyme expression. Energy Env Sci. 2016;9:2392–9.

77. Mock J, Zheng Y, Mueller AP, Ly S, Tran L, Segovia S, et al. Energy conservation associated with ethanol formation from H_2 and CO_2 in *Clostridium autoethanogenum* involving electron bifurcation. Metcalf WW, editor. J Bacteriol. 2015;197:2965–80.

78. Noorman H. An industrial perspective on bioreactor scale-down: What we can learn from combined large-scale bioprocess and model fluid studies. Biotechnol J. 2011;6:934–43.

79. Villadsen J, Nielsen JH, Lidén G, Nielsen JH. Bioreaction engineering principles. 3rd ed. New York: Springer; 2011.

80. Noorman HJ, Heijnen JJ, Ch. A. M. Luyben K. Linear relations in microbial reaction systems: A general overview of their origin, form, and use. Biotechnol Bioeng. 1991;38:603–18.

81. Monod J. The Growth of Bacterial Cultures. Annu Rev Microbiol. 1949;3:371–94.

82. Herbert D, Elsworth R, Telling RC. The Continuous Culture of Bacteria; a Theoretical and Experimental Study. J Gen Microbiol. 1956;14:601–22.

83. Pirt SJ. The maintenance energy of bacteria in growing cultures. Proc R Soc Lond B Biol Sci. 1965;163:224–31.

84. Chen J, Gomez JA, Höffner K, Barton PI, Henson MA. Metabolic modeling of synthesis gas fermentation in bubble column reactors. Biotechnol Biofuels [Internet]. 2015 [cited 2015 Oct 8];8. Available from: http://www.biotechnologyforbiofuels.com/content/8/1/89

85. van't Riet K, Tramper J. Basic bioreactor design. New York: M. Dekker; 1991.

86. Doran PM. Bioprocess engineering principles. 2nd ed. Amsterdam ; Boston: Elsevier/Academic Press; 2013.

87. Gu C, Kim GB, Kim WJ, Kim HU, Lee SY. Current status and applications of genome-scale metabolic models. Genome Biol [Internet]. 2019 [cited 2018 Dec 16];20.

Available from: https://genomebiology.biomedcentral.com/articles/10.1186/s13059-019-1730-3

88. Haringa C, Tang W, Wang G, Deshmukh AT, van Winden WA, Chu J, et al. Computational fluid dynamics simulation of an industrial P. chrysogenum fermentation with a coupled 9-pool metabolic model: Towards rational scale-down and design optimization. Chem Eng Sci. 2018;175:12–24.

89. Rizzi M, Baltes M, Theobald U, Reuss M. In vivo analysis of metabolic dynamics in Saccharomyces cerevisiae: II. Mathematical model. Biotechnol Bioeng. 1997;55:592–608.

90. Visser D, Heijnen JJ. Dynamic simulation and metabolic re-design of a branched pathway using linlog kinetics. Metab Eng. 2003;5:164–76.

91. Chassagnole C, Noisommit-Rizzi N, Schmid JW, Mauch K, Reuss M. Dynamic modeling of the central carbon metabolism of *Escherichia coli*. Biotechnol Bioeng. 2002;79:53–73.

92. Weiner M, Tröndle J, Albermann C, Sprenger GA, Weuster-Botz D. Perturbation Experiments: Approaches for Metabolic Pathway Analysis in Bioreactors. In: Bao J, Ye Q, Zhong J-J, editors. Bioreact Eng Res Ind Appl II [Internet]. Berlin, Heidelberg: Springer Berlin Heidelberg; 2015 [cited 2020 May 20]. p. 91–136. Available from: http://link.springer.com/10.1007/10_2015_326

93. van Gulik WM. Fast sampling for quantitative microbial metabolomics. Curr Opin Biotechnol. 2010;21:27–34.

94. Almquist J, Cvijovic M, Hatzimanikatis V, Nielsen J, Jirstrand M. Kinetic models in industrial biotechnology – Improving cell factory performance. Metab Eng. 2014;24:38–60.

95. Heijnen JJ. Approximative kinetic formats used in metabolic network modeling. Biotechnol Bioeng. 2005;91:534–45.

96. Visser D, Schmid JW, Mauch K, Reuss M, Heijnen JJ. Optimal re-design of primary metabolism in Escherichia coli using linlog kinetics. Metab Eng. 2004;6:378–90.

97. Schrödinger E. What is life? The physical aspect of the living cell. Cambridge University Press; 1944.

98. von Stockar U. Biothermodynamics of live cells: a tool for biotechnology and biochemical engineering. J Non-Equilib Thermodyn [Internet]. 2010 [cited 2022 Apr 13];35. Available from: https://www.degruyter.com/document/doi/10.1515/jnetdy.2010.024/html

99. Taymaz-Nikerel H, Jamalzadeh J, Espah Borujeni A, Verheijen PJT, van Gulik WM, Heijnen JJ. A thermodynamic analysis of dicarboxylic acid production in microorganisms. In: von Stockar U, editor. Thermodyn Biochem Eng [Internet]. EFPL Press; 2013 [cited 2016 Nov 29]. p. 547–79. Available from: http://www.crcnetbase.com/doi/abs/10.1201/b15428-27

100. von Stockar U, van der Wielen LAM, editors. Biothermodynamics: The Role of Thermodynamics in Biochemical Engineering [Internet]. 0 ed. EPFL Press; 2013 [cited 2021 Oct 15]. Available from: https://www.taylorfrancis.com/books/9781466582170

101. Heijnen JJ, van Dijken JP. In search of a thermodynamic description of biomass yields for the chemotrophic growth of microorganisms. Biotechnol Bioeng. 1992;39:833–58.

102. Maskow T, von Stockar U. How reliable are thermodynamic feasibility statements of biochemical pathways? Biotechnol Bioeng. 2005;92:223–30.

103. Vojinović V, von Stockar U. Influence of uncertainties in pH, pMg, activity coefficients, metabolite concentrations, and other factors on the analysis of the thermodynamic feasibility of metabolic pathways. Biotechnol Bioeng. 2009;103:780–95.

104. von Stockar U, editor. Thermodynamic Analysis Of Metabolic Pathways. Thermodyn Biochem Eng [Internet]. EFPL Press; 2013 [cited 2016 Nov 29]. p. 581–604. Available from: http://www.crcnetbase.com/doi/abs/10.1201/b15428-28

105. Nagarajan H, Sahin M, Nogales J, Latif H, Lovley DR, Ebrahim A, et al. Characterizing acetogenic metabolism using a genome-scale metabolic reconstruction of *Clostridium ljungdahlii*. Microb Cell Factories. 2013;12:118.

106. Mohammadi M, Mohamed AR, Najafpour GD, Younesi H, Uzir MH. Kinetic studies on fermentative production of biofuel from ssynthesis gas using *Clostridium ljungdahlii*. Sci World J. 2014;2014:1–8.

107. Camacho Ardila Y, Figueroa JEJ, Lunelli B, Maciel Filho R, Wolf Maciel MR. Simulation of ethanol production via fermentation of the synthesis gas using aspen plus. Chem Eng Trans. 2014;37:637–42.

108. de Medeiros EM, Posada JA, Noorman H, Filho RM. Dynamic modeling of syngas fermentation in a continuous stirred-tank reactor: Multi-response parameter estimation and process optimization. Biotechnol Bioeng. 2019;116:2473–87.

109. Heffernan JK, Mahamkali V, Valgepea K, Marcellin E, Nielsen LK. Analytical tools for unravelling the metabolism of gas-fermenting Clostridia. Curr Opin Biotechnol. 2022;75:102700.

110. Greene J, Daniell J, Köpke M, Broadbelt L, Tyo KEJ. Kinetic ensemble model of gas fermenting Clostridium autoethanogenum for improved ethanol production. Biochem Eng J. 2019;148:46–56.

111. Bertsch J, Müller V. Bioenergetic constraints for conversion of syngas to biofuels in acetogenic bacteria. Biotechnol Biofuels [Internet]. 2015 [cited 2016 Oct 6];8. Available from: http://www.biotechnologyforbiofuels.com/content/8/1/210

112. Müller V, Hess V. The Minimum Biological Energy Quantum. Front Microbiol [Internet]. 2017 [cited 2018 Dec 12];8. Available from: http://journal.frontiersin.org/article/10.3389/fmicb.2017.02019/full

113. Mahamkali V, Valgepea K, de Souza Pinto Lemgruber R, Plan M, Tappel R, Köpke M, et al. Redox controls metabolic robustness in the gas-fermenting

acetogen *Clostridium autoethanogenum*. Proc Natl Acad Sci. 2020;117:13168–75.

114. Norman ROJ, Millat T, Schatschneider S, Henstra AM, Breitkopf R, Pander B, et al. Genome-scale model of C. autoethanogenum reveals optimal bioprocess conditions for high-value chemical production from carbon monoxide. Eng Biol. 2019;3:32–40.

115. Chen J, Henson MA. In silico metabolic engineering of Clostridium ljungdahlii for synthesis gas fermentation. Metab Eng. 2016;38:389–400.

116. Redl S, Sukumara S, Ploeger T, Wu L, Ølshøj Jensen T, Nielsen AT, et al. Thermodynamics and economic feasibility of acetone production from syngas using the thermophilic production host *Moorella thermoacetica*. Biotechnol Biofuels. 2017;10:150.

117. Michailos S, Emenike O, Ingham D, Hughes KJ, Pourkashanian M. Methane production via syngas fermentation within the bio-CCS concept: A techno-economic assessment. Biochem Eng J. 2019;150:107290.

118. Noorman HJ, Heijnen JJ. Biochemical engineering's grand adventure. Chem Eng Sci. 2017;170:677–93.

119. Demirbas A. Biofuels securing the planet's future energy needs. Energy Convers Manag. 2009;50:2239–49.

120. UNFCCC. Adoption of the Paris Agreement [Internet]. 2015. Available from: https://unfccc.int/resource/docs/2015/cop21/eng/l09r01.pdf

121. Jesse Daystar, Ronalds Gonzalez, Carter Reeb, Richard A. Venditti, Trevor Treasure, Robert Abt, et al. Economics, Environmental Impacts, and Supply Chain Analysis of Cellulosic Biomass for Biofuels in the Southern US: Pine, Eucalyptus, Unmanaged Hardwoods, Forest Residues, Switchgrass, and Sweet Sorghum. BioResources. 2014;9:393–444.

122. Munasinghe PC, Khanal SK. Biomass-derived syngas fermentation into biofuels: Opportunities and challenges. Bioresour Technol. 2010;101:5013–22.

123. Bridgwater AV. The technical and economic feasibility of biomass gasification for power generation. Fuel. 1995;74:631–53.

124. Moncada J, Posada JA, Ramírez A. Early sustainability assessment for potential configurations of integrated biorefineries. Screening of bio-based derivatives from platform chemicals: Early sustainability assessment for potential configurations of integrated biorefineries. Screening of bio-based derivatives from platform chemicals. Biofuels Bioprod Biorefining. 2015;9:722–48.

125. Liew FM, Köpke M, Dennis S. Gas Fermentation for Commercial Biofuels Production. In: Fang Z, editor. Liq Gaseous Solid Biofuels - Convers Tech [Internet]. InTech; 2013 [cited 2015 Sep 9]. Available from: http://www.intechopen.com/books/liquid-gaseous-and-solid-biofuels-conversion-techniques/gas-fermentation-for-commercial-biofuels-production

126. Phillips JR, Klasson KT, Clausen EC, Gaddy JL. Biological Production of Ethanol from Coal Synthesis Gas. Appl Biochem Biotechnol. 1993;39/40.

127. Liu K, Atiyeh HK, Stevenson BS, Tanner RS, Wilkins MR, Huhnke RL. Mixed culture syngas fermentation and conversion of carboxylic acids into alcohols. Bioresour Technol. 2014;152:337–46.

128. Phillips JR, Atiyeh HK, Tanner RS, Torres JR, Saxena J, Wilkins MR, et al. Butanol and hexanol production in *Clostridium carboxidivorans* syngas fermentation: Medium development and culture techniques. Bioresour Technol. 2015;190:114–21.

129. Köpke M, Mihalcea C, Liew F, Tizard JH, Ali MS, Conolly JJ, et al. 2,3-butanediol production by acetogenic bacteria, an alternative route to chemical synthesis, using industrial waste gas. Appl Environ Microbiol. 2011;77:5467–75.

130. Do YS, Smeenk J, Broer KM, Kisting CJ, Brown R, Heindel TJ, et al. Growth of *Rhodospirillum rubrum* on synthesis gas: Conversion of CO to H_2 and poly-β-hydroxyalkanoate. Biotechnol Bioeng. 2007;97:279–86.

131. Bengelsdorf FR, Straub M, Dürre P. Bacterial synthesis gas (syngas) fermentation. Environ Technol. 2013;34:1639–51.

132. Dürre P, Eikmanns BJ. C1-carbon sources for chemical and fuel production by microbial gas fermentation. Curr Opin Biotechnol. 2015;35:63–72.

133. Vasudevan D, Richter H, Angenent LT. Upgrading dilute ethanol from syngas fermentation to n-caproate with reactor microbiomes. Bioresour Technol. 2014;151:378–82.

134. Siedlecki M, De Jong W, Verkooijen AHM. Fluidized Bed Gasification as a Mature And Reliable Technology for the Production of Bio-Syngas and Applied in the Production of Liquid Transportation Fuels—A Review. Energies. 2011;4:389–434.

135. Piccolo C, Bezzo F. A techno-economic comparison between two technologies for bioethanol production from lignocellulose. Biomass Bioenergy. 2009;33:478–91.

136. Abubackar HN, Veiga MC, Kennes C. Biological conversion of carbon monoxide: rich syngas or waste gases to bioethanol. Biofuels Bioprod Biorefining. 2011;5:93–114.

137. Mohammadi M, Najafpour GD, Younesi H, Lahijani P, Uzir MH, Mohamed AR. Bioconversion of synthesis gas to second generation biofuels: A review. Renew Sustain Energy Rev. 2011;15:4255–73.

138. Zhu Y, Jones SB, Biddy MJ, Dagle RA, Palo DR. Single-step syngas-to-distillates (S2D) process based on biomass-derived syngas – A techno-economic analysis. Bioresour Technol. 2012;117:341–51.

139. Swanson RM, Platon A, Satrio JA, Brown RC. Techno-economic analysis of biomass-to-liquids production based on gasification. Fuel. 2010;89:S11–9.

140. Seabra JEA, Tao L, Chum HL, Macedo IC. A techno-economic evaluation of the effects of centralized cellulosic ethanol and co-products refinery options with sugarcane mill clustering. Biomass Bioenergy. 2010;34:1065–78.

141. Choi D, Chipman DC, Bents SC, Brown RC. A Techno-economic Analysis of Polyhydroxyalkanoate and Hydrogen Production from Syngas Fermentation of

Gasified Biomass. Appl Biochem Biotechnol. 2010;160:1032–46.

142. Hamelinck CN, Suurs RAA, Faaij APC. International bioenergy transport costs and energy balance. Biomass Bioenergy. 2005;29:114–34.

143. Van Dael M, Van Passel S, Pelkmans L, Guisson R, Swinnen G, Schreurs E. Determining potential locations for biomass valorization using a macro screening approach. Biomass Bioenergy. 2012;45:175–86.

144. Gómez A, Rodrigues M, Montañés C, Dopazo C, Fueyo N. The potential for electricity generation from crop and forestry residues in Spain. Biomass Bioenergy. 2010;34:703–19.

145. Ma J, Scott NR, DeGloria SD, Lembo AJ. Siting analysis of farm-based centralized anaerobic digester systems for distributed generation using GIS. Biomass Bioenergy. 2005;28:591–600.

146. Ronalds Gonzalez, Richard Philips, Daniel Saloni, Hasan Jameel, Robert Abt, Adrian Pirraglia, et al. Biomass to Energy invthe Southern United States: Supply Chain and Delivered Cost. BioResources. 2011;6:2954–76.

147. Jan E.G. van Dam, Wolter Elbersen, René van Ree. Setting up international biobased commodity trade chains [Internet]. Netherlands Enterprise Agency; 2014. Available from: http://english.rvo.nl/sites/default/files/2014/06/Setting%20up%20international%20biobased%20commodity%20trade%20chains%20-%20May%202014.pdf

148. M. Worley, J. Yale. Biomass Gasification Technology Assessment. Colorado: NREL; 2012 Oct p. 358.

149. Hamelinck C, Faaij A, Denuil H, Boerrigter H. Production of FT transportation fuels from biomass; technical options, process analysis and optimisation, and development potential. Energy. 2004;29:1743–71.

150. D. Ramachandriya K, K. Kundiyana D, M. Sharma A, Kumar A, K. Atiyeh H, L. Huhnke R, et al. Critical factors affecting the integration of biomass gasification and syngas fermentation technology. AIMS Bioeng. 2016;3:188–210.

151. Siedlecki M, De Jong W, Verkooijen AHM. Fluidized Bed Gasification as a Mature And Reliable Technology for the Production of Bio-Syngas and Applied in the Production of Liquid Transportation Fuels—A Review. Energies. 2011;4:389–434.

152. Wayne Doherty, Anthony Reynolds, David Kennedy. Aspen Plus Simulation of Biomass Gasification in a Steam Blown Dual Fluidised Bed. School of Mechanical and Transport Engineering at ARROW@DIT; 2013.

153. Straathof AJJ, Alvarez-Góez D, Noorman H, Heijnen JJ. Syngas fermentation: Conceptual process design. Lille Grand Palais, France; 2014.

154. Soccol CR, Vandenberghe LP de S, Medeiros ABP, Karp SG, Buckeridge M, Ramos LP, et al. Bioethanol from lignocelluloses: Status and perspectives in Brazil. Bioresour Technol. 2010;101:4820–5.

155. Shinners K, Binversie B, Muck R, Weimer P. Comparison of wet and dry corn stover harvest and storage. Biomass Bioenergy. 2007;31:211–21.

156. Demirbaş A. Sustainable cofiring of biomass with coal. Energy Convers Manag. 2003;44:1465–79.

157. Rafael Monteiro Sbampato. Investment project in a Brazilian eucalyptus farm [Internet]. [Milaan]: Politecnico di Milano; 2011. Available from: https://www.politesi.polimi.it/bitstream/10589/64221/1/Sbampato_Rafael.pdf

158. Cuiping L, Chuangzhi W, Yanyongjie, Haitao H. Chemical elemental characteristics of biomass fuels in China. Biomass Bioenergy. 2004;27:119–30.

159. Lv PM, Xiong ZH, Chang J, Wu CZ, Chen Y, Zhu JX. An experimental study on biomass air–steam gasification in a fluidized bed. Bioresour Technol. 2004;95:95–101.

160. Channiwala SA, Parikh PP. A unified correlation for estimating HHV of solid, liquid and gaseous fuels. Fuel. 2002;81:1051–63.

161. Dayton DC, Jenkins BM, Turn SQ, Bakker RR, Williams RB, Belle-Oudry D, et al. Release of Inorganic Constituents from Leached Biomass during Thermal Conversion. Energy Fuels. 1999;13:860–70.

162. Wright MM, Daugaard DE, Satrio JA, Brown RC. Techno-economic analysis of biomass fast pyrolysis to transportation fuels. Fuel. 2010;89:S2–10.

163. Al Arni S, Bosio B, Arato E. Syngas from sugarcane pyrolysis: An experimental study for fuel cell applications. Renew Energy. 2010;35:29–35.

164. Leinonen A, Valtion teknillinen tutkimuskeskus. Harvesting technology of forest residues for fuel in the USA and Finland. Espoo: Technical Research Centre of Finland; 2004.

165. Jayes W. Density of sugar factory products [Internet]. Sugar Eng. 2016 [cited 2016 Oct 12]. Available from: http://www.sugartech.co.za/density/

166. J.E. Atchison, J. R. Hettenhaus. Innovative Methods for Corn Stover Collecting, Handling, Storing and Transporting [Internet]. NREL; 2003 Mar. Available from: http://www.afdc.energy.gov/pdfs/33893.pdf

167. Mark Holmgren, Ken Casavant, Eric Jessup. Review of Transportation Costs for Alternative Fuels [Internet]. Pullman: Washington State University; 2007 Dec. Report No.: 25. Available from: http://ses.wsu.edu/wp-content/uploads/2015/03/Report25_TransCostsAltFuels.pdf

168. Lima J. The wood density of 3 Eucalyptus saligna Smith clones in relation to age. Ann Sci For. 1995;52:347–52.

169. Jonker JGG, van der Hilst F, Junginger HM, Cavalett O, Chagas MF, Faaij APC. Outlook for ethanol production costs in Brazil up to 2030, for different biomass crops and industrial technologies. Appl Energy. 2015;147:593–610.

170. Macedo IC, Seabra JEA, Silva JEAR. Green house gases emissions in the production and use of ethanol from sugarcane in Brazil: The 2005/2006 averages and a prediction for 2020. Biomass Bioenergy. 2008;32:582–95.

171. Graham RL, Nelson R, Sheehan J, Perlack RD, Wright LL. Current and Potential U.S. Corn Stover Supplies. Agron J. 2007;99:1.

172. Carolynn E. Sarlls. A comparison of Empirical and Theoretical Eucalyptus Yields in Brazil. Knoxville: The University of Tennessee; 2010. Available from: http://web.ornl.gov/sci/ees/cbes/Trip%20Reports/P2%20Oladosu%20and%20Sarlis%202010%20POSTER%20Eucalypts%20Productivity%20Theory%20vs%20Empirical%20%20Compatibility%20Mode.pdf

173. Stape JL, Binkley D, Ryan MG, Fonseca S, Loos RA, Takahashi EN, et al. The Brazil Eucalyptus Potential Productivity Project: Influence of water, nutrients and stand uniformity on wood production. For Ecol Manag. 2010;259:1684–94.

174. Goldemberg J, Coelho ST, Guardabassi P. The sustainability of ethanol production from sugarcane. Energy Policy. 2008;36:2086–97.

175. Murphy CW, Kendall A. Life cycle inventory development for corn and stover production systems under different allocation methods. Biomass Bioenergy. 2013;58:67–75.

176. Seabra JEA, Macedo IC, Chum HL, Faroni CE, Sarto CA. Life cycle assessment of Brazilian sugarcane products: GHG emissions and energy use. Biofuels Bioprod Biorefining. 2011;5:519–32.

177. Rosillo Callé F, Bajay SV, Rothman H. Industrial uses of biomass energy the example of Brazil [Internet]. London; New York: Taylor & Francis; 2000 [cited 2015 Dec 15]. Available from: http://public.eblib.com/choice/publicfullrecord.aspx?p=168564

178. Luo L, van der Voet E, Huppes G. An energy analysis of ethanol from cellulosic feedstock–Corn stover. Renew Sustain Energy Rev. 2009;13:2003–11.

179. Grootscholten TIM, Steinbusch KJJ, Hamelers HVM, Buisman CJN. Chain elongation of acetate and ethanol in an upflow anaerobic filter for high rate MCFA production. Bioresour Technol. 2013;135:440–5.

180. Posada JA, Patel AD, Roes A, Blok K, Faaij APC, Patel MK. Potential of bioethanol as a chemical building block for biorefineries: Preliminary sustainability assessment of 12 bioethanol-based products. Bioresour Technol. 2013;135:490–9.

181. Budavari S, editor. The Merck index: an encyclopedia of chemicals, drugs, and biologicals. 11th ed., centennial ed. Rahway, N.J., U.S.A: Merck; 1989.

182. Kleerebezem R, Van Loosdrecht MCM. A Generalized Method for Thermodynamic State Analysis of Environmental Systems. Crit Rev Environ Sci Technol. 2010;40:1–54.

183. Heijnen J. A thermodynamic approach to predict black box model parameters for microbial growth. Biothermodynamics. First edition. Switzerland: EPFL Press; 2013.

184. Husebye J, Brunsvold AL, Roussanaly S, Zhang X. Techno economic evaluation of amine based CO_2 capture: impact of CO_2 concentration and steam supply. Energy Procedia. 2012;23:381–90.

185. NREL. Lignocellulosic Biomass to Ethanol Process Design and Economics Utilizing Co-Current Dilute Acid Prehydrolysis and Enzymatic Hydrolysis for Corn Stover. 2002.

186. Garcia AA, King CJ. The use of basic polymer sorbents for the recovery of acetic acid from dilute aqueous solution. Ind Eng Chem Res. 1989;28:204–12.

187. Hlavacek M. Break-up of oil-in-water emulsions induced by permeation through a microfiltration membrane. J Membr Sci. 1995;102:1–7.

188. Sridhar S. Zur Abtrennung von Butandiol-2,3 aus Fermenter-Brühen mit Hilfe der Umkehrosmose: Zur Abtrennung von Butandiol-2,3 aus Fermenter-Brühen mit Hilfe der Umkehrosmose. Chem Ing Tech. 1989;61:252–3.

189. Walas SM. Chemical process equipment selection and design [Internet]. Boston: Butterworth-Heinemann; 1990 [cited 2016 Feb 22]. Available from: http://app.knovel.com/hotlink/toc/id:kpCPESD003/chemical-process-equipment

190. Cuellar MC, Heijnen JJ, van der Wielen LAM. Large-scale production of diesel-like biofuels - process design as an inherent part of microorganism development. Biotechnol J. 2013;8:682–9.

191. Schmid A, Kollmer A, Mathys RG, Witholt B. Developments toward large-scale bacterial bioprocesses in the presence of bulk amounts of organic solvents. Extremophiles. 1998;2:249–56.

192. Heeres AS, Picone CSF, van der Wielen LAM, Cunha RL, Cuellar MC. Microbial advanced biofuels production: overcoming emulsification challenges for large-scale operation. Trends Biotechnol. 2014;32:221–9.

193. Peters MS, Timmerhaus KD. Plant design and economics for chemical engineers. 4. ed. New York: McGraw-Hill; 1991.

194. Davis L, Scarlata T, Tan E, Ross J, Lukas J, Sexton D. Process Design and Economics for the Conversion of Lignocellulosic Biomass to Hydrocarbons: Dilute-Acid and Enzymatic Deconstruction of Biomass to Sugars and Catalytic Conversion of Sugars to Hydrocarbons. National Renewable Energy Laboratory; 2015 Mar. Report No.: NREL/TP-5100-62498.

195. Seider WD, Seader JD, Lewin D, Widagdo S, editors. Product and process design principles: synthesis, analysis, and evaluation. 3. ed., international student version. Hoboken, NJ: Wiley; 2010.

196. Ulrich G, Vasudevan P. How to estimate utility costs. Chem Eng. 2006;

197. Towler GP, Sinnott RK. Chemical engineering design: principles, practice, and economics of plant and process design. 2nd ed. Boston, MA: Butterworth-Heinemann; 2013.

198. International Energy Agency. Key world energy statistics. France: IEA; 2015.

199. U.S. Department of Energy. U.S. Billion-ton Update: Biomass Supply for a Bionergy and Bioproducts Industry [Internet]. 2011. Available from: https://www1.eere.energy.gov/bioenergy/pdfs/billion_ton_update.pdf

200. US Environmental Protection Agency. Biomass Resources [Internet]. Biomass CHP Catalog; 2007. Available from: http://www.epa.gov/sites/production/files/2015-07/documents/biomass_combined_heat_and_power_catalog_of_technologies_v.1.1.pdf

201. E4tech, RE-CORD, WUR. From the Sugar Platform to biofuels and biochemicals. London; 2015 Apr.

202. Dias MOS, Junqueira TL, Cavalett O, Cunha MP, Jesus CDF, Rossell CEV, et al. Integrated versus stand-alone second generation ethanol production from sugarcane bagasse and trash. Bioresour Technol. 2012;103:152–61.

203. William Edwards. Estimating a Value for Corn Stover [Internet]. Iowa State University; 2014. Available from: https://www.extension.iastate.edu/agdm/crops/pdf/a1-70.pdf

204. ISO. ISO 14040 Environmental managemnet - Life cycle assessment - Principles and framework [Internet]. ISO; 1997. Available from: http://web.stanford.edu/class/cee214/Readings/ISOLCA.pdf

205. ISO. ISO 14044 Environmental management - Life cycle assessment - Requirements and guidelines [Internet]. ISO; 2006. Available from: https://www.saiglobal.com/pdftemp/previews/osh/iso/updates2006/wk26/iso_14044-2006.pdf

206. Posada JA, Brentner LB, Ramirez A, Patel MK. Conceptual design of sustainable integrated microalgae biorefineries: Parametric analysis of energy use, greenhouse gas emissions and techno-economics. Algal Res. 2016;17:113–31.

207. Tsiropoulos I, Faaij APC, Seabra JEA, Lundquist L, Schenker U, Briois J-F, et al. Life cycle assessment of sugarcane ethanol production in India in comparison to Brazil. Int J Life Cycle Assess. 2014;19:1049–67.

208. Kim S, Dale BE. Regional variations in greenhouse gas emissions of biobased products in the United States—corn-based ethanol and soybean oil. Int J Life Cycle Assess. 2009;14:540–6.

209. U.S. Energy Information Administration. Carbon Dioxide Emissions Coefficients [Internet]. 2013. Available from: http://www.eia.gov/environment/emissions/co2_vol_mass.cfm

210. Roy P, Dutta A, Deen B. Greenhouse gas emissions and production cost of ethanol produced from biosyngas fermentation process. Bioresour Technol. 2015;192:185–91.

211. Martín M, Grossmann IE. Energy optimization of bioethanol production via gasification of switchgrass. AIChE J. 2011;57:3408–28.

212. Sassner P, Galbe M, Zacchi G. Techno-economic evaluation of bioethanol production from three different lignocellulosic materials. Biomass Bioenergy. 2008;32:422–30.

213. Wingren A, Galbe M, Zacchi G. Techno-Economic Evaluation of Producing Ethanol from Softwood: Comparison of SSF and SHF and Identification of Bottlenecks. Biotechnol Prog. 2008;19:1109–17.

214. Galbe M, Zacchi G. A review of the production of ethanol from softwood. Appl Microbiol Biotechnol. 2002;59:618–28.

215. Cheali P, Posada JA, Gernaey KV, Sin G. Economic risk analysis and critical comparison of optimal biorefinery concepts: Economic risk analysis and critical comparison of optimal biorefinery concepts. Biofuels Bioprod Biorefining [Internet]. 2016 [cited 2016 Jun 24]; Available from: http://doi.wiley.com/10.1002/bbb.1654

216. Villanueva Perales AL, Reyes Valle C, Ollero P, Gómez-Barea A. Technoeconomic assessment of ethanol production via thermochemical conversion of biomass by entrained flow gasification. Energy. 2011;36:4097–108.

217. He J, Zhang W. Techno-economic evaluation of thermo-chemical biomass-to-ethanol. Appl Energy. 2011;88:1224–32.

218. Hunpinyo P, Cheali P, Narataruksa P, Tungkamani S, Chollacoop N. Alternative route of process modification for biofuel production by embedding the Fischer–Tropsch plant in existing stand-alone power plant (10MW) based on biomass gasification – Part I: A conceptual modeling and simulation approach (a case study in Thailand). Energy Convers Manag. 2014;88:1179–92.

219. Tecnon Orbichem. 1,4-butanediol [Internet]. Orbichem. 2013 [cited 2016 Feb 24]. Available from: https://www.google.nl/url?sa=t&rct=j&q=&esrc=s&source=web&cd=1&ved=0ahUKEwiz9dHfu5DLAhVCKw8KHcfUAZkQFgggMAA&url=http%3A%2F%2Fwww.orbichem.com%2Fuserfiles%2FCNF%2520Samples%2Fbdo_13_11.pdf&usg=AFQjCNFqaEXzG90mvu2TTpVqYMHuLZT6BQ&cad=rja

220. Agler MT, Wrenn BA, Zinder SH, Angenent LT. Waste to bioproduct conversion with undefined mixed cultures: the carboxylate platform. Trends Biotechnol. 2011;29:70–8.

221. Kenealy WR, Cao Y, Weimer PJ. Production of caproic acid by cocultures of ruminal cellulolytic bacteria and *Clostridium kluyveri* grown on cellulose and ethanol. Appl Microbiol Biotechnol. 1995;44:507–13.

222. Cornelio C. Techno-Economic and Environmental Analysis of Oil Crop and Forestry Residues based Biorefineries for Biojet Fuel production in Brazil. Barcelona, Spain; 2016.

223. Muñoz I, Flury K, Jungbluth N, Rigarlsford G, i Canals LM, King H. Life cycle assessment of bio-based ethanol produced from different agricultural feedstocks. Int J Life Cycle Assess. 2014;19:109–19.

224. Cherubini F, Bird ND, Cowie A, Jungmeier G, Schlamadinger B, Woess-Gallasch S. Energy- and greenhouse gas-based LCA of biofuel and bioenergy systems: Key issues, ranges and recommendations. Resour Conserv Recycl. 2009;53:434–47.

225. Gabrielle B, Gagnaire N. Life-cycle assessment of straw use in bio-ethanol production: A case study based on biophysical modelling. Biomass Bioenergy. 2008;32:431–41.

226. Woods J, Bauen A. Technology status review and carbon abatement potential of renewable transport fuels in the UK [Internet]. Department of trade and industry; 2003. Available from: http://www.fcrn.org.uk/sites/default/files/DTI_Technology_status_review.pdf

227. Adom F, Dunn JB, Han J, Sather N. Life-Cycle Fossil Energy Consumption and Greenhouse Gas Emissions of Bioderived Chemicals and Their Conventional Counterparts. Environ Sci Technol. 2014;48:14624–31.

228. van Duuren JBJH, Brehmer B, Mars AE, Eggink G, dos Santos VAPM, Sanders JPM. A limited LCA of bio-adipic acid: Manufacturing the nylon-6,6 precursor adipic acid using the benzoic acid degradation pathway from different feedstocks. Biotechnol Bioeng. 2011;108:1298–306.

229. Xu D, Lewis RS. Syngas fermentation to biofuels: Effects of ammonia impurity in raw syngas on hydrogenase activity. Biomass Bioenergy. 2012;45:303–10.

230. Abubackar HN, Fernández-Naveira Á, Veiga MC, Kennes C. Impact of cyclic pH shifts on carbon monoxide fermentation to ethanol by *Clostridium autoethanogenum*. Fuel. 2016;178:56–62.

231. Senaratne R, Liu S. Management of Ethanol Concentration During Syngas Fermentation.

232. Martin ME, Richter H, Saha S, Angenent LT. Traits of selected *Clostridium* strains for syngas fermentation to ethanol: Syngas Fermentation Strain Comparison. Biotechnol Bioeng. 2016;113:531–9.

233. Heijnen JJ, van Loosdrecht MCM, Tijhuis L. A black box mathematical model to calculate auto- and heterotrophic biomass yields based on Gibbs energy dissipation. Biotechnol Bioeng. 1992;40:1139–54.

234. Heijnen JJ, van't Riet K. Mass transfer, mixing and heat transfer phenomena in low viscosity bubble column reactors. Chem Eng J. 1984;28:B21–42.

235. Wilke CR, Chang P. Correlation of diffusion coefficients in dilute solutions. AIChE J. 1955;1:264–70.

236. Groen D. Macromixing in bioreactors [PhD Thesis]. [Delft]: Technische Universiteit Delft; 1994.

237. Chisti Y. Pneumatically Agitated Bioreactors in Industrial and Environmental Bioprocessing: Hydrodynamics, Hydraulics, and Transport Phenomena. Appl Mech Rev. 1998;51:33.

238. Sinnott RK, Coulson JM, Richardson JF, Sinnott RK. Chemical engineering design. 4. ed., reprinted. Amsterdam: Elsevier, Butterworth-Heinemann; 2006.

239. Wieckert C, Obrist A, Zedtwitz P von, Maag G, Steinfeld A. Syngas Production by Thermochemical Gasification of Carbonaceous Waste Materials in a 150 kW_{th} Packed-Bed Solar Reactor. Energy Fuels. 2013;27:4770–6.

240. Couto ND, Silva VB, Monteiro E, Rouboa A. Assessment of municipal solid wastes gasification in a semi-industrial gasifier using syngas quality indices. Energy. 2015;93:864–73.

241. de Medeiros EM, Posada JA, Noorman H, Osseweijer P, Maciel Filho R. Hydrous bioethanol production from sugarcane bagasse via energy self-sufficient gasification-fermentation hybrid route: Simulation and financial analysis. J Clean Prod. 2017;168:1625–35.

242. Griffin DW, Schultz MA. Fuel and chemical products from biomass syngas: A comparison of gas fermentation to thermochemical conversion routes. Environ Prog Sustain Energy. 2012;31:219–24.

243. Köpke M, Held C, Hujer S, Liesegang H, Wiezer A, Wollherr A, et al. *Clostridium ljungdahlii* represents a microbial production platform based on syngas. Proc Natl Acad Sci. 2010;107:13087–92.

244. Ragsdale SW, Pierce E. Acetogenesis and the Wood–Ljungdahl pathway of CO_2 fixation. Biochim Biophys Acta BBA - Proteins Proteomics. 2008;1784:1873–98.

245. Schuchmann K, Müller V. Autotrophy at the thermodynamic limit of life: a model for energy conservation in acetogenic bacteria. Nat Rev Microbiol. 2014;12:809–21.

246. Abubackar HN, Veiga MC, Kennes C. Carbon monoxide fermentation to ethanol by *Clostridium autoethanogenum* in a bioreactor with no accumulation of acetic acid. Bioresour Technol. 2015;186:122–7.

247. Kerby R, Zeikus JG. Growth of *Clostridium thermoaceticum* on H_2/CO_2 or CO as energy source. Curr Microbiol. 1983;8:27–30.

248. Xie B-T, Liu Z-Y, Tian L, Li F-L, Chen X-H. Physiological response of *Clostridium ljungdahlii* DSM 13528 of ethanol production under different fermentation conditions. Bioresour Technol. 2015;177:302–7.

249. Hurst KM, Lewis RS. Carbon monoxide partial pressure effects on the metabolic process of syngas fermentation. Biochem Eng J. 2010;48:159–65.

250. Straub M, Demler M, Weuster-Botz D, Dürre P. Selective enhancement of autotrophic acetate production with genetically modified *Acetobacterium woodii*. J Biotechnol. 2014;178:67–72.

251. Atiyeh HK, Philips JR, Huhnke R. Fermentation control for optimization of syngas utilization [Internet]. Stillwater, Oklahoma; 2016. Available from: https://patentscope.wipo.int/search/en/detail.jsf?docId=WO2016077778&tab=PCTBIBLIO&maxRec=1000

252. Phillips J, Huhnke R, Atiyeh H. Syngas fermentation: a microbial conversion process of gaseous substrates to various products. Fermentation. 2017;3:28.

253. Hu P, Bowen SH, Lewis RS. A thermodynamic analysis of electron production during syngas fermentation. Bioresour Technol. 2011;102:8071–6.

254. Chen J, Gomez JA, Höffner K, Phalak P, Barton PI, Henson MA. Spatiotemporal modeling of microbial metabolism. BMC Syst Biol [Internet]. 2016 [cited 2018 Dec 13];10. Available from: http://www.biomedcentral.com/1752-0509/10/21

255. Liu JK, Lloyd C, Al-Bassam MM, Ebrahim A, Kim J-N, Olson C, et al. Predicting proteome allocation, overflow metabolism, and metal requirements in a model

acetogen. Henry C, editor. PLOS Comput Biol. 2019;15:e1006848.

256. Pardo-Planas O, Atiyeh HK, Phillips JR, Aichele CP, Mohammad S. Process simulation of ethanol production from biomass gasification and syngas fermentation. Bioresour Technol. 2017;245:925–32.

257. Valgepea K, Loi KQ, Behrendorff JB, Lemgruber R de SP, Plan M, Hodson MP, et al. Arginine deiminase pathway provides ATP and boosts growth of the gas-fermenting acetogen Clostridium autoethanogenum. Metab Eng. 2017;41:202–11.

258. Li X, Griffin D, Li X, Henson MA. Incorporating hydrodynamics into spatiotemporal metabolic models of bubble column gas fermentation. Biotechnol Bioeng. 2019;116:28–40.

259. Lapin A, Müller D, Reuss M. Dynamic Behavior of Microbial Populations in Stirred Bioreactors Simulated with Euler−Lagrange Methods: Traveling along the Lifelines of Single Cells †. Ind Eng Chem Res. 2004;43:4647–56.

260. Henstra AM. CO metabolism of *Carboxydothermus hydrogenformans* and *Archaeoglobus fulgidus* [Internet] [PhD Thesis]. Wageningen University; 2006 [cited 2019 Sep 4]. Available from: http://edepot.wur.nl/34992

261. Poehlein A, Schmidt S, Kaster A-K, Goenrich M, Vollmers J, Thürmer A, et al. An ancient pathway combining carbon dioxide fixation with the generation and utilization of a sodium ion gradient for ATP synthesis. Driessen A, editor. PLoS ONE. 2012;7:e33439.

262. de Kok S, Meijer J, van Loosdrecht MCM, Kleerebezem R. Impact of dissolved hydrogen partial pressure on mixed culture fermentations. Appl Microbiol Biotechnol. 2013;97:2617–25.

263. Heijnen JJ. Bioenergetics of Microbial Growth. In: Flickinger MC, Drew SW, editors. Encycl Bioprocess Technol [Internet]. Hoboken, NJ, USA: John Wiley & Sons, Inc.; 2002 [cited 2017 Apr 11]. p. 265–91. Available from: http://doi.wiley.com/10.1002/0471250589.ebt026

264. Skidmore BE, Baker RA, Banjade DR, Bray JM, Tree DR, Lewis RS. Syngas fermentation to biofuels: Effects of hydrogen partial pressure on hydrogenase efficiency. Biomass Bioenergy. 2013;55:156–62.

265. Ahmed A, Lewis RS. Fermentation of biomass-generated synthesis gas: Effects of nitric oxide. Biotechnol Bioeng. 2007;97:1080–6.

266. Adams MWW, Mortensen LE. The physical and catalytic properties of hydrogenase II of *Clostridium pasteurianum*. A comparison with hydrogenase I. J Biol Chem. 1984;259:7045–55.

267. Dobrindt U, Blaut M. Purification and characterization of a membrane-bound hydrogenase from *Sporomusa sphaeroides* involved in energy-transducing electron transport. Arch Microbiol. 1996;165:141–7.

268. Rich JJ, King GM. Carbon monoxide consumption and production by wetland peats. FEMS Microbiol Ecol. 1999;28:215–24.

269. Xie H, Bélanger S, Demers S, Vincent WF, Papakyriakou TN. Photobiogeochemical cycling of carbon monoxide in the southeastern Beaufort Sea in spring and autumn. Limnol Oceanogr. 2009;54:234–49.

270. MacCallum SN. Tropospheric carbon monoxide: satellite observations and their applications [Internet] [PhD Thesis]. [Scotland]: The University of Edinburgh; 2010 [cited 2018 Sep 20]. Available from: http://hdl.handle.net/1842/4342

271. Greening C, Constant P, Hards K, Morales SE, Oakeshott JG, Russell RJ, et al. Atmospheric Hydrogen Scavenging: from Enzymes to Ecosystems. Müller V, editor. Appl Environ Microbiol. 2015;81:1190–9.

272. Giraldo-Gomez E, Goodwin S, Switzenbaum MS. Influence of mass transfer limitations on determination of the half saturation constant for hydrogen uptake in a mixed-culture CH_4-producing enrichment. Biotechnol Bioeng. 1992;40:768–76.

273. Novelli PC, Lang PM, Masarie KA, Hurst DF, Myers R, Elkins JW. Molecular hydrogen in the troposphere: Global distribution and budget. J Geophys Res Atmospheres. 1999;104:30427–44.

274. Intergovernmental Panel on Climate Change. Summary for policymakers. In: Stocker TF, Qin D, Plattner G, Tignor M, Allen S, Boschung J, et al., editors. Clim Change 2013 Phys Sci Basis Contrib Work Group Fifth Assess Rep Intergov Panel Clim Change [Internet]. Cambridge University Press; 2013 [cited 2019 Oct 4]. Available from: http://www.climatechange2013.org/images/report/WG1AR5_SPM_FINAL.pdf

275. Gaddy J, Arora D, Ko CW, Phillips JR, Basu R, Wikstrom C, et al. Methods for increasing the production of ethanol from microbial fermentation. 2007.

276. Roels JA. Energetics and kinetics in biotechnology. Amsterdam ; New York: Elsevier Biomedical Press; 1983.

277. Heijnen JJ, Van't Riet K. Mass transfer, mixing and heat transfer phenomena in low viscosity bubble column reactors. Chem Eng J. 1984;28:B21–42.

278. Weber FJ, Hartmans S. Prevention of clogging in a biological trickle-bed reactor removing toluene from contaminated air. Biotechnol Bioeng. 1996;50:91–7.

279. Lettinga G, van Velsen AFM, Hobma SW, de Zeeuw W, Klapwijk A. Use of the upflow sludge blanket (USB) reactor concept for biological wastewater treatment, especially for anaerobic treatment. Biotechnol Bioeng. 1980;22:699–734.

280. Philips J, Rabaey K, Lovley DR, Vargas M. Biofilm formation by *Clostridium ljungdahlii* is induced by sodium chloride stress: experimental evaluation and transcriptome analysis. Yang S, editor. PLOS ONE. 2017;12:e0170406.

281. Molitor B, Richter H, Martin ME, Jensen RO, Juminaga A, Mihalcea C, et al. Carbon recovery by fermentation of CO-rich off gases – Turning steel mills into biorefineries. Bioresour Technol. 2016;215:386–96.

282. Stephanopoulos G. Challenges in Engineering Microbes for Biofuels Production. Science. 2007;315:801–4.

283. Chang IS, Kim BH, Lovitt RW, Bang JS. Effect of CO partial pressure on cell-recycled continuous CO fermentation by *Eubacterium limosum* KIST612. Process Biochem. 2001;37:411–21.

284. Park S-J, Moon S-H, Lee H-J, Lim J-J, Kim J-M, Seo J, et al. A comparison of human cord blood- and embryonic stem cell-derived endothelial progenitor cells in the treatment of chronic wounds. Biomaterials. 2013;34:995–1003.

285. Shen Y, Brown R, Wen Z. Enhancing mass transfer and ethanol production in syngas fermentation of *Clostridium carboxidivorans* P7 through a monolithic biofilm reactor. Appl Energy. 2014;136:68–76.

286. Kataoka H, Takeuchi H, Nakao K, Yagi H, Tadaki T, Otake T, et al. Mass transfer in a large bubble column. J Chem Eng Jpn. 1979;12:105–10.

287. dos Santos KG, Eckert CT, De Rossi E, Bariccatti RA, Frigo EP, Lindino CA, et al. Hydrogen production in the electrolysis of water in Brazil, a review. Renew Sustain Energy Rev. 2017;68:563–71.

288. Phillips JR, Klasson KT, Clausen EC, Gaddy JL. Biological production of ethanol from coal synthesis gas: Medium development studies. Appl Biochem Biotechnol. 1993;39–40:559–71.

289. Shaikh A, Al-Dahhan M. Scale-up of Bubble Column Reactors: A Review of Current State-of-the-Art. Ind Eng Chem Res. 2013;52:8091–108.

290. Humbird D, Davis R, McMillan JD. Aeration costs in stirred-tank and bubble column bioreactors. Biochem Eng J. 2017;127:161–6.

291. Guo K, Wang T, Yang G, Wang J. Distinctly different bubble behaviors in a bubble column with pure liquids and alcohol solutions: Distinctly different bubble behaviors in a bubble column. J Chem Technol Biotechnol. 2017;92:432–41.

292. Sander R. Compilation of Henry's law constants (version 4.0) for water as solvent. Atmospheric Chem Phys. 2015;15:4399–981.

293. Dalkilic AS, Wongwises S. A performance comparison of vapour-compression refrigeration system using various alternative refrigerants. Int Commun Heat Mass Transf. 2010;37:1340–9.

294. Almeida Benalcázar E, Noorman H, Maciel Filho R, Posada-Duque J. Hybrid Model for Ethanol Production via Syngas Fermentation: Coupling between a Thermodynamics-based Black-box Model of Bacterial Reactions and Mass Transfer in a Large-scale Bubble Column Bioreactor. Proc 27th Eur Biomass Conf Exhib. 2019;27-30 May 2019:1408–17.

295. Vane LM. Separation technologies for the recovery and dehydration of alcohols from fermentation broths. Biofuels Bioprod Biorefining. 2008;2:553–88.

296. Vasconcelos JMT, Rodrigues JML, Orvalho SCP, Alves SS, Mendes RL, Reis A. Effect of contaminants on mass transfer coefficients in bubble column and airlift contactors. Chem Eng Sci. 2003;58:1431–40.

297. Sun Y, Nozawa T, Furusaki S. Gas holdup and volumetric oxygen transfer coefficient in a three-phase fluidized bed bioreactor. J Chem Eng Jpn. 1988;21:15–20.

298. Shen Y, Brown R, Wen Z. Syngas fermentation of *Clostridium carboxidivorans* P7 in a hollow fiber membrane biofilm reactor: Evaluating the mass transfer coefficient and ethanol production performance. Biochem Eng J. 2014;85:21–9.

299. Shen Y, Brown RC, Wen Z. Syngas fermentation by *Clostridium carboxidivorans* P7 in a horizontal rotating packed bed biofilm reactor with enhanced ethanol production. Appl Energy. 2017;187:585–94.

300. van den Heuvel JC, Vredenbregt LHJ, Portegies-Zwart I, Ottengraf SPP. Acceleration of mass transfer in methane-producing loop reactors. Antonie Van Leeuwenhoek. 1995;67:125–30.

301. Tian L, Cervenka ND, Low AM, Olson DG, Lynd LR. A mutation in the AdhE alcohol dehydrogenase of Clostridium thermocellum increases tolerance to several primary alcohols, including isobutanol, n-butanol and ethanol. Sci Rep [Internet]. 2019 [cited 2018 Dec 14];9. Available from: http://www.nature.com/articles/s41598-018-37979-5

302. Gmehling J, Onken U, Arlt W, editors. Vapor-liquid equilibrium data collection: tables and diagrams of data for binary and multicomponent mixtures up to moderate pressures; constants of correlation equations for computer use. Pt. 1: Aqueous-organic systems. 2. ed., 3. printing. Frankfurt am Main: Dechema; 1991.

303. Kurihara K, Minoura T, Takeda K, Kojima K. Isothermal Vapor-Liquid Equilibria for Methanol + Ethanol + Water, Methanol + Water, and Ethanol + Water. J Chem Eng Data. 1995;40:679–84.

304. COP-UNFCCC. Report of the Conference of the Parties on its 21st session, held in Paris from 30 November to 13 December 2015 : addendum [Internet]. 2016 Jan. Report No.: FCCC/CP/2015/10/Add.1. Available from: https://digitallibrary.un.org/record/831052/files/FCCC_CP_2015_10_Add.1-EN.pdf

305. Bitnere K, Searle S. Effective policy design for promoting investment in advanced alternative fuels [Internet]. United States: International Council on Clean Transportation; 2017. Available from: https://theicct.org/sites/default/files/publications/Advanced-alternative-fuels_ICCT-white-paper_21092017_vF.pdf

306. European Parliament. Directive 2018/2001 of the European Parliament and of the Council of 11 December 2018 on the promotion of the use of energy from renewable sources [Internet]. L 328/82 Dec 21, 2018. Available from: https://eur-lex.europa.eu/legal-content/EN/TXT/?uri=uriserv:OJ.L_.2018.328.01.0082.01.ENG&toc=OJ:L:2018:328:TOC

307. Liew F, Martin ME, Tappel RC, Heijstra BD, Mihalcea C, Köpke M. Gas fermentation - A flexible platform for commercial scale production of low-carbon-fuels and chemicals from waste and renewable feedstocks. Front Microbiol. 2016;7:694.

308. Achinas S, Horjus J, Achinas V, Euverink GJW. A PESTLE Analysis of Biofuels Energy Industry in Europe. Sustainability. 2019;11:5981.

309. Teixeira LV, Moutinho LF, Romão-Dumaresq AS. Gas fermentation of C1 feedstocks: commercialization status

and future prospects: Commercialization Status of Gas fermentation of C1 feedstocks. Biofuels Bioprod Biorefining. 2018;12:1103–17.

310. Sun X, Atiyeh HK, Huhnke RL, Tanner RS. Syngas fermentation process development for production of biofuels and chemicals: A review. Bioresour Technol Rep. 2019;7:100279.

311. Oswald F, Stoll IK, Zwick M, Herbig S, Sauer J, Boukis N, et al. Formic Acid Formation by Clostridium ljungdahlii at Elevated Pressures of Carbon Dioxide and Hydrogen. Front Bioeng Biotechnol [Internet]. 2018 [cited 2018 Dec 17];6. Available from: http://journal.frontiersin.org/article/10.3389/fbioe.2018.00006/full

312. Leang C, Ueki T, Nevin KP, Lovley DR. A Genetic System for *Clostridium ljungdahlii*: a Chassis for Autotrophic Production of Biocommodities and a Model Homoacetogen. Appl Environ Microbiol. 2013;79:1102–9.

313. Simpson SD, Fleming SE, Havill AM, Trevethick SR. Process for producing chemicals using microbial fermentation of substrates comprising carbon monoxide. 2012.

314. Simpson SD, Conrado R, Mihalcea C. Integrated Fermentation And Electrolysis Process [Internet]. Skokie, IL; 2017 [cited 2019 Jan 3]. Available from: https://www.lens.org/lens/patent/021-512-927-177-233/fulltext

315. Trevethick SR, Bromley JC, Waters GW, Kopke M, Tran L, Jensen RO. Multi-stage Bioreactor Processes [Internet]. Skokie, IL; 2017 [cited 2019 Jan 3]. Available from: https://www.lens.org/lens/patent/085-544-595-640-866/fulltext

316. Sakai S, Nakashimada Y, Yoshimoto H, Watanabe S, Okada H, Nishio N. Ethanol production from H_2 and CO_2 by a newly isolated thermophilic bacterium, Moorella sp. HUC22-1. Biotechnol Lett. 2004;26:1607–12.

317. Daniel SL, Hsu T, Dean SI, Drake HL. Characterization of the H_2- and CO-dependent chemolithotrophic potentials of the acetogens *Clostridium thermoaceticum* and *Acetogenium kivui*. J Bacteriol. 1990;172:4464–71.

318. Bredwell MD, Srivastava P, Worden RM. Reactor Design Issues for Synthesis-Gas Fermentations. Biotechnol Prog. 1999;15:834–44.

319. Kim Y-K, Lee H. Use of magnetic nanoparticles to enhance bioethanol production in syngas fermentation. Bioresour Technol. 2016;204:139–44.

320. Yasin M, Jeong Y, Park S, Jeong J, Lee EY, Lovitt RW, et al. Microbial synthesis gas utilization and ways to resolve kinetic and mass-transfer limitations. Bioresour Technol. 2015;177:361–74.

321. Asimakopoulos K, Gavala HN, Skiadas IV. Reactor systems for syngas fermentation processes: A review. Chem Eng J. 2018;348:732–44.

322. Li X. System And Method For Improved Gas Dissolution [Internet]. Auckland; 2016 [cited 2019 Jan 3]. Available from: https://www.lens.org/lens/patent/064-006-359-302-339/fulltext

323. de Medeiros EM, Noorman H, Maciel Filho R, Posada JA. Production of ethanol fuel via syngas fermentation: Optimization of economic performance and energy efficiency. Chem Eng Sci X. 2020;5:100056.

324. Almeida Benalcázar E, Noorman H, Maciel Filho R, Posada JA. Modeling ethanol production through gas fermentation: a biothermodynamics and mass transfer-based hybrid model for microbial growth in a large-scale bubble column bioreactor. Biotechnol Biofuels. 2020;13:59.

325. Almeida Benalcázar E, Noorman H, Maciel Filho R, Posada JA. Assessing the sensitivity of technical performance of three ethanol production processes based on the fermentation of steel manufacturing offgas, syngas and a 3:1 mixture between H_2 and CO_2. Proc 30th Eur Symp Comput Aided Process Eng. Milano, Italy: Elsevier; 2020.

326. Remus R, IPTS. Best available techniques (BAT) reference document for iron and steel production industrial emissions directive 2010/75/EU (integrated pollution prevention and control) [Internet]. Luxembourg: Publications Office of the European Union; 2013 [cited 2019 Feb 14]. Available from: http://bookshop.europa.eu/en/best-available-techniques-bat-reference-document-for-iron-and-steel-production-pbLFNA25521/

327. NEDO. Japanese technologies for energy savings / GHG emissions reduction. Japan: New Energy and Industrial Technology Development Organization; 2008.

328. Rey Porto M, Carretero T, Aguado M, Garde R. H_2 production in Sotavento wind farm. Proc WHEC. Essen - Germany; 2010.

329. Harrison K, Martin G, Ramsden T, Kramer W, Novachek F. The Wind-to-Hydrogen Project: Operational Experience, Performance Testing, and Systems Integration. National Renewable Energy Laboratory; 2009 Mar. Report No.: NREL/TP-550-44082.

330. Bieda B. Life cycle inventory processes of the ArcelorMittal Poland (AMP) S.A. in Kraków, Poland—basic oxygen furnace steel production: A case study. Int J Life Cycle Assess. 2012;17:463–70.

331. Dutta A, Talmadge M, Hensley J, Worley M, Dudgeon D, Barton D, et al. Process design and economics for conversion of lignocellulosic biomass to ethanol: thermochemical pathway by indirect gasification and mixed alcohol synthesis [Internet]. National Renewable Energy Laboratory; 2011 May. Report No.: NREL/TP-5100-51400. Available from: https://www.nrel.gov/docs/fy11osti/51400.pdf

332. Ciferno J, Marano J. Benchmarking biomass gasification technologies for fuels, chemicals and hydrogen production [Internet]. United States: E2S; 2002 Jun. Available from: https://www.netl.doe.gov/sites/default/files/netl-file/BMassGasFinal.pdf

333. Li X, Cossey BJ, Trevethick SR. Fermentation Of Gaseous Substrates [Internet]. 2017 [cited 2019 Jan 3]. Available from: https://www.lens.org/lens/patent/056-651-816-481-136/fulltext

334. Beneke D. Understanding distillation using column profile maps. Hoboken, New Jersey: Wiley; 2013.

335. Rochelle GT. Amine Scrubbing for CO_2 Capture. Science. 2009;325:1652–4.

336. CGEE. Second-generation sugarcane bioenergy & biochemicals: Advanced lowcarbon fuels for transport and industry [Internet]. Brasilia: Center for Strategic Studies and Management (CGEE); 2017. Available from: https://www.cgee.org.br/documents/10182/734063/Ethanol2G_web.pdf

337. Humbird D, Davis S, Tao L, Kinchin C, Hsu D, Aden A, et al. Process design and economics for biochemical conversion of lignocellulosic biomass to ethanol: Dilute-acid pretreatment and enzymatic hydrolysis of corn stover [Internet]. Colorado, USA: National Renewable Energy Laboratory; 2011 May. Report No.: NREL/TP-5100-47764. Available from: https://www.nrel.gov/docs/fy11osti/47764.pdf

338. Millinger M, Meisel K, Budzinski M, Thrän D. Relative greenhouse gas abatement cost competitiveness of biofuels in Germany. Energies. 2018;11:615.

339. Burchart-Korol D. Life cycle assessment of steel production in Poland: a case study. J Clean Prod. 2013;54:235–43.

340. Ladage S, Blumenberg M, Franke D, Bahr A, Lutz R, Schmidt S. On the climate benefit of a coal-to-gas shift in Germany's electric power sector. Sci Rep. 2021;11:11453.

341. Grant T, Anderson C, Hooper B. Comparative life cycle assessment of potassium carbonate and monoethanolamine solvents for CO_2 capture from post combustion flue gases. Int J Greenh Gas Control. 2014;28:35–44.

342. Mehmeti A, Angelis-Dimakis A, Arampatzis G, McPhail S, Ulgiati S. Life cycle assessment and water footprint of hydrogen production methods: from conventional to emerging technologies. Environments. 2018;5:24.

343. Caduff M, Huijbregts MAJ, Althaus H-J, Koehler A, Hellweg S. Wind power electricity: the bigger the turbine, the greener the electricity? Environ Sci Technol. 2012;46:4725–33.

344. IRENA. Future of wind: Deployment, investment, technology, grid integration and socio-economic aspects (A Global Energy Transformation paper) [Internet]. Abu Dhabi: International Renewable Energy Agency; 2019 Oct. Available from: https://www.irena.org/-/media/Files/IRENA/Agency/Publication/2019/Oct/IRENA_Future_of_wind_2019.pdf

345. Aden A, Ruth M, Ibsen K, Jechura J, Neeves K, Sheehan J, et al. Lignocellulosic biomass to ethanol process design and economics utilizing co-current dilute acid prehydrolysis and enzymatic hydrolysis for corn stover [Internet]. National Renewable Energy Laboratory; 2002. Available from: https://www.nrel.gov/docs/fy02osti/32438.pdf

346. Kwak T-H, Lee S, Park J-W, Maken S, Yoo YD, Lee S-H. Gasification of municipal solid waste in a pilot plant and its impact on environment. Korean J Chem Eng. 2006;23:954–60.

347. Yao J, Kraussler M, Benedikt F, Hofbauer H. Techno-economic assessment of hydrogen production based on dual fluidized bed biomass steam gasification, biogas steam reforming, and alkaline water electrolysis processes. Energy Convers Manag. 2017;145:278–92.

348. Access Intelligence LLC. Economic indicators: CEPCI [Internet]. Chem. Eng. 2019 [cited 2019 Oct 24]. Available from: http://www.chemengonline.com/

349. European Parliament. Directive 2009/28/EC of the European Parliament and of the Council of 23 April 2009 on the promotion of the use of energy from renewable sources and amending and subsequently repealing Directives 2001/77/EC and 2003/30/EC [Internet]. 2009/28/EC 2009. Available from: https://eur-lex.europa.eu/legal-content/EN/TXT/PDF/?uri=CELEX:32009L0028&from=EN

350. Burhenne S. Monte Carlo based uncertainty and sensitivity analysis for building performance simulation [Doctoral thesis]. [Aachen]: Karlsruhe Institute of Technology; 2013.

351. Saltelli A, Ratto M, Andres T, Campolongo F, Cariboni J, Gatelli D, et al. Global sensitivity analysis. The primer [Internet]. Chichester, UK: John Wiley & Sons, Ltd; 2007 [cited 2018 Dec 22]. Available from: http://doi.wiley.com/10.1002/9780470725184

352. Kechkar M, Sayed W, Cabrol A, Aziza M, Ahmed Zaid T, Amrane A, et al. Isolation and identification of yeast strains from sugarcane molasses, dates and figs for ethanol production under conditions simulating algal hydrolysate. Braz J Chem Eng. 2019;36:157–69.

353. Verlaan P. Modeling and characterization of an airlift-loop bioreactor [Internet] [PhD Thesis]. [Wageningen]: Wageningen University; 1987. Available from: https://edepot.wur.nl/201465

354. Simpson SD. CCU-Now: fuels and chemicals from Waste [Internet]. New Dehli, India; 2018 [cited 2018 Jul 26]. Available from: https://ec.europa.eu/info/events/renewable-energy-events/eu-india-conference-advanced-biofuels-2018-mar-07_en

355. Deb K. Multi-objective optimization using evolutionary algorithms. 1st ed. Chichester ; New York: John Wiley & Sons; 2001.

356. Yusoff Y, Ngadiman MS, Zain AM. Overview of NSGA-II for Optimizing Machining Process Parameters. Procedia Eng. 2011;15:3978–83.

357. Huang W-D, Zhang Y-HP. Energy efficiency analysis: biomass-to-wheel efficiency related with biofuels production, fuel distribution, and powertrain systems. Saks V, editor. PLoS ONE. 2011;6:e22113.

358. Kurtz J, Sprik S, Bradley TH. Review of transportation hydrogen infrastructure performance and reliability. Int J Hydrog Energy. 2019;44:12010–23.

359. The International Consortium for Fire Safety, Health & The Environment. Safety issues regarding fuel cell vehicles and hydrogen fueled vehicles [Internet]. Washington DC - USA & Boras - Sweden: The

International Consortium for Fire Safety, Health & The Environment; 2011. Available from: https://dps.mn.gov/divisions/sfm/programs-services/Documents/Responder%20Safety/Alternative%20Fuels/FuelCellHydrogenFuelVehicleSafety.pdf

360. Euro NCAP. Test Results - Hyundai NEXO: Standard Safety Equipment [Internet]. Euro NCAP; 2018. Available from: https://cdn.euroncap.com/media/51395/euroncap-2018-hyundai-nexo-datasheet.pdf

361. World Steel Association. World steel in figures 2019 [Internet]. United States: World Steel Association AISBL; 2019. Available from: https://www.worldsteel.org/en/dam/jcr:96d7a585-e6b2-4d63-b943-4cd9ab621a91/World%2520Steel%2520in%2520Figures%25202019.pdf

362. BP plc. BP Statistical Review of World Energy 2019 [Internet]. United Kingdom: BP p.l.c; 2019 Jun. Available from: https://www.bp.com/content/dam/bp/business-sites/en/global/corporate/pdfs/energy-economics/statistical-review/bp-stats-review-2019-full-report.pdf

363. Ljungdahl LG, Wood HG. Total synthesis of acetate from CO_2 by heterotrophic bacteria. Annu Rev Microbiol. 1969;23:515–38.

364. Traunecker J, Preuß A, Diekert G. Isolation and characterization of a methyl chloride utilizing, strictly anaerobic bacterium. Arch Microbiol. 1991;156:416–21.

365. Daniel SL, Keith ES, Yang H, Lin Y-S, Drake HL. Utilization of methoxylated aromatic compounds by the acetogen *Clostridium thermoaceticum*: Expression and specificity of the co-dependent O-demethylating activity. Biochem Biophys Res Commun. 1991;180:416–22.

366. Simpson SD. Acid production by fermentation. 2012.

367. Simpson SD, Tran PL, Mihalcea C, Fung J, Liew FM. Production of butanediol by anaerobic microbial fermentation. 2011.

368. Wainaina S, Horváth IS, Taherzadeh MJ. Biochemicals from food waste and recalcitrant biomass via syngas fermentation: A review. Bioresour Technol. 2018;248:113–21.

369. Pinto T, Flores-Alsina X, Gernaey KV, Junicke H. Alone or together? A review on pure and mixed microbial cultures for butanol production. Renew Sustain Energy Rev. 2021;147:111244.

370. Burton F. Carbon Recycling Makes CNBC Disruptor List for 3rd time! [Internet]. LanzaTech. 2019 [cited 2020 Mar 13]. Available from: https://www.lanzatech.com/2019/05/17/carbon-recycling-makes-cnbc-disruptor-list-for-3rd-time/

371. Barbosa SG, Peixoto L, Alves JI, Alves MM. Bioelectrochemical systems (BESs) towards conversion of carbon monoxide/syngas: A mini-review. Renew Sustain Energy Rev. 2021;135:110358.

372. Stoll IK, Boukis N, Sauer J. Syngas Fermentation to Alcohols: Reactor Technology and Application Perspective. Chem Ing Tech. 2020;92:125–36.

373. Elisiário MP, De Wever H, Van Hecke W, Noorman H, Straathof AJJ. Membrane bioreactors for syngas permeation and fermentation. Crit Rev Biotechnol. 2021;1–17.

374. Liew F, Henstra AM, Köpke M, Winzer K, Simpson SD, Minton NP. Metabolic engineering of Clostridium autoethanogenum for selective alcohol production. Metab Eng. 2017;40:104–14.

375. Molitor B, Marcellin E, Angenent LT. Overcoming the energetic limitations of syngas fermentation. Curr Opin Chem Biol. 2017;41:84–92.

376. Köpke M, Simpson SD. Pollution to products: recycling of 'above ground' carbon by gas fermentation. Curr Opin Biotechnol. 2020;65:180–9.

377. Cha S, Lim HG, Kwon S, Kim D, Kang CW, Jung GY. Design of mutualistic microbial consortia for stable conversion of carbon monoxide to value-added chemicals. Metab Eng. 2021;64:146–53.

378. Mishra A, Ntihuga JN, Molitor B, Angenent LT. Power-to-Protein: Carbon Fixation with Renewable Electric Power to Feed the World. Joule. 2020;4:1142–7.

379. Bourgade B, Minton NP, Islam MA. Genetic and metabolic engineering challenges of C1-gas fermenting acetogenic chassis organisms. FEMS Microbiol Rev. 2021;45:fuab008.

380. Liew FE, Nogle R, Abdalla T, Rasor BJ, Canter C, Jensen RO, et al. Carbon-negative production of acetone and isopropanol by gas fermentation at industrial pilot scale. Nat Biotechnol. 2022;40:335–44.

381. Maddox IS, Steiner E, Hirsch S, Wessner S, Gutierrez NA, Gapes JR, et al. The cause of "acid-crash" and "acidogenic fermentations" during the batch acetone-butanol-ethanol (ABE-) fermentation process. J Mol Microbiol Biotechnol. 2000;2:95–100.

382. Min F, Kopke M, Dennis S. Gas Fermentation for Commercial Biofuels Production. In: Fang Z, editor. Liq Gaseous Solid Biofuels - Convers Tech [Internet]. InTech; 2013 [cited 2020 Mar 13]. Available from: http://www.intechopen.com/books/liquid-gaseous-and-solid-biofuels-conversion-techniques/gas-fermentation-for-commercial-biofuels-production

383. Cotter JL, Chinn MS, Grunden AM. Influence of process parameters on growth of *Clostridium ljungdahlii* and *Clostridium autoethanogenum* on synthesis gas. Enzyme Microb Technol. 2009;44:281–8.

384. Liu K, Atiyeh HK, Tanner RS, Wilkins MR, Huhnke RL. Fermentative production of ethanol from syngas using novel moderately alkaliphilic strains of *Alkalibaculum bacchi*. Bioresour Technol. 2012;104:336–41.

385. Maddipati P, Atiyeh HK, Bellmer DD, Huhnke RL. Ethanol production from syngas by *Clostridium* strain P11 using corn steep liquor as a nutrient replacement to yeast extract. Bioresour Technol. 2011;102:6494–501.

386. Datar RP, Shenkman RM, Cateni BG, Huhnke RL, Lewis RS. Fermentation of biomass-generated producer gas to ethanol. Biotechnol Bioeng. 2004;86:587–94.

387. Perez JM, Richter H, Loftus SE, Angenent LT. Biocatalytic reduction of short-chain carboxylic acids into

their corresponding alcohols with syngas fermentation. Biotechnol Bioeng. 2013;110:1066–77.

388. Kracke F, Virdis B, Bernhardt PV, Rabaey K, Krömer JO. Redox dependent metabolic shift in *Clostridium autoethanogenum* by extracellular electron supply. Biotechnol Biofuels [Internet]. 2016 [cited 2017 Oct 18];9. Available from: http://biotechnologyforbiofuels.biomedcentral.com/articles/10.1186/s13068-016-0663-2

389. Abubackar H, Veiga M, Kennes C. Ethanol and acetic acid production from carbon monoxide in a clostridium strain in batch and continuous gas-fed bioreactors. Int J Environ Res Public Health. 2015;12:1029–43.

390. Klasson KT, Ackerson MD, Clausen EC, Gaddy JL. Bioconversion of synthesis gas into liquid or gaseous fuels. Enzyme Microb Technol. 1992;14:602–8.

391. Henstra AM, Sipma J, Rinzema A, Stams AJ. Microbiology of synthesis gas fermentation for biofuel production. Curr Opin Biotechnol. 2007;18:200–6.

392. Sauer U, Dürre P. Differential induction of genes related to solvent formation during the shift from acidogenesis to solventogenesis in continuous culture of *Clostridium acetobutylicum*. FEMS Microbiol Lett. 1995;125:115–20.

393. Marcellin E, Behrendorff JB, Nagaraju S, DeTissera S, Segovia S, Palfreyman RW, et al. Low carbon fuels and commodity chemicals from waste gases – systematic approach to understand energy metabolism in a model acetogen. Green Chem. 2016;18:3020–8.

394. Patakova P, Branska B, Sedlar K, Vasylkivska M, Jureckova K, Kolek J, et al. Acidogenesis, solventogenesis, metabolic stress response and life cycle changes in Clostridium beijerinckii NRRL B-598 at the transcriptomic level. Sci Rep. 2019;9:1371.

395. Zampieri G, Vijayakumar S, Yaneske E, Angione C. Machine and deep learning meet genome-scale metabolic modeling. Nielsen J, editor. PLOS Comput Biol. 2019;15:e1007084.

396. Spahn S, Brandt K, Müller V. A low phosphorylation potential in the acetogen Acetobacterium woodii reflects its lifestyle at the thermodynamic edge of life. Arch Microbiol. 2015;197:745–51.

397. Klamt S, Schuster S, Gilles ED. Calculability analysis in underdetermined metabolic networks illustrated by a model of the central metabolism in purple nonsulfur bacteria. Biotechnol Bioeng. 2002;77:734–51.

398. Da Fonte Lameiras F. Transport processes in the production of organic acids from lignocellulosic feedstocks by Aspergillus niger [Internet]. Delft University of Technology; 2018 [cited 2018 Sep 14]. Available from: http://resolver.tudelft.nl/uuid:38c1fd73-bff2-4660-aa40-48a4c28e16f7

399. Aklujkar M, Leang C, Shrestha PM, Shrestha M, Lovley DR. Transcriptomic profiles of Clostridium ljungdahlii during lithotrophic growth with syngas or H2 and CO2 compared to organotrophic growth with fructose. Sci Rep [Internet]. 2017 [cited 2019 Jan 18];7. Available from: http://www.nature.com/articles/s41598-017-12712-w

400. Tan Y, Liu J, Chen X, Zheng H, Li F. RNA-seq-based comparative transcriptome analysis of the syngas-utilizing bacterium *Clostridium ljungdahlii* DSM 13528 grown autotrophically and heterotrophically. Mol Biosyst. 2013;9:2775.

401. Heffernan JK, Valgepea K, de Souza Pinto Lemgruber R, Casini I, Plan M, Tappel R, et al. Enhancing CO2-Valorization Using Clostridium autoethanogenum for Sustainable Fuel and Chemicals Production. Front Bioeng Biotechnol. 2020;8:204.

402. Keitel G, Onken U. THE EFFECT OF SOLUTES ON BUBBLE SIZE IN AIR-WATER DISPERSIONS. Chem Eng Commun. 1982;17:85–98.

403. Zieminski SA, Caron MM, Blackmore RB. Behavior of Air Bubbles in Dilute Aqueous Solutions. Ind Eng Chem Fundam. 1967;6:233–42.

404. Diez-Gonzalez F, Russell JB. The ability of *Escherichia coli* O157:H7 to decrease its intracellular pH and resist the toxicity of acetic acid. Microbiology. 1997;143:1175–80.

405. Dusséaux S, Croux C, Soucaille P, Meynial-Salles I. Metabolic engineering of Clostridium acetobutylicum ATCC 824 for the high-yield production of a biofuel composed of an isopropanol/butanol/ethanol mixture. Metab Eng. 2013;18:1–8.

406. Desai RP, Nielsen LK, Papoutsakis ET. Stoichiometric modeling of Clostridium acetobutylicum fermentations with non-linear constraints. J Biotechnol. 1999;71:191–205.

407. Alberty RA. Thermodynamics of biochemical reactions. Hoboken, N.J: Wiley-Interscience; 2003.

408. Miller SL, Smith-Magowan D. The Thermodynamics of the Krebs Cycle and Related Compounds. J Phys Chem Ref Data. 1990;19:1049.

409. Baroody EE, Carpenter GA. Heats of formation of propellant compounds (U). US; 1972. Report No.: Task No. 331-003/067-1/UR2402-001 for Naval Ordance Station.

410. Schink B. Fermentation of 2,3-butanediol by *Pelobacter carbinolicus sp. nov.* and *Pelobacter propionicus sp. nov.*, and evidence for propionate formation from C_2 compounds. Arch Microbiol. 1984;137:33–41.

411. Saville G, Gundry HA. The heats of combustion, solution and ionization of lactic acid. Trans Faraday Soc. 1959;55:2036.

412. Heijnen SJ, Verheijen PJT. How to Obtain True and Accurate Rate-Values. Methods Enzymol [Internet]. Elsevier; 2011 [cited 2022 Jan 8]. p. 457–508. Available from: https://linkinghub.elsevier.com/retrieve/pii/B9780123851185000232

413. Öztürk SS, Schumpe A, Deckwer W-D. Organic liquids in a bubble column: Holdups and mass transfer coefficients. AIChE J. 1987;33:1473–80.

414. Wagenaar ECH. Influence of ethanol on the bubble size and the gas-liquid mass transfer of oxygen [BSc Thesis]. [Delft]: Delft University of Technology; 2021.

415. Nadal-Rey G, McClure DD, Kavanagh JM, Cornelissen S, Fletcher DF, Gernaey KV. Understanding gradients in industrial bioreactors. Biotechnol Adv. 2021;46:107660.

416. Delvigne F, Destain J, Thonart P. A methodology for the design of scale-down bioreactors by the use of mixing and circulation stochastic models. Biochem Eng J. 2006;28:256–68.

417. Noorman H. Scale-Up and Scale-Down. In: Villadsen J, editor. Fundam Bioeng [Internet]. Weinheim, Germany: Wiley-VCH Verlag GmbH & Co. KGaA; 2015 [cited 2017 Apr 17]. p. 463–98. Available from: http://doi.wiley.com/10.1002/9783527697441.ch16

418. Sweere APJ, Luyben KChAM, Kossen NWF. Regime analysis and scale-down: Tools to investigate the performance of bioreactors. Enzyme Microb Technol. 1987;9:386–98.

419. Haringa C, Tang W, Deshmukh AT, Xia J, Reuss M, Heijnen JJ, et al. Euler-Lagrange computational fluid dynamics for (bio)reactor scale down: An analysis of organism lifelines. Eng Life Sci. 2016;16:652–63.

420. de Jonge LP, Buijs NAA, ten Pierick A, Deshmukh A, Zhao Z, Kiel JAKW, et al. Scale-down of penicillin production in *Penicillium chrysogenum*. Biotechnol J. 2011;6:944–58.

421. Douma RD, Deshmukh AT, de Jonge LP, de Jong BW, Seifar RM, Heijnen JJ, et al. Novel insights in transport mechanisms and kinetics of phenylacetic acid and penicillin-G in Penicillium chrysogenum. Biotechnol Prog. 2012;28:337–48.

422. de Jonge L, Buijs NAA, Heijnen JJ, van Gulik WM, Abate A, Wahl SA. Flux response of glycolysis and storage metabolism during rapid feast/famine conditions in *Penicillium chrysogenum* using dynamic ^{13} C labeling. Biotechnol J. 2014;9:372–85.

423. Theobald U, Mailinger W, Baltes M, Rizzi M, Reuss M. In vivo analysis of metabolic dynamics in Saccharomyces cerevisiae : I. Experimental observations. Biotechnol Bioeng. 1997;55:305–16.

424. Saa PA, Nielsen LK. Formulation, construction and analysis of kinetic models of metabolism: A review of modelling frameworks. Biotechnol Adv. 2017;35:981–1003.

425. Wu L, Wang W, Van Winden WA, Van Gulik WM, Heijnen JJ. A new framework for the estimation of control parameters in metabolic pathways using lin-log kinetics: Control parameter estimation using lin-log kinetics. Eur J Biochem. 2004;271:3348–59.

426. Heijnen JJ, van Gulik WM, Shimizu H, Stephanopoulos G. Metabolic flux control analysis of branch points: an improved approach to obtain flux control coefficients from large perturbation data. Metab Eng. 2004;6:391–400.

427. Almeida Benalcázar E, Heijnen JJ, Maciel Filho R, Posada JA, Noorman H. Modeling of syngas fermentation: integration of a Gibbs free energy-constrained black-box model and an ATP-constrained metabolic model. Dev.

428. Abrahamson B. Conceptual Design and Evaluation of a Commercial Syngas Fermentation Process [Master thesis]. [Delft]: Technische Universiteit Delft; 2019.

429. Feijó Delgado F, Cermak N, Hecht VC, Son S, Li Y, Knudsen SM, et al. Intracellular Water Exchange for Measuring the Dry Mass, Water Mass and Changes in Chemical Composition of Living Cells. Polymenis M, editor. PLoS ONE. 2013;8:e67590.

430. Hughmark GA. Power Requirements and Interfacial Area in Gas-Liquid Turbine Agitated Systems. Ind Eng Chem Process Des Dev. 1980;19:638–41.

431. Puiman L, Abrahamson B, Lans RGJM van der, Haringa C, Noorman HJ, Picioreanu C. Alleviating mass transfer limitations in industrial external-loop syngas-to-ethanol fermentation. Chem Eng Sci. 2022;259:117770.

432. Mislov D, Cifrek M, Krois I, Dzapo H. Measurement of dissolved hydrogen concentration with clark electrode. 2015 IEEE Sens Appl Symp SAS [Internet]. Zadar, Croatia: IEEE; 2015 [cited 2021 Jul 30]. p. 1–5. Available from: http://ieeexplore.ieee.org/document/7133656/

433. Kuhlmann J, Witte F, Heineman WR. Electrochemical Sensing of Dissolved Hydrogen in Aqueous Solutions as a Tool to Monitor Magnesium Alloy Corrosion. Electroanalysis. 2013;25:1105–10.

434. Mann M, Miebach K, Büchs J. Online measurement of dissolved carbon monoxide concentrations reveals critical operating conditions in gas fermentation experiments. Biotechnol Bioeng. 2021;118:253–64.

435. Puiman L, Elisiário MP, Crasborn LML, Wagenaar LECH, Straathof AJJ, Haringa C. Gas mass transfer in syngas fermentation broths is enhanced by ethanol. Biochem Eng J. 2022;185:108505.

436. Noorman HJ, Romein B, Luyben KChAM, Heijnen JJ. Classification, error detection, and reconciliation of process information in complex biochemical systems. Biotechnol Bioeng. 1996;49:364–76.

437. Bioenergy International. LanzaTech commission world's first commercial waste gas to ethanol plant. Bioenergy Int [Internet]. 2018 Dec 6 [cited 2022 Apr 30]; Available from: https://bioenergyinternational.com/lanzatech-commission-worlds-first-commercial-waste-gas-ethanol-plant-china/

438. Noorman HJ, Baksteen J, Heijnen JJ, Luyben ChAMK. The bioreactor overflow device: an undesired selective separator in continuous cultures? J Gen Microbiol. 1991;137:2171–7.

439. Straathof AJJ. Modelling of end-product inhibition in fermentation. Biochem Eng J. 2023;191:108796.

440. von Stockar U, Marison IW. The use of calorimetry in biotechnology. Bioprocesses Eng [Internet]. Berlin, Heidelberg: Springer Berlin Heidelberg; 1989 [cited 2022 Apr 22]. p. 93–136. Available from: http://link.springer.com/10.1007/BFb0009829

441. Taymaz-Nikerel H, de Mey M, Ras C, ten Pierick A, Seifar RM, van Dam JC, et al. Development and application of a differential method for reliable

metabolome analysis in *Escherichia coli*. Anal Biochem. 2009;386:9–19.

Acknowledgements

Alguna vez leí que si uno quiere llegar rápido, tiene que ir solo, pero si uno quiere llegar lejos, es mejor ir acompañado. Gracias Evita y Rafaela, mis viajeras, mi familia de 3 (que en un Mayo se hizo de 5 con el Antón y el Nicanor), gracias por venir conmigo.

Gracias papá y mamá. Cuánta vida ha pasado en estos años! Carito, cuidale al Joaquín. Gracias a mis abuelas, Fabiola y Adriana. Descansen Adrianitas.

Thank you Patricia, Henk, Rubens and John. Thank you for all your support, given in your own ways.

In sort of chronological order en in diferentes linguagens. Cheers to my friends Kasper, Zhizhen, Farahnaz, Baudine, Wijb, Luuk, Vidhvath y por supuesto, cheers Gustavo y Claudia. Thank you Anka, Guilherme e Joni. Joni, manda abraços para sua mãe! Abraço pro Julio, Mari, Maya, Alejo, Fer, Lucas, Danny Alex Lachos Perez, Evelyn, Filipe, Manô, abraço pras crianças. Que ótima comida que a gente comia junto. Saudades. Abrazos al comandante Pedro Castro, Mari Pili, David y Shirley. Abraço Marcia, Carla, Suranny, Gabi, Marcelo, Shella e meu amigo Oluwaseyi. Saudades do carnaval pra sempre. Abrazo Henry! Abrazo a todos en Ibarra y en Quito; aunque no nos vimos mucho estos años, yo les he llevado conmigo a donde he ido.

Abrazos para toda la Bartolomé Salóm 337, la Maldonado 618, la Quito 643 y a la Rue de Profondsart 13!

Cheers to my friends on my way back to Nederland, Luiz, Michael, Lars (met dank aan Lars voor de samenvatting en las conversas bacanas), Haneef, Sivaramakrishnan Chandrasekaran, Oriol, Marijn y la Mona.

Quién sabe lo que nos depara el futuro?

Venga!

Aguardo con mis brazos abiertos.

Curriculum vitae

Eduardo was born in Quito, Ecuador in 1985. He went the University in the same city and obtained his Bachelor diploma in Chemical Engineering in 2012 from the National Polytechnic School. During the last years of his bachelor Eduardo was involved in a project with Prof. Neyda Espín about the production of enzyme extracts with ligninolytic activity. After years of being a technician at a company doing Environmental Impact studies, he went back to academia as a teaching assistant at the National Polytechnic School. During this time, he was awarded a scholarship from the Ecuadorian government and traveled to the Netherlands where, two years after his arrival, in 2016, he received his MSc. Life Science & Technology diploma at Delft University of Technology in 2016. He got involved in the dual-degree PhD program between Delft University of Technology and State University of Campinas in Brazil, and after >6 years he is denfending his PhD dissertation.

List of publications

1. Almeida Benalcázar, E., Noorman, H., Maciel Filho, R., Posada, J.A., "A systematic approach for the processing of experimental data from anaerobic syngas fermentations", Chapter in: *Computer Aided Chemical Engineering*, **2022**, 1303-1308.
2. Almeida Benalcázar, E., Noorman, H., Maciel Filho, R., Posada, J.A., "Decarbonizing ethanol production via gas fermentation: Impact of the $CO/H_2/CO_2$ mix source on greenhouse gas emissions and production costs", *Computers and Chemical Engineering*, **2022**, 107670.
3. Ortega-Pacheco, D., Castro-Verdezoto, P.L., Mendoza-Jiménez, M., Almeida Benalcázar, E., Castro, M.P., "Social and Economic Contribution of the Bioeconomic Sector in Ecuador: A Methodological Approach", Chapter in: *Sustainable Bioeconomy. Pathways to Sustainable Development Goals*, **2020**, 35-65.
4. Almeida Benalcázar, E., Noorman, H., Maciel Filho, R., Posada, J.A., "Assessing the sensitivity of technical performance of three ethanol production

processes based on the fermentation of steel manufacturing offgas, syngas and a 3:1 mixture between H_2 and CO_2", Chapter in: *Computer Aided Chemical Engineering*, **2020**, 589-594.

5. Almeida Benalcázar, E., Noorman, H., Maciel Filho, R., Posada, J.A., "Modeling ethanol production through gas fermentation: a biothermodynamics and mass transfer-based hybrid model for microbial growth in a large-scale bubble column bioreactor", *Biotechnology for Biofuels*, **2020**, 13:59.
6. Almeida Benalcázar, E., Noorman, H., Maciel Filho, R., Posada, J.A., "Hybrid model for ethanol production via syngas fermentation: Coupling between a thermodynamics-based black-box model of bacterial reactions and mass transfer in a large-scale bubble column bioreactor", *European Biomass Conference and Exhibition Proceedings*, **2019**.
7. Almeida Benalcázar, E., Gevers-Deynoot, B., Noorman, H., Osseweijer, P., Posada, J.A., "Production of bulk chemicals from lignocellulosic biomass via thermochemical conversion and syngas fermentation: a comparative techno-economic and environmental assessment of different site-specific supply chain configurations", *Biofuels, Bioproducts and Biorefining*, **2017**, 861-886.